New Configuration for Trigeneration Systems Driven by Renewable Energy Resources

Von der Fakultät für Ingenieurwissenschaften

der Universität Bayreuth

zur Erlangung der Würde einer

Doktor-Ingenieurin (Dr.-Ing.)

genehmigte Dissertation

von

Mehri Akbari Kordlar, Karshenasi arshad reshteh-ye mohandesi-ye mekanik
(Master im Fach Maschinenbauingenieurwesen) / Universität Tabriz

aus

Oroumieh / Iran

Erstgutachter: Prof. Dr.-Ing. D. Brüggemann

Zweitgutachter: Prof. Dr.-Ing. A. Jess

Tag der mündlichen Prüfung: 20.02.2026

Lehrstuhl für Technische Thermodynamik und Transportprozesse (LTTT)

Universität Bayreuth

2026

Abstract

Designing an efficient tri-generation system is essential for optimizing energy use in distribution networks. The primary challenge is meeting the heating and cooling demand, due to differences in the heating or cooling to power ratio between network requirements and system output, complicating configuration and design. This study proposes and analyses two adjustable tri-generation systems powered by geothermal brine. The systems are designed for flexible heating, cooling, and power generation, taking into account both exergetic and economic aspects. For the analysis, annual simulations are performed using typical days according to guideline VDI 4655. These days are determined based on the time of year, user behaviour, and cloudiness. The district heating network considers a fluctuating heat demand throughout the day, with load profiles derived from operational data of an existing geothermal heat plant. For power generation, a Kalina cycle using an ammonia-water solution is implemented. For cooling generation, an absorption refrigeration cycle with the same solution is developed. A domestic heat exchanger is used to meet the heating demand.

The heat exchangers are designed for maximum heat transfer rate under design conditions. Off-design calculations are applied based on the heat exchanger design and turbine models. A parametric analysis is conducted to evaluate the influence of operational parameters on system performance under design condition. The impact of varying heating demands and ambient temperatures on the exergetic performance of the systems during winter and summer is also examined under off-design conditions. An annual simulation is performed to meet the demand of a specific district network, considering the climate conditions in Germany under both design and off-design scenarios. The economic evaluation involves a detailed investment analysis based on net present value to determine the effect of operational parameters on the levelized cost of electricity.

The exergetic results indicate that the exergy efficiency of the proposed systems increases with rising heating demand. It ranges from 48 % to 59 % in winter and from 34 % to 42 % in summer. The increase in exergy efficiency depends on the configuration of the systems, the heating and cooling demand, the supply heating temperature, and the net power produced by the systems. The analysis of the exergy destruction rate also reveals that it decreases as heating demand increases, ranging from 3557 kW to 2983 kW in winter and from 4720 kW to 4094 kW in summer.

From an economic perspective, a detailed evaluation based on the levelized Cost of Electricity indicates that the discount rate, cost escalation, system lifespan, and systems output are the parameters with the most significant impact. The levelized Cost of Electricity increases with a rise in supply heating temperature and decreases with an increase in the temperature of geothermal hot water. Additionally, the levelized Cost of Electricity can vary significantly, potentially doubling, with an increase in drilling costs.

Kurzfassung

Die Auslegung eines effizienten Trigenerationssystems ist entscheidend für die Optimierung des Energieeinsatzes in Verteilnetzen. Die zentrale Herausforderung besteht darin, den Wärme- und Kältebedarf zu decken, da das Verhältnis von Wärme- bzw. Kälte- zu Strombedarf zwischen Netzanforderungen und Systemoutput variiert und dadurch die Konfiguration sowie das Design erschwert werden. In dieser Arbeit werden zwei anpassbare, mit geothermischer Sole betriebene Trigenerationssysteme vorgeschlagen und analysiert. Die Systeme ermöglichen eine flexible Wärme-, Kälte- und Stromerzeugung unter Berücksichtigung exergetischer und ökonomischer Aspekte. Für die Analyse werden Jahressimulationen mit typischen Tagen nach VDI 4655 durchgeführt, wobei Jahreszeit, Nutzerverhalten und Bewölkungsgrad berücksichtigt werden. Das Fernwärmenetz weist dabei einen schwankenden Wärmebedarf auf, basierend auf Lastprofilen einer bestehenden geothermischen Heizzentrale. Zur Stromerzeugung wird ein Kalina-Kreislauf mit einer Ammoniak-Wasser-Lösung eingesetzt, zur Kälteerzeugung ein Absorptionsprozess mit derselben Lösung. Zur Deckung des Wärmebedarfs dient ein Haushaltswärmetauscher.

Die Wärmetauscher sind für maximale Wärmeübertragungsraten unter Auslegungsbedingungen ausgelegt. Berechnungen unter Nicht-Auslegungsbedingungen basieren auf der Wärmetauscherkonstruktion und den Turbinenmodellen. Eine parametrische Analyse untersucht den Einfluss von Betriebsparametern auf die Systemleistung. Darüber hinaus wird der Einfluss variierender Wärmebedarfe und Umgebungstemperaturen auf die exergetische Performance im Winter und Sommer betrachtet. Zusätzlich wird eine Jahressimulation durchgeführt, um den Bedarf eines spezifischen Fernwärmenetzes zu decken, wobei die Klimabedingungen in Deutschland sowohl unter Auslegungs- als auch unter Nicht-Auslegungsszenarien berücksichtigt werden. Die ökonomische Bewertung umfasst eine Investitionsanalyse auf Basis des Kapitalwertes, um den Einfluss der Betriebsparameter auf die Stromgestehungskosten zu bestimmen.

Die Ergebnisse zeigen, dass die Exergieeffizienz mit steigendem Wärmebedarf zunimmt und im Winter Werte zwischen 48 % und 59 %, im Sommer zwischen 34 % und 42 % erreicht. Der Anstieg hängt von der Systemkonfiguration, dem Wärme- und Kältebedarf, der Vorlauftemperatur sowie der Nettostromproduktion ab. Die Exergiedestruktion nimmt mit steigendem Wärmebedarf ab und verringert sich im Winter von 3557 kW auf 2983 kW sowie im Sommer von 4720 kW auf 4094 kW.

Die ökonomische Bewertung verdeutlicht, dass Diskontsatz, Kostensteigerungen, Lebensdauer und Bohrkosten den größten Einfluss auf die Stromgestehungskosten haben. Diese steigen mit höherer Vorlauftemperatur, sinken mit zunehmender Temperatur des geothermischen Heißwassers und können sich bei höheren Bohrkosten deutlich verändern – im Extremfall sogar verdoppeln.

Contents

Nomenclature

Symbols

A	Heat transfer area	m^2
C	Cost	$
c	Cost per unit of energy	$/Wh
D	Diameter	m
d	Diameter	m
$\dot{E}$	Exergy rate	W
e	Specific exergy	J/kg
F	Factor, specified with subscripts	J/kg
h	Specific enthalpy	J/kg
$\bar{h}$	Heat transfer coefficient	W/$(m^2.K)$
k	Thermal conductivity of the fluid	W/ (m.K)
L	Length	m
l	Distance, specified with subscripts	m
M	Molar weight	kg/mol
$\dot{m}$	Mass flow rate	kg/s
N	Number, specified with subscripts	-
n	Frequency of days	-
p	Pressure	bar
Pr	Prandtl number	-
$\hat{q}$	Heat flux	W/m^2
$\dot{Q}$	Heat added to the system	W
Qu	Quality	-
r	General rate, specified with subscripts	-
Re	Reynolds number	-
s	Specific entropy	J/(kg.K)
T	Temperature	℃
u	Velocity of the fluid	m/s
U_0	Overall heat transfer coefficient	W/$(m^2.K)$
U_{int}	Internal energy of the system	J
$\dot{W}$	Net produced power	W
WEG	water-ethylene glycol mixture	-
v	Velocity	m/s
V	Volume of the system	m^3
x	Ammonia concentration	%
X	Distance, specified with subscripts	m
z	Height at the state point	m

Greek Symbols

α	Fluid thermal diffusivity	m^2/s
η_{energy}	Energy efficiency	%
η_{exergy}	Exergy efficiency	%
η_{is}	Isentropic efficiency	%
ρ	Density	kg/m^3

ΔT_{LMTD}	logarithmic mean temperature differences	℃
μ	Dynamic viscosity of the fluid	Pa.s
θ	Angular coordinate, specified with subscripts	Rad
Φ	Constant mass flow coefficient	-
ϖ	Revolving speed of the axial flow turbine	rpm
Y_{id}	Stodola's constant	-
Symbols with subscript		
$A_{fr,t}$	Area occupied by tubes in the window section	m^2
$A_{fr,w}$	Gross (total) window area	m^2
$A_{o,bp}$	Flow bypass area of one baffle	m^2
$A_{o,cr}$	Flow area at or near the shell centerline for one crossflow section	m^2
$A_{o,sb}$	Shell-to-baffle leakage flow area	m^2
$A_{o,tp}$	Tube-to-baffle leakage flow area	m^2
$A_{o,w}$	Net flow area in one window section	m^2
C_0	Original cost (at the year when it was obtained)	$
$c_{heating}$	cost per unit of energy for heating	$/Wh
$c_{cooling}$	cost per unit of energy for cooling	$/Wh
$c_{electricity}$	cost per unit of energy for electricity	$/Wh
C_{aux}	Auxiliary facility costs	$
$C_{BM,i}$	Bare module cost	$
$C^0_{BM,i}$	Bare module cost of equipment	$
$C_{cooling}$	Net revenue associated with producing cooling	$
$C_{drilling}$	Geothermal drilling cost	$
$C_{electricity}$	Net revenue generated from electricity production	$
C_{ref}	Cost at the reference year	$
$C_{heating}$	Net revenue from the heating production	$
C_p	Specific heat	J/(kg.K)
C^0_P	Cost of equipment	$
$C_{o\&m}$	Operation and maintenance costs	$
C_{TM}	Total module cost	$
CF_t	Net cash inflow	$
D_{baffle}	Diameter of baffle	m
$D_{h,w}$	Hydraulic diameter of the window section	m
D_{ctl}	Diameter of the circle through the centres of the outermost tubes	m
D_{otl}	Diameter of the outer tube limit	m
D_s	shell inside diameter	m
$\dot{E}_D$	Exergy destruction rate	kW
$\dot{E}_F$	Fuel exergy rate	kW
$\dot{E}_L$	Loss exergy rate	kW
$\dot{E}_P$	Product exergy rate	kW
$\mathrm{e}^0_{\mathrm{ch}}$	Standard chemical exergy	J/mol
F_{BM}	Bare module factor	-
F_b	Factor of effect of thermosiphon-type circulation	-
F_f	Boiling enhancement factor	-
F_M	Material factor	-

F_P	Pressure factor	-
F_T	LMTD correction factor	-
F_s	Suppression factor	-
F_w	Number of tubes in one window section	-
$\bar{h}_{nb}$	Convective boiling heat transfer	$W/(m^2.K)$
$\bar{h}_{cb}$	Nucleate boiling heat transfer	$W/(m^2.K)$
$\bar{h}_{LO}$	Heat transfer coefficient if the liquid were flowing	$W/(m^2.K)$
$\bar{h}_{nc}$	Nucleate boiling heat transfer coefficient (TEMA K)	$W/(m^2.K)$
$\bar{h}_p$	Pool boiling heat transfer coefficient	$W/(m^2.K)$
I_0	Cost index in the year when the original cost was obtained	$
I_{ref}	Cost index in the reference year	$
$L_{b,c}$	Central baffle spacing	m
$L_{b,i}$	Inlet baffle spacing	mm
$L_{b,o}$	Outlet baffle spacing	
ℓ_c	baffle cut, distance from the baffle tip to the shell inside diameter	m
$\dot{m}_{geo}$	Mass flow rate of geothermal hot water	kg/s
N_b	Number of baffles in a plate-baffled shell-and-tube exchanger	-
N_t	Number of tubes	-
$N_{r,cw}$	Number of effective tube rows during flow through one window zone	-
$N_{r,cc}$	Number of effective tube rows during flow on one crossflow section	-
$N_{t,b}$	total number of tubes associated with one segmental baffle	-
$N_{t,w}$	Number of tubes in the window zone	-
P_c	Critical pressure	bar
P_g	Operational pressure of the equipment	bar
p_t	Tube pitch, center-to-center distance between tubes	m
r_d	Discount rate	%
r_e	Escalation rate	%
r_i	Inflation rate	%
T_0	Ambient Temperature	℃
T_{dead}	Dead state temperature	℃
T_c	Cold side temperature in heat exchanger	℃
T_h	Hot side temperature in heat exchanger	℃
T_{geo}	Geothermal hot water temperature	℃
X_ℓ	Longitudinal (parallel to the flow) tube pitch	m
X_t	Transverse (perpendicular to the flow) tube pitch	m
X_{tt}	Lockhart and Martinelli parameter	-
θ_b	Bend deflection angle	deg
θ_{ctl}	Angle between the baffle cut and two radii	rad
Δh_{is}	shows the isentropic enthalpy drops	J/kg

Abbreviations

ABS	Absorber
ARC	absorption refrigeration cycle
BOI	Boiler
C	Cooling demand
CV	Control volume
D	Destruction
DEP	Dephlepmator

DHE	Domestic heat exchanger
EVA	Evaporator
EX	Expansion valve
Eq.	Equation
GEO	Geothermal hot water
GEN	Generator
H	Heating demand
INT	Internal heat exchanger
KC	Kalina cycle
L	Loss
LCOE	Levelized cost of electricity
NPV	Net present value
p	Product
pp	Pinch point
Pu	Pump
SEP	Separator
SHE	Solution heat exchanger
TCI	total capital investment
TIP	Turbine inlet pressure
TUR	Turbine

1 Introduction

In recent years, heatwaves have affected numerous countries around the globe, setting alarming temperature records and highlighting the urgent need to address climate change [1-5]. For instance, in 2021, Canada experienced a historic heatwave [6], with temperatures reaching an all-time high of 49.6 °C in Lytton [7], British Columbia, leading to devastating wildfires and significant loss of life. In Europe, the summer of 2019 was marked by extreme heatwaves, with France [8] recording its highest temperature ever of 46.0 °C in Vérargues [9]. In the summer of 2019, Germany faced an unprecedented heatwave, with temperatures rising to 42.6 °C in Lingen, Emsland [10]. In the Middle East, countries like Kuwait [11] and Iraq [12] have regularly seen temperatures soar above 50 °C in recent years, putting immense pressure on infrastructure and water resources. Such extreme weather events have underscored the critical necessity of addressing climate change, with a specific focus on curtailing greenhouse gas emissions from the energy sector [13]. In response, there has been a significant shift towards renewable energy sources, which are key in the global effort to reduce CO2 emissions [14]. Renewable energy offers a cleaner, sustainable alternative for meeting energy demands and reducing environmental impact.

Globally, many countries are making significant strides in promoting renewable energy. China, the world's largest producer of solar and wind energy, had installed over 250 GW of solar power and over 280 GW of wind power by the end of 2020, continuing to invest heavily in renewable energy infrastructure [15]. In the United States, renewable energy sources accounted for about 20 % of electricity generation in 2020, with states like California and Texas leading in wind and solar investments [16]. India has set ambitious targets to achieve 175 GW of renewable energy capacity by 2022 and 450 GW by 2030, with significant progress particularly in solar energy [17]. Denmark generates almost half of its electricity from wind turbines and aims to be carbon-neutral by 2050 [18], while Spain's renewables accounted for about 44 % of electricity production by 2020, driven by large-scale solar thermal plants [19].

The use of renewable energy for electricity has seen significant growth globally over the past few decades. In 2023, the United States saw notable advancements in renewable energy consumption, with the total energy use reaching around 29,300 TWh. Of this, heating and cooling (excluding electricity) represented 40 %, transportation accounted for 27 %, and net electricity usage comprised 33 %. The proportion of renewable electricity increased to 25 %, driven by significant contributions from wind, solar, and hydroelectric power [20]. China also saw substantial progress in 2023, with a total energy consumption of about 40,300 TWh. Heating and cooling, excluding electricity, represented 45 % of this total, transportation 18 %, and net electricity usage 37 %. The share of renewable electricity increased to 32 %, driven by significant investments in wind and solar power as part of China's efforts to peak carbon emissions before 2030 and achieve carbon neutrality by 2060 [21]. Germany continued to lead in renewable energy consumption in 2023 [22], with around 2400 billion kWh of total energy use. Heating and cooling accounted for 46 %, transportation 27 %, and net electricity usage 27 %, with over 50 % of electricity coming from renewable sources like wind and solar power [23]. The reduction in nuclear energy following the decommissioning of three power plants, combined with a decreased reliance on natural gas, led to an increased reliance on lignite and hard coal, accounting for 31.4 % of the electricity mix.

Wind energy emerges as the paramount contributor, accounting for a significant portion of the renewable energy sector [24]. Following wind energy, biomass, photovoltaics, and hydro power substantively contribute to the renewable mix, with biomass and photovoltaics alone constituting a noteworthy percentage. However, geothermal energy, despite its relatively minor input, together with other renewable sources, plays a role in the diversification of the energy portfolio [25]. Germany shows a growing commitment to renewable energy, setting ambitious targets for the future. By 2030, it is expected that renewable sources will meet a substantial 65 % of the country's electricity demand [26]. This goal is in line with dedication of Germany to cutting carbon emissions, securing energy supplies, and fostering economic growth via sustainable means. Geothermal energy also offers a renewable option for combined heating, cooling, and power generation. Geothermal energy harnesses the Earth's internal heat, providing a stable and sustainable energy source. Unlike intermittent renewable sources like wind and solar, geothermal energy can supply continuous power, making it a reliable component of a diversified energy portfolio. As of 2023, geothermal power plants worldwide have an installed capacity of over 14 GW, contributing to approximately 0.3 % of global electricity generation [27]. Countries with significant geothermal resources, such as the United States, the Philippines, Indonesia, and Iceland, have been leading the way in geothermal electricity production. For example, the United States is the largest producer of geothermal electricity, with an installed capacity of around 3.7 GW, primarily in states like California and Nevada. Indonesia and the Philippines also have substantial geothermal capacities, with over 2 GW each, leveraging their volcanic geology. Geothermal energy is not only used for electricity generation but also for direct applications such as district heating, greenhouse heating, and industrial processes. Europe, for instance, has over 300 geothermal district heating networks, with a combined capacity of more than 5.5 GW for heating and cooling [28]. In response to these needs, Germany is directing its research and development efforts toward enhancing these versatile geothermal systems. This focus addresses efficiency challenges while also establishing Germany as a leader in advancing sustainable and innovative energy solutions. These efforts testify to the commitment of the country to achieve environmental goals and set a global standard in utilizing renewable energy. Therefore, this research focuses on systems which produce electricity, heating, and cooling driven by geothermal sources.

This study focuses on leveraging geothermal energy to meet seasonal energy demands effectively. Specifically, during the winter months, geothermal energy will be utilized to generate the necessary heating and electricity, ensuring that homes and businesses remain warm and operational despite the cold temperatures. This approach not only reduces reliance on fossil fuels but also provides a stable and consistent energy source. In contrast, during the summer, geothermal systems will offer a comprehensive solution by addressing the needs for heating, cooling, and electricity. The geothermal energy will power air conditioning systems to keep indoor environments comfortable while continuing to supply electricity and hot water. This dual functionality highlights geothermal energy's capacity to adapt to varying seasonal requirements and provides a year-round, sustainable energy solution. By harnessing the internal heat of earth, this research aims to demonstrate the versatility and efficiency of geothermal systems in delivering sustainable energy solutions throughout the year. The study will explore the technical and economic feasibility of widespread geothermal energy use, analyse the environmental benefits, and propose strategies for integrating geothermal technology into existing energy infrastructures. Through this comprehensive analysis, the research seeks to underscore the potential of geothermal energy to significantly reduce carbon emissions, enhance energy security, and contribute to a more sustainable and resilient energy future.

2 Literature review

Recent developments in thermodynamic systems have increasingly emphasized the use of renewable energy. This trend signifies a key shift towards more sustainable and efficient energy solutions in both research and practical applications [29]. This literature review investigates various studies focused on the thermodynamic analysis of co-generation [30-34], tri-generation [35-38], and multi-generation [39-42] systems that utilize renewable energy sources. These systems are renowned for their impressive efficiency in meeting electricity, heating, and cooling demands. Consequently, they have attracted considerable interest from the academic community, industry operators, and energy suppliers. The review aims to synthesize key findings and insights from recent research, highlighting the technological advancements, operational efficiencies, and potential applications of these systems in various sectors. By examining the evolution and current state of renewable-driven thermodynamic systems, this review provides a comprehensive understanding of their role and impact in the broader context of energy sustainability and efficiency. Geothermal energy, in particular, stands out as a significant potential within the realm of renewable energy sources. It offers a constant and reliable source of heat, which is critical for the effective functioning of thermodynamic systems. The reliability of geothermal energy stems from its consistent temperature, which does not vary significantly between summer and winter, unlike other renewable sources that are subject to seasonal and weather fluctuations. This stable temperature allows for predictable and efficient energy production throughout the year.

2.1 Co-generation systems

A co-generation system, also known as a combined heat and power (CHP) or combined cooling and power (CCP) system, is an efficient method of energy production that simultaneously generates electricity and useful thermal energy from a single heat source. By capturing and utilizing the heat that would otherwise be wasted in conventional power generation, CHP systems can achieve energy efficiencies of up to 80 – 90 % [43, 44]. This integrated approach not only reduces fuel consumption and greenhouse gas emissions but also provides a reliable supply of both electricity and heat for various applications, including residential, commercial, and industrial uses. This superior efficiency has driven many scholars to investigate the applications of CHP plants coupled with renewable energy sources [45]. Co-generation systems can be powered by a variety of fuels, including natural gas, biomass, biogas, and renewable sources like solar and geothermal energy, making them a versatile and sustainable solution for modern energy needs. These studies aim to optimize the performance and economic viability of such hybrid systems, demonstrating their potential for improved energy utilization and environmental benefits.

Yuan et al. [46] introduced an ocean thermal energy conversion (OTEC) based solar-assisted combined power and refrigeration cycle, designed for electricity generation and fishery cold storage. This system is depicted in Figure 2.1. The proposed cycle used ammonia-water as the working fluid and warm/cold seawater as the heating/cooling source. It included a two-stage ejector system, a turbine for power production, and an evaporator for refrigeration output. Additionally, a flat-plate solar collector was incorporated to increase the heating source temperature. To assess the performance of the system, a mathematical model and simulation program were developed. Comparison with a previous two-stage ejector OTEC cycle demonstrated that, while the solar-assisted cycle had a slightly lower power production efficiency of 2.27 %, it achieves a much higher comprehensive production efficiency of 7.89 % under the specified conditions.

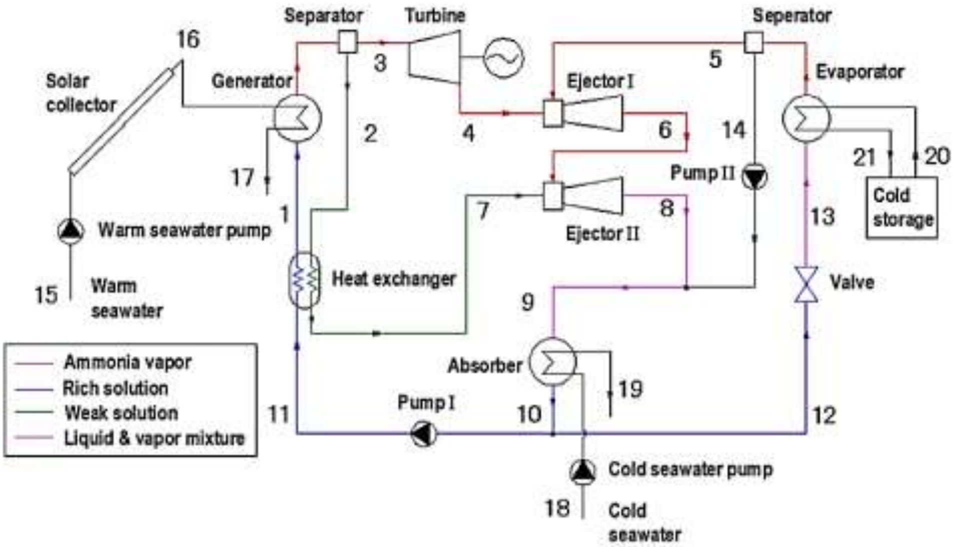

Figure 2.1: Schematic of the solar-assisted combined power and ejector refrigeration cycle by Yuan et al. [46]

Li et al. [47] introduced a solar combined heat and power system that incorporates an absorption heat pump. This system is designed to utilize mid-temperature solar heat and exhaust heat to enhance solar energy utilization and boost electricity generation. This system, as shown in Figure 2.2, is based on the 1 MW solar thermal power tower plant located in Beijing, China. The dynamic simulation accurately predicted the thermodynamic performance of the system under various operating modes on a typical winter day. The results presented that the flexible heating supply of the system effectively met user-generated heating demands. The absorption heat pump system recovered 914 MJ of condensate heat with an average COP of 1.52. Additionally, the system generated 217 kWh of extra power through the regenerative cycle. Overall, it produced 6214 kWh of power and 14,502 MJ of usable thermal energy, achieving a solar energy utilization efficiency of 15.96 %, an increase of 4.55 percentage points.

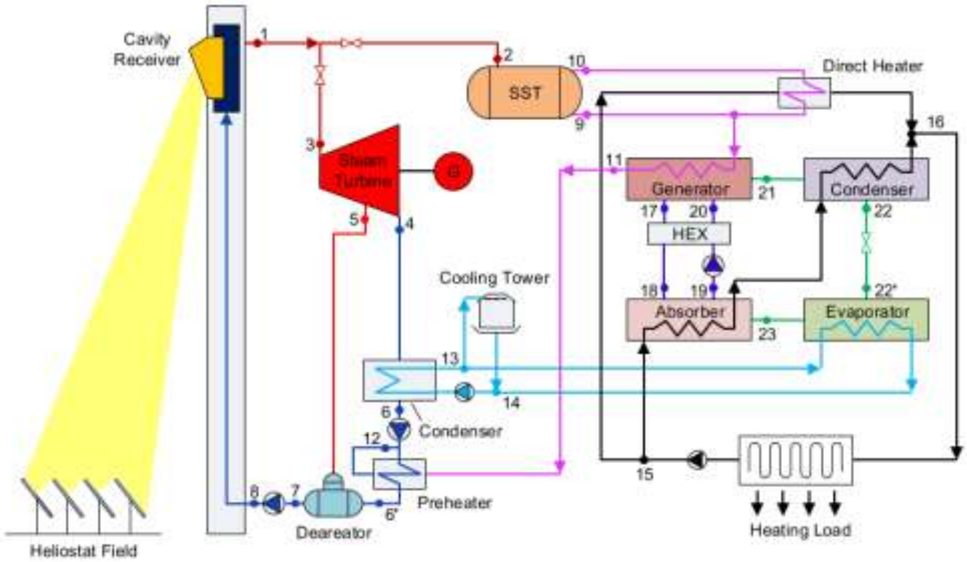

Figure 2.2: Schematic diagram of the solar CHP system proposed by Li et al. [47]

Wang et al. [48] proposed an ammonia-water-based combined heating and power (CHP) system suitable for low-grade heat sources, integrating a superheated Kalina cycle with a compression heat pump cycle to simultaneously provide power and hot air to users. The schematic diagram is presented in Figure 2.3. They developed mathematical models of the CHP system for simulation and analysis. An exergy loss analysis under preliminary design operation conditions indicated that the vapor generator and heat supplier are the primary sources of exergy destruction within the equipment. Thermodynamic parameter analysis revealed that there is an optimal high pressure that maximizes system exergy efficiency. Within certain ranges, a lower middle pressure, a lower separation temperature, a higher low pressure, and a higher ammonia mass fraction in the basic solution contribute to higher exergy efficiencies. The turbine inlet temperature has minimal impact on the exergy efficiency of the system.

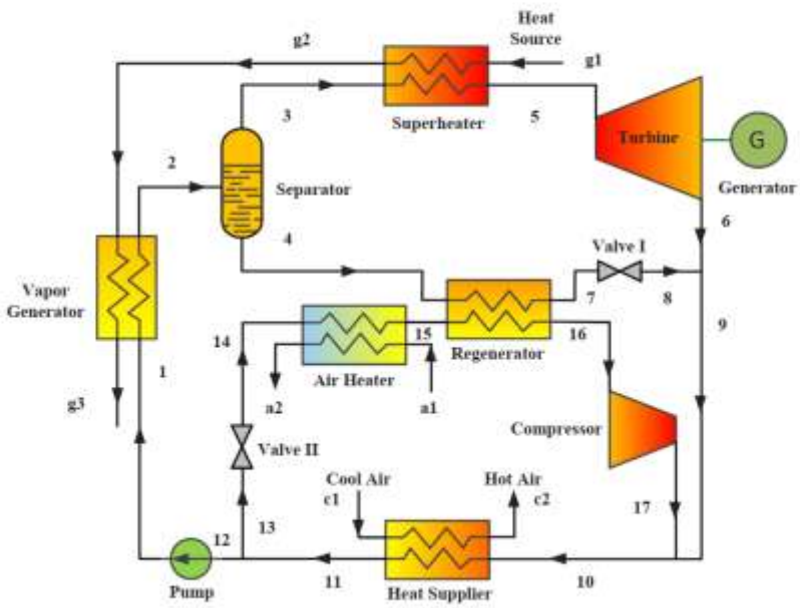

Figure 2.3: Ammonia-water based combined heating and power system, proposed by Wang et al. [48]

Khanmohammadi et al. [49] introduced a parabolic solar collector integrated combined power and refrigeration system featuring a thermoelectric generator, as illustrated in figure 2.3. This system comprises a parabolic trough solar collector, a supercritical Brayton cycle, a transcritical Rankine cycle, a vapor-compression refrigeration cycle, and thermoelectric generator modules (TEG). The results indicated that the incorporation of thermoelectric units enhanced the exergy performance of the system, with an exergy destruction rate of 803.4 kW, compared to 821.38 kW for the system without the thermoelectric generator. Parametric analyses demonstrated that various system parameters similarly affect the performance of both combined power and refrigeration with and without TEG. Additionally, the exergo-economic analysis revealed that the cost of generated power for TEG I and II was 0.6311 US$/h and 2.202 US$/h, respectively, while the cooling costs were 0.994 US$/h and 0.7462 US$/kWh.

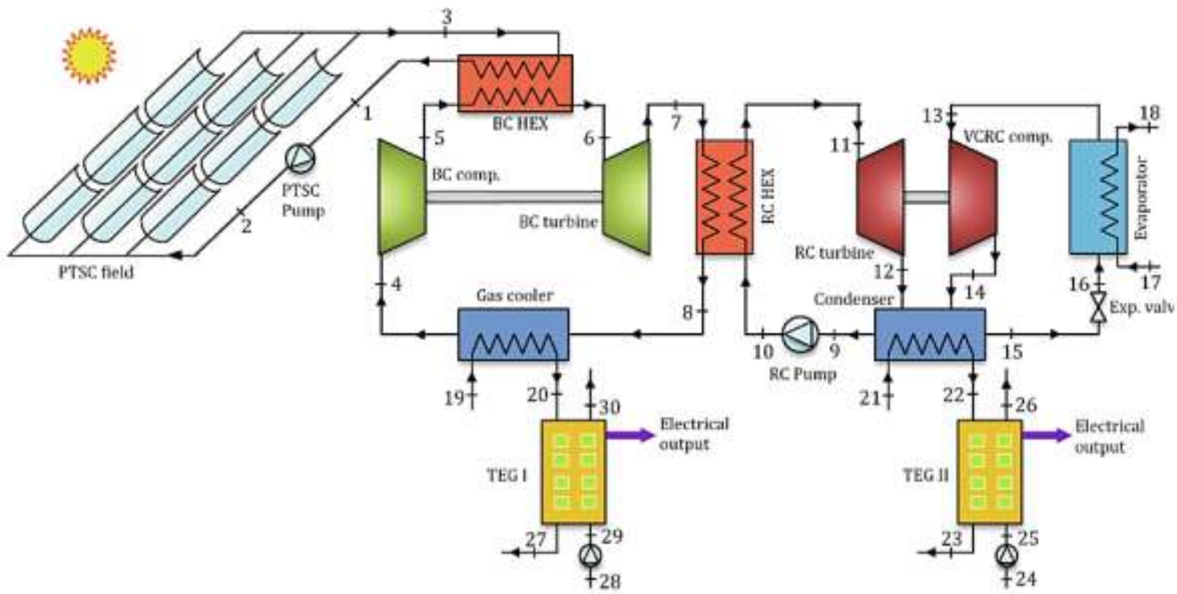

Figure 2.4: The schematic representation of the parabolic solar collector integrated power and cooling system, proposed by Khanmohammadi et al. [49]

Chen et al. [50] evaluated a hybrid renewable energy system that integrates solar thermal energy with a biomass-fired Combined Heat and Power plant. As sketched in Figure 2.5, the biomass-fired CHP plant mainly consists of a water-cooled vibrating grate boiler, condensing steam turbine, and electric generator (EG). During the heating season, which lasts from October 15th to April 15th of the following year, a portion of the steam extracted at stage 3 in Figure 2.5 is used to heat the supply water in the primary heating network's supply-water heater, thereby providing heat to the local residents. The system used parabolic trough collectors to harvest solar heat, which is then fed into the steam cycle of the biomass plant. The hybrid solar-biomass CHP system proposed by Chen et al. [50] is shown in Figure 2.6. This solar heat is utilized to drive an absorption heat pump for heating or to warm the feedwater entering the boiler, thus saving extraction steam, and boosting power output. The thermodynamic and economic performance of the hybrid system was assessed based on a typical biomass-fired cogeneration plant, under different operation modes and solar conditions. The results indicated that the solar-to-electricity conversion efficiency could reach 19.38 % or 16.92 % depending on the operation mode. The study concluded that the cogeneration mode was superior to the power generation mode, with the system capable of generating 2803.04 MWh of solar-based electricity annually at a levelized cost of electricity of 0.1306 $/kWh, highlighting its economic and environmental benefits.

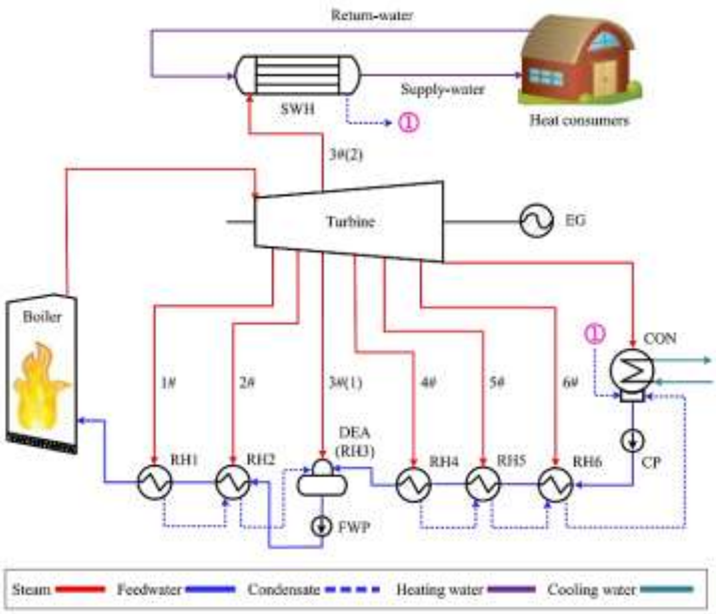

Figure 2.5: Diagram of the biomass-fired CHP plant proposed by Chen et al. [50]

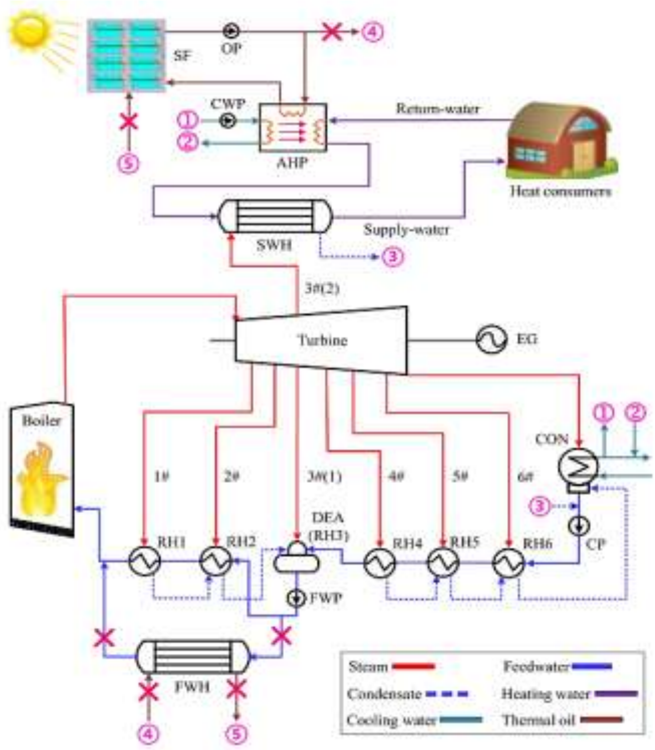

Figure 2.6: Diagram of the solar-aided biomass-fired CHP plant proposed by Chen et al. [50]

2.2 Tri /multi-generation systems

A tri-generation system, also known as combined cooling, heat, and power (CCHP), is an advanced energy solution that simultaneously produces electricity, useful heat, and cooling from a single fuel source. This approach significantly enhances overall energy efficiency and environmental sustainability by utilizing the waste heat from electricity generation for additional purposes. Tri-generation systems achieve higher overall efficiencies compared to separate heat and power systems. The efficiency can reach up to 80 – 90 % [51, 52], as they capture and repurpose waste heat for cooling purposes using absorption chillers. These systems can operate on a variety of fuels, including natural gas, biomass, biogas, and renewable energy sources such as solar and geothermal energy. This versatility allows for greater flexibility and sustainability in meeting energy needs [53, 55].

Sahoo et al. [56] introduced a polygeneration process for the simultaneous production of power, vapor absorption refrigeration (VAR) cooling, and multi-effect humidification and dehumidification (MEHD) desalination using different heat sources in a hybrid solar-biomass (HSB) system with enhanced energy efficiency. It is shown in Figure 2.7. This approach addressed energy demands from renewable sources and helped reduce carbon dioxide emissions. The VAR cooling system operated using extracted heat from the turbine, and the condenser heat from the VAR system was utilized in the desalination process to produce drinking water as needed. Although electricity production decreased due to heat extraction for VAR cooling and desalination, the overall system meets energy requirements and increases primary energy savings (PES). The thermodynamic evaluation and optimization of the HSB system in the polygeneration process for combined power, cooling, and desalination identified the effects of various operating parameters. The polygeneration process in the HSB system achieved primary energy savings of 50.5 %, with the energy output increased to 78.12 % compared to a simple power plant.

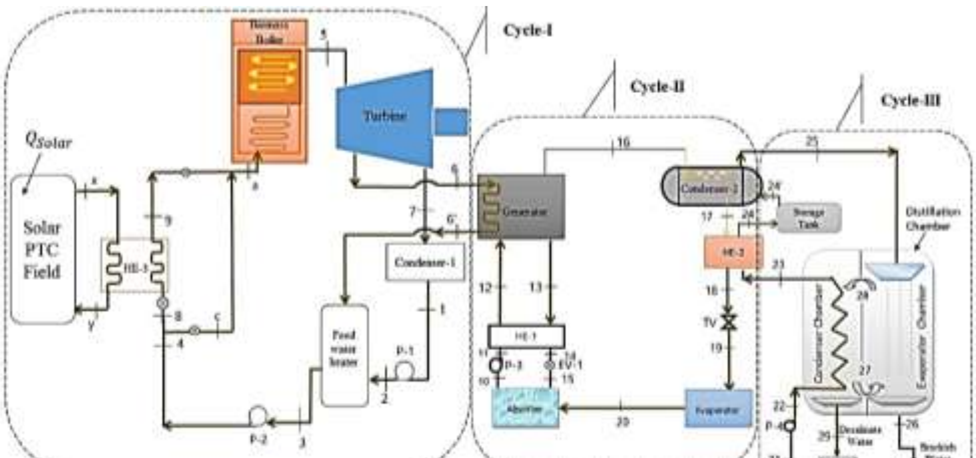

Figure 2.7: Schematic diagram of hybrid solar-biomass power plant with combined power, cooling, and desalination in polygeneration process, proposed by Sahpoo et al. [56]

Eisavi et al.
[57] presented a combined cooling, heating, and power (CCHP) system driven by solar energy, as illustrated in Figure 2.8. This system incorporated an Organic Rankine Cycle (ORC), a double-effect lithium bromide-water absorption refrigeration system, and heat exchangers to produce electricity, cooling, and heating, respectively. To evaluate the efficiencies and losses of the system, energy and exergy analyses were performed. The performance of this cycle was compared with a similar combined cycle that employs a single-effect absorption chiller in its cooling subsystem. The study investigated the impact of several key thermodynamic parameters on cycle performance. The findings indicated that, with the same input heat, replacing a single-effect absorption chiller with a double-effect absorption refrigeration system could increase cooling power by up to 48.5 %, enhancing system performance. Concurrently, heating power increased by 20.5 %, leading to a rise in cogeneration heat and power efficiency to 96.0 %, though net electrical power production decreases by 27 %. Additionally, it was found that the solar collectors exhibit a high rate of exergy destruction.

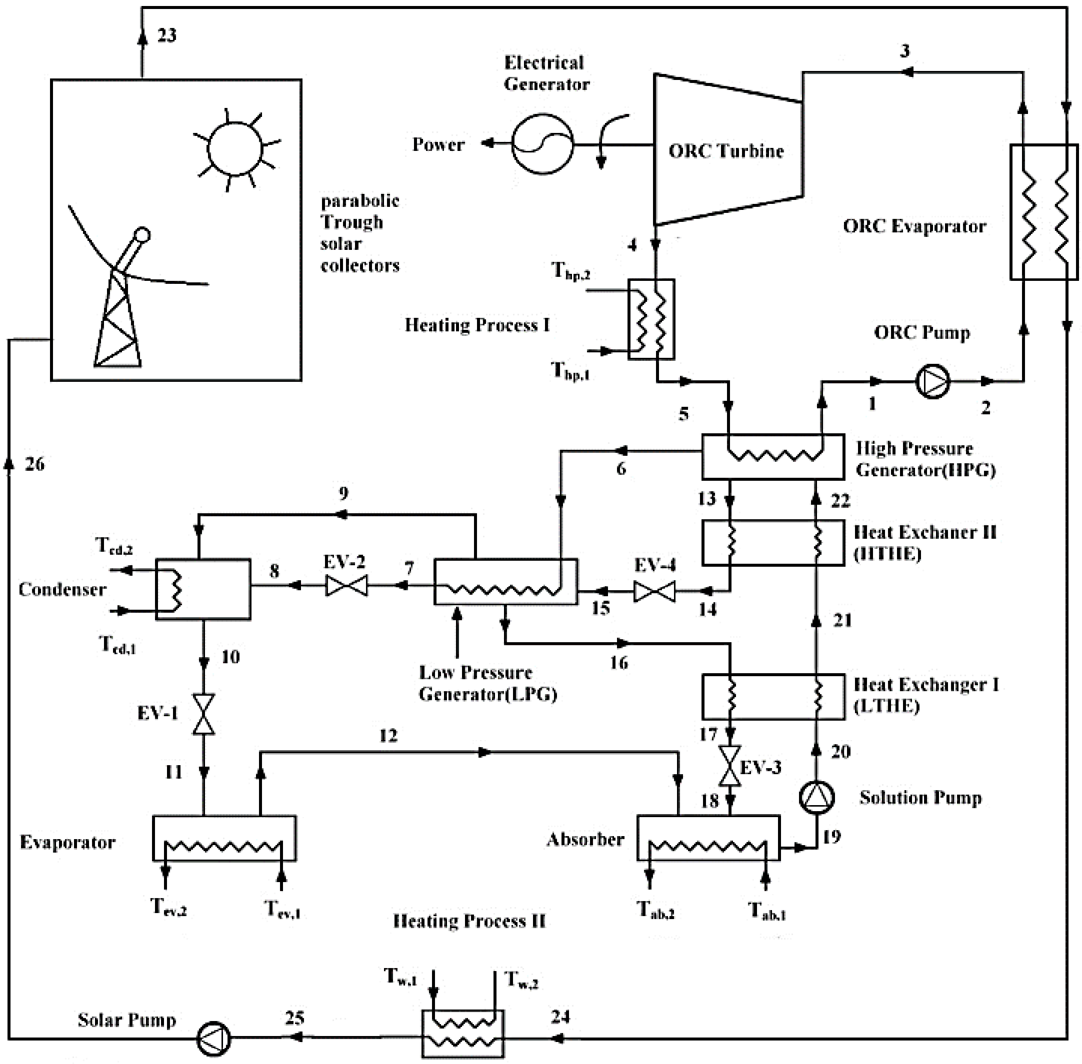

Figure 2.8: Schematic of CCHP system, proposed by Eisavi et al. [57]

Wang et al. [58] presented a combined cooling, heating, and power (CCHP) system based on solar thermal biomass gasification. Figure 2.9 illustrates the schematic diagram of the proposed system. With a capacity of 100 kW electricity, the design parameters were used to simulate and analyse thermodynamic performances, as well as energy and exergy flow diagrams for cooling and heating modes. The system achieved average energy and exergy efficiencies of 56 % and 28 %, respectively, and the solar-to-biomass energy ratio was approximately 0.19 at full load. The solar integration improved the product gas heating value by 55.09 % and reduces biomass consumption by 9.22 % and 2.02 % in cooling and heating modes, respectively, demonstrating the system effectiveness of the system and feasibility in enhancing biomass energy utilization.

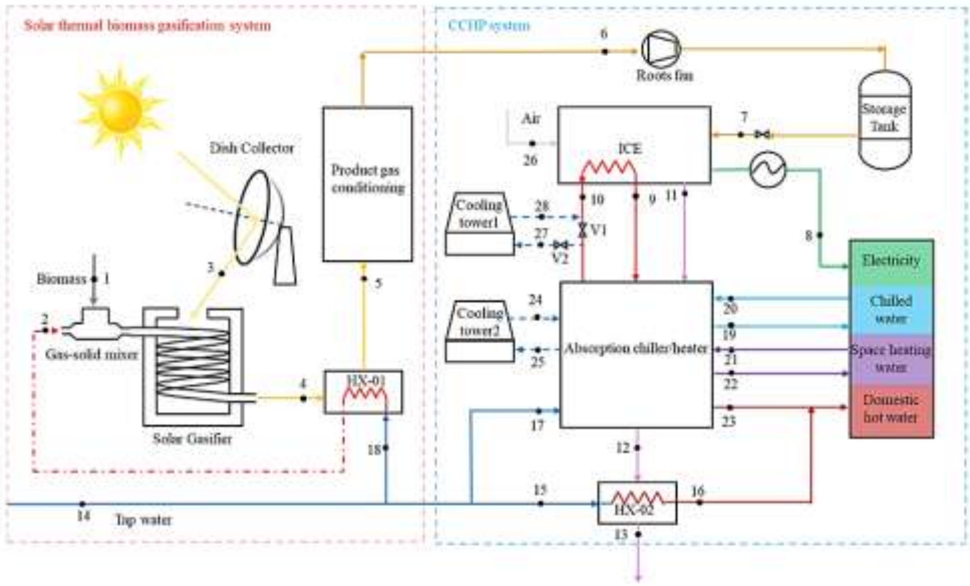

Figure 2.9: Flowcharts of the tri-generation system based on solar thermal biomass gasification proposed by Wang et al. [58]

Alirahmi et al. [59] proposed a multi-generation system utilizing geothermal energy and parabolic trough solar collectors to simultaneously produce power, cooling, freshwater, hydrogen, and heat, as illustrated in Figure 2.10. The power generation component integrated a combined steam Rankine cycle and an organic Rankine cycle, employing ten different refrigerants, with R123 demonstrating the best performance. Additionally, four fluids were tested as geothermal fluids, with Therminol 59 showing the highest efficiency. The study identified solar intensity, geothermal mass flow rate, geothermal fluid temperature, and steam turbine inlet pressure as key parameters influencing exergy efficiency and cost. The system was analysed from energy, exergy, and exergoeconomic perspectives. To enhance system performance, a multi-objective optimization genetic algorithm was applied, linking Engineering Equation Solver and MATLAB software via the Dynamic Data Exchange method. The optimization results revealed that the system's exergy efficiency reaches 29.95 % and the total unit cost is 129.7 $/GJ at the optimal point.

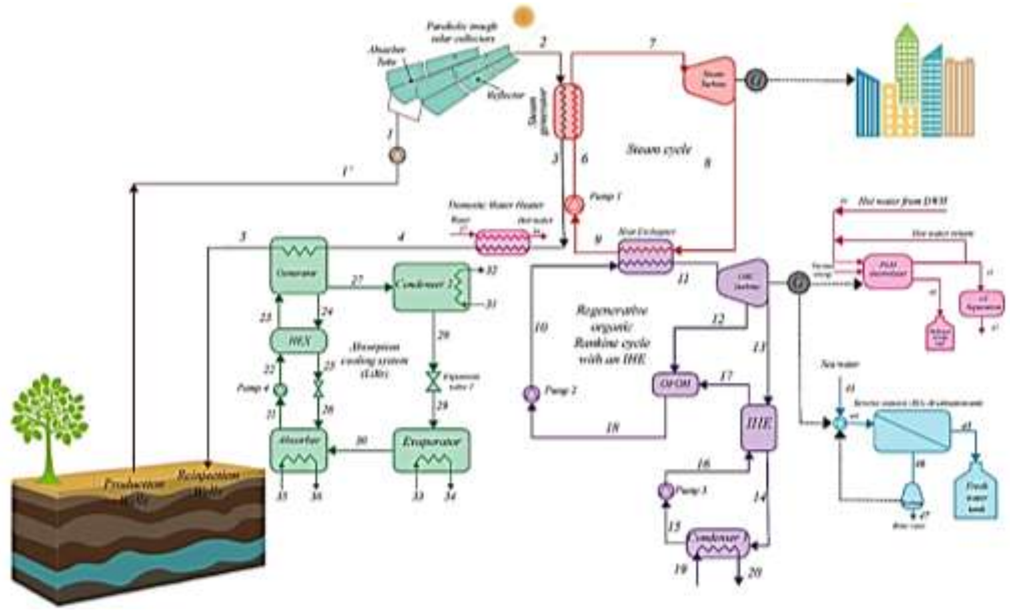

Figure 2.10: Schematic diagram of the multi-generation energy system based on geothermal and solar, proposed by Alirahmi et al. [59]

Chen et al. [60] proposed a combined cooling, heating and power (CCHP) system driven by parabolic trough collectors. In addition, geothermal energy is utilized as lower-grade heat. The flowchart of the hybrid CCHP system proposed by Chen et al. is depicted in Figure 2.11. The CCHP system consisted of three main units: concentrating solar thermal device, organic Rankine cycle and absorption heat pump units. The results of the exergo-economic performance showed that the absorption heat pump could achieve a coefficient of performance ranging from 1.38 to 2.37 depending on the operational mode. The annual energy and exergy efficiencies of the tri-generation system were found to be 56.5 % and 9.6 %, respectively. In addition, the specific exergo-economic cost of electricity produced by the system is 0.12 $/kWh, while the cost for hot water is significantly higher at 0.31 $/kWh.

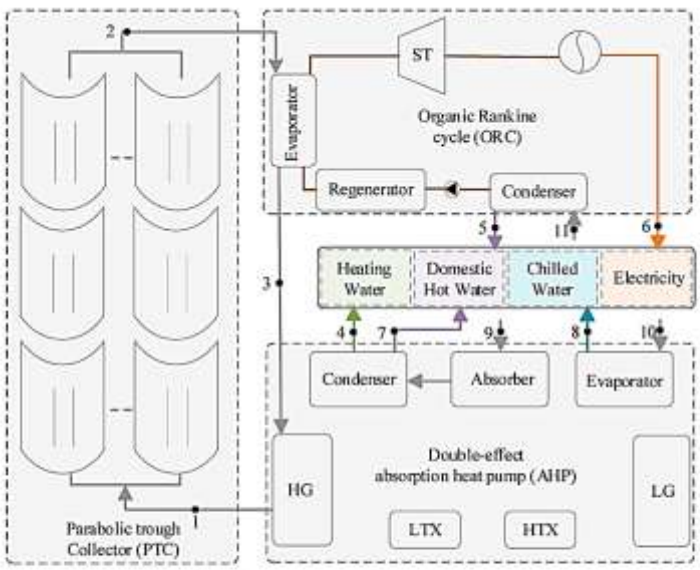

Figure 2.11: Combined cooling, heating and power proposed system by Chen et al. [60]

2.3 Co-generation systems for geothermal applications

There is a diverse range of studies in this field that investigate the efficiency, sustainability, and technological aspects of cogeneration systems powered by geothermal energy. These studies collectively underscore the potential of geothermal sources to significantly contribute to the global energy mix, while also highlighting the challenges and opportunities inherent in their implementation [61,62]. This literature review aims to make these findings, offering a comprehensive understanding of the current advancements and prospects of geothermal-driven cogeneration systems.

Eller et al. [63] proposed a geothermal power plant based on the organic Rankine cycle (ORC) to convert the thermal power of brine into electricity, with the efficiency and profitability of these power plants enhanced by additional heat supply. The system is shown in Figure 2.12. A dynamic simulation model of a double-stage ORC was developed to perform annual return simulations and validated against operational data from an existing power plant in the German Molasse Basin. Results indicated that additional heat extraction increases exergetic efficiency and profitability by up to 7.9 % and 16.1 %, respectively, with the combined configuration slightly outperforming the parallel configuration. Efficiency improvements of up to 1.3 % and economic benefits with annual returns increased by at least 2.5 million euros were observed.

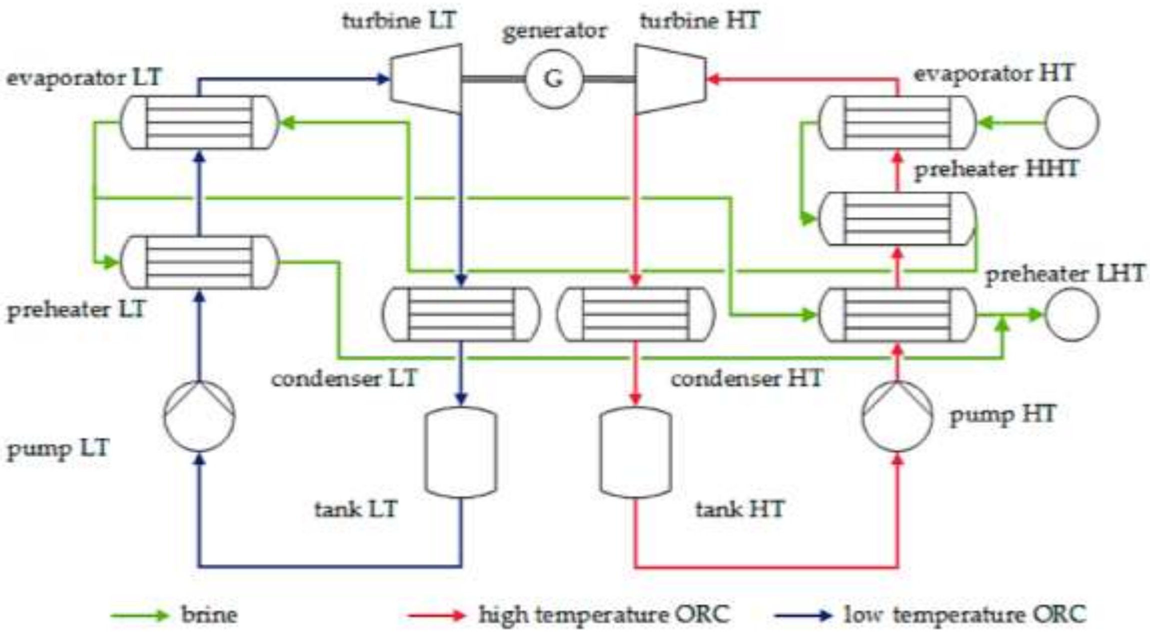

Figure 2.12: Scheme of the double-stage organic Rankine cycle (ORC) power plant, proposed by Eller et al. [63]

Barkhordarian et al. [64] proposed an ammonia-water co-generation system, depicted in Figure 2.13, that combines the Kalina cycle with the ejector refrigeration cycle to simultaneously provide power and cooling. The system, utilizing a heat source temperature of 300 ℃ , features two evaporators capable of producing refrigeration output at different temperature levels and capacities, with the first evaporator pressure independently selectable. One notable feature of this cycle is its adjustable power-to-cooling ratio, which can be modified by changing the reboiler reflux ratio. Design calculations for the base case condition, with a power-to-cooling ratio of 5.28, indicated that the system produced 114.8 kW of refrigeration and 605.9 kW of power. The system's thermal efficiency was determined to be 19 %, while the exergy efficiency stood at 38.97 %, all evaluated at a constant ambient temperature of 27 °C.

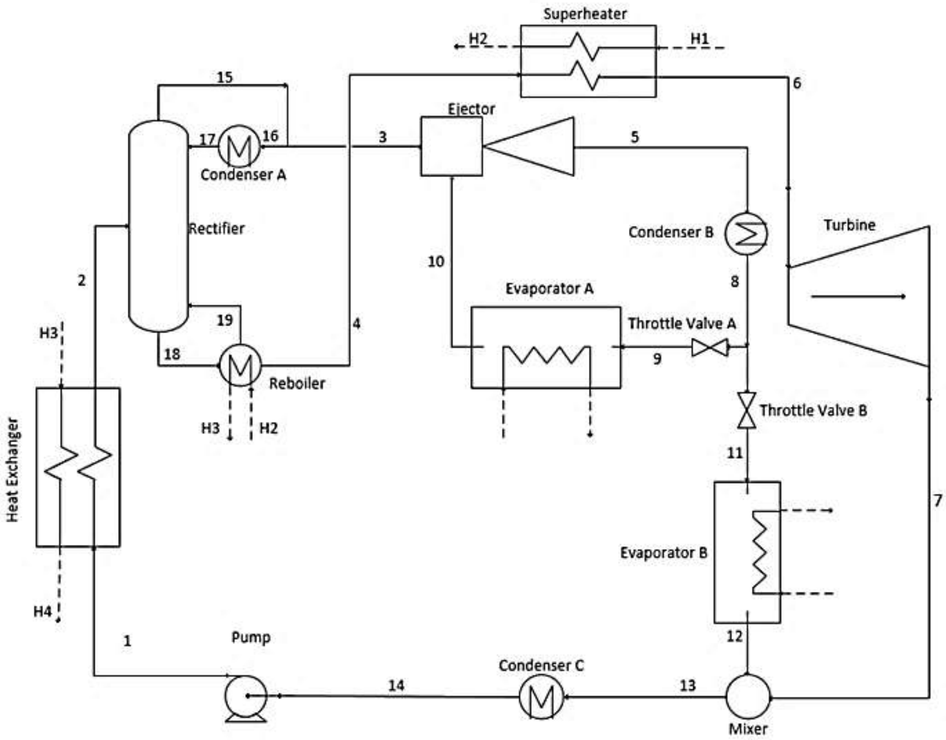

Figure 2.13: Schematic diagram of combined power/refrigeration cycle, proposed by Barkhordarian et al. [64]

A renewable energy system combining geothermal energy with liquid air energy storage for efficient power generation and district cooling is introduced by Çetin et al. [65]. The system integrated various cycles: a turbine ejector cogeneration cycle, an air liquefaction cycle, a liquid air direct expansion cycle, and a cryogenic organic Rankine cycle. It operated in three modes: normal, charging, and discharging. Utilizing a geothermal source at 180 °C with a 100 kg/s flow rate, the system could produce 15,470 kW of power and 4800 kW of cooling. It boasted a 41.07 % round-trip efficiency and a 60.43 % exergy efficiency in cryogenic energy storage. The paper also investigated how factors like geothermal temperature, system size, turbine mass split ratio, and mass flow rate affect performance, providing valuable insights for optimizing such renewable energy systems.

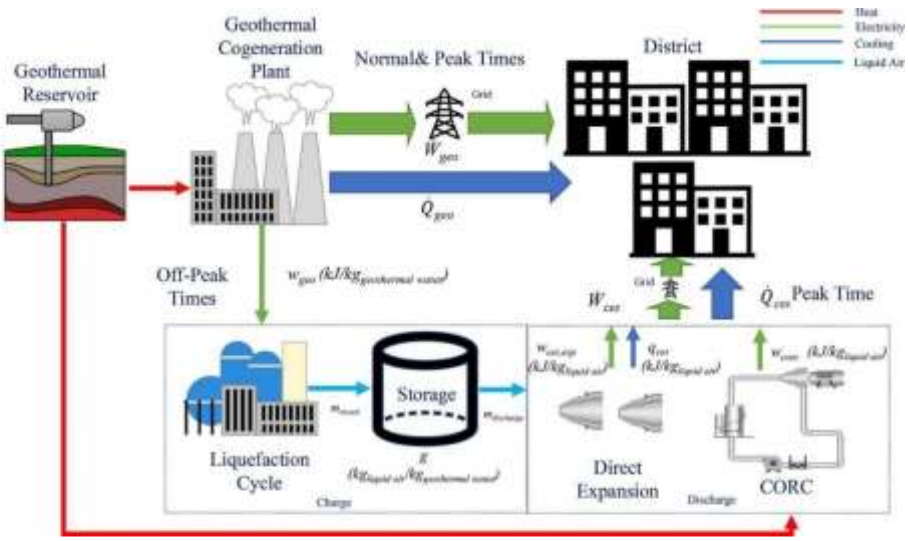

Figure 2.14: Schematic diagram of combined power/refrigeration cycle, proposed by Çetin et al. [65]

In the study by Wang et al. [66], a combined cooling and power generation system based on flash-binary geothermal of 188 °C is presented. This system was significant for cogeneration applications, integrating the Organic Rankine Cycle (ORC) with an ejector refrigeration cycle, constituting the binary subsystem. A key feature of this system was its utilization of zeotropic mixtures, enhancing the efficiency of the binary unit. The feasibility of the system was evaluated using energy and exergy analysis, followed by optimization with a genetic algorithm. This optimization yielded substantial improvements, including an increase in total cooling capacity, net output power, energy efficiency, and exergetic efficiency. For the specific zeotropic mixture of Pentane (0.533)/Butane (0.467), the system achieved a cooling capacity of 330.7 kW, net output power of 1.687 MW, thermal efficiency of 19.20 %, and exergetic efficiency of 53.27 %. In addition, the highest exergy destruction rates within the binary unit were observed in the generator and ejector components.

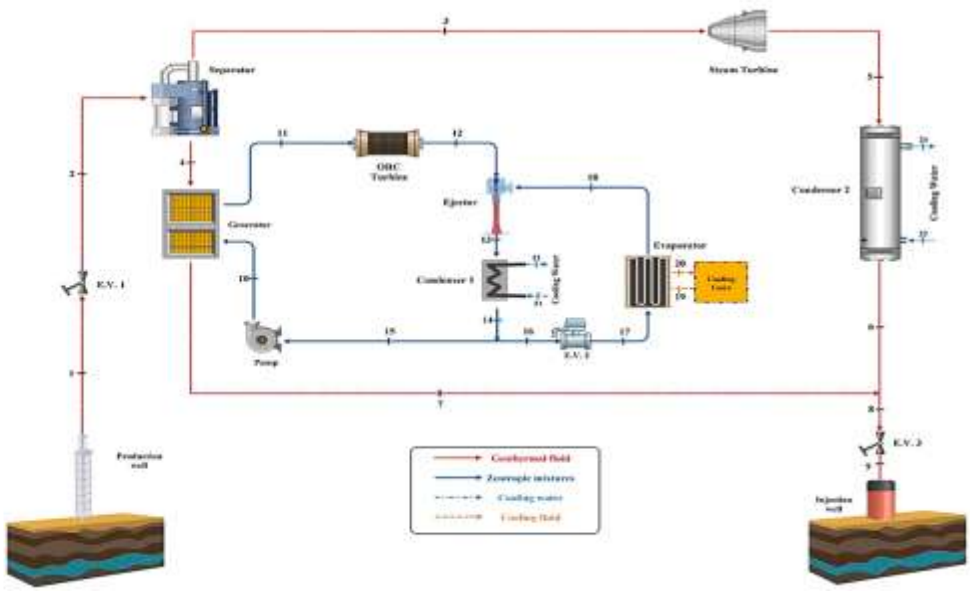

Figure 2.15: Schematic diagram of combined power/refrigeration cycle, proposed by Wang et al. [66]

In the study by Leveni and Cozzolino [67], a modified Goswami cycle-based geothermal system is proposed for efficient and simultaneous production of cooling and power. This system is shown in Figure 2.16. The system standed out for its simplicity, featuring fewer components, which leads to reduced heat loss and improved energy conversion efficiency. In addition, the design of the system included an internal recovery of heat rejected by the rectifier, enhancing overall efficiency. The system was modelled in detail to assess exergy destruction, performance, and component costs. A comparative evaluation with a cascade system (Organic Rankine Cycle with a water/lithium bromide absorption chiller) under the conditions of the Torre Alfina geothermal reservoir in Italy demonstrated the Goswami system's superior performance. The Goswami cycle in the study utilized geothermal source outlet temperatures ranging from 117.85 °C to 111.85 °C, while the cascade system operated at 82.85 °C. In terms of efficiency, the Goswami cycle achieved an exergy efficiency of 35.53 %, outperforming the 32.77 % of the cascade system. Economically, the component cost for the Goswami cycle was more favorable, totaling 11.8 million euros, compared to 14.6 million euros for the cascade system.

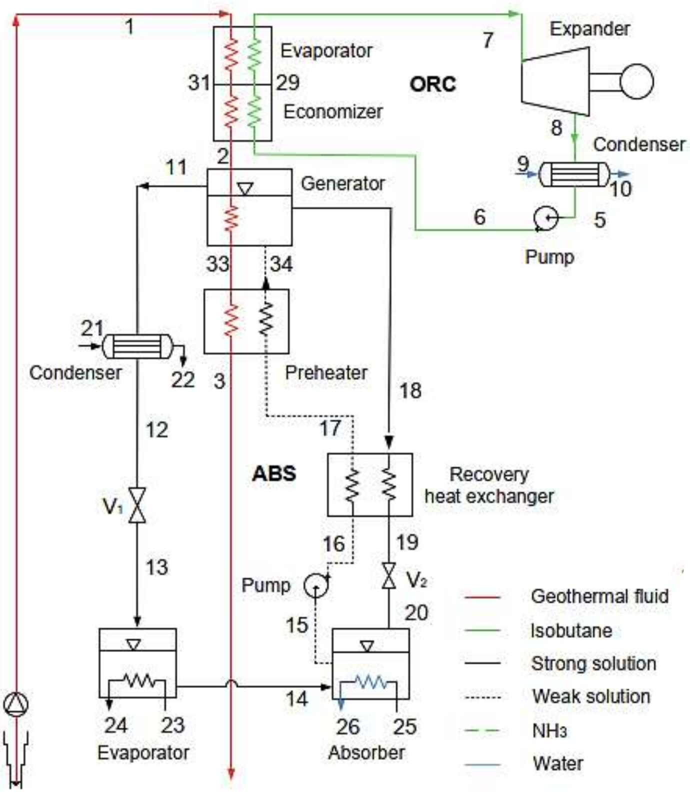

Figure 2.16: Plant schematics: cascade ORC/ABS proposed by Leveni and Cozzolino [67]

2.4 Tri /multi-generation systems for geothermal applications

The literature on tri-generation systems powered by geothermal energy addresses their potential to enhance the efficiency of the global energy mix and sustainability [68]. Studies have focused on various aspects, including the optimization of system efficiency, the integration of sustainable practices, and the technological advancements necessary for the effective implementation of these systems [69]. Geothermal tri-generation systems are lauded for their ability to provide a stable, low-carbon energy source that can significantly reduce emissions and energy consumption [70]. The research also discusses the challenges faced, such as high initial costs and technological barriers. However, the potential for innovation in materials, smart technologies, and renewable integration offers promising ways for overcoming these challenges. This review aims to gather these findings, providing a clear view of the progress and possibilities in the field of geothermal tri-generation energy systems [71].
Ghaebi et al. [72] proposed a multi-generation system utilizing a geothermal heat source, producing cooling, heating, power, and freshwater simultaneously. The system included a Kalina cycle, an absorption refrigeration cycle, a humidification-dehumidification desalination system, and a domestic water heater. Exergoeconomic optimization revealed optimal thermal efficiency at 94.84 %, exergy efficiency at 47.89 %, and total sum unit cost of products at 89.95 $/GJ. A parametric study showed that thermal and exergy efficiencies can be optimized by adjusting various operational parameters, enhancing overall system performance.

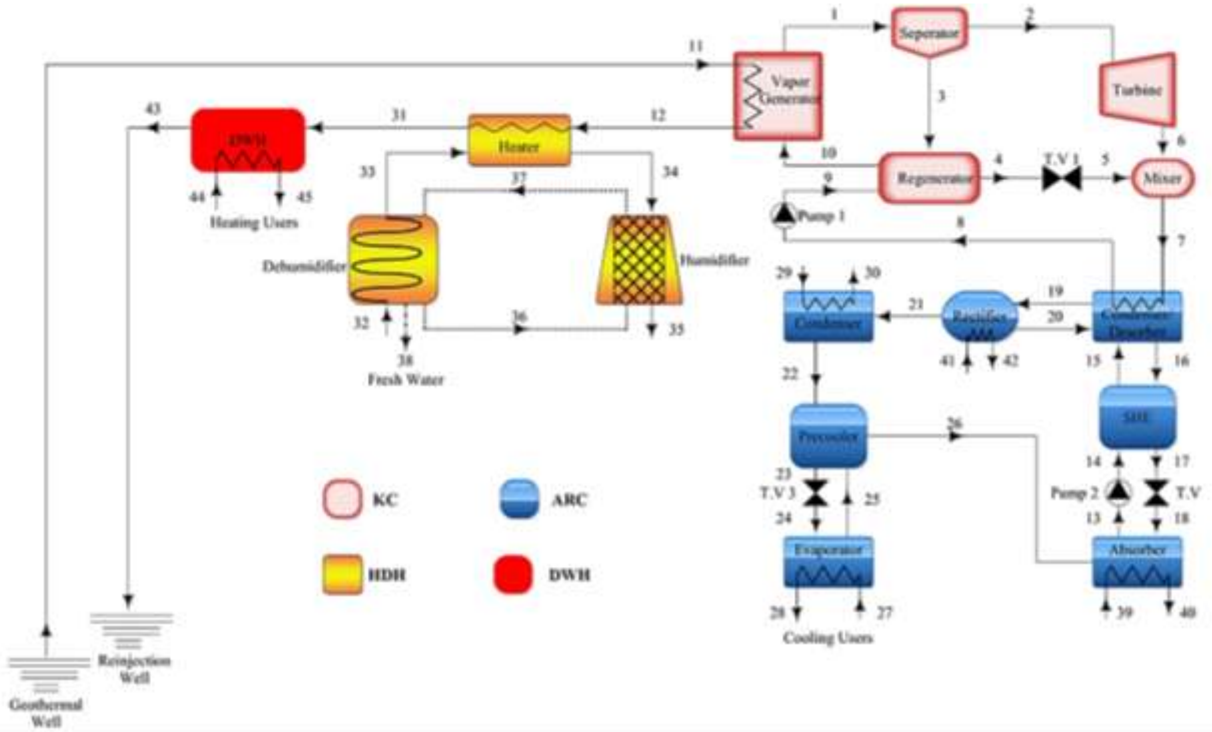

Figure 2.17: Schematic diagram of the proposed multi-generation system by Ghaebi et al. [72] for cooling, heating, power, and freshwater production

Musharavati et al. [73] investigated a multi-generation system driven by a geothermal heat source of 170 °C to provide electricity, cooling, heating, and freshwater. The system is a combination of an absorption chiller, an organic flash cycle, a concentrated photovoltaic module, a reverse osmosis unit, and thermoelectric modules as shown in Figure 2.18. Key performance metrics such as energy efficiency, exergy efficiency, the rate of exergy destruction, net power output, and the rate of electrical cost have been established. The influence of various operational variables, including geothermal temperature, flash vessel inlet pressure, and pump outlet pressure, on the principal outputs of the system was systematically investigated. Thermal modelling results revealed that, compared to a conventional setup, the proposed system achieves improvements of 5.46 % in energy efficiency, 20.16 % in exergy efficiency, and a 70.85 kW increase in net output power. Additionally, exergo-economic analyses identified the thermoelectric generator module and heat exchanger as the components with the highest exergy destruction cost rates, at 11.34 $/h and 8.98 $/h respectively. Through the application of multi-objective optimization scenarios, it was determined that the first scenario yields the most cost-effective operation, with the electricity cost rate reaching a minimum of 108.4 $/h.

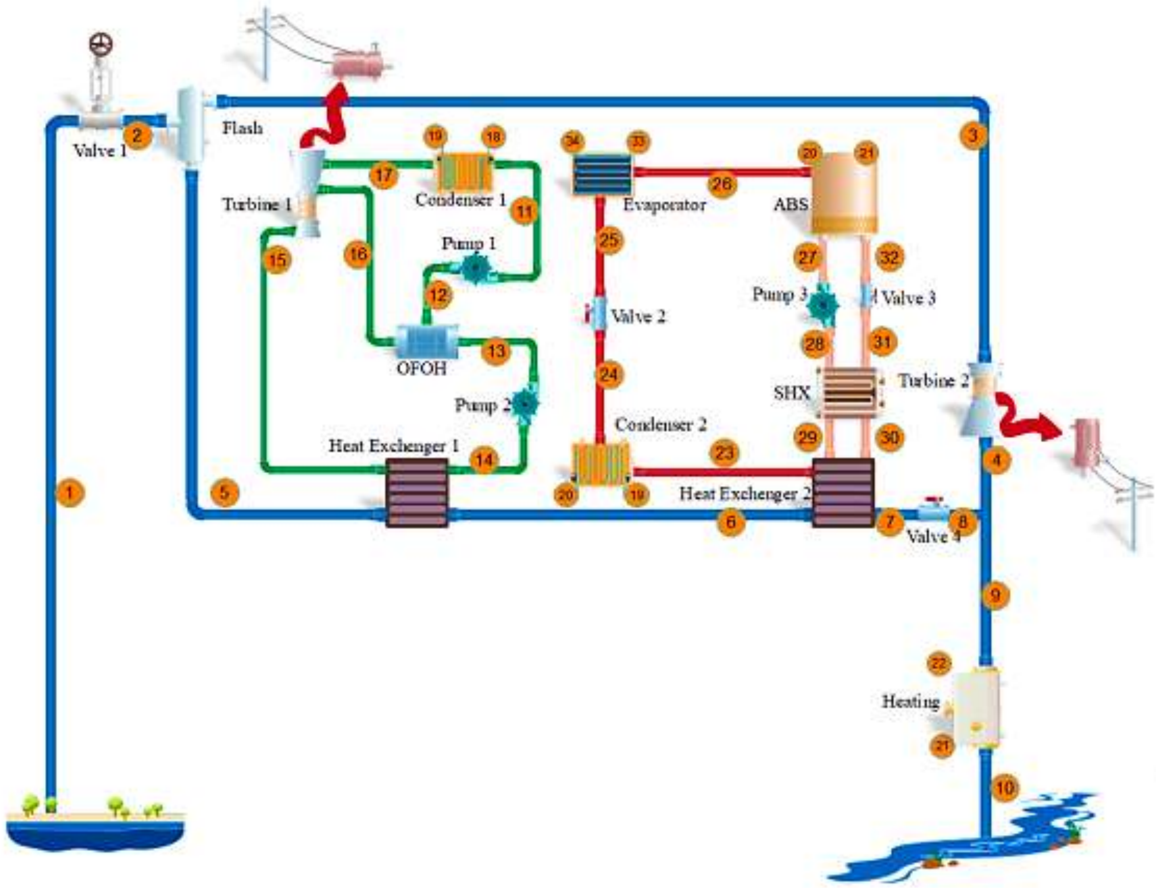

Figure 2.18: Layout of proposed system by Musharavati et al. [73]

Yilmaz [74] proposed a combined system for multi-generation products at the geothermal temperature of 160 °C. The system has two organic Rankine cycles using n-pentane and n-butane as their working fluids. Additionally, the system included an absorption cooling cycle that operates with a lithium bromide-water solution and a Proton Exchange Membrane electrolyser. Comprehensive thermodynamic assessments and environmental impact analyses was conducted to evaluate the efficacy of the system and its contribution to reducing greenhouse gas emissions. An environmental impact assessment specifically addressed the potential reductions in greenhouse gas emissions by comparing the performance of the system with traditional non-renewable energy-based fuel systems used for power generation. The findings indicated that the total energy and exergy efficiencies of the plant are 63.28 % and 55.99 %, respectively. Within the system, ORC-1 and ORC-2 exhibit energy efficiencies of 22.31 % and 25.18 %, respectively. The outputs for heating, cooling, and hydrogen production were determined to be 806.4 kW, 758 kW, and 9.0036 kg/h, correspondingly. Furthermore, it was estimated that the cycle can prevent approximately 26,421 tonnes of CO_2 emissions annually when compared to a coal-powered plant of equivalent power generation capacity.

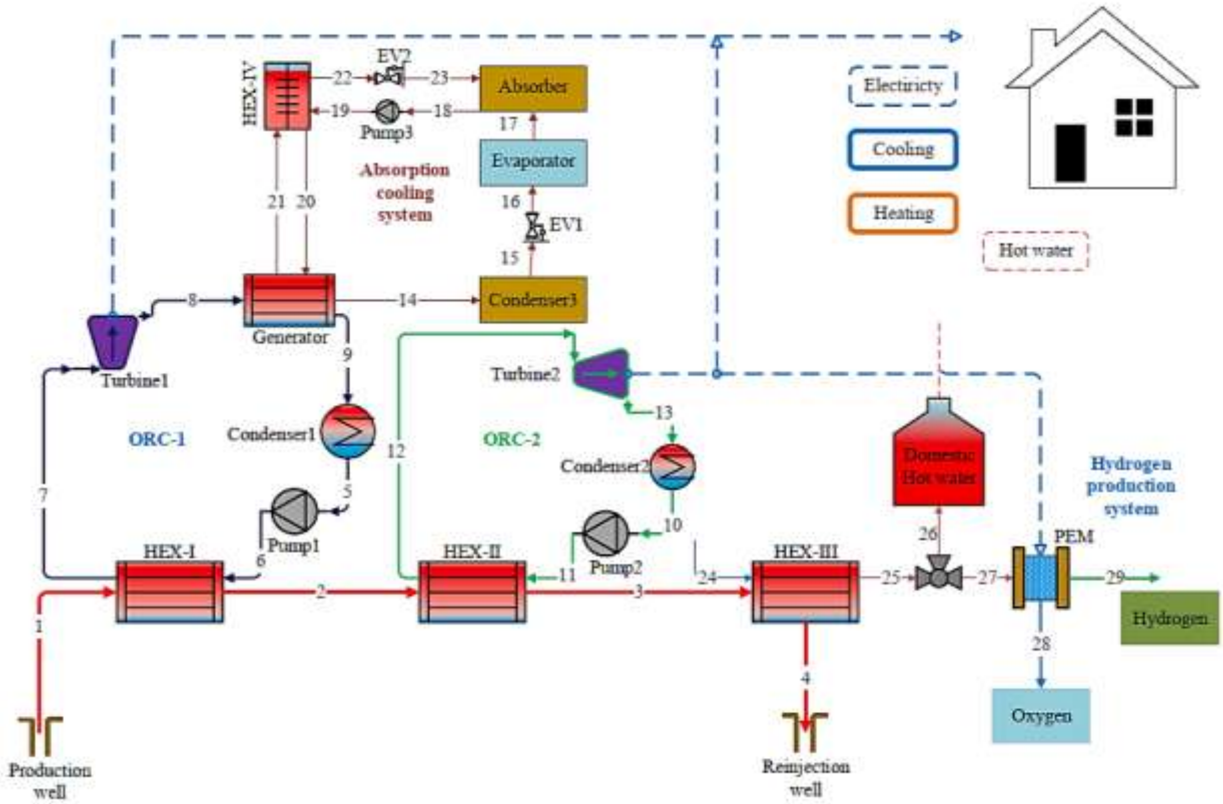

Figure 2.19: The schematic layout of the suggested combined plant by Yilmaz [74]

The thermodynamic and economic analysis of a multi-generation system to produce fresh water, electricity, cooling, and heating were presented by Gnaifaid et al. [75]. The facility harnessed geothermal heat at a benchmark temperature of 200 °C through an integrated single flash-binary power system that includes a reinjection mechanism. Thermodynamic analysis of the operation of the system showed that it could achieve an overall energy efficiency up to 61 % and an exergy efficiency of 37.8 %, with the operating costs fluctuating between 160 to 330 US$ per hour. Through optimization techniques, the study found that the system could reach an optimal exergy efficiency of 58 % at an operational cost of 242 US$ per hour. The findings underscored the economic advantages of geothermal energy for producing freshwater, positioning it as a highly cost-effective and sustainable option among renewable energy technologies. Additionally, the use of a flash/binary power generation setup was shown to enhance the efficiency of the system and contributed to reductions in the cost of electricity production. The electricity cost was calculated as 0.06 $/kWh.

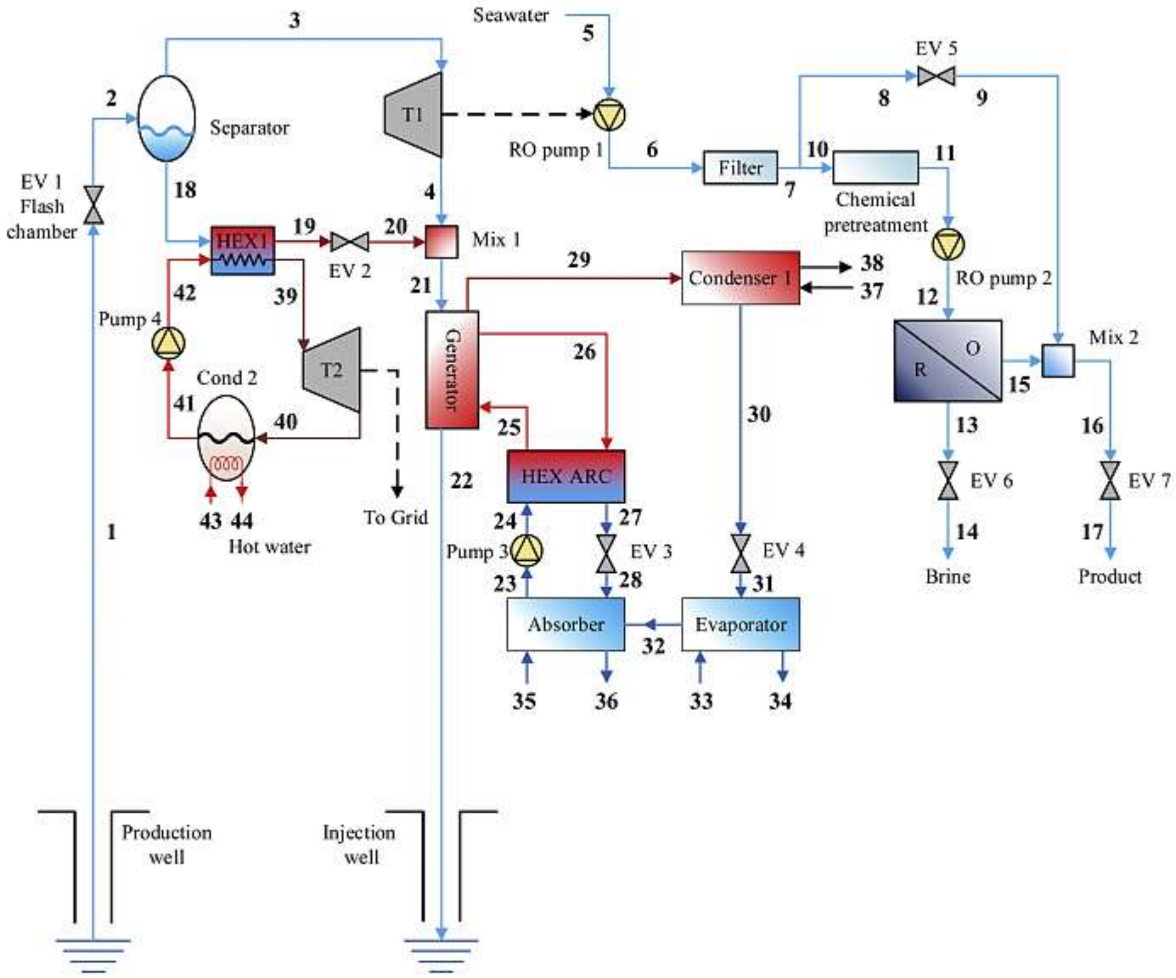

Figure 2.20: Schematics of the geothermal energy driven multigeneration plant, proposed by Gnaifaid et al. [75]

Behnama et al. [76] developed a small-scale tri-generation system using a geothermal heat source of 95 °C to produce fresh water, hot water, and electricity. The system used a single-stage absorption heat transformer to increase the heat source temperature for a desalination process and to provide water heating, while an ORC is employed for electricity generation. The study showed that higher absorber and condenser temperatures reduced the efficiency of the system and increased the levelized cost of energy, especially at lower geothermal temperatures. Nevertheless, the system was economically favourable, with a lower levelized cost of energy compared to a standalone ORC system and a competitive levelized cost of water when matched with small-scale desalination units. At a geothermal temperature of 100 °C, the system could produce 0.662 kg/s of fresh water, 161.5 kW of electrical power, and a heat load of 246 kW.

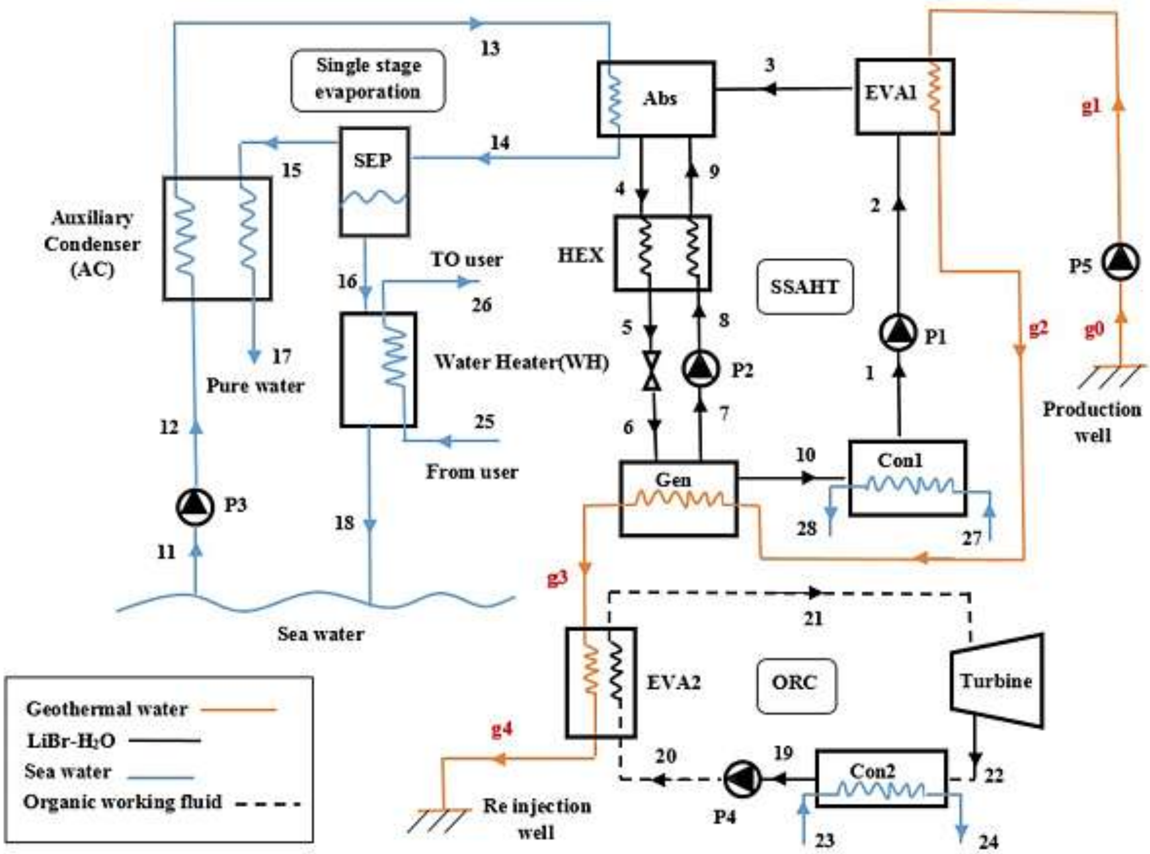

Figure 2.21: Schematic diagram of the trigeneration system, proposed by Behnama et al. [76]

Akbari Kordlar et al. [77] proposed a tri-generation using an ammonia-water solution as a working fluid driven by the geothermal heat source of 138 °C. The system combined a modified absorption refrigeration cycle with a Kalina cycle, using an ammonia-water mixture as the working fluid. Sensitivity analysis was performed to understand the effects of operational parameters on system performance. The system could meet the required heating and cooling demands. Optimization is carried out with two goals: maximizing exergy efficiency and minimizing total exergy destruction rate. Results indicated a trade-off between these goals, with the highest exergy efficiency achieved at the cost of increased exergy destruction, and the lowest exergy destruction achieved at the cost of reduced exergy efficiency.

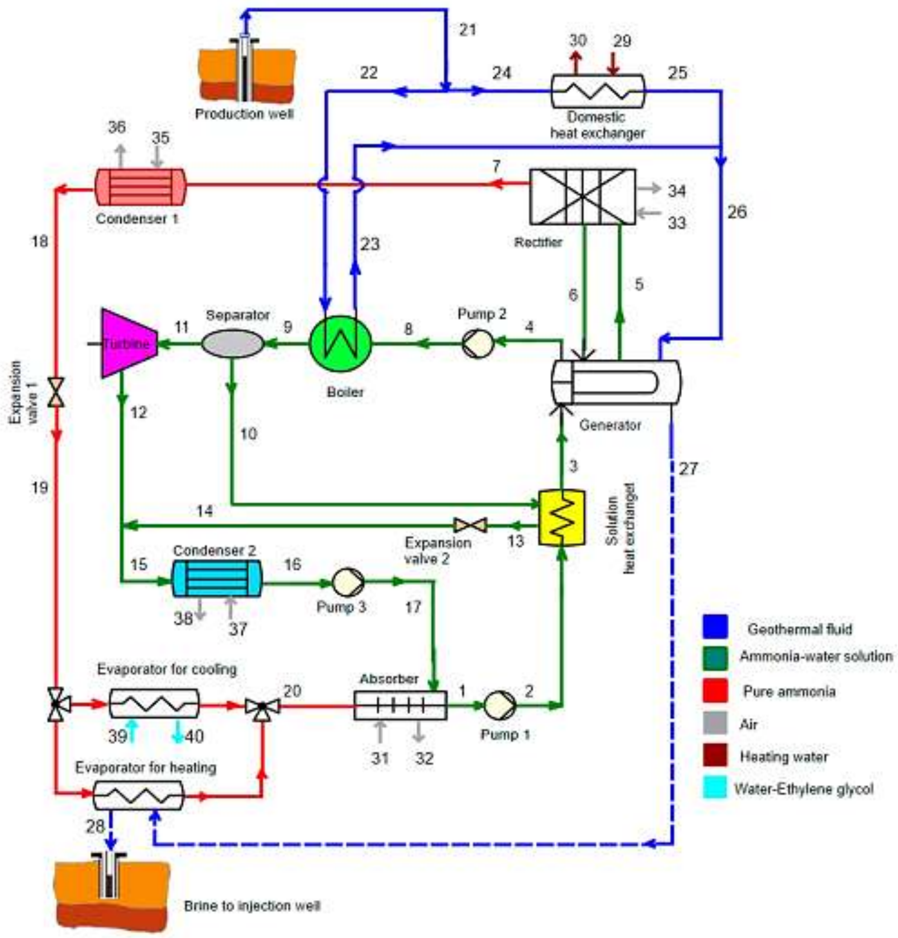

Figure 2.22: Schematic diagram of the proposed tri-generation system, proposed by Akbari Kordlar et al. [77]

The literature review discusses cogeneration and multigeneration systems driven by solar, biomass or geothermal water, some of which incorporate the Kalina cycle or absorption refrigeration systems. Because these two systems play a role in cogeneration, trigeneration, and multigeneration systems, a review of the literature on the Kalina cycle and absorption refrigeration cycles is provided. The Kalina cycle was developed by Aleksandr Kalina [78] in the late 1970s and early 1980s. Since then, there have been several modifications tailored to specific applications [79]. The Kalina cycle is essentially a modified Rankine cycle that utilizes a mixture of two working fluids, water and ammonia, as illustrated in Figure 2.23. In contrast, a conventional Rankine cycle uses only water as the working fluid. According to the Kalina cycle can achieve a 10 – 20 % enhancement in exergy efficiency compared to the conventional Rankine cycle [79]. The thermodynamic properties of ammonia are particularly attractive; the concentration of ammonia in the working fluid improves thermodynamic reversibility, leading to higher performance in the cycle [81]. A simple Kalina cycle comprises a heater, separator, turbine, recuperator, separator, absorber, condenser, and pump. The mixture of ammonia and water enters the recuperator before the heater. The hot mixture exits the heater in liquid and vapor phases and undergoes phase separation in the separator. After leaving the separator, the ammonia vapor enters the turbine for expansion. As it expands in the turbine, the thermal energy in the working fluid is transformed into mechanical energy, and then into electricity via a coupled generator. After leaving the turbine, the low-temperature and low-pressure vapor enters the absorber. In the absorber, the weak solution and the strong solution streams are mixed. The mixture is then directed to the condenser to decrease the temperature of the concentrated solution. This produces a concentrated solution, which is then pumped to the heater after passing through the recuperator.

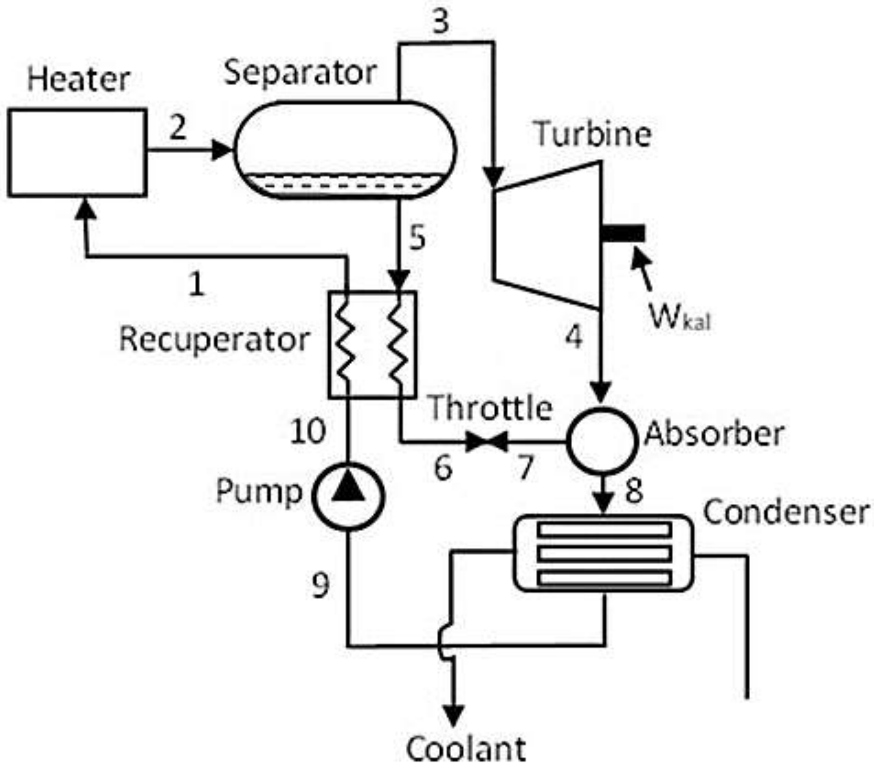

Figure 2.23: Simple schematic diagram of Kalina cycle, proposed by Kalina [78]

In 1859, Ferdinand Carré [82] introduced the aqua-ammonia absorption refrigeration system, utilizing ammonia as the refrigerant and water as the absorbent as shown in Figure 2.24. The absorption refrigeration cycle closely resembles the vapor compression cycle in its use of a circulating refrigerant, evaporator, condenser, and expansion device. However, instead of a compressor, the absorption cycle employs a chemical absorption process and a generator, with a pump facilitating circulation and pressure changes. Due to the strong affinity of water for ammonia, connecting an evaporator containing ammonia to a vessel with water causes the ammonia vapor to be absorbed, creating low pressure in the evaporator. This absorption process takes place in a vessel known as the absorber. It is not necessary to use pure water; a weak ammonia solution in water is sufficient to absorb ammonia vapor. The resulting strong ammonia solution is then heated in a generator to release the ammonia vapor, allowing the weak ammonia solution to be continuously recycled back to the absorber.

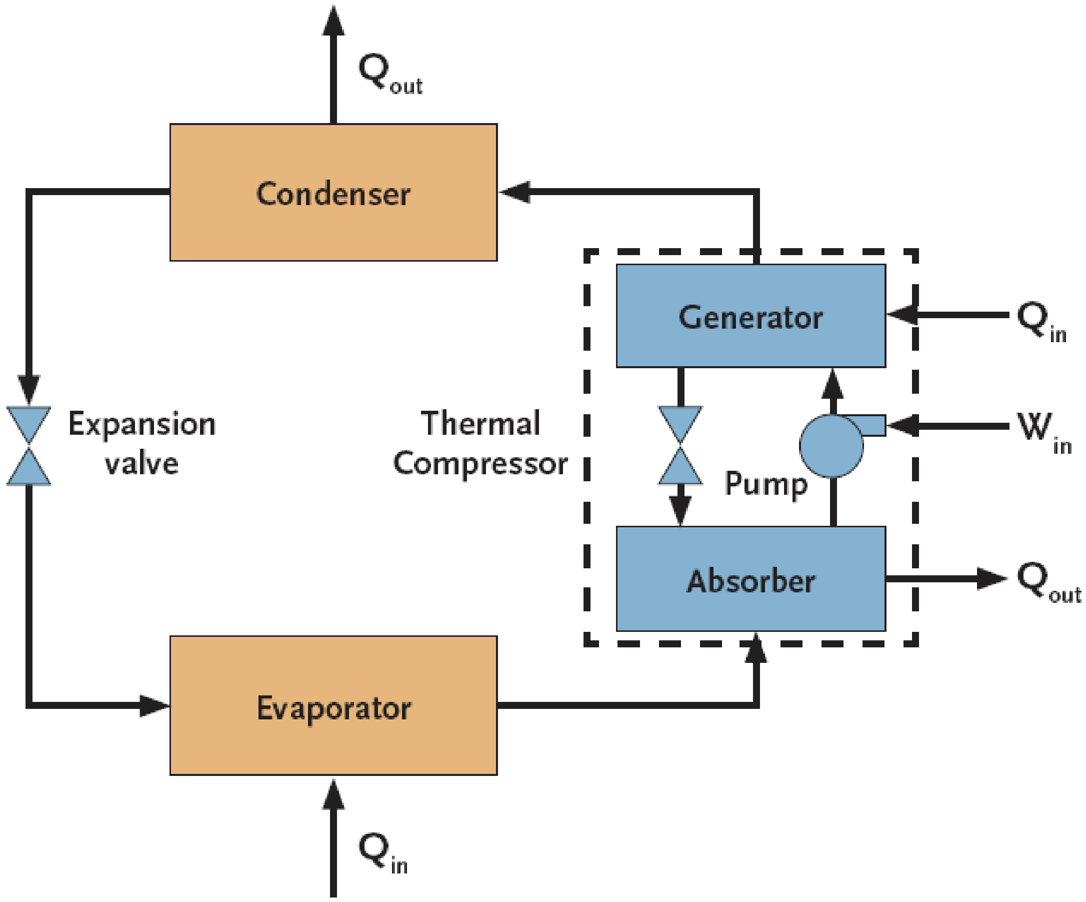

Figure 2.24: Simple schematic diagram absorption cycle, proposed by Carré [82]

2.5 Open research questions

The review of existing literature on co-generation, tri-generation and multi-generation systems driven by geothermal hot water reveals some open research problems. These systems, which aim to simultaneously generate electricity, heating, and cooling, are critical for sustainable energy solutions. However, current research has identified substantial gaps that hinder their optimization and widespread adoption. Addressing these gaps is crucial for improving the effectiveness, reliability, and economic viability of such systems, ultimately leading to more sustainable and efficient energy use. Below are the identified research gaps and questions:

- The integration of annual simulation and off-design evaluation into system analyses is currently lacking.
- There is a significant gap in the study of electricity, heating, and cooling systems that consider variable ambient temperatures and the associated demand fluctuations, particularly under off-design conditions.

- There is a lack of comprehensive analysis on how different heat exchanger designs and turbine performance curves impact system performance in variable conditions.
- Current systems often employ different working fluids for the separate functions of power and cooling generation, such as natural hydrocarbons or fluorinated refrigerants for electricity generation and LiBr-water solutions for cooling applications. This practice has been identified as contributing to increased maintenance and capital costs.
- The potential of low-grade heat sources, like geothermal hot water, in tri-generation systems demands greater attention. Further research is needed to optimize the integration of geothermal energy into tri-generation systems to enhance their contribution to the energy mix.

In response to these identified gaps, this research introduces tri-generation systems that operate using geothermal water and are driven by a single working fluid. The suggested working fluid; an ammonia-water solution, has the potential to improve energy utilization efficiency and reduce system irreversibility due to its variable boiling and condensation temperatures [83,84]. This approach aims to address the challenges of variable ambient temperatures, optimize heat exchanger and turbine performance, and improve overall system efficiency and sustainability.

3 Structure and objectives of this work

In this thesis, various concepts for flexible electricity, heating and cooling generation from geothermal energy are investigated. Due to fluctuating heating and cooling demands and variable environmental conditions, the system often operates in partial load regions. As outlined in the previous section, this work employs quasi-stationary models for a thorough analysis of partial load operations in a tri-generation systems driven by geothermal sources. These models are necessary for understanding how the system performs under varying load conditions, which is essential given the fluctuating demand for electricity, heating, and cooling.

The models are designed to simulate the quasi-stationary responses of the tri-generation system to changes in geothermal energy availability and user demand. This includes examining how the system adapts to shifts in heating, cooling, and power requirements throughout different times of the day or seasons. Additionally, the study extends to evaluating the efficiency and performance of the system under these partial load conditions. The goal is to optimize the operation of tri-generation systems to ensure they are not only energy efficient but also reliable and capable of meeting the energy needs in a sustainable manner, even when operating below full capacity. This comprehensive analysis forms a critical part of the thesis, aiming to contribute to the advancement of geothermal energy utilization in the realm of renewable energy technology.

Regarding the district heating network, an examination of different supply and return temperatures, as well as peak loads, is undertaken. Beyond the thermodynamic assessment, a comprehensive economic analysis is also conducted. The overall objective is to investigate the following research questions:

i. How does the net produced power of tri-generation systems respond to changes in the pinch point temperature differences in the heat exchangers during winter days under design condition?

ii. How do the exergy efficiency, net produced power, and part load performances of tri-generation systems respond to changes in heating demand during winter days under off-design condition, and what is the underlying reason for this variation?

iii. How do the exergy efficiency, net produced power and part load performances of tri-generation systems respond to changes in heating demand during summer days under off-design condition, and what could be the underlying reason for this variation?

iv. How does the total exergy destruction rate of tri-generation systems respond to changes in heating demand during winter and summer days under off-design condition?

v. How do ambient temperature variations affect the exergy efficiency of tri-generation systems during different seasonal conditions under off-design condition, and what are the observed net produced power trends for tri-generation systems in both winter and summer days?
vi. How does the total exergy destruction rate of tri-generation systems respond to changes in ambient temperature during winter and summer days under off-design condition?
vii. How does the levelized cost of electricity for tri-generation systems relate to the pinch point temperature differences in the heat exchangers?
viii. How does the levelized cost of electricity for tri-generation systems relate to the supply heating and geothermal hot water temperatures?

Chapter 4 provides a detailed introduction and description of the two proposed tri-generation systems. Additionally, it illustrates how these systems operate under different seasonal conditions, specifically focusing on their performance during winter and summer. Chapter 5 of this study explains the methodology employed in the research, clarifying the correlations used for simulating the systems to analyse them from thermodynamic and thermoeconomic perspectives. Additionally, this chapter describes the heating and cooling demands that these systems are designed to meet. It also details the approach taken to analyse the systems in off-design mode, including the specific requirements and parameters needed for these calculations. Chapter 6 presents the results of all calculations conducted in this study. Initially, it focuses on validating and verifying all the cycles utilized in the proposed systems, ensuring the reliability of the simulations. This is followed by detailed exergetic analyses, where the impact of various boundary conditions is thoroughly investigated. Finally, the chapter searches into the economic evaluations, examining the effects of different economic boundary conditions.

4 Proposed systems

The proposed systems are composed of three separate yet interconnected subsystems, each playing a key role in the overall functionality and efficiency of the operation. This varied approach offers a wide-ranging and flexible performance, meeting different requirements and situations in its field of use.

4.1 Separated system

In Figure 4.1, the schematic diagram displays the proposed separated tri-generation system that interconnects three distinct cycles, each designed to perform a specific function: electricity, heating, and cooling generation.

The tri-generation system employs geothermal water, which is identified at state 16, as its primary energy source for heating and electricity generation. This geothermal stream is separated into two paths to serve different functions within the system. The first path, marked as state 17, flows through the domestic heat exchanger. Here, it transfers its heat to the secondary fluid between states 14 and 15. During this heat exchange process, the geothermal water cools down as it proceeds to state 18. At the same time, the secondary fluid at state 14, absorbs the heat. The absorption of heat raises the temperature of the secondary fluid, creating a hot stream at state 15, which can then be utilized to meet the domestic heating requirements of the system. The second path of the divided geothermal water, flowing from state 19 to state 21. It provides the necessary heat for the Kalina cycle, facilitating the power generation component of the tri-generation system. During summer days, the combination of geothermal water returning from the domestic heat exchanger and the output from the Kalina cycle provides the essential heat to the absorption refrigeration cycle, moving from state 22 to state 23. The heat exchange processes between geothermal water and the working fluids in the domestic heat exchanger, Kalina cycle, and absorption refrigeration cycle are depicted in Figure 4.2.

In the Kalina cycle, an ammonia-water mixture is employed as the working fluid for power production. The T-s diagram of the Kalina cycle is shown in Figure 4.3. In this cycle, the saturated liquid working fluid at state 1, having a quality of zero, is pressurized to a higher pressure by a pump. The fluid then proceeds to state 2, entering an internal heat exchanger, where it is preheated by the outgoing warm fluid from state 6, improving the overall efficiency of the cycle by recovering residual heat. At state 3, the preheated fluid is further heated in the pre-boiler. This heat is supplied by a geothermal source at states 20 and 21, which provides a sustainable and consistent flow of thermal energy.

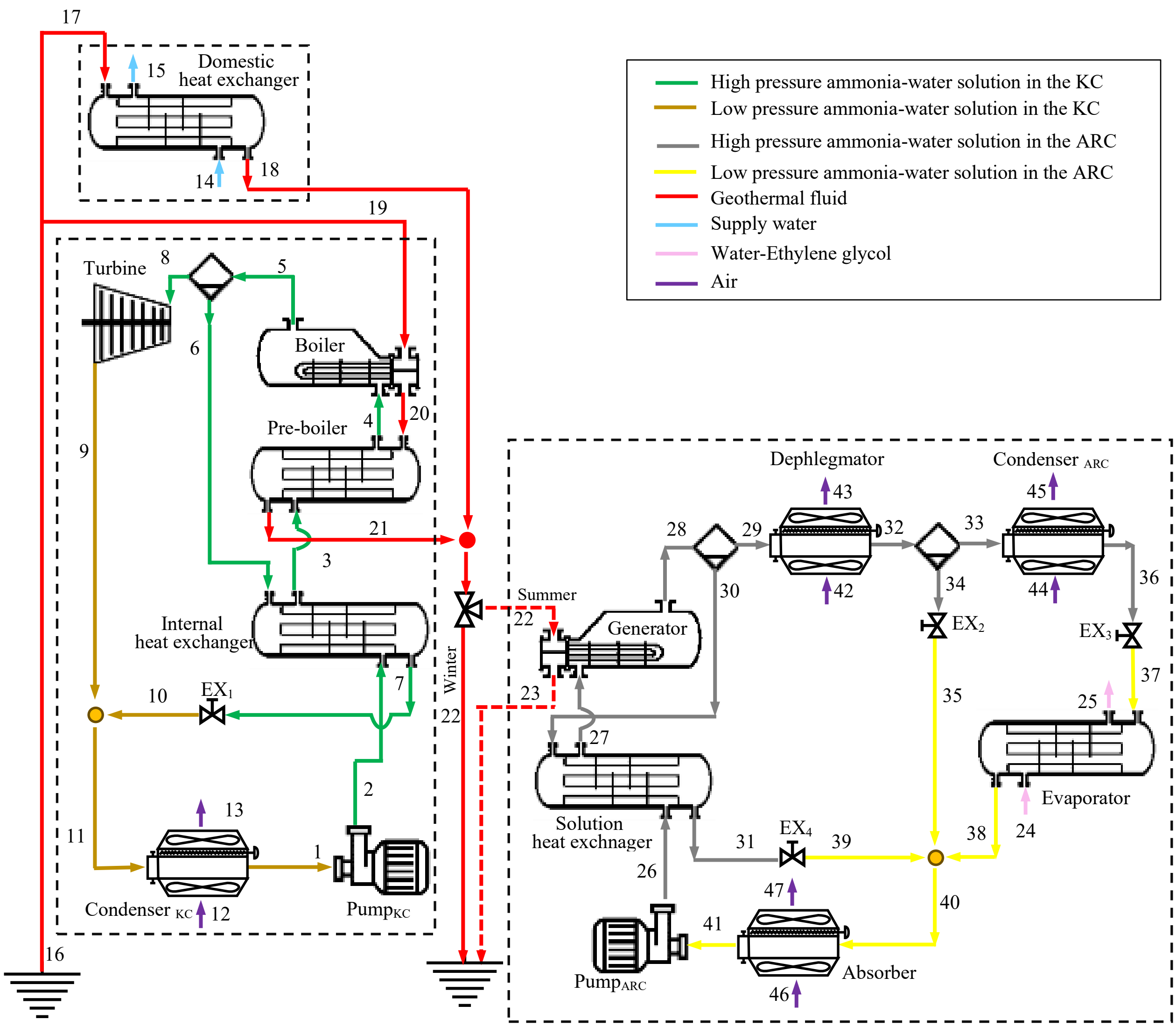

Figure 4.1: Schematic diagram of the proposed separated tri-generation system

At state 4, despite the increase in temperature from the geothermal heating, the working fluid maintains a quality of zero, remaining in a saturated liquid state, indicating that no vaporization has occurred at this point. Upon leaving the pre-boiler, the saturated liquid working fluid then enters the boiler at state 5, where it continues to absorb heat from the geothermal water at states 19 and 20. This additional energy input causes the temperature of the working fluid to rise to its boiling point, initiating a phase change. At the exit of the boiler (state 5), the working fluid is now in a mixed-phase state with a certain quality, indicating the presence of both liquid and vapor. This prepares the working fluid for its entry into the turbine, where the energy can be effectively converted into mechanical work.

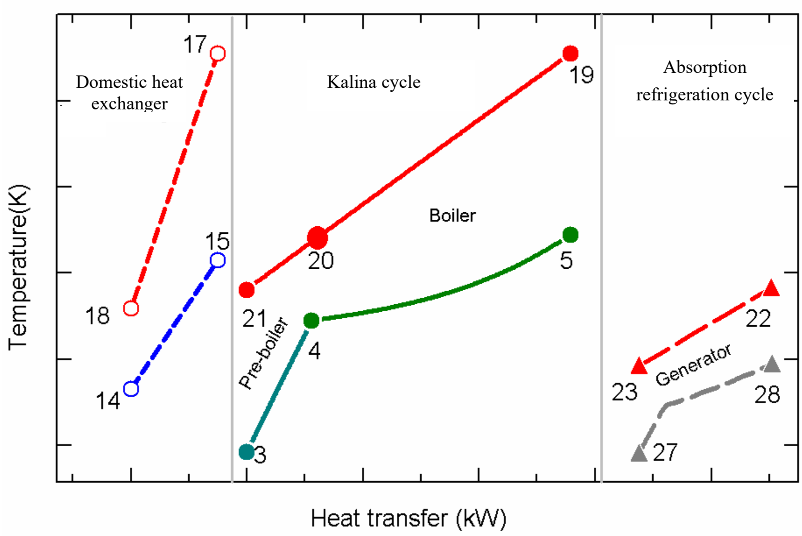

Figure 4.2: Heat transfer process in the domestic heat exchanger, the pre-boiler, the boiler, and the generator in the separated tri-generation system.

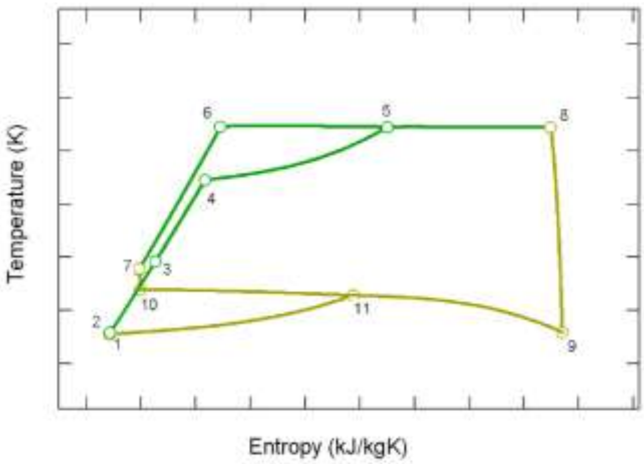

Figure 4.3: T-s diagram of the Kalina cycle in the separated tri-generation system

When the working fluid, heated in the boiler by the geothermal source, reaches state 5, it undergoes a division process in the separator. At this point, state 5 splits into two separate streams. The first stream (state 8) is composed of saturated vapor, destined for the turbine where it will expand to generate mechanical work (electricity production). The second stream (state 6), consisting of saturated liquid with a quality of zero, remains fully in the liquid phase. This saturated liquid portion is then redirected back to the internal heat exchanger, identified as state 6 in the cycle. This regenerative action allows for internal heat recovery, enhancing the overall efficiency of the system. By preheating the working fluid before it enters the pre-boiler and boiler, the cycle effectively minimizes the additional thermal energy required from the geothermal source. After relinquishing the heat of state 6 in the internal heat exchanger, the coolant stream (state 7) exits the internal heat exchanger at a lower temperature. The high pressure of the fluid in state 7 is reduced using an expansion valve, which decreases the pressure to a lower level, reaching state 10. Following this pressure reduction, the fluid from state 10 is then combined with the outgoing streams from the turbine at state 9. At state 9, the working fluid, after having expanded in the turbine and performed mechanical work, is in a reduced energy state and typically exhibits a lower temperature and pressure. The mixture of state 11 is a combination of the reduced-pressure fluid from state 10 with the turbine exhaust at state 9. At state 11 in the Kalina cycle, the mixture enters the condenser. Within the condenser, this mixed fluid undergoes a cooling process. The primary function of the condenser is to reject heat from the working fluid to the air from state 12 to state 13, which is essential for transforming the fluid back into a saturated liquid. The transition to a saturated liquid at the exit of the condenser ensures that the fluid is in the proper phase and condition to be fed back into the pump and begin the cycle again.

The geothermal water, after completing its purpose in the domestic heat exchanger and the pre-boiler of the Kalina cycle, exits as two separate streams from state 18 and state 21, respectively. These outgoing streams are then combined to form state 22. During winter, when there is no requirement for cooling, this combined stream at state 22 is driven back to the geothermal source. On the other hand, in the summer days when there is a demand for cooling, state 22 serves as a heat source in the generator of the absorption refrigeration cycle, contributing to the provision of the necessary cooling demand.

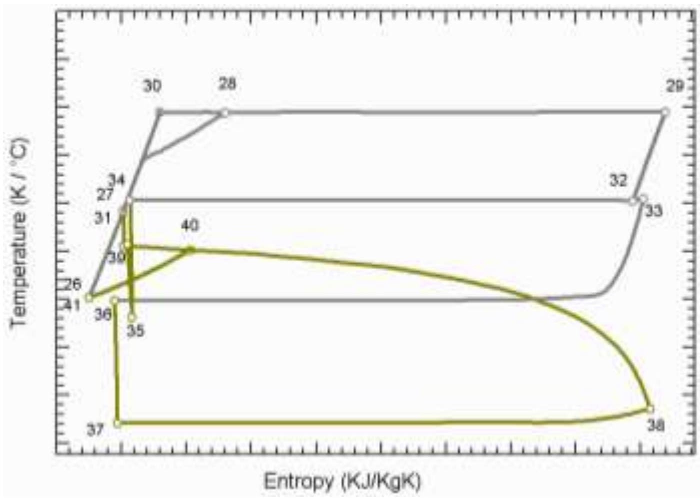

Figure 4.4: T-s diagram of the absorption refrigeration cycle in the separated tri-generation system

An ammonia-water mixture is utilized as the refrigerant in the cooling production process. Figure 4.4 displays the T-s diagram for the absorption refrigeration cycle. In this cycle, the refrigerant at state 41 is pressurized to the high-pressure level of the system by the pump. This high-pressure refrigerant at state 26 then flows to the solution heat exchanger, where it is preheated by exchanging heat with the saturated liquid stream at state 30. The preheated ammonia-water mixture then proceeds to state 27, reaching the generator of the cycle. Inside the generator, the refrigerant is boiled by the thermal energy supplied by geothermal water at state 22, which is a blend of the return flows from the domestic heat exchanger and the pre-boiler. After the geothermal water exchanges heat with the ammonia-water refrigerant in the generator, it exits the system at state 23 and is returned to the geothermal source. In the generator, the high-pressure ammonia-water refrigerant mixture undergoes a phase change. it exits the generator at state 28. This vapor stream then enters a separator, where it undergoes a division process. At this point, state 28 is split into two distinct streams. State 29, which is saturated liquid, is directed to the solution heat exchanger. Within the solution heat exchanger, the saturated liquid at state 29 transfers its heat to the incoming stream that is on its way to the generator. After relinquishing its heat, the stream exits the solution heat exchanger at state 31. This process of heat exchange within the solution heat exchanger is important for preheating the refrigerant mixture before it enters the generator, thereby enhancing the efficiency of the absorption refrigeration cycle. The second part of the division in the separator consists of saturated vapor, exiting at state 29. This vapor, at state 29, is directed into the dephlegmator, where it undergoes a heat exchange process with air flowing from state 42 to state 43. Within the dephlegmator, the saturated vapor loses temperature due to this heat exchange. Upon exiting the dephlegmator at state 32, the refrigerant mixture is in a two-phase state, consisting of both liquid and vapor. This two-phase mixture then moves to a second separator, where it is divided once more. The first part, at state 34, is a saturated liquid. The second part, leaving the second separator at state 33, is a saturated vapor and characterized by a rich ammonia content, indicating a higher concentration of ammonia in the refrigerant mixture. This rich ammonia refrigerant, proceeding from state 33, is channeled into the condenser. During the condensation process within the condenser, it loses its heat to the air from state 44 to state 45. As a result, at the exit of the condenser, marked as state 36, the refrigerant emerges as a saturated liquid with a high concentration of ammonia. This rich ammonia refrigerant stream, after exiting the condenser at state 36, passes through an expansion valve at state 37. During this process, the stream undergoes a reduction in pressure, which also leads to a decrease in temperature. Subsequently, the low-temperature, low-pressure refrigerant is directed into the evaporator. In the evaporator, the refrigerant absorbs heat from a water-ethylene glycol (WEG) stream flowing from state 24 to state 25. This absorption of heat allows the refrigerant to satisfy the required cooling demand of the system. After the heat exchange in the evaporator, the refrigerant, having absorbed the necessary heat, leaves the evaporator at state 38. This step is essential for completing the refrigeration cycle and providing the desired cooling effect. The saturated liquid streams at states 31 and 35 undergo pressure reduction through expansion valves, a necessary step to prepare them for mixing with the exit stream of the evaporator at state 38. State 40 in the system represents the mixed stream resulting from the combination of states 39, 35, and 38. This combined stream is then directed to the absorber, where it undergoes a heat exchange process with air from state 46 to state 47. During this interaction, the mixed stream exchanges heat with the air, leading to a phase change that transforms it into a saturated liquid. This transformation is crucial as it prepares the stream to re-enter the pump, allowing it to continue circulating within the absorption refrigeration cycle.

4.2 Combined system

In Figure 4.5, the schematic diagram displays the proposed combined tri-generation system. In the combined tri-generation system, the heating and power sections function similarly to those in the separated tri-generation system. These sections are explained in section 4.1. However, there is a variation in the operation of this system during summer days. In this configuration, the solution heat exchanger is bypassed. Instead, the exit stream at state 7 in the Kalina cycle is directed to state 48. The fluid in state 7 is a two-phase mixture. Subsequently, this mixture is then separated into two distinct phases using a separator. The first part of this division is a saturated vapor, exiting as state 27, which is then directed through the generator. The second part is a saturated liquid, identified at state 49, which proceeds to a mixer where it is combined with the stream at state 30. In addition, the exit stream from the pump at state 26 is directed to mix with stream 9. The other components and states of the absorption refrigeration cycle are explained in detail in section 4.1. This adjustment enhances the overall efficiency and economic performance of the system.

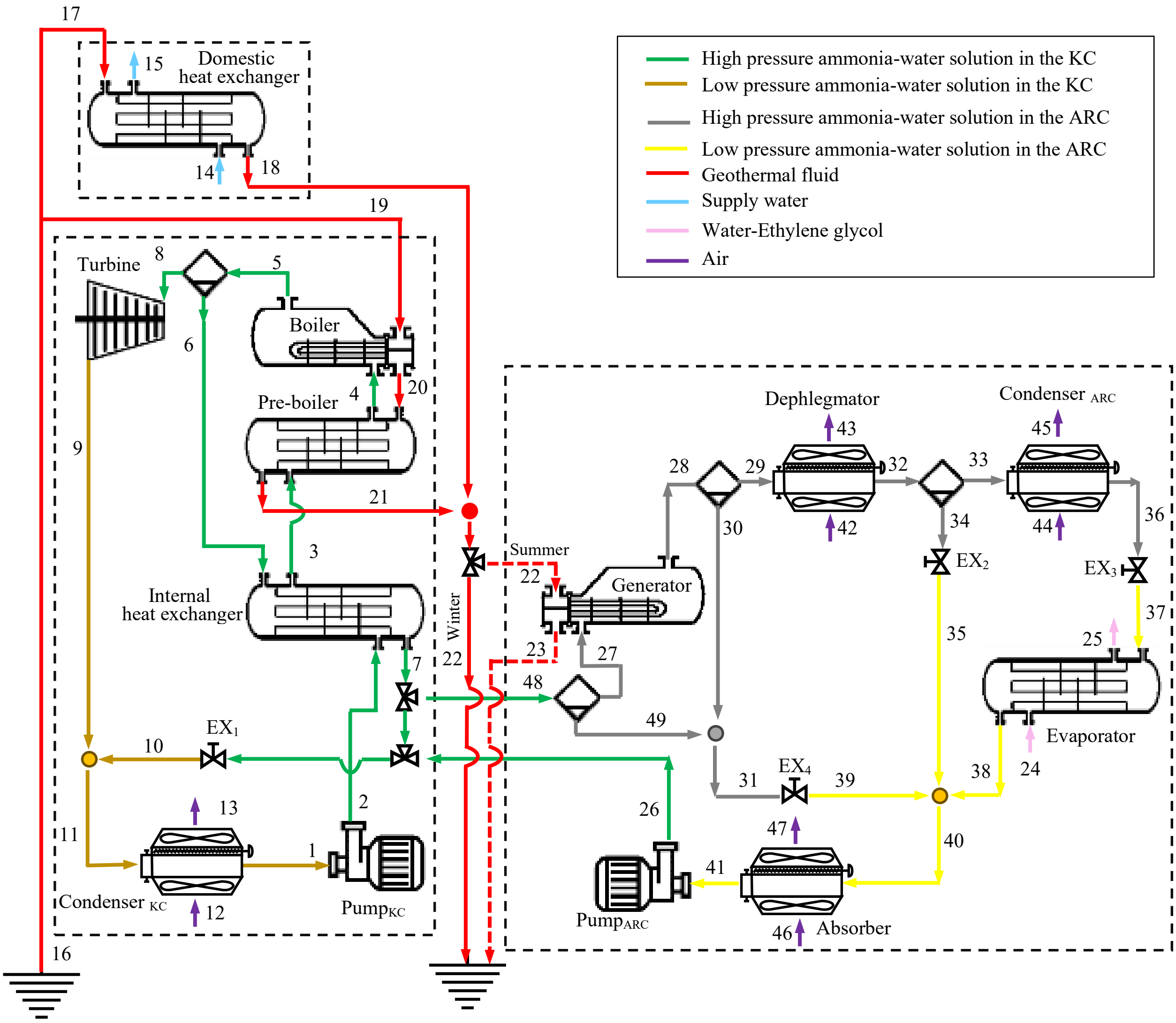

Figure 4.5: Schematic diagram of the proposed combined tri-generation system

5 Methodology

To evaluate the performance of a system, each of its components is considered as a separate control volume, facilitating a detailed simulation and analysis based on thermodynamic principles. The comprehensive mathematical model formulated encompasses mass, energy, and exergy balance equations, ensuring a thorough understanding of the behaviour and efficiency of the systems [85]. The Engineering Equation Solver (EES) [86] software is utilized for the simulation, providing robust computational capabilities necessary for solving complex thermodynamic equations. To increase the accuracy of the simulation, the fluid properties of ammonia-water solution, water, and water-ethylene glycol mixture are carefully incorporated using established correlations from previous research works. The correlations from Ibrahim et al. [87] and Wagner et al. [88] are used to characterize the properties of the ammonia-water solution and water, respectively. Additionally, the thermodynamic and transport properties of water-ethylene glycol are estimated using correlations from Fujuita et al. [89] and Lee et al. [90], ensuring a comprehensive and reliable analysis. The heat exchangers are designed using Aspen [91] and simulated with EES. This meticulous approach ensures that the simulation results are based on reliable data, providing reliable understandings that can guide informed decisions and optimizations for improved system performance and efficiency.

5.1 The conservation of mass principle

The conservation of mass principle for a control volume is a fundamental concept in fluid mechanics and thermodynamics that maintains the consistency of mass within a designated system, regardless of the transformations or processes it experiences.
Mathematically, the conservation of mass for a control volume can be expressed as [92]:

$$\frac{dm_{CV}}{dt} = \sum_{in} \dot{m} - \sum_{out} \dot{m} \tag{5.1}$$

where $\frac{dm_{CV}}{dt}$ represents the rate of change of mass in the control volume, $\sum_{in} \dot{m}$ is the sum of mass flow rates entering the control volume and $\sum_{out} \dot{m}$ is the sum of mass flow rates exiting the control volume. This equation essentially states that the change in mass inside the control volume over time is equal to the net mass flow rate into the control volume. In scenarios where the system reaches a steady state, the mass within the control volume remains constant over time, leading to a simplified form of the conservation of mass principle:

$$\sum_{in} \dot{m} = \sum_{out} \dot{m} \tag{5.2}$$

This indicates that, at steady state, the total mass flow rate entering the control volume is equal to the total mass flow rate exiting the control volume.
The conservation of mass principle is vital for analysing and optimizing fluid and thermodynamic systems, ensuring safety, efficiency, and environmental compliance across various industries. It aids in predicting system behaviour, validating models, and making informed design decisions, contributing significantly to the stability and sustainability of operations.

5.2 The conservation of energy

In the analysis of thermodynamic processes, it is essential to carefully adhere to the first law of thermodynamics. This fundamental principle, also known as the law of energy conservation, specifies that energy cannot be created nor destroyed in an isolated system. The first law of thermodynamics can be represented as [93]:

$$\Delta U_{int} = Q - W \tag{5.3}$$

where, ΔU is the change in the internal energy of the system, Q is the heat added to the system and W is the work done by the system on its surroundings. This form is typically applied to closed systems where no mass enters or leaves the system. For control volume, which is a specified volume in space through which mass can flow, the first law of thermodynamics accounts for both energy changes due to heat and work interactions and changes due to mass flowing into and out of the control volume. The equation is as follows [94]:

$$\sum(\dot{m}h)_{in} - \sum(\dot{m}h)_{out} + \sum \dot{Q}_{cv} - \sum \dot{W}_{cv} = \frac{dE_{cv}}{dt} \tag{5.4}$$

where, $\sum(\dot{m}h)_{in}$ is the sum of the mass flow rates in multiplied by their specific enthalpy, $\sum(\dot{m}h)_{out}$ is the sum of the mass flow rates out multiplied by their specific enthalpy, $\sum \dot{Q}_{cv}$ is the rate of heat transfer into the control volume, $\sum \dot{W}_{cv}$ is the rate of work done by the control volume and $\frac{dE_{cv}}{dt}$ represents the rate of change of total energy within the control volume. This form of the first law includes the energy carried by mass entering and leaving the control volume. It is crucial for analyzing processes in open systems like power plants or refrigeration cycles, where fluid flows through components and undergoes various thermodynamic processes. It ensures that all energy exchanges are accounted for, allowing for accurate predictions of system performance and efficiency.

5.3 Exergy analysis

Exergy analysis offers a detailed measure of energy efficiency in thermodynamic systems. It achieves this by identifying the detailed locations and processes where energy waste occurs. Consequently, it reveals key opportunities for improving both system performance and sustainability. It explores into the true potential of energy to perform work, highlighting the gap between actual and ideal processes, which is crucial for optimizing system designs, reducing environmental impact, and achieving economic savings through improved energy utilization.
Exergy represents the maximum useful work possible from a system at a given state relative to a specified environment. For a control volume, the exergy balance equation can be derived from the first and second laws of thermodynamics and considers the flow of mass, heat, and work across the boundaries of the system. In general, the exergy E of a system can be expressed as the sum of four terms [95]:

$$E = U_{int} - U_{\mathrm{int},0} + p_0(V - V_0) - T_0(S - S_0) + \sum \dot{m}_k e_k \tag{5.5}$$

where, the subscript 0 specifies the dead state. U_{int} and $U_{int,0}$ are the internal energy of the system and the dead state, respectively, p_0 is the pressure of the dead state, V and V_0 are the volume of the system and the dead state, respectively, T_0 is the temperature of the dead state, S and S_0 are the entropy of the system and the dead state, respectively, $\dot{m}_k$ is the mass flow rate of each component k entering or leaving the system and e_k is the specific exergy of each component k. For a control volume where mass and energy can cross the boundaries, the steady-state exergy balance can be given by [96]:

$$\dot{E} = \dot{Q}\left(1 - \frac{T_0}{T}\right) - \dot{W} + \sum \dot{m}_{in} e_{in} - \sum \dot{m}_{out} e_{out} + \dot{E}_{destroyed} \tag{5.6}$$

where, $\dot{E}$ is the rate of change of exergy within the control volume, $\dot{Q}$ is the heat transfer rate across the boundary at an absolute temperature T, $\dot{E}_{destroyed}$ is the rate of exergy destruction within the control volume due to irreversibilities. It is important to note that this equation applies to a steady state process. For transient processes, the exergy balance would also include the time rate of change of exergy within the control volume. Exergy destruction is a key part of this analysis as it identifies where and how potential work is lost due to inefficiencies and irreversibilities in the process. The specific exergy of each state point of a substance is the sum of the physical exergy ($e_{physical}$) and the chemical exergy ($e_{chemical}$) as follows [96]:

$$e = e_{physical} + e_{chemical} \tag{5.7}$$

Physical exergy considers the energy that can be extracted due to differences in temperature, pressure, and phase from the reference state, often using temperature and entropy differences to calculate it. The specific physical exergy can be calculated using the following equation [97]:

$$e_{physical} = (h - h_0) - T_0(s - s_0) + g(z - z_0) + \frac{1}{2}(v^2 - {v_0}^2) \quad (5.8)$$

where, h and h_0 are the specific enthalpy at the state point and dead state, respectively. S and s_0 are the specific entropy at the state point and dead state, respectively. The acceleration due to gravity (approximately 9.81 m/s²) is shown by g. z and z_0 are the height at the state point and dead state, which is often taken as zero. v and v_0 are the velocity at the state point and dead state, often taken as zero. By ignoring the effect of kinetic and potential exergies, the specific exergy is considered as follows in the absence of magnetic, electrical, nuclear and surface tension effects:

$$e_{physical} = (h - h_0) - T_0(s - s_0) \quad (5.9)$$

Chemical exergy takes into account the potential to do work through chemical transformation, and it depends on the chemical composition and the reference environmental state. To obtain the chemical exergy of the ammonia-water mixture, the following relation is expressed:

$$e_{chemical(NH_3/H_2O)} = \dot{m}\left[\left(\frac{X}{M_{NH_3}}\right)e^0_{ch,NH_3} + \left(\frac{1-X}{M_{H_2O}}\right)e^0_{ch,H_2O}\right] \quad (5.10)$$

Here the standard chemical exergy for ammonia (e^0_{ch,NH_3}) and water (e^0_{ch,H_2O}) is considered as 336.684 and 45 kJ/kmol, respectively [97].

5.4 Energy and exergy efficiencies

In thermodynamic analysis, energy efficiency, which is also referred to as first-law efficiency, is a measure of how well a system uses its input energy. It is a simple concept, focusing on the quantity of energy without considering its quality or form. The energy efficiency can be defined by the equation:

$$\eta_{\text{energy}} = \frac{\dot{Q}_{\text{out}}}{\dot{Q}_{\text{in}}} \quad (5.11)$$

In the proposed separated and combined tri-generation systems, the input energy on winter and summer days is as follows:

$$\dot{Q}_{\text{in,winter}} = \dot{m}_{16}(h_{16} - h_{22}) \quad (5.12)$$

$$\dot{Q}_{\text{in,summer}} = \dot{m}_{16}(h_{16} - h_{23}) \quad (5.13)$$

The output energy for the proposed separated and combined systems during winter and summer days is as follows:

$$\dot{Q}_{\text{out,winter}} = \dot{W}_{net} + \dot{Q}_{heating} \quad (5.14)$$

$$\dot{Q}_{\text{out,summer}} = \dot{W}_{net} + \dot{Q}_{heating} + \dot{Q}_{cooling} \tag{5.15}$$

Here, the net power produced, as well as the cooling and heating demand, are calculated as follows:

$$\dot{W}_{net} = \dot{W}_{Turbine} - \sum \dot{W}_{Pumps} - \sum \dot{W}_{fans} \tag{5.16}$$

$$\dot{Q}_{heating} = \dot{m}_{14}(h_{15} - h_{14}) \tag{5.17}$$

$$\dot{Q}_{cooling} = \dot{m}_{24}(h_{25} - h_{24}) \tag{5.18}$$

$\dot{W}_{Turbine}$ represents the output power of the turbine, calculated as $\dot{m}_7.(h_7 - h_8)$. $\dot{W}_{fans}$ and $\dot{W}_{Pumps}$ indicate the required power for the fans in the tube-fin exchangers and for the pumps, respectively. The power that must be provided to the fan is calculated as follows [98]:

$$\dot{W}_{fan} = \frac{(\Delta P_{total})_{fan}\dot{v}_{fan}}{\eta_{fan}} \tag{5.19}$$

where $(\Delta P_{total})_{fan}$ is the total pressure change across the fan, $\dot{v}_{fan}$ is the volumetric flow rate through the fan, and η_{fan} is the efficiency of the fan.

Exergy efficiency is also known as second-law efficiency. It takes into account the quality or grade of energy. It assesses how effectively a system uses energy, considering its potential to do useful work. It provides visions into irreversibilities and actual useful work potential of a system. Exergy efficiency gives a more realistic assessment of system performance and potential improvements, especially in terms of reducing waste and inefficiency. The exergy efficiency can be defined by the equation:

$$\eta_{\text{exergy}} = \frac{\dot{E}_{\text{out}}}{\dot{E}_{\text{in}}} \tag{5.20}$$

In the proposed separated and combined tri-generation systems, the input exergy on winter and summer days is as follows:

$$\dot{E}_{\text{in,winter}} = \dot{E}_{16} - \dot{E}_{22} \tag{5.21}$$

$$\dot{E}_{\text{in,summer}} = \dot{E}_{16} - \dot{E}_{23} \tag{5.22}$$

The output exergy for the proposed separated and combined systems during winter and summer days is as follows:

$$\dot{E}_{\text{out,winter}} = \dot{W}_{net} + \dot{E}_{heating} \tag{5.23}$$

$$\dot{E}_{\text{out,summer}} = \dot{W}_{net} + \dot{E}_{heating} + \dot{E}_{cooling} \tag{5.24}$$

Here, the cooling and heating exergies, are calculated as follows:

$$\dot{E}_{heating} = \dot{E}_{15} - \dot{E}_{14} \tag{5.25}$$

$$\dot{E}_{cooling} = \dot{E}_{25} - \dot{E}_{24} \tag{5.26}$$

5.5 Exergy destruction analysis

Exergy destruction is associated with thermodynamic inefficiencies and irreversibilities in a process. These inefficiencies could arise from factors such as friction, uncontrolled heat transfer, mixing of different substances, chemical reactions not in equilibrium, and other non-ideal behaviours. The more the exergy destruction, the less efficient the process is in terms of converting input energy into useful work. The fundamental equation for exergy analysis is the exergy balance, which can be formulated as [99]:

$$\dot{E}_{D,k} = \dot{E}_{F,k} - \dot{E}_{P,k} - \dot{E}_{L,k} \tag{5.27}$$

where, $\dot{E}_{D,k}$ is the exergy destruction rate within the system of each component k. $\dot{E}_{F,k}$ is the exergy rate of the fuel entering the system for each component k. It is the maximum work potential of the fuel under the given conditions. $\dot{E}_{P,k}$ represents the exergy rate of the products leaving the system of each component k. It accounts for the work potential remaining in the output of the process. $\dot{E}_{L,k}$ accounts for the exergy rate losses due to heat transfer, waste materials, or other inefficiencies not accounted for in the exergy destruction. The exergy equation for fuel, products, as well as the exergy losses for each component of the system, which are shown in Figure 4.1 and Figure 4.5, are listed in Table 5.1.

Table 5.1: Exergy Equations for Fuel, Products, and Exergy Losses for Each Component

	$\dot{E}_F$	$\dot{E}_P$	$\dot{E}_L$
Heating unit			
Domestic heat exchanger	$\dot{E}_{17} - \dot{E}_{18}$	$\dot{E}_{15} - \dot{E}_{14}$	-
Kalina cycle			
Pre-boiler	$\dot{E}_{20} - \dot{E}_{21}$	$\dot{E}_4 - \dot{E}_3$	-
Boiler	$\dot{E}_{19} - \dot{E}_{20}$	$\dot{E}_5 - \dot{E}_4$	-
Internal heat exchanger	$\dot{E}_6 - \dot{E}_7$	$\dot{E}_3 - \dot{E}_2$	-
Kalina cycle condenser	$\dot{E}_{11} - \dot{E}_1$	-	$\dot{E}_{13} - \dot{E}_{12}$
Kalina cycle pump	$\dot{W}_{Pump.KC}$	$\dot{E}_2 - \dot{E}_1$	
Turbine	$\dot{E}_8 - \dot{E}_9$	$\dot{W}_{Turbine}$	
Absorption refrigeration cycle			
Generator	$\dot{E}_{22} - \dot{E}_{23}$	$\dot{E}_{28} - \dot{E}_{27}$	-
Solution heat exchanger*	$\dot{E}_{30} - \dot{E}_{31}$	$\dot{E}_{27} - \dot{E}_{26}$	-
Evaporator	$\dot{E}_{11} - \dot{E}_1$	$\dot{E}_{13} - \dot{E}_{12}$	-
Dephlegmator	$\dot{E}_{29} - \dot{E}_{32}$	-	$\dot{E}_{43} - \dot{E}_{42}$
ARC condenser	$\dot{E}_{33} - \dot{E}_{36}$	-	$\dot{E}_{45} - \dot{E}_{44}$
Absorber	$\dot{E}_{40} - \dot{E}_{41}$	-	$\dot{E}_{47} - \dot{E}_{46}$
ARC pump	$\dot{W}_{Pump.ARC}$	$\dot{E}_{41} - \dot{E}_{26}$	-

* In separated system

The total exergy destruction rate of the system can be determined using two methods: either by summing the exergy destruction rates of all components, or by calculating the difference between the input exergy and the sum of the exergy of product in the system, as well as the exergy losses, as follows [97]:

$$\dot{E}_{D,tot} = \dot{E}_{in} - \dot{E}_{out} - \dot{E}_{Losses} \quad (5.28)$$

The term of $\dot{E}_{in}$ can be calculated with equations (5.21) and (5.22) during winter and summer days, respectively. The output exergy of the system, or the exergy of the products, is determined by summing the net produced power and heating exergy during winter. For summer days, this sum also includes cooling exergy. These calculations are detailed in Equations (5.23) and (5.24), respectively. The exergy losses during winter consist solely of the exergy loss from the Kalina cycle condenser. In contrast, during summer days, the exergy losses encompass the combined losses from the condensers of the Kalina and absorption refrigeration cycles, as well as from the dephlegmator and absorber. The equations detailing these terms are listed in Table 5.1.

5.6 Economic analysis

Economic considerations are crucial for the feasibility of energy conversion systems, which must balance technical efficiency with financial viability. Thermo-economic analysis is essential to ensure that these systems are not only energy-efficient but also economically sustainable, taking into account costs such as capital investment and operational expenses. This comprehensive approach helps in identifying cost-effective and practical solutions within the energy sector.

The system in question consists of various components, each associated with unique investment costs. These costs are calculated based on the heat transfer areas and the capacities of the rotating equipment. The formula to determine the total capital investment (TCI) is as follows [100]:

$$TCI = C_{TM} + C_{drilling} + C_{aux} \quad (5.29)$$

Here, C_{TM} is the total module cost. This represents the overall cost of the modules or components of the system. It includes the expenses associated with the core components or modules of the project. In energy systems, this might encompass the cost of turbines, generators, heat exchangers, and other primary equipment. The total module cost includes both direct costs (like materials and labour directly associated with the construction and installation of the equipment) and indirect costs (such as administrative expenses, transportation, and insurance). $C_{drilling}$ refers to the drilling cost. This includes the expenses related to geothermal drilling. This includes the expenses for drilling wells, site preparation, and the installation of necessary infrastructure for extraction or exploration. Drilling costs can vary greatly depending on the depth and complexity of the drilling operation, the geographical location, and the technology used. C_{aux} is the auxiliary facility costs. This component covers the costs of auxiliary facilities and infrastructure required for the project. It can include the development of access roads, buildings (like control rooms, maintenance workshops, and storage facilities), and utilities (such as water, electricity, and sewage systems). Auxiliary facility costs also encompass expenses for site preparation, landscaping, and environmental mitigation measures if required. The total module cost is calculated as [100]:

$$C_{TM} = 1.18 \sum_{i=1}^{n_{eq}} C_{BM,i} \tag{5.30}$$

$C_{BM,i}$ shows the bare module cost (including direct and indirect costs) of equipment i. This term refers to the cost of each individual component or piece of equipment in the system, including both direct and indirect costs associated with that specific equipment. It is a comprehensive cost that often includes the purchase price, transportation, installation, and any additional expenses required to make the equipment operational. The n_{eq} represents the total number of equipment or components in the system. The bare module cost is expressed as [101]:

$$C_{BM} = C_P^0 F_{BM} \tag{5.31}$$

where C_P^0 indicates the cost of equipment at base conditions. It typically covers the purchase price or the manufacturing cost of the equipment. F_{BM} shows the bare module. This factor is a multiplier that accounts for additional expenses beyond the base cost of the equipment. These expenses might include installation costs, indirect costs like engineering and administrative fees, as well as any special requirements for the equipment's operation, such as specific construction materials or adaptations for handling certain pressures or temperatures.
The equipment cost at base condition is determined according to Equation (5.32) [102]:

$$\log_{10}(C_P^0) = K_1 + K_2 \log_{10}(Y) + K_3[\log_{10}(Y)]^2 \tag{5.32}$$

Here K_1, K_2 and K_3 are empirical constants or coefficients. They are determined from historical data or industry standards. Each of these constants plays a role in adjusting the model to fit real-world cost data more accurately. Their values can vary based on the type of equipment, industry, and economic factors. The symbol Y typically represents a size measure of the equipment, such as capacity, area, volume, or power. The exact nature of Y depends on the context in which this model is used. It is a key variable in determining the cost, as larger or more complex equipment usually correlates with higher costs.
The bare module factor can be obtained from [100]:

$$F_{BM} = B_1 + B_2 F_M F_P \tag{5.33}$$

where, B_1 and B_2 are constants determined empirically or from industry standards. B_1 could represent a base factor that applies to all equipment universally, while B_2 might be a multiplier that adjusts the factor based on specific conditions or requirements of the project. The F_M is material factor. This factor accounts for variations in costs due to different materials used in the equipment. The F_P shows the pressure factor. This factor adjusts the cost for equipment that operates under different pressure conditions than standard conditions. High-pressure equipment typically requires additional design considerations, stronger materials, and more rigorous testing, all of which can increase the cost. The pressure correction factor is calculated as [101]:

$$\log_{10}(F_P) = C_1 + C_2 \log_{10}(p_g) + C_3\left[\log_{10}(p_g)\right]^2 \tag{5.34}$$

Here, p_g represents the operational pressure of the equipment, generally measured in bar. It is a crucial variable as it directly influences the pressure factor. C_1, C_2, and C_3 are empirical constants or coefficients. They are determined through historical data, experimental results, or industry standards. Each constant adjusts the model to align more closely with real-world data, allowing for accurate estimations across different pressure ranges.
The auxiliary facility cost is calculated as [102]:

$$C_{aux} = 0.30 \sum_{i=1}^{n_{eq}} C_{BM,i}^{0} \tag{5.35}$$

where, n_{eq} represents the number of equipment or components in the system. The $C_{BM,i}^{0}$ is the bare module cost of equipment i at base conditions. This term refers to the cost of each individual piece of equipment or component in its basic form, without additional modifications or adaptations for specific project requirements (without material and pressure correction factors). It includes the purchase price and any other initial costs associated with the equipment. Table 5.2 represents the different parameters which are used to calculate the total capital investment.

Table 5.2: Equipment cost factors [100-102]

	Y(unit)	K_1	K_2	K_3	C_1	C_2	C_3	B_1	B_2	F_M	F_{BM}
Shell and tube heat exchanger	$A_{HX}(\mathrm{m}^2)$	4.8306	-0.8509	0.3187	-0.00164	-0.00627	0.0123	1.63	1.66	1.4	Eq. (5.33)
Kettle reboiler	$A_{HX}(\mathrm{m}^2)$	4.8306	-0.8509	0.3187	0.03881	-0.11272	0.081183	1.63	1.66	1.8	Eq. (5.33)
Air-cooled heat exchanger	$A_{HX}(\mathrm{m}^2)$	4.0336	0.2341	0.0497	-0.125	0.15361	-0.02861	0.96	1.21	1.2	Eq. (5.33)
Turbine	$\dot{W}_{Tur}(\mathrm{kW})$	2.6259	1.4398	-0.1776	-	-	-	-	-	-	3.5
Pump	$\dot{W}_{PU}(\mathrm{kW})$	3.339	0.0536	0.1538	-0.3935	0.3957	-0.00226	1.89	1.35	1.55	Eq. (5.33
Fan	$\dot{W}_{fan}(\mathrm{kW})$	3.339	-0.3533	0.4477	-	-	-	-	-	-	2.8

All cost data used in an economic analysis must be brought to the same reference year; the year used as a basis for the cost calculations. For cost data based on conditions at a different time, this is done with the aid of an appropriate cost index (CI) [103]:

$$C_{ref} = C_0 \times \frac{I_{ref}}{I_0} \tag{5.36}$$

where, C_{ref} denotes the cost normalized to the reference year. C_0 represents the original cost at the year of acquisition. I_{ref} is the cost index corresponding to the reference year, and I_0 is the cost index for the year when the original cost was reported. The cost index is a crucial inflation indicator utilized for adjusting the costs of equipment, materials, labour, and supplies in line with current economic conditions. Prominent cost indices include the Chemical Engineering

(CE) Plant Cost Index and the Marshall and Swift (M&S) Equipment Cost Index. The CE Plant Cost Index, reported monthly in 'Chemical Engineering' magazine, focuses on construction costs for chemical plants and is recommended for estimating the total costs of entire plants or multiple components. In contrast, the M&S Equipment Cost Index, featured in both 'Chemical Engineering' and the 'Oil and Gas Journal,' is tailored towards construction costs for a variety of chemical process industries and is better suited for appraising single equipment items in thermal design projects. In this work, the M&S Equipment Cost Index is used. The M&S Equipment Cost Index was 394 in 2001, indicating the cost level of that year, and rose to 596 by 2020, reflecting the economic changes over the intervening period [104].

In order to evaluate the profitability of investments or projects, particularly in capital budgeting, net present value (NPV) is extensively utilized. It enables the assessment of the profitability of the investment by comparing the present value of all incoming and outgoing cash flows over the duration of the project. This method provides a comprehensive view of the financial implications of a project, helping decision-makers understand whether the potential returns justify the initial and ongoing investments. The equation for calculating NPV is [103]:

$$NPV = -TCI + \sum_{n=1}^{t} \frac{CF_t \times (1 + r_e)^n}{(1 + r_{d,real})^n} \tag{5.37}$$

where CF_t represents the net cash inflow (revenues minus costs) in year t. This changes every year and can include ongoing operational revenues and expenses. The term r_e is escalation rate. It is the rate at which cash flows are expected to increase annually due to factors like inflation, price increases, or productivity improvements. This rate adjusts the cash flow of each year to reflect expected changes in value over time. It is an important factor in long-term projects where costs and revenues are not static. The $r_{d,real}$ is the real discount rate. This rate is used to discount future cash flows back to their present value. The real discount rate excludes inflation, focusing on the underlying return or cost. It reflects the time value of money, acknowledging that money available now is worth more than the same amount in the future due to its potential earning capacity.

To remove the effects of inflation from the nominal discount rate and to determine the real discount rate for an investment, the following Fisher Equation is used [103]:

$$r_{d,real} = \frac{1 + r_{d,nominal}}{1 + r_i} - 1 \tag{5.38}$$

Here, $r_{d,nominal}$ shows the nominal discount rate. This is the discount rate that includes the effect of inflation. The term r_i is the inflation rate. This represents the rate at which the general level of prices for goods and services is rising, and subsequently, how purchasing power is falling.

The net cash inflow:

$$CF_t = (C_{heating} + C_{cooling} + C_{electricity}) - C_{o\&m} \tag{5.39}$$

The term $C_{o\&m}$ is operation and maintenance costs. These are the costs associated with operating and maintaining a system or facility. It could include labour, materials, routine repairs, and general maintenance expenses. It is assumed to amount to 3 % of the total investment cost [105]. The term $C_{heating}$ refers to the net revenue from the heating production. This can vary depending on the type of heating system used, the energy prices, and the efficiency of the heating system. The term $C_{cooling}$ in Equation (5.39) is the net revenue associated with producing cooling. Factors that influence this cost include the type of cooling system, energy prices, and the efficiency of the system. The term $C_{electricity}$ refers to the net revenue generated from electricity production. This is primarily influenced by factors such as market energy prices, operational efficiency of power plants, technological advancements in energy production and storage, environmental regulations, and geopolitical events affecting fuel availability and costs. In this study, the net revenue associated with heating, cooling, and electricity are calculated using the following correlations:

$$C_{heating} = c_{heating} \cdot \dot{Q}_{heating} \cdot t_{use,heating} \tag{5.40}$$

$$C_{cooling} = c_{cooling} \cdot \dot{Q}_{cooling} \cdot t_{use,cooling} \tag{5.41}$$

$$C_{electricity} = c_{electricity} \cdot \dot{W}_{net} \cdot t_{use,electricity} \tag{5.42}$$

Here, the terms $c_{heating}$, $c_{cooling}$, and $c_{electricity}$ represent the cost per unit of energy for heating, cooling, and electricity, respectively. The operational times used for heating, cooling, and electricity are denoted by $t_{use,heating}$, $t_{use,cooling}$, and $t_{use,electricity}$ respectively, indicating the duration over which the systems operate within a given period.

The levelized cost of electricity (LCOE) is an important metric in the energy sector, calculated to provide a consistent measure of the average cost per unit of electricity generated across the lifespan of a power plant. This calculation is essential for comparing the economic feasibility and competitiveness of various energy generation technologies, irrespective of their distinct operational characteristics and capital expenditure profiles. The levelized cost of electricity can be defined as [103]:

$$LCOE = TCI + \frac{\sum_{n=1}^{t} \frac{(C_{o\&m} - (C_{heating} + C_{cooling})) \times (1 + r_e)^n}{(1 + r_{d,real})^n}}{\sum_{n=1}^{t} \frac{\dot{W}_{net} \times (1 + r_e)^n}{(1 + r_{d,real})^n}} \tag{5.43}$$

Both inflation rate and escalation rate can have a significant influence on the Levelized Cost of Electricity (LCOE). Inflation affects the LCOE by changing the value of money over time. When calculating LCOE, future costs and revenues are often discounted back to their present value. Inflation can alter these values, affecting the overall calculation. If the LCOE is calculated in real terms (excluding inflation), it reflects the cost of electricity in constant dollars. If it is calculated in nominal terms (including inflation), it reflects the cost in future dollars, which might be higher due to the decreasing purchasing power of money. The escalation rate refers to the rate at which specific costs (like operation and maintenance) are expected to increase over time, often due to factors beyond inflation. Incorporating escalation rates in LCOE calculations ensures a more accurate and realistic estimate of long-term costs.

5.7 Turbine model

Multi-stage axial flow turbines are integral to co- and tri-generation systems, efficiently handling pressure ratios through multiple stages, each optimized for enhanced energy extraction and conversion. However, in these applications where turbine nozzles are not choked, the variation of extraction pressures with flow to subsequent stages is highly nonlinear [106]. In this regard, the more adaptive 'Law of the Ellipse' originally developed by Stodola in 1927 [107], offers a robust alternative. Stodola's ellipse method takes into account variations in mass flow rate and extraction steam conditions, providing a reliable means to evaluate the aerodynamic performance of turbines under off-design conditions. This methodology allows for accurate performance assessments and predictions. Suitable for both controlled and uncontrolled expansions, it accommodates various turbine configurations, including those with sonic choking or fewer stages. Proven in practical applications, the Law of the Ellipse predicts pressures that correspond well with manufacturer data from several high-backpressure cogeneration turbines and utility systems, validating its efficacy over traditional linear methods. A constant mass flow coefficient Φ for the turbine can be derived based on the conditions at the turbine's inlet [108]:

$$\Phi_{Design} = \left(\dot{m}_{TUR}\frac{\sqrt{T_{TUR,in}}}{p_{TUR,in}}\right)_{Design} \tag{5.44}$$

The off-design mass flow rate of a turbine is given by [109]:

$$(\dot{m}_{TUR})_{Off-design} = \sqrt{\frac{\left(\mathrm{p}_{TUR,in}^2 - \mathrm{p}_{TUR,out}^2\right)_{Off-design}}{\left(T_{TUR,in}\right)_{Off-design} Y_{id}}} \tag{5.45}$$

where Y_{id} represents Stodola's constant, which is determined by the following calculation [109]:

$$Y_{id} = \frac{\left(\mathrm{p}_{TUR,\mathrm{in}}^2 - \mathrm{p}_{TUR,out}^2\right)_{Design}}{\left(\mathrm{p}_{TUR,in}^2\right)_{Design} \Phi_{Design}^2} \tag{5.46}$$

The method for calculating the off-design efficiency is described as follows [110]:

$$\eta_{tur} = \eta_{tur,design} - 2\left[\frac{\varpi_{Off-design}}{\varpi_{Design}}\sqrt{\frac{(\Delta h_{is})_{Design}}{(\Delta h_{is})_{Off-design}}} - 1\right]^2 \tag{5.47}$$

where ϖ is the revolving speed of the axial flow turbine and is considered as 3000 rpm [110]. Δh_{is} shows the isentropic enthalpy drops.

5.8 Heat exchanger model

The most common equation for calculating the heat transfer rate in heat exchangers is expressed as [111]:

$$\dot{Q} = F_T U A \, \Delta T_{LMTD} \tag{5.48}$$

where U is the overall heat transfer coefficient, the area of the heat exchanger is A and ΔT_{LMTD} represents the logarithmic mean temperature difference between the hot and cold streams in the heat exchanger. The term F_T represents the correction factor for multiple pass layout. The logarithmic mean temperature difference is calculated using the equation [111]:

$$\Delta T_{LMTD} = \frac{\Delta T_1 - \Delta T_2}{ln\left(\frac{\Delta T_1}{\Delta T_2}\right)} = \frac{\left(T_{h,out} - T_{c,in}\right) - \left(T_{h,in} - T_{c,out}\right)}{\ln\left[\frac{\left(T_{h,out} - T_{c,in}\right)}{\left(T_{h,in} - T_{c,out}\right)}\right]} \tag{5.49}$$

Here, ΔT_1 and ΔT_2 are the temperature differences between the hot and cold fluids at each end of the heat exchanger.

Shell-and-tube heat exchangers and tube-fin heat exchangers are two commonly selected types of heat exchangers in this work, satisfying the diverse requirements of various processes. These requirements include addressing the corrosive nature of the working fluid, handling maintenance and cleaning issues, and accommodating variations in the phase change process, which may differ based on the location (shell or tube side). Shell-and-tube heat exchangers are among the most prevalent types of exchangers, favored largely due to their straightforward design, durability, and cost-effectiveness in terms of both acquisition and maintenance. Their adaptable construction allows for operation under a wide range of temperatures and pressures, with virtually no limitations in this regard. This adaptability, combined with the ease of cleaning and the ability to handle high-pressure applications, makes them a popular choice in various industrial applications, including chemical processing, power plants, and oil refineries [112]. In the process and power industries, tube-fin exchangers, also known as air-cooled exchangers, are extensively utilized, particularly as condensers. This is a specialized type of heat exchanger which is particularly useful in areas where cooling water is either unavailable or presents a risk of corrosion. These exchangers use air as the cooling medium instead of water, making them suitable for challenging environments and various industrial applications. This kind of heat exchanger, characterized by a relatively lower heat transfer coefficient, offers the advantage of bypassing the high expenses associated with managing cooling water. Consequently, on a total cost basis, they are quite cost-effective [112]. To accurately determine the off-design performance of the system, each of the heat exchangers under consideration is specifically designed taking into account a variety of crucial parameters. These parameters include factors like flow rates, temperature differences, material properties, and thermal efficiencies, ensuring that the exchangers are optimized for diverse operating conditions beyond their standard design points.

Table 5.3 displays the shell and tube heat exchangers utilized in the proposed systems shown in Figure 4.1 and Figure 4.5. As indicated in Table 5.3, the geothermal water in the domestic heat exchanger, boiler, and pre-boiler is directed through the tube side. This design decision is driven by the dissolved salts and the corrosive nature of the geothermal fluid, compounded by temperature fluctuations. These factors can cause scaling, a process where mineral deposits build up on surfaces, thereby reducing heat transfer efficiency. To counteract this, the geothermal fluid is routed through the tube side of the heat exchangers. This approach simplifies maintenance and tube cleaning, which is vital for maintaining operational efficiency and extending the lifespan of the equipment. In addition, the choice of heat exchangers is influenced by the specific processes occurring within the system. For instance, as shown in Table 5.3, in boiler and generator where boiling occurs on the shell side of the heat exchangers, the kettle reboiler (TEMA K) becomes an indispensable component. This type of heat exchanger is adept at handling the boiling process, making it an ideal choice for these applications. Its capability to ensure efficient and stable operation perfectly aligns with the essential operational requirements of handling the boiling process in these systems. Furthermore, the selection of the TEMA E configuration for the heat exchangers was primarily influenced by its characteristics that favour minimal pressure drop, ease of maintenance, and cost-effectiveness. The single-pass shell design of TEMA E ensures efficient heat transfer and simplifies cleaning and inspection, making it ideal for systems where these factors are critical. This choice aligns with the goals of maximizing thermal efficiency while managing costs and maintaining simplicity in operations.

Table 5.3: The shell and tube heat exchangers used in the proposed systems displayed in Figure 4.1 and Figure 4.5 (the number of different states is the same in both systems).

Shell and tube heat exchanger		
	Shell side	Tube side
Heating unit		
Domestic heat exchanger	single-phase (streams 14 and 15) → TEMA E	single-phase (streams 17 and 18)
Kalina cycle		
Pre-boiler	single-phase (streams 3 and 4) → TEMA E	single-phase (streams 20 and 21)
Boiler (Kettle reboiler)	phase change (streams 4 and 5) → TEMA K	single-phase (streams 19 and 20)
Internal heat exchanger	single-phase (streams 2 and 3) → TEMA E	single-phase (streams 6 and 7)
Absorption refrigeration cycle		
Generator (Kettle reboiler)	phase change (streams 25 and 26) → TEMA K	single-phase (streams 22 and 23)
Solution heat exchanger	single-phase (streams 24 and 25) → TEMA E	single-phase (streams 28and 29)
Evaporator	single-phase (streams 45 and 46) → TEMA E	Phase change (streams 35 and 36)

Furthermore, in the cooling section of the both systems, the evaporator is designed to guide a rich ammonia-water solution through its tubes, where it undergoes a phase change from vapor to liquid. This specific arrangement is chosen to maximize the efficiency of the phase change. The tubes provide a controlled environment, essential for precise management of the phase transition and for safely handling the high pressure of the refrigerant. As well, the tube design, characterized by its smaller diameter, significantly improves heat transfer by increasing the surface area in contact with the refrigerant. This feature is crucial for enhancing the heat exchange efficiency, which is central to the performance of the evaporator. Moreover, the water-ethylene glycol mixture is led through the shell side of the evaporator. This side of the system is designed to handle a larger volume, making it ideal for dispersing the heat absorbed from the ammonia-water solution. The design of the shell side benefits from the coolant operating at a more moderate pressure. This aspect, combined with the flexibility to regulate the flow rate of the coolant, enhances the overall thermal management, contributing to a more efficient and controlled heat exchange process.

The air-cooled heat exchangers utilized in the proposed systems are represented in Table 5.4. In geothermal power plants, the selection of air-cooled condensers is particularly advantageous, especially considering the typical locations of these resources. Often situated in remote, inland, or arid areas where water is scarce, air serves as a readily available and environmentally friendly coolant. This choice not only reduces ecological impacts by eliminating the need for water extraction and discharge but also offers operational benefits [113]. Air-cooled systems generally require less maintenance, are less prone to scaling and corrosion, and do not necessitate water treatment, leading to lower operating costs and enhanced reliability due to their simpler design with fewer components. These factors collectively make air-cooled condensers a fitting and efficient choice for geothermal power plants.

Table 5.4: The air-cooled heat exchanger used in the proposed systems displayed in Figure 4.1 and Figure 4.5 (the number of different states is the same in both systems).

Air-cooled heat exchanger	
	Tube side
Kalina cycle	
Kalina cycle condenser	single-phase (streams 11 and 1)
Absorption refrigeration cycle	
Dephlegmator	single-phase (streams 27 and 30)
ARC condenser	phase change (streams 31 and 34)
Absorber	single-phase (streams 37 and 38)

Different correlations used to design heat exchangers and determine heat transfer coefficients are expressed in the following subsections.

5.8.1 Shell & tube heat exchanger

The correction factor F in Equation (5.48) is calculated in shell and tube heat exchangers as defined in References [112] and [114].

$$P_{S\&T} = \frac{T_{c,out} - T_{c,in}}{T_{h,in} - T_{c,in}} \tag{5.50}$$

$$R_{S\&T} = \frac{T_{h,in} - T_{h,out}}{T_{c,out} - T_{c,in}} \tag{5.51}$$

$P_{S\&T}$ is measure of the ratio of the heat transferred to the heat which would be transferred if the same cold fluid temperature was raised to the hot fluid inlet temperature; therefore, $P_{S\&T}$ is the temperature effectiveness of the heat exchanger on the cold-fluid side.

For $R_{S\&T} \neq 1$, then,

$$\alpha_{S\&T} = \left(\frac{1 - R_{S\&T}P_{S\&T}}{1 - P_{S\&T}}\right)^{1/N_{Shell}} \tag{5.52}$$

$$S_{S\&T} = \frac{\alpha_{S\&T} - 1}{\alpha_{S\&T} - \mathrm{R}_{S\&T}} \tag{5.53}$$

$$F_{S\&T} = \frac{\sqrt{{R_{S\&T}}^2 + 1}\, ln\left(\frac{1 - S_{S\&T}}{1 - R_{S\&T}S_{S\&T}}\right)}{(R_{S\&T} - 1)\ln\left[\frac{2 - S_{S\&T}\left(R_{S\&T} + 1 - \sqrt{{R_{S\&T}}^2 + 1}\right)}{2 - S_{S\&T}\left(R_{S\&T} + 1 + \sqrt{{R_{S\&T}}^2 + 1}\right)}\right]} \tag{5.54}$$

where, α_{LMTD} and S_{LMTD} are a factor related to the LMTD correction. The term N_{Shell} shows the number of shell-side passes.
For $R_{S\&T} = 1$, then,

$$S_{S\&T} = \frac{P_{S\&T}}{N_{Shell} - (N_{Shell} - 1)P_{LMTD}} \tag{5.55}$$

$$F_{S\&T} = \frac{S_{S\&T}\sqrt{2}}{(1 - S_{S\&T})\ln\left[\frac{2 - S_{S\&T}(2 - \sqrt{2})}{2 - S_{S\&T}(2 + \sqrt{2})}\right]} \tag{5.56}$$

In applications involving single-phase shell fluid, shell and tube heat exchangers of the TEMA E type, characterized by a single-pass shell and counterflow design, are typically selected. The TEMA K type, also known as a kettle reboiler, is employed for shell fluid applications involving two phases, specifically for partially vaporizing the shell fluid. This section derives the geometrical information necessary for rating such an exchanger using the Bell–Delaware method. The original geometry proposed by Bell [115] has been modified according to suggestions by Taborek as shown in Figure 5.1 [116]. As shown in Figure 5.1, the gross window area (i.e., without tubes in the window) or the area of segment ABC corresponding to the window section ($A_{fr,w}$) is [117]:

$$A_{fr,w} = \frac{\pi}{4}D_s^2\left(\frac{\theta_b}{2\pi} - \frac{\sin\theta_b}{2\pi}\right) = \frac{D_s^2}{4}\left[\frac{\theta_b}{2} - (1 - \frac{2\ell_c}{D_s})\sin\frac{\theta_b}{2}\right] \tag{5.57}$$

where θ_b is the angle in radians between two radii intersected at the inside shell wall with the baffle cut and is given by:

$$\theta_b = s\ \cos^{-1}(1 - \frac{2\ell_c}{D_s}) \tag{5.58}$$

In equation (5.57) and (5.58) the term D_s shows Shell inside diameter and the term ℓ_c is the Clearance between the baffle edge and the shell inside diameter.

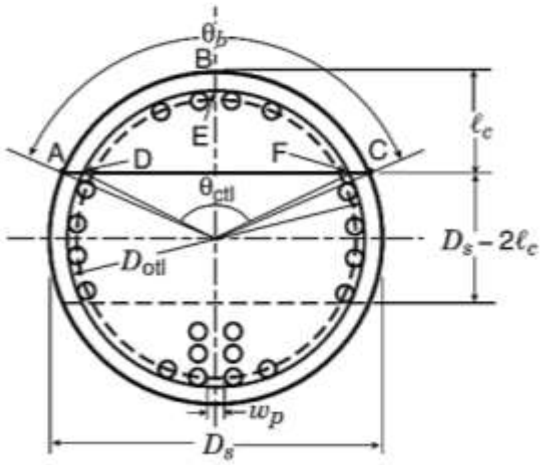

Figure 5.1: Nomenclature for basic baffle geometry relations for a single segmental exchanger from[116]

To calculate the number of tubes in the window zone, the tube field is considered uniformly distributed within the shell cross section. This idealization may be violated in cases where there are tube pass lanes (in multiphases exchanger) or when tubes are removed due to impingement plates in the nozzle entry area. However, for the purpose of this calculation, these discrepancies are ignored, assuming they cause negligible second-order effects. Therefore, the fraction F_w of the number of tubes in one window section encircled by the centerline of the outer tube row (as illustrated in Fig. 8.9) is [117]:

$$F_w = \frac{area\ of\ the\ segment\ DEF}{area\ of\ the\ circle\ with\ D_{ctl}} = \frac{\theta_{ctl}}{2\pi} - \frac{\sin\theta_{ctl}}{2\pi} \tag{5.59}$$

where θ_{ctl} is the angle in radians between the baffle cut and two radii of a circle through the centers of the outermost tubes (see Figure 5.1) as follows:

$$\theta_{ctl} = 2\cos^{-1}(\frac{D_s - 2\ell_c}{D_{ctl}}) \tag{5.60}$$

where $D_{ctl} = D_{otl} - d_0$. Consequently, the number of tubes in the window section is obtained from:

$$N_{t,w} = F_w N_t \tag{5.61}$$

Here, N_t shows the number of tubes and the area occupied by tubes in the window section is:

$$A_{fr,t} = \frac{\pi}{4} d_0^2 N_{t,w} = \frac{\pi}{4} d_0^2 F_w N_t \tag{5.62}$$

The net flow area in one window section is then:

$$A_{o,w} = A_{fr,w} - A_{fr,t} \tag{5.63}$$

By application of the conventional definition, the hydraulic diameter of the window section of a segmental baffle is:

$$D_{h,w} = \frac{4A_{o,w}}{\mathrm{P}} = \frac{4A_{o,w}}{\pi d_0 N_{t,w} + \pi D_s({}^{\theta_b}/_{2\pi})} \tag{5.64}$$

where θ_b is given by Equation (5.58) and P is the wetted perimeter (of all tubes and the shell within the window region); the wetted perimeter of the baffle edge is usually neglected. This $D_{h,w}$ is used for shell-side pressure drop calculations in laminar flow (Re<100).

The final geometrical input required for the window section is the effective number of tube rows in crossflow, necessary for the heat transfer and pressure drop correlations. The fluid in the window section effectively makes a 180° turn while flowing from one internal crossflow section to another. In the window region, the fluid exhibits both crossflow and longitudinal flow components of varying magnitudes depending on the position. Based on visual and experimental evidence [118], the effective distance of penetration for crossflow in the tube field in the baffle window is approximately $0.4\ell_{c,eff}$ in the region AB in Figure 5.2b while flowing away from the internal crossflow section, and about $0.4\ell_{c,eff}$ in the region BC in Figure 5.2b while flowing toward the internal crossflow section. Here, $0.4\ell_{c,eff}$ is the distance between the baffle cut and D_{ctl} (Figure 5.1). Hence, the number of effective tube rows in crossflow in the window section is calculated as follows [117]:

$$N_{r,cw} = \frac{0.8\ell_{c,eff}}{\mathrm{X}_\ell} = \frac{0.8}{\mathrm{X}_\ell}\left[\ell_c - \frac{1}{2}(D_s - D_{ctl})\right] \tag{5.65}$$

The fraction Fc of the total number of tubes in the crossflow section is found from:

$$F_c = 1 - 2F_w = 1 - \frac{\theta_{ctl}}{\pi} + \frac{\sin\theta_{ctl}}{\pi} \tag{5.66}$$

where the expression for F_w is obtained from Equation (5.59). The number of tube rows $N_{r,cc}$ crossed during flow through one crossflow section between baffle tips may be obtained from a drawing or direct count or may be estimated from:

$$N_{r,cc} = \frac{D_s - 2\ell_c}{\mathrm{X}_\ell} \tag{5.67}$$

where X_ℓ is the longitudinal tube pitch for various tube layouts.

The crossflow area at or near the shell centerline for one crossflow section may be estimated from:

$$A_{o,cr} = \left[D_s - D_{otl} + \frac{D_{ctl}}{\mathrm{X}_t}(\mathrm{X}_t - \mathrm{d}_0)\right] L_{b,c} \tag{5.68}$$

for 30° and 90° tube layout bundles. Here ${}^{D_{ctl}}/_{\mathrm{X}_t}$ denotes the number of $(\mathrm{X}_t - \mathrm{d}_0)L_{b,c}$ free-flow area in the given tube row. This equation is also valid for a 45° tube bundle having ${}^{p_t}/_{d_0} \geq 1.707$ and for a 60° tube bundle having ${}^{p_t}/_{d_0} \geq 3.732$.

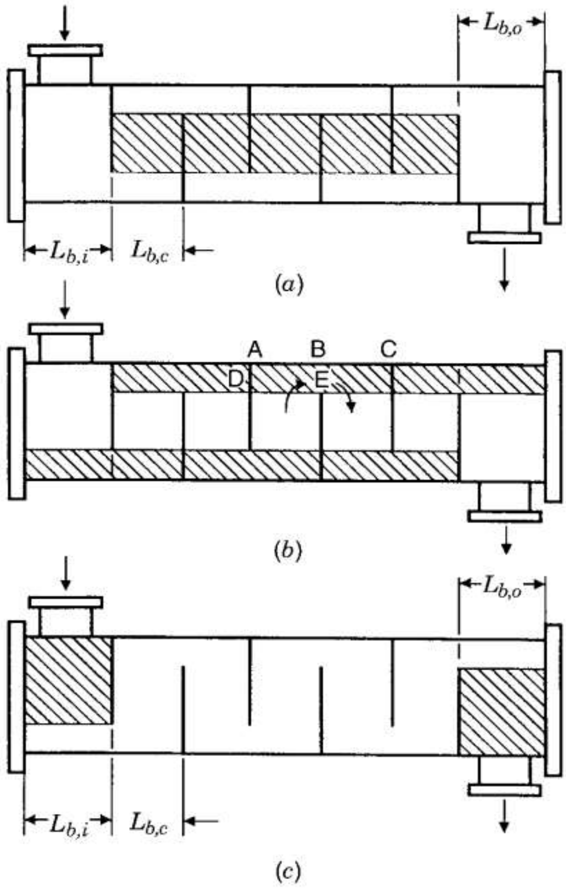

Figure 5.2: TEMA E shell exchanger: (a) internal cross flow sections, (b) window sections; (c) entrance and exit sections from Taborek [116]

The number of baffles N_b is required to compute the total number of crossflow and window sections. It should be determined from the drawings or a direct count. Otherwise, compute it from the geometry of Figure 5.2c as [117]:

$$N_b = \frac{L - L_{b,i} - L_{b,o}}{L_{b,c}} + 1 \tag{5.69}$$

where $L_{b,c}$ is the central baffle spacing, and $L_{b,i}$ and $L_{b,o}$ are the baffle spacings in the inlet and outlet regions.

Flow area available for bypass streams C and F (see Figure 5.3) associated with one crossflow section, normalized with respect to the crossflow open area at or near the shell centerline, is:

$$F_{bp} = \frac{A_{o,bp}}{A_{o,cr}} = \frac{(D_s - D_{otl} + 0.5 N_p w_p) L_{b,c}}{A_{o,cr}} \tag{5.70}$$

where N_p is the number of pass divider lanes through the tube field that are parallel to the crossflow stream B, w_p is the width of the pass divider lane (Figure 5.1), and $A_{o,cr}$ is given by Equation (5.68). Since the tube field is on both sides of the pass divider bypass lane, the F stream is more effective in terms of heat transfer than the C stream. Hence, the effective bypass lane width is considered as $0.5w_p$, as indicated in Equation (5.70).

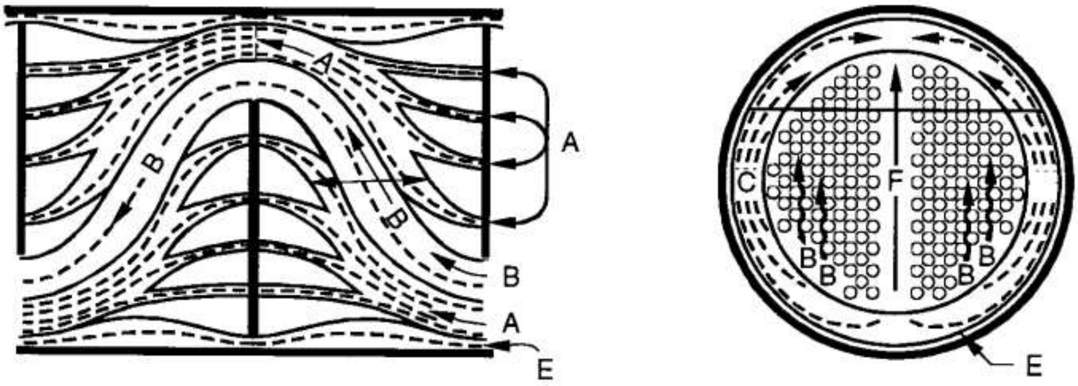

Figure 5.3: Shell side flow distribution and identification of various streams [116]

The total number of tubes associated with one baffle is:

$$N_{t,b} = N_t(1 - F_w) = N_t\left(\frac{1 + F_c}{2}\right) \tag{5.71}$$

where the value of F_w was substituted from the first equality of equation (5.66). If the diametral clearance (the difference between the baffle hole diameter d_1 and the tube outside diameter d_0) is δ_{tb} $(= d_1 - d_0)$, the total tube-to-baffle leakage area for one baffle is:

$$A_{o,tp} = \frac{\pi}{4}\left[(d_0 + \delta_{tb})^2 - {d_0}^2\right]N_t(1 - F_w) \approx \frac{\pi d_0 \delta_{tb} N_t(1 - F_w)}{2} \tag{5.72}$$

Finally, the shell-to-baffle leakage area for one baffle is associated with the gap between the shell inside diameter and the baffle. Note that this gap exists only within the sector ABC in Figure 5.4. The shell-to-baffle leakage area:

$$A_{o,sb} = \pi D_s \frac{\delta_{sb}}{4}\left(1 - \frac{\theta_b}{2\pi}\right) \tag{5.73}$$

where $\delta_{sb} = D_s - D_{baffle}$ and θ_b in radians is given by equation (5.58).

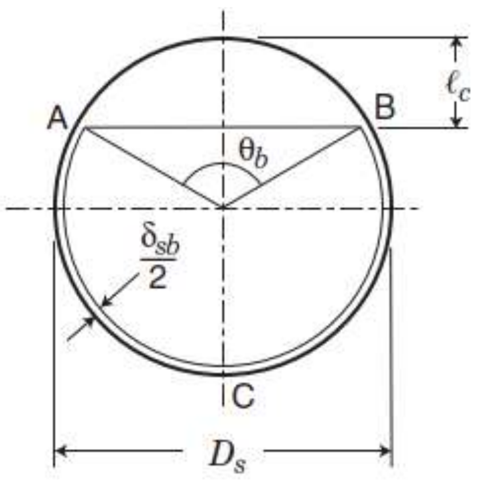

Figure 5.4: Single segmental baffle geometry showing shell-to-baffle diametral clearance δ_{sb}

The overall heat transfer coefficient (U_0) for the shell and tube heat exchanger is an important parameter for its design and efficiency. It is calculated using the following equation [120]:

$$\frac{1}{U_0} = \frac{1}{\bar{h}_{shell}} + R_{shell,f} + \frac{d_0 \ln(d_0/d_i)}{2k_w} + R_{tube,f}\frac{d_0}{d_i} + \frac{1}{\bar{h}_{tube}}\frac{d_0}{d_i} \tag{5.74}$$

where $\bar{h}_{shell}$ is the heat transfer coefficient on the shell side, $\bar{h}_{tube}$ shows the heat transfer coefficient on the tube side, $R_{shell,f}$ and $R_{tube,f}$ indicate the fouling factor for the shell and tube sides, respectively. It is a dimensionless number that describes the flow regime (laminar or turbulent flow) and is the ratio of inertial forces to viscous forces within the fluid. It is based on the velocity of the fluid, density, viscosity, and the characteristic of the tube length (usually diameter). In this analysis, fouling factors are omitted from consideration due to the simplicity of the calculations. The terms d_0 and d_i show the external and internal diameter of the tubes, respectively. k_w is the thermal conductivity of the the tube wall material. The equation balances the resistances to heat transfer from both the shell and tube sides, including the effects of fouling and the conductive resistance through the tube wall. This comprehensive approach ensures a more accurate and reliable design and analysis of the heat exchanger's performance under various operating conditions.

5.8.1.1 Tube side (single phase)

The heat transfer in the single-phase process inside the tube ($\bar{h}_{tube}$) is calculated according to the Dittus-Boelter equation [119]:

$$\bar{h}_{tube} = 0.024\frac{k_l}{d_i}{\mathrm{Pr}_{tube}}^{1/3}{\mathrm{Re}_{tube}}^{0.8}\left(\frac{\mu_t}{\mu_t^w}\right)^{0.14} \tag{5.75}$$

$$\mathrm{Pr} = \frac{\nu}{\alpha} \tag{5.76}$$

$$\mathrm{Re} = \frac{\rho u L}{\mu} \tag{5.77}$$

where k_l represents the thermal conductivity of the fluid in the tube. Pr_{tube} shows the Prandtl number of the liquid in the tube side. It is a dimensionless number that characterizes the relative thickness of the momentum and thermal boundary layers. It is the ratio of kinematic viscosity (ν) to thermal diffusivity (α). Re_{tube} is the tube side Reynolds number. The Reynolds number is the ratio of inertial forces to viscous forces within a fluid flow. It helps determine the flow regime of the fluid, indicating whether the flow will be laminar or turbulent. This dimensionless number is crucial for predicting and understanding the behaviour of fluid flows in various applications. The term μ_t is the dynamic viscosity of the fluid in the tube. The dynamic viscosity of the fluid at the wall temperature is shown by μ_t^w. This term accounts for the viscosity variation due to the temperature difference between the fluid bulk and the tube wall. ${\mathrm{Re}_{tube}}^{0.8}$ indicates that the heat transfer coefficient is strongly dependent on the flow regime, as higher

Reynolds numbers typically correspond to turbulent flow, which enhances heat transfer due to increased fluid mixing. ${\Pr_{tube}}^{1/3}$ suggests a less strong but still significant dependence on the fluid's thermal properties. The term $\left(\frac{\mu_t}{\mu_t^w}\right)^{0.14}$ corrects for the temperature-dependent viscosity effects, which can be important in high-temperature applications. In Equation (5.77),ρ is the density of the fluid, u is the velocity of the fluid, L is a characteristic linear dimension (e.g., hydraulic diameter).

5.8.1.2 Tube side (phase change for pure substances) [117]

The process of evaluating heat transfer (h_{tube}) during the phase change of pure substances within a vertical tube can be determined using the methodology outlined by the Chen correlation. This approach is delineated in reference:

$$\bar{h}_{tube} = \bar{h}_{cb} + \bar{h}_{nb} = F_f \bar{h}_{LO} + F_s \bar{h}_p \tag{5.78}$$

Here the total heat transfer coefficient for phase change in a tube, is composed of the contributions from the convective boiling component ($\bar{h}_{cb}$) and the nucleate boiling component ($\bar{h}_{nb}$). The term $\bar{h}_{LO}$ is the heat transfer coefficient if the liquid were flowing on its own at that point in the channel (single-phase convective correlation), and $\bar{h}_p$ is the pool boiling coefficient for the same wall superheat. F_f (boiling enhancement factor) allows for the increase in velocity of the liquid vapor and F_s (suppression factor) allows for the decrease in bubble activity due to the steepening of the temperature gradient. The method for obtaining h_{nb} is based on the Forster and Zuber correlation [121, 122], whereby Chen uses the pool boiling correlation with a suppression factor, S.

By using experimental data from different sources, Chen determined experimental values of the convective boiling enhancement factor, F, and based it on the Lockhart and Martinelli parameter, X_{tt}.

$$\frac{1}{X_{tt}} = \frac{Qu}{(1-Qu)^{0.9}} \left(\frac{\rho_l}{\rho_v}\right)^{0.5} \left(\frac{\mu_v}{\mu_l}\right)^{0.1} \tag{5.79}$$

where, Qu is the vapor quality (or void fraction), representing the fraction of the fluid in the vapor phase. The terms ρ_l and ρ_v are the densities of the liquid and vapor phases, respectively. The terms μ_l and μ_v are the viscosities of the liquid and vapor phases, respectively.

The enhancement factor, therefore, can be determined by the following equation to fit the curve proposed by Chen:

$$\begin{aligned} &\text{For } 1/X_{tt} \leq 0.1,\ F_f = 1; \\ &\text{For } 1/X_{tt} \geq 0.1, F_f = 2.35(0.213 + 1/X_{tt})^{0.736} \end{aligned} \tag{5.80}$$

To simplify the calculations of h_{LO}, a liquid heat transfer coefficient for zero vapor quality, h_{LO}, can be found to be constant throughout the length of the tube. Using the Dittus-Boelter correlation:

$$\bar{h}_{LO} = 0.023\mathrm{Re}_{tube}{}^{0.8}\mathrm{Pr}_{tube}{}^{0.4}\frac{\mathrm{k}_l}{d_i} \tag{5.81}$$

The correlation of Forster and Zuber for nucleate boiling is as follows [122]:

$$\bar{h}_p = 0.00122\frac{k_L^{0.79}C_{P,L}^{0.45}\rho_L^{0.49}g_c^{0.25}\Delta T_e^{0.24}\Delta P_{sat}^{0.75}}{\sigma^{0.5}\mu_L^{0.29}\lambda^{0.24}\rho_V^{0.24}} \tag{5.82}$$

Here k_L represents the liquid thermal conductivity, affecting how heat is conducted through the liquid medium. $C_{P,L}$ is the liquid specific heat at constant pressure, which determines the amount of heat needed to change the temperature of the liquid. The terms ρ_L and ρ_V represent the densities of the liquid and vapor, respectively. The term g_c is the gravitational acceleration constant, which can affect the buoyancy-driven flow in boiling. ΔT_e shows the excess temperature, typically the difference between the tube wall temperature (T_w) and the saturation temperature at system pressure (T_{sat}), driving the phase change process ($\Delta T_e = T_w - T_{sat}$). The term σ is the surface tension, which plays a crucial role in the formation and stability of vapor bubbles. The term μ_L is the liquid viscosity, impacting the flow characteristics of the liquid around the bubbles. The term λ represents the latent heat of vaporization, the heat required to convert the liquid phase into vapor without changing temperature. The expression ΔP_{sat} ($\Delta P_{sat} = P_{sat}(T_w) - P_{sat}(T_{sat})$ quantifies the difference in saturation pressure between the wall temperature ($P_{sat}(T_w)$) and the saturation temperature ($P_{sat}(T_{sat})$). This represents the pressure differential due to the temperature difference at these two points.
The term S in Equation (5.78) depends on the two-phase flow Reynolds number [117]:

$$F_s = \frac{1}{1 + 2.53 \times 10^{-6}(Re_{TP})^{1.17}} \tag{5.83}$$

$$\mathrm{Re}_{TP} = (\frac{\dot{m}d_i}{\mu_l})(1 - x)F^{1.25} \tag{5.84}$$

In calculating the heat transfer coefficient in tubes for an ammonia-water mixture, it is important to consider the effect of mixtures when using correlations intended for pure substances.

Mixture effects [123]

Experimental evidence has consistently shown that the heat transfer rate during nucleate boiling in mixtures is typically lower than that in pure substances. This phenomenon can be attributed to the preferential accumulation of more volatile components in the vapor bubbles, which consequently enriches the surrounding liquid with less volatile, higher boiling point components. This enrichment leads to an increase in the liquid's temperature near the heating surface, thereby diminishing the effective temperature gradient driving the heat transfer. Additionally, a concentration gradient is established, introducing a mass-transfer resistance alongside the existing thermal resistance. Consequently, the effective heat transfer coefficient for a mixture might even be lower than that of any pure component under similar conditions. Schlünder conducted an in-depth analysis of the intertwined heat and mass transfer processes occurring during the boiling of mixtures. From this analysis, he proposed a specific equation to calculate the heat transfer coefficient, accounting for the unique dynamics of boiling mixtures. This equation integrates factors that consider the differences in volatility among the components, the resulting concentration gradients, and the impact of these factors on the boiling process.

$$\bar{h}_{kb} = \bar{h}_{ideal}\left\{1 + (h_{ideal}/\hat{q})\left[1 - \exp(\frac{-\hat{q}}{\rho_L \lambda \beta})\right]\sum_{i=1}^{k-1}\left(T_{sat,k} - T_{sat,i}\right)(y_i - x_i)\right\}^{-1} \tag{5.85}$$

Here k shows the number of components and the index of the highest boiling component, $T_{sat,k}$ and $T_{sat,i}$ are the saturation temperatures of the nth and its components, respectively. The terms y_i and x_i are the mole fractions of its component in the vapor and liquid phases, respectively. The terms λ and β are constants or parameters that characterize the boiling process (these might be specific to the fluid mixture or the boiling conditions). h_{ideal} is an average of the pure component values that is obtained as:

$$\bar{h}_{ideal} = \left[\sum_{i=1}^{k-1} \frac{x_i}{h_{nb,i}}\right]^{-1} \tag{5.86}$$

5.8.1.3 Tube side (phase change for mixtures)

The heat transfer coefficient inside the vertical tube during the phase change process (h_{tube}) is calculated using the correlation developed by Mishra et al. [124] for an ammonia-water mixture, based on their experimental data:

$$\bar{h}_{tube} = C\bar{h}_L(\frac{1}{X_{tt}})^m \mathrm{Bo}^n \tag{5.87}$$

Here the term Bo is the boiling number, a dimensionless number characterizing the boiling process. It is typically defined as the ratio of the boiling heat flux ($\dot{q}$) to the product of the liquid velocity (λ) and the latent heat of vaporization (G) [125]:

$$\mathrm{Bo} = \frac{\dot{q}}{G\lambda} \tag{5.88}$$

the terms h_L and X_{tt} can be calculated using Equations (5.75) and (5.79), respectively. In equation (5.87), the values of the constants C, m and n were modified to 65, 0.5, and 0.15, respectively, based on the work of Riveta and Bestwere [126]. According to data provided by Khir et al. [127], these constants for an ammonia-water solution can be considered as 5.64, 0.23, and 0.05.

5.8.1.4 Shell side (TEMA E)

In shell and tube heat exchangers, particularly for the shell side in a TEMA E configuration, the Bell-Delaware method is often employed to determine the shell side heat transfer coefficient and pressure drop. This method is recognized for its detailed approach in considering various corrections factors affecting heat transfer and fluid flow. The shell side heat transfer coefficient (h_{shell}) is calculated using the equation [117]:

$$\bar{h}_{shell} = \bar{h}_{id}\, J_c\, J_l J_b\, J_s\, J_r \tag{5.89}$$

h_{id} represents the ideal heat transfer coefficient for pure crossflow in a rectangular tube bank. This coefficient forms the base value, which is then adjusted by the correction factors. J_c is the correction factor for baffle configuration, which accounts for the effects of baffle cut and spacing on heat transfer. J_l accounts for the leakage effects, including leakages between tubes and baffles, as well as between baffles and the shell. J_b is the correction factor for bypass effects due to bundle and pass partition. J_s corrects for variable baffle spacing, particularly at the inlet and outlet sections of the heat exchanger. J_r adjusts for the temperature gradient that can build up in the laminar flow region. The value of h_{id} is further expressed as [117]:

$$\bar{h}_{id} = j_i C_{ps} \left(\frac{\dot{m}_s}{A_s}\right) \left(\frac{k_s}{Cp_s \mu_s}\right)^{2/3} \left(\frac{\mu_s}{\mu_s^w}\right)^{0.14} \tag{5.90}$$

The subscripts ‘s’ and ‘w’ in Equation (5.90) show the shell side and the wall, respectively. Here, C_{ps} , k_s, μ_s, and $\dot{m}_s$ refer to the specific heat, thermal conductivity, dynamic viscosity, and mass flow rate of the shell-side fluid, respectively, while A_s is the flow area. The subscript ‘w’ refers to the wall conditions, highlighting the importance of wall properties in overall heat transfer. The Colburn j-factor for an ideal tube bank is represented as [128]:

$$j_i = a_1 \left(\frac{1.33}{P_T/d_0}\right)^{a} (\mathrm{Re}_s)^{a_2} \tag{5.91}$$

where P_T shows the tube pitch, Re_s the Reynolds number on the shell side. and the exponent a is calculated as follows [128]:

$$a = \frac{a_3}{1 + 0.14(\mathrm{Re}_s)^{a_4}} \tag{5.92}$$

The constants a_1, a_2 and a_3 are obtained from Ref. [128] are shown in Table 5.5 . The correlation factors in Equations. (5.91) and (5.92) are listed in Table 5.5.

Table 5.5: Correlation coefficient for j_i, Equations (5.91) and (5.92)

Layout angel	Reynolds number	a_1	a_2	a_3	a_4
30°	10^5-10^4	0.321	-0.388	1.450	0.519
	10^4-10^3	0.321	-0.388		
	10^3-10^2	0.593	-0.477		
	10^2-10^1	1.360	-0.657		
	<10	1.400	-0.667		
45°	10^5-10^4	0.370	-0.396	1.930	0.500
	10^4-10^3	0.370	-0.396		
	10^3-10^2	0.730	-0.500		
	10^2-10^1	0.498	-0.656		
	<10	1.550	-0.667		
90°	10^5-10^4	0.370	-0.395	1.187	0.370
	10^4-10^3	0.107	-0.266		
	10^3-10^2	0.408	-0.460		
	10^2-10^1	0.900	-0.631		
	<10	0.970	-0.667		

5.8.1.5 Shell side (TEMA K)

The boiling heat transfer coefficient on the shell side for the tube bundle is calculated according to the Pelan correlation. This correlation is particularly useful in systems where both nucleate boiling and natural convection contribute to the overall heat transfer process [129]:

$$\bar{h}_{b,shell} = F_b \bar{h}_{nb} + \bar{h}_{nc} \tag{5.93}$$

Where the term h_{nc} represents the nucleate boiling heat transfer coefficient. This is a key parameter in boiling heat transfer and is influenced by factors such as the surface characteristics, fluid properties, and temperature difference. The term F_b is a factor that accounts for the effect of thermosiphon-type circulation within the tube bundle. Thermosiphon circulation refers to the natural convection cycle that occurs due to density differences in the fluid as it heats up and cools down, driving a flow loop without the need for a mechanical pump. The term h_{nb} is the heat transfer coefficient for the liquid phase under natural convection. This coefficient depends on the properties of the fluid, the geometry of the system, and the temperature gradient.

The modified Mostinski correlation [129] is a detailed approach to calculating the nucleate boiling heat transfer coefficient (h_{nb}) for a pure component in a mixture. This correlation takes into account the unique properties of each component in the mixture, such as its critical pressure and reduced pressure:

$$\bar{h}_{nb,i} = 0.00417\, p_{c,i}^{0.69}\, \hat{q}_i^{0.7} F_{p,i} \tag{5.94}$$

where p defines the critical pressure for the pure component i, $\hat{q}_i$ is the heat flux, $F_{p,i}$ is the pressure correction factor for the pure component i [129]:

$$F_{p,i} = 1.8\, p_{r,i}^{0.17} + 4\, p_{r,i}^{1.2} + 10\, p_{r,i}^{10} \tag{5.95}$$

In Equation (5.95), $p_{r,i}$ is the reduced pressure for the pure component *i* and is calculated as:

$$p_{r,i} = \frac{p_i}{p_{c,i}} \tag{5.96}$$

The factor F_b in Equation (5.94) is found by the following equation [129]:

$$F_b = 1.0 + 0.1\left[\frac{0.785 d_b}{C_1^*(p_T/d_0)^2 d_0} - 1.0\right]^{0.75} \tag{5.97}$$

Here d_b is the bundle diameter or outer tube-limit diameter, d_0 shows the external diameter of tube, and C_1^* considers 1.0 for the square layout and 0.866 for the triangular layout.
The Natural Convection Heat Transfer Coefficient (h_{nc}) can be attained as [130]:

$$\bar{h}_{nc} = \left\{0.60 + \frac{0.387(\mathrm{Gr\,Pr})^{1/6}}{[1+(0.559/\mathrm{Pr})^{9/16}]^{8/27}}\right\}^2 \frac{k}{d} \tag{5.98}$$

where, Gr is the Grashof number and calculated as explained in Ref. [129]. However, the h_{nc} has a relatively small contribution to the total heat transfer except when the excess temperature difference is less than about 4 °C; $\Delta T_e = T_s - T_{sat}$. T_s is the solid surface temperature and T_{sat} is the saturation temperature at system pressure. For larger temperature differences, Palen [129] considered a rough approximation for h_{nc} of 1000 W/m^{2}K for water and aqueous solutions.

5.8.2 Air cooled heat exchanger

The overall heat transfer coefficient for the air-cooled heat exchanger is calculated by [131]:

$$\frac{1}{U_0} = \left(\frac{1}{\bar{h}_{tube}} + R_{D,tube}\right)\frac{A_{tot}}{A_i} + \frac{A_{tot}\ln(d_r/d_i)}{2\pi k_{tube} L} + \frac{R_{con}A_{tot}}{A_{con}} + \frac{1}{\eta_w \bar{h}_{air}} + \frac{R_{D,air}}{\eta_w} \tag{5.99}$$

Here, $\bar{h}_{air}$ is the air side heat transfer coefficient, $R_{D,tube}$ shows the tube side fouling factor, R_{con} is the contact resistance, $R_{D,air}$ indicates the air side fouling factor. In this analysis, fouling factors and contact resistance are omitted from consideration due to the simplicity of the calculations. A_{tot} shows the total external surface area of the finned tube, A_i is the internal surface area of tube ($\pi d_i L$), A_{con} represents the contact area between the fin and tube wall, d_r depicts the external diameter of the root tube, L is the tube length, η_w shows the weighted efficiency of the finned surface and k_{tube} illustrates the thermal conductivity of the tube wall.
The correction factor F_T in Equation (5.48) is calculated in air cooled heat exchangers as defined in References [132,134]

$$P_{ACHE} = \frac{T_{air,out} - T_{air,in}}{T_{h,in} - T_{air,in}} \tag{5.100}$$

$$R_{ACHE} = \frac{T_{h,in} - T_{h,out}}{T_{air,out} - T_{air,in}} \tag{5.101}$$

P_{ACHE} is measure of the ratio of the heat transferred to the heat which would be transferred if the same cold fluid temperature was raised to the hot fluid inlet temperature; therefore, P_{ACHE}

is the temperature effectiveness of the heat exchanger on the cold-fluid side. The correction factor can be calculated as [135]:

$$F_{LMTD} = \frac{\ln\left(\frac{1 - R_{ACHE}P_{ACHE}}{1 - P_{ACHE}}\right)}{(NTU_{ACHE})(\frac{1}{R_{ACHE}} - 1)} \tag{5.102}$$

$$\mathrm{NTU}_{ACHE} = -R_{ACHE}\ln(1 - \varepsilon_{ACHE}) \tag{5.103}$$

$$\varepsilon_{ACHE} = -\frac{(\ln(1 - R_{ACHE}P_{ACHE}))}{R_{ACHE}} \tag{5.104}$$

Here, NTU_{ACHE} is a measure of the heat exchanger size relative to the heat capacity rate of the fluids and ε_{ACHE} shows the ratio of the actual heat transfer to the maximum possible heat transfer.

5.8.2.1 Tube side (condensation process)

The heat transfer coefficient of condensation for the pure fluid inside the horizontal tube is given by the Shah correlation [136]:

$$\bar{h}_{tube,pure} = \bar{\mathrm{h}}_{LO}\{(1 - Qu)^{0.8} + 3.8Qu^{0.76}(1 - Qu)^{0.04}P_r^{-0.38}\} \tag{5.105}$$

where, the term h_{LO} is calculated with Equation (5.75) , P_r shows the reduced pressure and obtained from Equation (5.96) and Qu is the vapour quality. Bell and Mueller [137] recommended the following procedure to correct the mixture condensation effects in tubes:

$$\frac{1}{\bar{h}_{tube}} = \frac{1}{\bar{h}_{tube,pure}} + \frac{Y_V}{\bar{h}_V} \tag{5.106}$$

Here, $\bar{\mathrm{h}}_V$ depicts the heat transfer coefficient in the gaseous phase. Y_V is the ratio between the sensible part of the mixture condensation and the latent part is given by [138]:

$$Y_V = xC_{Pv}\frac{\Delta T_{glide}}{\Delta H_{vap}} \tag{5.107}$$

where C_{Pv} is the heat capacity of the gaseous phase, ΔT_{glide} is the temperature glide during condensation, which represents the temperature range over which the phase change occurs in mixtures. The term ΔH_{vap} is the enthalpy change associated with vaporization (or latent heat of vaporization). Y_V quantifies the effect of the sensible heat transfer relative to the latent heat transfer in the mixture, which is particularly important for mixtures with non-negligible temperature glide during phase change.

5.8.2.2 Air side

According to the recommended correlation by Ganguli et al. [139], the heat transfer coefficient in the air side is calculated as:

$$\bar{h}_{air} = 0.38\frac{k_{air}}{d_r}\mathrm{Pr}_{air}{}^{1/3}\mathrm{Re}_{air}{}^{0.6}\left(\frac{A_{tot}}{A_0}\right)^{-0.15} \tag{5.108}$$

where, A_0 is the total surface area of the finned tube ($\pi d_r L$), k_{air} shows the air side thermal conductivity. A_{tot} is the total external surface area of the finned tube.
The pressure drop in the air side is a sum of two primary components: one due to frictional losses in the air flow through the tube bundle, and the other due to dynamic losses associated with the air exiting the fan ring:

$$(\Delta P_{total})_{fan} = \frac{2\, f_{air}\, N_r\, G_{air}^2}{\rho_{air}} + \frac{\alpha_{fr}\, \rho_{fr}\, V_{fr}^2}{2\, g_c} \tag{5.109}$$

Here N_r is the number of tube rows through which the air passes. G_{air} indicates the mass velocity (mass flow rate per unit area) of the air. The term α_{fr} is a kinetic energy correction factor, accounting for the non-uniform velocity distribution in the fan discharge. The term ρ_{fr} depicts the density of the air leaving fan ring. V_{fr} displays the velocity of air leaving the fan ring. f_{air} shows the friction factor correlation and, for the flow of air across tube banks with equilateral triangular pitch, is calculated by correlation of Robinson and Briggs [140]:

$$\mathrm{f}_{air} = 18.93\ \mathrm{Re}_{air}{}^{-0.316}\left(\frac{P_T}{d_r}\right)^{-0.927} \tag{5.110}$$

5.9 Heating and cooling demand profiles

The proposed system is examined by utilizing information obtained from an established geothermal district heating network situated in the Molasse Basin, which is found in the southern region of Germany [141]. This region is known for its geological characteristics that make it a valuable source of geothermal energy. The Southern German Molasse Basin plays a vital role in electricity and heating demand due to its significant geothermal potential [30]. Geothermal energy harnessed from this region reduces its reliance on fossil fuels and lowers greenhouse gas emissions, promoting both energy sustainability and environmental conservation [141]. The VDI 4655 method [142], which originates from the research of Eller et al. [141], is employed to examine the annual system performance, considering both climatic conditions and the associated energy demand. This method offers a structured and systematic approach for considering heating and cooling system performance, considering climate zones, and categorizing days based on weather conditions to enable precise evaluations of energy demand. It utilizes test reference years (TRY) and frequency-based analysis to reflect real-world usage patterns, ultimately supporting the nation's transition to greener, more efficient heating and cooling solutions and enhancing energy sustainability while reducing carbon emissions. This method adopts a comprehensive approach, systematically classifying days into ten distinct categories based on their specific weather conditions, involving variables like mean ambient temperature and cloudiness. These ten typical day types establish a valuable framework for assessing system performance and energy demand, accounting for both seasonal and day type differentiations. The categorization includes distinctions between summer (S), winter (W), and transition (T) seasons, as well as the categorization of regular days such as workdays (W) and Sundays (S). Additionally, fine (F) and cloudy (C) days are meticulously differentiated, providing a strong foundation for achieving accurate and reliable results in the evaluation of energy system efficiency and performance. However, there is no differentiation between fine and cloudy days during the summer season (X). These ten typical day categories, including WWF, WWC, WSF, WSC, TWC, TSC, TSF, TWF, SWX, and SSX, provide a detailed overview of energy demand throughout the year. The division of Germany into different climate zones and the consideration of test reference years (TRY) contribute to a dynamic evaluation process, wherein the number of typical days (n) varies seasonally and aligns with climate variations, ensuring a comprehensive assessment of energy system efficiency and performance. Table 10 displays the various climate zones found in Germany. The test reference years data include parameters like temperature, solar radiation, wind speed, and other meteorological information for various months, hours, and days, enabling engineers and designers to make informed decisions about the design and efficiency of buildings and their energy systems. It is worth noting that these reference years can vary depending on the location in Germany, and different datasets may be used for different regions or cities to account for local climate variations. This study involves the simulation of diverse typical days for TRY13, which are linked to the Southern German Molasse Basin.

Table 5.6: Test reference years according to VDI 4655 [30]

Climate Zone	Number of Typical Days (Frequency of the Different Typical Days)									
	WWF	WWC	WSF	WSC	TWC	TSC	TSF	TWF	SWX	SSX
…										
TRY12	23	57	2	16	91	18	8	27	104	19
TRY13	29	91	6	19	72	10	15	37	73	13
TRY14	22	115	5	25	81	15	11	42	42	7
…										

The annual system performances are determined by weighting these typical days based on their frequency, denoted as n. In order to examine a quasi-stationary simulation, Table 2 displays the corresponding mean heating and cooling demands, which are calculated in accordance with the mean ambient temperature. This data is based on calculations from the research conducted by Eller et al. [141].

Table 5.7: Mean values of heating and cooling demands depending on the mean ambient temperature as well as annual frequency *n* of these typical days according to VDI 4655 [141]

	WWF	WWC	WSC	WSF	TSC	TWC	TSF	TWF	SWX	SSX
	n=91	n=29	n=19	n=6	n=10	n=72	n=15	n=37	n=13	n=73
$T_{mean,ambient}$ (°C)	-6	0	1	2.5	5	8	13.5	14	15	20
$\dot{Q}_{mean,heating}$ (MW)	12	12	10.8	11.8	5.8	6	4.8	6	4	2
$\dot{Q}_{mean,cooling}$ (MW)	-	-	-	-	-	-	-	-	3	5

Based on the information provided in Table 5.7, it is apparent that the heating and cooling demands are related with the mean ambient temperature and specific conditions.

- Heating demand and ambient temperature: it is evident that the heating demand increases as the mean ambient temperature decreases. In other words, colder weather leads to higher heating demands.
- Effect of cloudy days: on cloudy days, particularly in the afternoon, the heating demand significantly rises when compared to fine days. This indicates that weather conditions, such as cloud cover, have a substantial impact on heating requirements.
- Heating demand on Sundays vs. workdays: when analyzing heating demand on Sundays and workdays, a general trend emerges. The heating demand tends to be lower on Sundays, with only minor variations. This suggests that on weekends, there is a consistent, lower need for heating compared to the working days.
- Cooling demand in summer: During summer days, cooling demand becomes essential to maintain a comfortable temperature in living spaces. As temperatures rise, cooling systems are required to keep the indoor environment within an acceptable comfort range.

Due to a lack of available data concerning cooling demand in Germany, the calculation of cooling requirements necessitates some thoughtful assumptions and considerations. The determination of the cooling demand relies on the application of the Hourly Analysis Program [143] commonly known as Carrier, drawing from data obtained from residential structures within Germany. The program, known for its precision and reliability in the field of heating, ventilation, and air conditioning (HVAC) analysis, provided valuable insights into the energy needs of the property. This process considers a numerous of factors, including the outside temperature, design specifications, and various contributors, such as the condition of the roof, walls, and windows. Additionally, it considers internal influences such as lighting, the presence of occupants, and the operation of equipment, as well as the impact of ventilation and the infiltration of external air. All these aspects collectively shape and influence the cooling requirements within the context of the analysis [144].

The comprehensive analysis conducted on the multi-family house situated in the temperate region of southern Germany, with an area of 245 square meters, employed the Carrier program to determine the heating and cooling demands essential for ensuring a comfortable living environment. The results of the analysis clearly revealed the maximum heating requirement for the property, which stood at 0.069 kW per square meter. This parameter is important as it directly influences the size and capacity of the heating system to be installed, ensuring that during the coldest periods, the building can be adequately warmed to provide a comfortable living space for the occupants. On the other hand, the cooling demand was calculated to be 0.029 kW per square meter. This is an important parameter, especially considering the potential for heatwaves and increased temperatures during the summer months, ensuring that the cooling systems of the building are appropriately capable of maintaining a cool and comfortable indoor environment. In this regard, the maximum cooling demand is calculated to be about 5 MW as follows:

$$Max\ heating\ demand\ \rightarrow 12\ \mathrm{MW}\ \rightarrow \frac{12\ \mathrm{MW}}{0.069\ \mathrm{kW}/\mathrm{m^2}} \cong 172413\ \mathrm{m^2}$$

$$Max\ cooling\ demand\ \rightarrow 172413\ \mathrm{m^2} \times 0.029\ \frac{\mathrm{kW}}{\mathrm{m^2}} \cong 5\ \mathrm{MW}$$

Based on an approximate average area of 75 m^2 per district heating network, the total number of networks is estimated at 2,298. This estimate closely matches the values reported by Eller in Ref. [30].

5.10 Input data and boundary conditions

In the simulation of the on-design mode for the integrated energy system, several assumptions and boundary conditions are established to ensure accuracy and relevance to practical scenarios. The pivotal parameters for this mode are detailed in Table 5.8, which includes a comprehensive list of operational conditions and thermodynamic properties essential for the simulation. An essential parameter for the on-design mode is the ambient temperature, which is assumed to be 8 °C. This figure represents the annual mean temperature in Germany, as referenced in the literature [141]. This ambient temperature has a significant impact on the system performance and has been integrated into the simulation as a fundamental boundary condition. Another central boundary condition is the turbine inlet pressure, which is set at 30 bar. This output is directly influenced by the concentration of ammonia in the pre-boiler and the boiler, which is maintained at 0.8 kg (NH3)/kg(solution). This concentration is important in achieving the desired thermal and chemical properties of the working fluid, which, in turn, affects the efficiency and output of the energy conversion process.

The parameters and conditions outlined in this section are not only crucial for the fidelity of the simulation but also serve as a reference for the potential scale-up and real-world application of the system. They provide a basis for analysing the response of the system to different operational strategies and for evaluating its performance under various environmental and load conditions.

Table 5.8: Input data and boundary conditions used for the design condition of the systems and simulate the processes.

Parameter	Symbol	Value
Dead state pressure (bar)	P_{dead}	1
Dead state temperature (°C)	T_{dead}	$T_0 + 7$
Geothermal hot water temperature (°C) [141]	T_{geo}	138
Geothermal hot water mass flow rate (kg/s) [141]	$\dot{m}_{geo}$	120
Winter condition		
Ambient temperature (°C) [141]	T_0	8
Heating demand (MW) [141]	$\dot{Q}_H$	8
Summer condition		
Ambient temperature (°C)[145]	T_0	20
Heating demand (MW)	$\dot{Q}_H$	2
Cooling demand (MW)	$\dot{Q}_C$	4
Domestic heat exchanger		
Supply heating temperature (°C)[141]	T_{33}	90
Return heating temperature (°C)[141]	T_{32}	60
Pinch point difference in the domestic heat exchanger [141]	ΔT_{pp}	10
Kalina cycle		
Pump isentropic efficiency (%) [145]	$\eta_{is,PU}$	75
Turbine isentropic efficiency (%) [141]	$\eta_{is,TUR}$	85
Total fan efficiency (%)[145]	η_{fan}	70
Turbine inlet pressure (bar)	TIP	30
Ammonia concentration in the boiler (%)[145]	x_{17}	80
Pinch point temperature difference in boiler	$\Delta T_{pp,BOI}$	5
Endpoint temperature difference in the boiler	$\Delta T_{end,BOI}$	8
Pinch point difference in the internal heat exchanger	$\Delta T_{pp,INT}$	8
Pinch point difference in the Kalina condenser	$\Delta T_{pp,CON,KC}$	10
Absorption refrigeration cycle		
Ammonia concentration in the outlet stream of absorber (%)	x_1	50
Evaporator temperature (°C) [145]	T_{eva}	4
Pinch point difference in the ARC condenser	$\Delta T_{pp,CON,ARC}$	10
Pinch point difference in the absorber	$\Delta T_{pp,ABS}$	10
Ethylene glycol concentration	ζ_{42}	35
Inlet temperature of water- ethylene glycol	T_{42}	10
Temperature differences in evaporator	$T_{42} - T_{43}$	10

5.11 Design and off-design analysis

In thermodynamic systems, ensuring optimal functionality across a variety of conditions is vital. In thermodynamic analysis, the design calculation refers to the evaluation of a system or a component under its specified or intended operating conditions. Such an analysis ensures that parameters like temperature, pressure, flow rate, among others, associate with their proposed design specifications. This depicts an idealized setting where the system is expected to function at its optimal, with each component operating completely as designed. These design evaluations are important during the design stage, operating as the performance target against which the efficacy of the system is estimated.

Off-design analysis, in contrast, evaluates the performance of thermodynamic systems when they operate under conditions that deviate from their specified design conditions. In real-world scenarios, thermodynamic systems often need to operate under varying loads, fluctuating external temperatures, and other changing conditions, which means they frequently function at off-design points. Off-design analysis allows engineers to understand the system performance under these variable conditions, ensuring that the system remains efficient, safe, and reliable even when it is not operating under its ideal or intended conditions. It is essential for predicting an overall operational flexibility and efficiency of system over its lifetime [146]. Conducting off-design evaluations in thermodynamic systems means examining the system and performance of its components under conditions deviating from their intended design parameters. This method comprises data collection, equation formulation, computational processes, result interpretation, and proposing informed suggestions for enhancing and optimizing the system. Figure 5.5 outlines the sequence and interrelation of steps required for off-design evaluations in the proposed systems. Starting with design calculations, one must first discover the operational design parameters [147]. A crucial step in the off-design process is determining the maximum heat transfer rate for each heat exchanger during the design calculations, which is essential for finding the UA values of the heat exchangers or designing them. In this step, there are two ways to continue calculations with heat exchangers. One approach is to utilize the UA values from the design condition and, using the method presented by Menente [148], recalculate the UA for off-design conditions. Alternatively, by designing the heat exchanger, the U values can be determined based on specifics from the design mode. The UA heat exchange capacity is modified considering the actual mass flow rate:

$$\frac{(UA)_{off-design}}{(UA)_{design}} = \left(\frac{\dot{m}_{off-design}}{\dot{m}_{design}}\right)^{m} \tag{5.111}$$

The heat exchanger configuration determines the exponent m. The exponent m is set to 0.44 for the air-cooled condenser, 0.66 for the generator, solution heat exchanger and evaporators, 0.15 for the boiler [149, 150]. After this determination, heat exchangers are typified based on their individual applications. The final design of these exchangers is based on the determined maximum heat transfer capacity. Simultaneously, other crucial calculations are performed, including the isentropic enthalpy drops and Stodola's constant in the turbine. These calculations are essential for determining the turbine efficiency using Stodola's equation and for computing the turbine mass flow rate. Based on the Figure 5.5, the off-design evaluation progresses through iterative stages until convergence is reached. The fulfilment of this convergence is signified by the uniformity in various thermodynamic properties, such as temperature, pressure, and ammonia concentration, across the exit streams of some heat exchangers and the entrance streams of others. The evaluation is supposed complete when variations are confined within a 1 % limit.

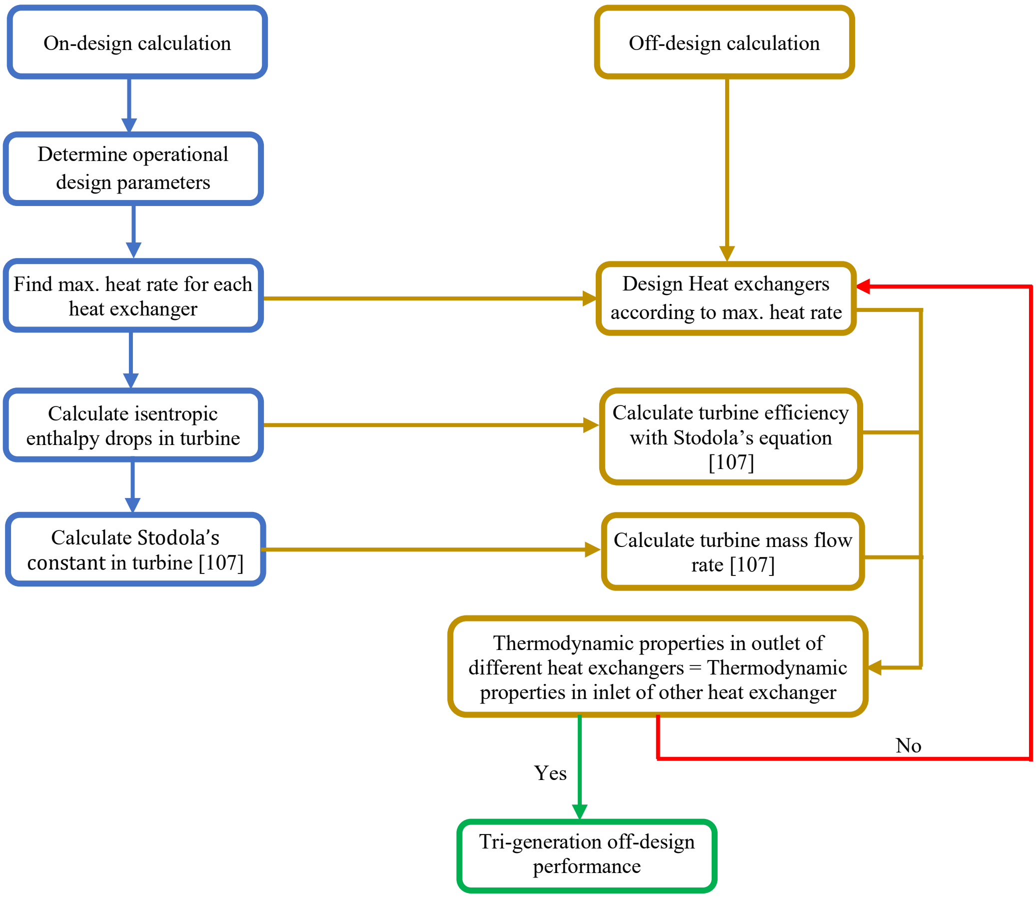

Figure 5.5: The procedure of off-design evaluation

In this study, for the annual calculation, the proposed tri-generation systems are subjected to varying boundary conditions, specifically under part-load scenarios [30]. In these systems, the performance of heat exchangers and turbines is fundamentally sensitive to off-design operating conditions. This sensitivity results from fluctuations in fluid properties due to temperature and pressure changes, efficiency variations established in altered flow dynamics and pressure ratios and differing thermal gradients that directly influence heat transfer. In addition, components may experience varied operational stresses, and their operation may deviate from established performance curves. Furthermore, the interconnected nature of system components means that alterations in one can have cascading effects on others, highlighting the importance of comprehensive off-design calculations [150].

6 Results and discussion

In this section, a thorough validation and verification of the models used in this work are conducted, ensuring confidence in the simulation results. This process involves the comparison of simulated outcomes with established benchmarks and real-world data, confirming the accuracy and reliability of the modelling approach. Subsequently, an in-depth investigation is carried out on the impact of various boundary conditions on the exergetic analysis of the introduced systems. By systematically altering these conditions and observing the resultant changes, valuable insights are gained into the sensitivity of the systems and operational variations. Furthermore, a comprehensive economic analysis of both systems is performed, evaluating their cost-effectiveness and financial feasibility. This economic perspective is crucial, as it offers a pragmatic view of the viability of the proposed systems, ensuring that the recommendations are technically sound and economically practical. The synthesis of these analyses forms a robust foundation for the proposed systems, reinforcing their potential for real-world application and scalability.

6.1 Validation and verification

Verification and validation are critical steps in the modelling and simulation of thermodynamic systems, as they ensure the accuracy, reliability, and credibility of the results. To quantify the differences between the data available in the literature or existing systems, and the data obtained from simulations in this study, the following approach is presented:

$$\text{Deviation} = \frac{\left|X_{reference\ data} - X_{simulation\ data}\right|}{X_{reference\ data}} \times 100\ \% \tag{6.1}$$

Referenced in section 4, the proposed systems are composed of three separate systems interconnected subsystems, each playing a key role in the overall functionality and efficiency of the operation. In addition, as detailed in section 5.8, shell and tube heat exchangers as well as tube-fin heat exchangers are commonly selected in this work to accommodate various processes, since these are two prevalent types of heat exchangers.

6.1.1 Validation results of power subsystems

The power subsystem, associated with the Kalina cycle, is validated based on the current power plant in Húsavík [151]. The comparison of actual Kalina cycle data, as presented by Ogriseck [151], with simulation results of this present work can be found in Table 6.1 at different state points (from state points 1-11). The states marked with stars (state points 1, 5 and 7) align with the current power plant in Húsavík, as they were used for validation purposes as input data. Key design parameters supporting this validation include geothermal brine mass flow rate and inlet temperature, turbine inlet pressure, condensing pressure, as well as live stream temperatures and pressures. A detailed examination of the table reveals the agreement between the two datasets. At specific state points like 5, 6, 7 for ammonia concentration and 8, 10, 11 for pressure, there is a significant alignment between the present work and the Húsavík data. With less than 0.7 % deviation, the match highlights how accurate current study is.

Table 6.1: Validation results of the Kalina cycle at different state points (1-11) for the present work (a) and the data from the existing power plant in Húsavík [151] (b)

Point	Temperature (K)		Pressure (kPa)		Ammonia concentration($\frac{kg_{NH_3}}{kg_{solution}}$)	
	(a)	(b)	(a)	(b)	(a)	(b)
1*	281.15	281.15	4.6	4.6	0.82	0.82
2	281.20	281.15	35.3	35.3	0.82	0.82
3	314.26	314.15	34.3	34.3	0.82	0.82
4	336.10	336.15	33.3	33.3	0.82	0.82
5*	389.15	389.15	32.3	32.3	0.82	0.82
6	389.15	389.15	32.3	32.3	0.973	0.97
7*	389.15	389.15	32.3	32.3	0.498	0.5
8	316.21	316.15	6.6	6.6	0.973	0.97
9	319.11	319.15	31.3	31.3	0.498	0.5
10	319.18	319.15	6.6	6.6	0.82	0.82
11	303.16	303.15	5.6	5.6	0.82	0.82

* These states are the same as the literature due to the use for validation purpose as input data.

6.1.2 Verification results of cooling subsystems

The cooling subsystem, linked with the absorption refrigeration system, has been verified using the data from the literature authored by Adewusi [152]. Table 6.2 reveals this comparison across various state points (from state points1-14), comparing parameters like pressure values and ammonia concentration at temperatures corresponding to these state points.

Table 6.2: Verification results of the absorption refrigeration cycle at different state points (1-14) for the present work (a) and the data reported by Adewusi [152] (b)

Point	Temperature (°C)		Pressure (bar)		Ammonia concentration ($\frac{kg_{NH_3}}{kg_{solution}}$)	
	(a)	(b)	(a)	(b)	(a)	(b)
1*	40	40	2,45	2.44	0.372	0.371
2	40.44	40.45	15.56	15.55	0.372	0.371
3*	110	110.06	15.56	15.55	0.372	0.371
4	130.32	130.31	15.56	15.55	0.272	0.271
5	40.44	40.45	15.56	15.55	0.272	0.271
6	40.70	40.71	2.45	2.44	0.2708	0.271
7	107	107.33	15.56	15.55	0.946	0.946
8	107	107.36	15.56	15.55	0.372	0.371
9	44.45	44.07	15.56	15.55	0.999	0.999
10*	40	40	15.56	15.55	0.999	0.999
11	16.75	16.88	15.56	15.55	0.999	0.999
12	-14.15	-14.14	2.45	2.44	0.999	0.999
13*	-10	-10	2.45	2.44	0.999	0.999
14	37.29	37.39	2.45	2.44	0.999	0.999

* These states are the same as the literature due to the use for validation purpose as input data.

The states denoted with stars (state points 1, 3, 10, and 13) correspond to the data presented by Adewusi, having been utilized for verification as input data. Primary design factors that facilitate this validation comprise of geothermal brine mass flow and inlet temperature, mass flow rate and inlet pressure of the turbine, condensing and evaporating temperature values, and the live stream temperatures and pressures. Observations from the table show a pronounced consistency between the two data sets. Conspicuously, both pressure and ammonia concentration values from the present work closely align with those reported by Adewusi, with a deviation of less than 0.7 %. This minimal disagreement underlines the reliability of the current results, confirming the design parameters and performance of the system.

6.1.3 Validation results of shell and tube heat exchangers

As discussed in Section 5.8.1, the shell and tube heat exchangers which are employed in this study are designed to operate with either a single phase or experience phase changes in both the shell and tube sides. This section focuses on presenting the comparative analysis of simulation data against reference data.

6.1.3.1 Validation results of single-phase in both shell and tube side

The shell and tube heat exchanger model, featuring a single phase in both shell and tube sides, is verified using corresponding values provided by Shah and Sekulic [153]. The shell side of the heat exchanger had an inside diameter of 0.336 meters and consisted of a single shell in series and parallel, following the TEMA E standards. The tube side featured a 45-degree rotated square tube pattern. The model had 102 tubes, each with an outside diameter of 19 mm and a wall thickness of 1.2 mm, arranged in two tube passes and spanning a length of 4.3 meters. For the baffles, the type used is single segmental with a cut of 25.8 %. The fluids are lubricating oil and seawater. The properties of these fluids are depicted in Table 6.3.

Table 6.3: Fluid properties used to verify the shell and tube heat exchanger, featuring a single phase in both the shell and tube sides, were evaluated by Shah and Sekulic [153]

Fluid	Density (kg/m^3)	Specigic heat (J/kg.K)	Dynamic viscosity (Pa.s)	Thermal conductivity (W/m^2K)	Prandtl number (-)
Oil at 63 °C	849	2094	0.0646	0.140	966
Seawater at 35 °C	993	4187	0.000723	0.634	4.77

The verification results are summarized in the Table 6.4 provided, which compares the velocity, heat transfer coefficient, exchanger area, and overall heat exchanger coefficient between the reported data by Shah and Sekulic and the present work. The velocities on the tube and shell sides are closely matched with the reported data, as are the heat transfer coefficients and exchanger areas, suggesting a good agreement. The overall heat exchanger coefficient for the present work is 707 W/m^2K, slightly below the reported value of 707.98 W/m^2K, indicating that the model closely replicates the established reference, thus validating the design approach and simulation model used in the present work.

Table 6.4: Comparative verification of the shell and tube heat exchanger with a single-phase in shell and tube sides: present study versus values of Shah and Sekulic [153]

Parameters	Reported data by Shah and Sekulik [153]		Present work	
	Tube side	Shell side	Tube side	Shell side
Velocity (m/s)	1.63	1.18	1.62	1.17
Heat transfer coefficient ($W/m^2.K$)	7837	998.56	7872	1006
Exchanger area (m^2)	26.18		26.76	
Overall heat exchanger coefficient ($W/m^2.K$)	707.98		707	

6.1.3.2 Validation results of phase change in tube side

The shell and tube heat exchanger model, which includes a phase change on the tube side, has been verified against the data provided by Shah and Sekulic [154]. Each tube has an outside diameter of 25 mm, a wall thickness of 2.1 mm, and the tube wall temperature is 453.7 K. Fluid properties inside the tube are given in Table 6.5. The quality of fluid is considered to be 0.2.

Table 6.5: Fluid properties used to verify the shell and tube heat exchanger, featuring a phase change in tube sides, were evaluated by Shah and Sekulic [154]

Fluid property	Value
Vapor density (kg/m^3)	18.09
Liquid density (kg/m^3)	567
Liquid heat capacity (J/kg · K)	2730
Liquid viscosity (kg/m · s)	156×10^{-6}
Vapor viscosity (kg/m · s)	7.11×10^{-6}
Liquid thermal conductivity (W/m · K)	0.086
Surface tension (dyne/cm)	8.2
Latent heat of vaporization (J/kg)	272,000
Critical pressure (kPa)	2550
Saturation temperature (K) at 310.3 kPa	437.5
Vapor pressure (kPa) at 453.7 K	416.6
Molecular weight	110.3

Table 6.6: Comparative verification of the shell and tube heat exchanger with a phase change in tube side: present study versus values of Shah and Sekulic [153]

Parameters	Reported data by Shah and Sekulik [153]	Present work
	Tube side	Tube side
Reynolds number	32,615	32,765
Heat transfer coefficient ($W/m^2.K$)	3784	3803

Table 6.6 presents the verification results, comparing Reynolds number, and heat transfer coefficient on the tube side of the present work with the reported data by Shah and Sekulic [153]. The heat exchanger being verified incorporates a fixed tube sheet design and operates with one shell and one tube passes. The conclusion drawn from the verification is that the present heat exchanger model aligns closely with data by Shah and [153], indicating an effective verification. The minor discrepancies observed are within acceptable ranges, confirming the validity of the heat exchanger design and the accuracy of the simulation model used in the current study.

6.1.3.3 Verification results of the kettle reboiler with phase change in shell side

The kettle reboiler design, specified for verification, incorporates a TEMA K shell and a tube bundle arranged in a square 45-degree pattern. For this verification, the shell side of the reboiler operates with a phase change and contains a mixture of propane (15 %), i-butane (25 %), and n-butane (60 %), while the tube side manages a single-phase flow of condensing steam [155]. The shell has an inside diameter of 5.047 inches (128.2 mm), with a single unit in both series and parallel configuration. Table 6.7 presents the verification results, which include a comparison of the heat transfer coefficient on the shell side as calculated in the present study, with values obtained from the Engineering Equation Solver software simulations. According to the table, the heat transfer coefficient values are 2969.73 W/m²K for the paper reference, 3051 W/m²K from the EES simulation.

The conclusion from these verification results indicates that while there is some variation between the different methods of calculation, the results of the present study are in a reasonable range when compared with established software models. This supports the reliability of the current design approach and simulation process for the kettle reboiler with the specified shell and tube configuration. The data from Serth [155] is used as a benchmark for the verification, ensuring that the model adheres to recognized standards in the field.

Table 6.7: Comparative verification of the kettle reboiler with phase change in shell side: present work versus of data reported in the literature by Serth [155]

Parameters	Reported data by Serth [155]	Present work
	Sell side	sell side
Convection heat transfer coefficient ($W/m^2.K$)	249.8	267
Nucleate boiling heat transfer coefficient ($W/m^2.K$)	1482.06	1568
Heat transfer coefficient ($W/m^2.K$)	2969.73	3051

6.1.4 Verification results of tube-fin heat exchangers

The input data for the verification of the air-cooled heat exchanger includes a tube layout with a 30-degree angle pattern and 254 aluminium tubes, each with a pitch of 1 meter and an outside diameter of 25.4 millimetres (1 inch). The tubes, with a wall thickness of 2.2 mm and a length of 0.98 meters, are arranged in a single pass and are organized into several rows. Additionally, the heat exchanger utilizes aluminium fins, featuring a G-finned type design. The fins have a tip diameter of 56 mm, a frequency of 354 fins per meter, and a thickness of 0.4 mm. The air-cooled heat exchanger in question, as part of the verification process, is comprised of one bay per unit and one bundle per bay, with 348 fins per meter and an inflow velocity of 2 m/s. Heating fluid in the tube side is vapour condensing at 130 °C. According to Table 6.8, the verification results show that the velocity, heat transfer coefficient, exchanger area, and overall heat exchanger coefficient on both the air side and tube side of the present work closely match the data reported in the literature by Schmidt [132]. The discrepancies between the present work and the published data are minimal, with a deviation of less than 1 %. This suggests that the differences are within a reasonable range, thereby demonstrating the validity of the developed simulation code for this type of heat exchanger.

Table 6.8: Comparative verification of the air-cooled heat exchanger of the present work and the data reported in the literature by Schmidt [132]

Parameters	Reported data by Schmidt [132]		Present work	
	Air side	Tube side	Air side	Tube side
Velocity (m/s)	4.13	898.7	4.128	900.1
Heat transfer coefficient (W/m^2.K)	22.49	10,454	22.62	12,879
Exchanger area (m^2)	127.58		128.2	
Overall heat exchanger coefficient (W/m^2.K)	21.37		21.3	

6.2 Results under design conditions

The thermodynamic and thermoeconomic analyses for the proposed systems under design conditions are performed using the input data presented in Table 5.8. Pressure and heat losses in the heat exchangers and pipelines are neglected to simplify the analysis and focus on the key decision parameters [56-82]. The parametric study is conducted to determine the effects of the decision parameters listed in Table 5.8 on system performance. In this study, only one parameter from Table 5.8 varies at a time while the other parameters remain constant. This approach allows for isolating and understanding the impact of each individual parameter, providing valuable insights into the system's behavior and performance.

6.2.1 Parametric analysis during winter days: on-design mode

Table A.1 in Appendix A illustrates the thermodynamic properties and mass flow rates of various streams presented in Figure 4.1, under design conditions during winter days. As shown in Table 5.8, the heat demand of 8 MW is met at an ambient temperature of 8 °C, which is used to analyze the system during winter days.

To meet an 8 MW heat demand, 25.9 kg/s of geothermal hot water at 138 °C enters the domestic heat exchanger and exits at 65 °C. On the cold side of the domestic heat exchanger, 63.6 kg/s of water at 60 °C absorbs heat from the geothermal hot water. This absorption raises the temperature of the water to 90 °C, which can then be used to meet the district heating demand. After meeting the heat demand, the remaining 94.1 kg/s of geothermal hot water is directed to the boiler and pre-boiler to heat the ammonia-water solution on the cold side of these heat exchangers. In the pre-boiler and boiler, 3309 kW and 22,770 kW of heat are transferred from the geothermal hot water, respectively, to increase the temperature and vapor content of the solution. The geothermal hot water leaves the pre-boiler at 72.7 °C and, after mixing with the stream leaving the domestic heat exchanger, returns to the reinjection sources at 70 °C.

The solution with an 80 % ammonia concentration leaves the boiler at 130 °C with a quality of 0.73 in a two-phase state. This two-phase stream is separated into saturated liquid and vapor streams at the same temperature. The poor saturated liquid ammonia-water solution, with a concentration of 42.14 % ammonia, is directed to the internal heat exchanger to preheat the stream entering the pre-boiler. In the internal heat exchanger, 2916 kW is added to the ammonia-water solution at 30 bar, increasing its temperature to 46 °C. The rich saturated vapor ammonia-water solution, with a concentration of 94.16 % ammonia, enters the turbine at 130 °C and 30 bar. After expanding to a pressure of 6.5 bar in the turbine, this stream produces 3366 kW of useful work. The low-pressure solution at 60.43 °C enters the condenser and, after transferring 22,816 kW to the air, leaves the condenser at a temperature of 18 °C. The exit stream from the condenser, after receiving 99.7 kW of power at the pump, reaches the high pressure of the system of 30 bar.

6.2.1.1 Variation in turbine inlet pressure

The effect of varying the turbine inlet pressure on net produced power under design conditions is shown in Figure 6.1. The analysis is conducted under winter conditions with an ambient temperature of 8 °C and a heating demand of 8 MW. As illustrated, there is a local maximum in net produced power as the turbine inlet pressure increases. From a turbine inlet pressure of 20 bar, where the net power output is 3017 kW, there is a noticeable increase in power output as the pressure rises. This upward trend continues until reaching a peak at 30 bar, where the net produced power is maximized at 3263 kW. Beyond this point, as the turbine inlet pressure continues to increase from 30 bar to 42 bar, the net produced power begins to decline, ultimately falling to 2921 kW at 42 bar. Due to the local maximum observed at 30 bar, the turbine inlet pressure is set at 30 bar in Table 5.8 as part of the boundary conditions.

The net produced power increases steeply from 20 bar to 30 bar, reaching a maximum at around 30 bar. Beyond this point, from 30 bar to 42 bar, the power decreases more gradually, with a lower slope. This indicates that the system responds more sensitively to increases in turbine inlet pressure below 30 bar than above it.

The justification for how the local maximum occurs by varying the turbine inlet pressure is illustrated in Figure 6.2. With an increase in turbine inlet pressure, the useful work produced by the turbine reaches a local maximum, while the work required by the pump to raise the pressure of the solution to high pressure of the system also increases. However, this increase does not have a significant effect on the local maximization of power produced by the turbine. By increasing the turbine inlet pressure, both the inlet and outlet enthalpies of the turbine decrease. However, the difference between these two enthalpies—or the turbine specific work—increases with an increase in turbine inlet pressure. The variation in turbine specific work and turbine mass flow rate with turbine inlet pressure is shown in Figure 6.2. As shown in the figure, the mass flow rate decreases with higher turbine inlet pressure, while the turbine specific work increases. The interaction of these two parameters—ascending and descending—results in a local maximum at 30 bar, as depicted in Figure 6.1.

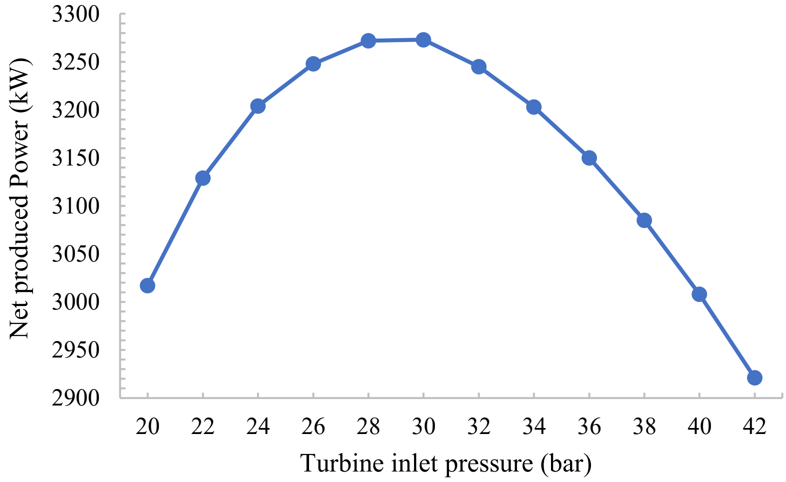

Figure 6.1. The impact of turbine inlet pressure on net produced power under design condition for ambient temperature of 8 °C and heat demand of 8 MW

Figure 6.3 illustrates how the total exergy destruction rate of the system varies with changes in turbine inlet pressure under design conditions, with an ambient temperature of 8 ℃ and a heat demand of 8 MW during winter days. The total exergy destruction rate decreases with an increase in turbine inlet pressure, dropping from 4350 kW at 20 bar to 2552 kW at a turbine inlet pressure of 42 bar. As shown in the figure, the slope of the decrease in total exergy destruction rate diminishes as the turbine inlet pressure increases. This indicates that while increasing the pressure initially leads to a more rapid reduction in exergy destruction, the effectiveness of this reduction lessens at higher pressures.

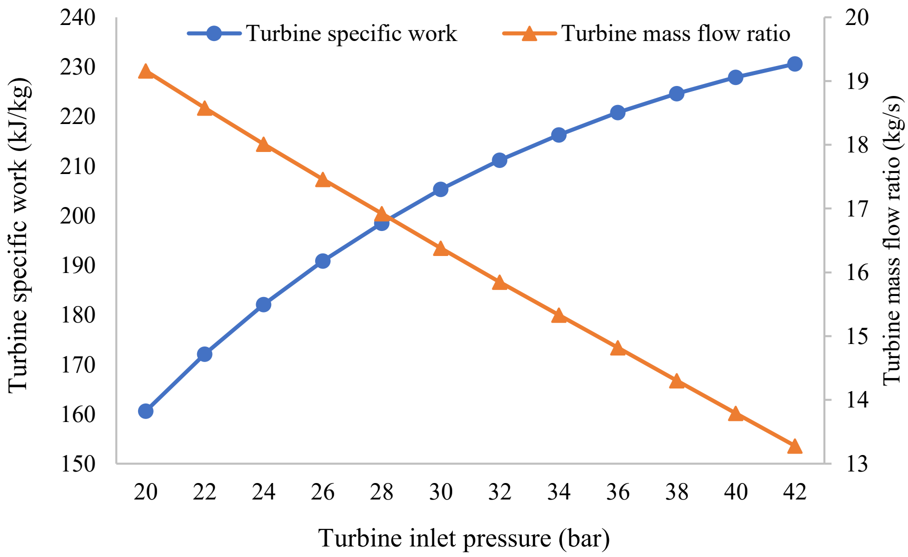

Figure 6.2: The effects of turbine inlet pressure on the turbine specific work and mass flow rate under design conditions during winter days ($T_0 = 8\,°C$, $\dot{Q}_H = 8$ MW)

As described in Equation (5.28), the total exergy destruction is calculated as the difference between the input exergy to the system and the sum of the produced exergy and exergy losses. With an increase in turbine inlet pressure, the input exergy to the system decreases due to the increase in the reinjection temperature, which consequently raises the reinjection exergy. The heating exergy remains constant despite an increase in turbine inlet pressure, as the heat demand is consistent. The net produced power reaches a local maximum at 30 bar, as illustrated in Figure 6.1. Additionally, the exergy losses from the condenser of the Kalina cycle decrease with increasing turbine inlet pressure. This reduction is due to the decreased heat transferred to the air in this condenser. The variation in produced exergy and exergy losses is negligible compared to the reduction in input exergy. Consequently, the total exergy destruction rate decreases with an increase in turbine inlet pressure.

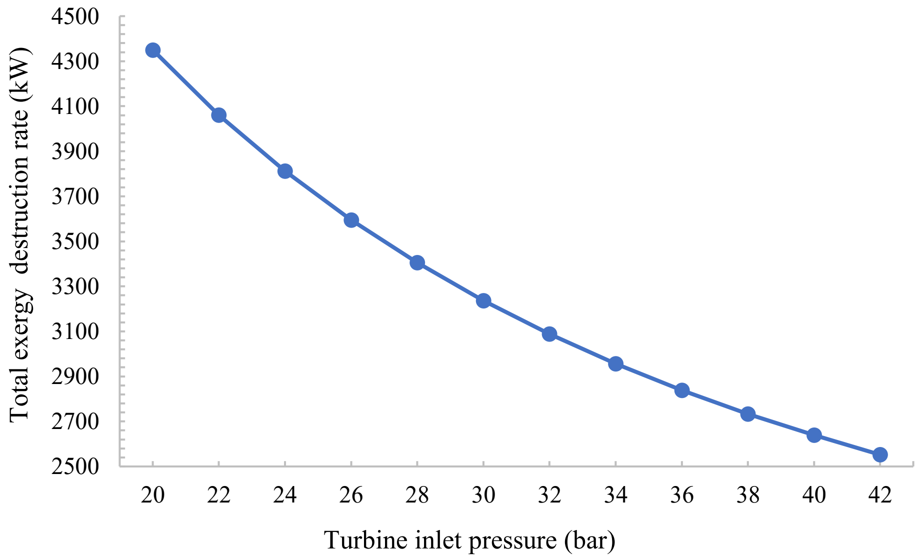

Figure 6.3: The effect of turbine inlet pressure on the total exergy rate of the system under design condition for ambient temperature of 8 °C and heat demand of 8 MW

Figure 6.4 illustrates the details of the total exergy destruction rate with variations in turbine inlet pressure under design conditions, with an ambient temperature of 8 °C and a heat demand of 8 MW during winter days. As shown in the figure, the exergy destruction rate in the Kalina cycle condenser decreases substantially from 2056 kW at 20 bar to 571 kW at 42 bar. The rate of reduction in exergy destruction in the Kalina cycle condenser decreases as the turbine inlet pressure increases. This indicates that while exergy destruction continues to decline with higher pressures, the extent of the reduction becomes less pronounced over time. This indicates that while exergy destruction continues to decline with higher pressures, the extent of the reduction becomes less pronounced with further increases in pressure. As the turbine inlet pressure increases, both the input and output exergy rates of the ammonia-water solution in the Kalina cycle condenser decrease. Consequently, the difference between these two parameters also becomes smaller at higher turbine inlet pressures. The exergy destruction rate, which is calculated as the difference between these two parameters, therefore decreases as well. Alternatively, it can be explained that with an increase in turbine inlet pressure, the turbine back temperature decreases, leading to a corresponding decrease in the Kalina cycle condenser inlet temperature of the ammonia-water solution. This reduction in temperature results in a smaller temperature difference between the cold and hot streams at the inlet of the Kalina cycle condenser. Consequently, the irreversibilities in the Kalina cycle condenser decrease, which in turn reduces the exergy destruction rate. In addition, the exergy destruction rate in the boiler decreases with an increase in turbine inlet pressure.

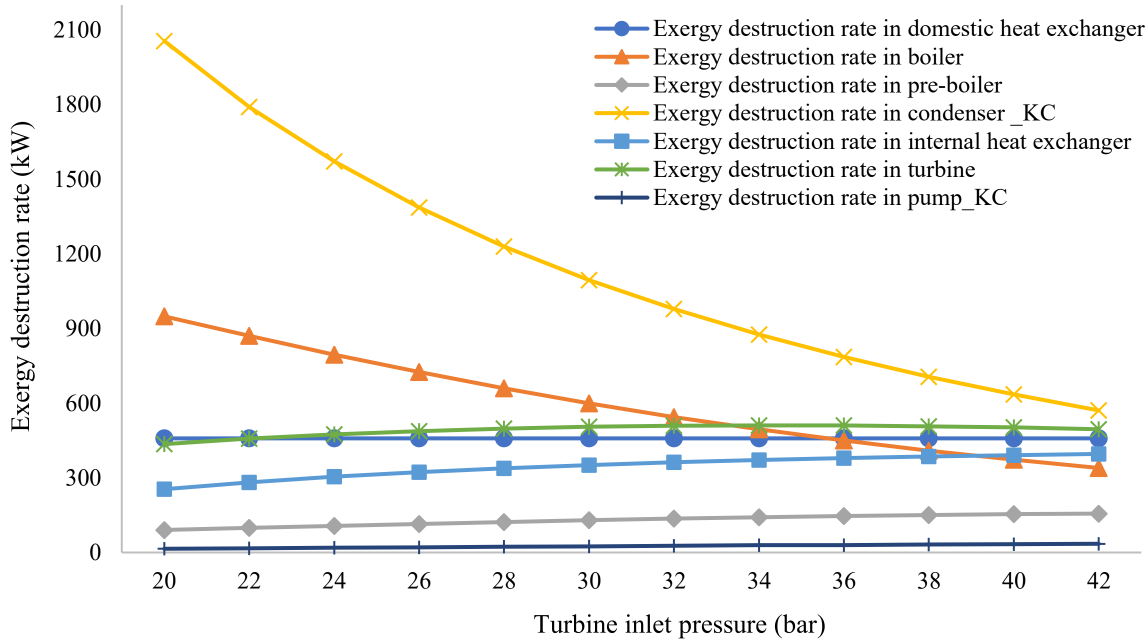

Figure 6.4: The impact of turbine inlet pressure on destruction rate of various components under design conditions for ambient temperature of 8 °C and heat demand of 8 MW

As indicated in the Figure 6.4, the exergy destruction rate decreases from 949 kW at 20 bar to 340 kW at 42 bar. The rate of reduction in the boiler is less steep compared to that in the Kalina cycle condenser. As the turbine inlet pressure increases, both the input and output exergy rates of the ammonia-water solution in the boiler decrease. Consequently, the exergy destruction rate also becomes smaller at higher turbine inlet pressures. Despite an increase in turbine inlet pressure, the heating exergy remains unchanged due to the consistent heat demand. As well, the exergy destruction rate in the turbine exhibits a local maximum with an increase in turbine inlet pressure. Furthermore, the exergy destruction rates in the internal heat exchanger, pre-boiler and Kalina cycle pump increase as the turbine inlet pressure rises. However, these local increases in the turbine and the rising rates in the internal heat exchanger, pre-boiler and Kalina cycle pump do not significantly impact the total exergy destruction rate of the system. Overall, the total exergy destruction rate, which represents the sum of all component destruction rates, decreases with higher turbine inlet pressures. The Kalina cycle pump and pre-boiler exhibit the lowest exergy destruction rates among the components of the system.

6.2.1.2 Variation in pinch point temperature difference in boiler

Figure 6.5 illustrates the pinch point temperature difference in the boiler ($\Delta T_{pp,BOI}$). This temperature difference is defined by the temperature disparities between the outlet hot stream of geothermal hot water and the inlet cold stream of ammonia-water solution in the boiler, or between the inlet hot stream of geothermal hot water and the outlet cold stream of ammonia-water solution in the pre-boiler; ($T_{20} - T_4$). These temperature differences can vary between 5 K and 20 K.

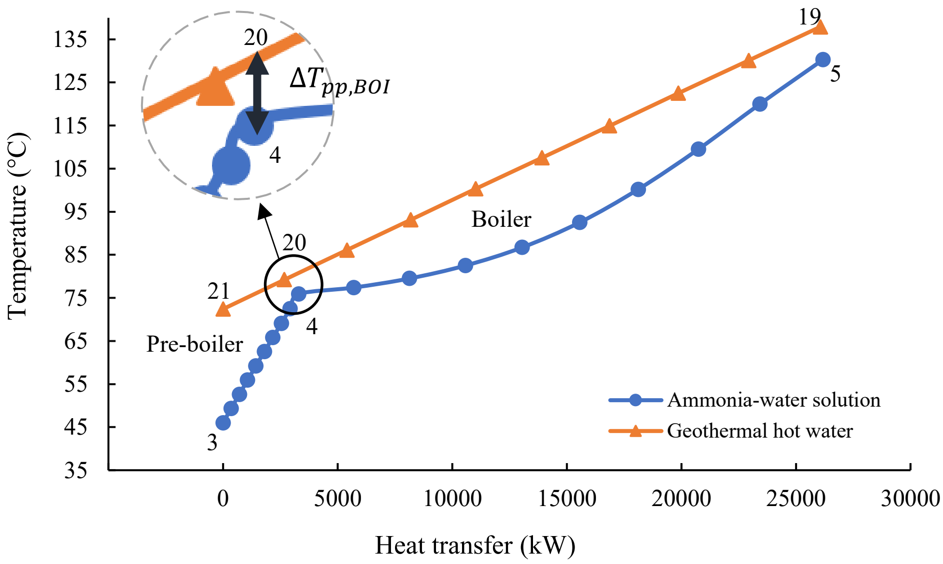

Figure 6.5: Heat transfer process in the boiler and pre-boiler versus temperature

Figure 6.6 illustrates how variations in the pinch point temperature difference in the boiler affect the net produced power and turbine mass flow rate during winter days, under design conditions with an ambient temperature of 8 ℃ and a heating demand of 8 MW. As demonstrated, an increase in the $\Delta T_{pp,BOI}$ is associated with a decrease in net produced power, dropping from 3263 kW at a 5 K pinch point temperature difference to 2413 kW at a 20 K pinch point temperature difference. Although the specific turbine work remains constant regardless of variations in the pinch point temperature difference, this constancy is due to all boundary conditions related to the turbine remaining unchanged. However, as depicted in the figure, the turbine mass flow rates decrease, which in turn leads to a reduction in net produced power, given that net power is the product of specific turbine work and turbine mass flow rate. As shown, the rate of decrease in both net produced power and turbine mass flow rate is the same. As the $\Delta T_{pp,BOI}$ increases, the inlet and outlet enthalpies of the ammonia-water solution (h_3, h_4, and h_5) in both the boiler and pre-boiler remain constant, maintaining the established boundary conditions of the system. However, the inlet and outlet temperatures of the geothermal hot water in the pre-boiler rise due to the increased pinch point temperature difference. This leads to higher enthalpies of the geothermal hot water, reducing the heat transfer to the boiler and pre-boiler. As a result, the mass flow rate of the ammonia-water solution in these components, and consequently in the turbine, decreases. The work of the Kalina cycle pump increases with an increase in the $\Delta T_{pp,BOI}$, although this increase does not significantly impact the overall performance of the system.

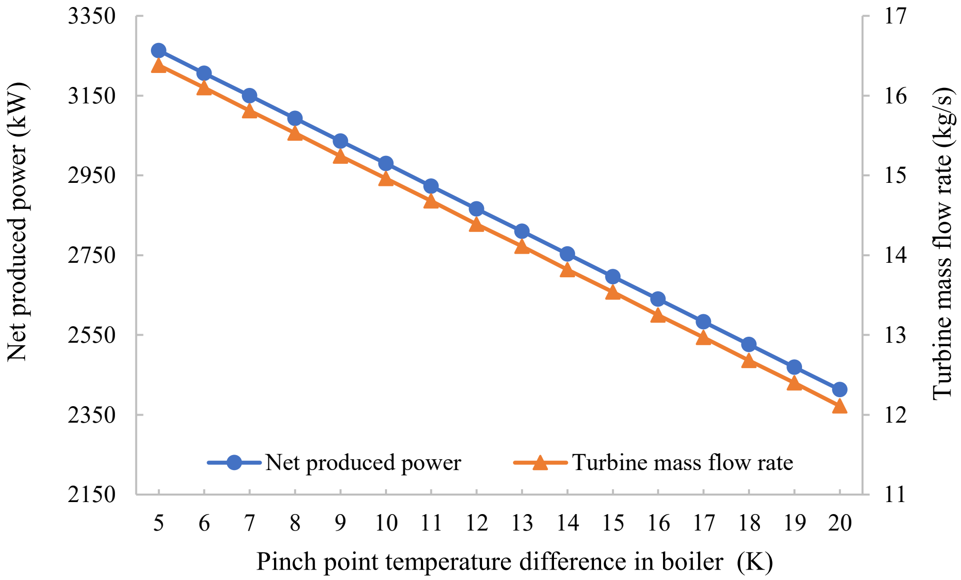

Figure 6.6: The impact of pinch point temperature difference in the boiler on net produced power and turbine mass flow rate under design conditions, with an ambient temperature of 8 °C and a heat demand of 8 MW during winter days

In Figure 6.7, the impact of the pinch point temperature difference in the boiler on the total exergy destruction rate and input exergy is depicted during winter, under design conditions with an ambient temperature of 8 °C and a heating demand of 8 MW. The total exergy destruction rate decreases as the $\Delta T_{pp,BOI}$ increases, moving from 3237 kW at a 5 K pinch point difference to 2915 kW at a 20 K difference. As detailed in Figure 6.6, the outlet temperature and enthalpy of the geothermal hot water from the pre-boiler increase with a higher pinch point temperature difference. This leads to a reduction in the inlet exergy of the system, as shown in the Figure 6.7. Additionally, the exergy heat of the system remains unchanged due to stable boundary conditions in the domestic heat exchangers. Consequently, as also shown in Figure 6.6, the net produced power decreases. Moreover, while the exergy losses in the Kalina cycle condenser decrease, this reduction has a minimal impact on the total exergy destruction rate. Ultimately, according to Equation (5.28), the total exergy destruction rate decreases.

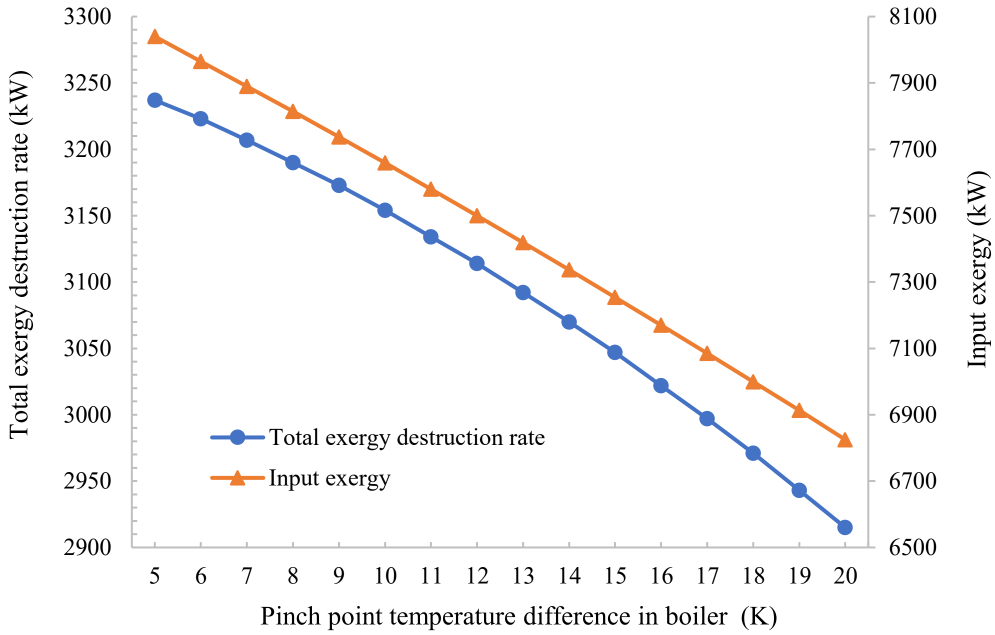

Figure 6.7: The influence of pinch point temperature difference in the boiler on total exergy destruction rate and input exergy during winter days, under design conditions with an ambient temperature of 8 °C and a heating demand of 8 MW

Figure 6.21 depicts how the exergy destruction rate of different components varies with changes in the pinch point temperature difference in the boiler, under design conditions that include an ambient temperature of 8 ℃ and a heat demand of 8 MW during winter days. As illustrated in the figure, the majority of the exergy destruction rate is attributed to the Kalina cycle condenser. It decreases with an increase in the $\Delta T_{pp,BOI}$, dropping from 1095 kW at a 5 K pinch point temperature difference to 809 kW at a 20 K difference. This reduction occurs due to a decrease in the mass flow rate in the condenser. As depicted in Figure 6.6, the turbine mass flow rate, and consequently the mass flow rate in the condenser, decreases with an increasing $\Delta T_{pp,BOI}$. In addition, due to the increasing temperature difference between the cold and hot streams at the inlet and outlet of the pre-boiler, as well as at the inlet of the boiler, associated with an increase in the $\Delta T_{pp,BOI}$, the irreversibilities in both the boiler and pre-boiler increase. This rise in irreversibilities results in an increase in the exergy destruction rate of both the boiler and pre-boiler. Furthermore, the exergy destruction rate of the turbine and internal heat exchanger decreases as the $\Delta T_{pp,BOI}$ increases, as illustrated in the Figure 6.8. The rate at which the exergy destruction rate decreases for the component is greater than the rate at which it increases. As a result, the total exergy destruction rate, which is the sum of all the component destruction rates, decreases overall.

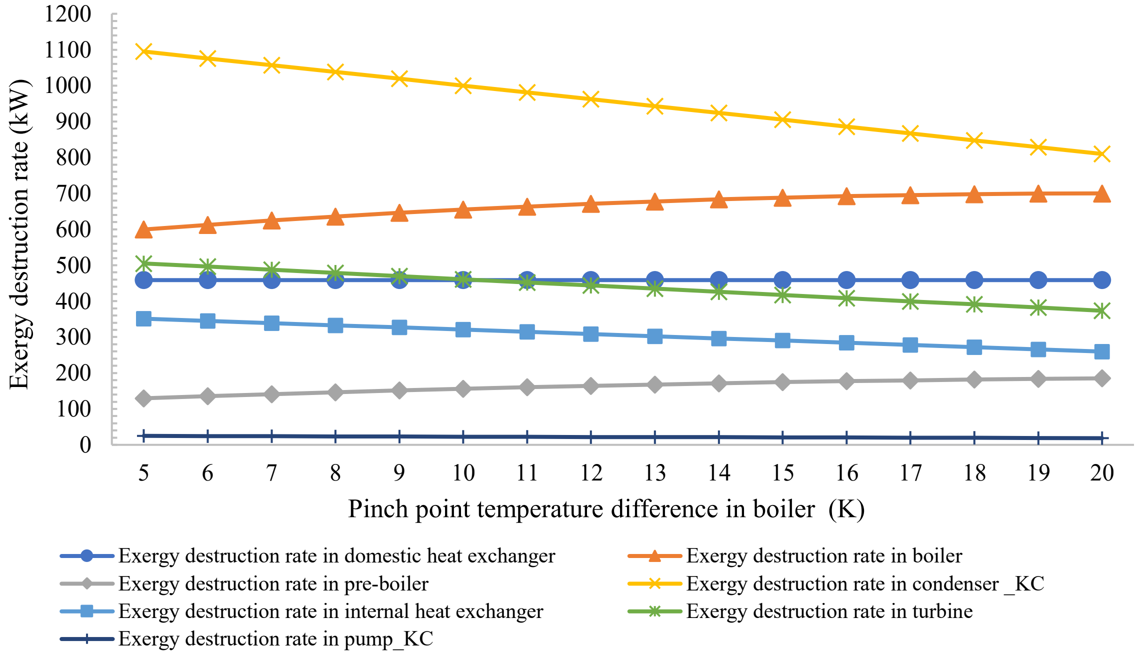

Figure 6.8: The impact of pinch point temperature difference in the boiler on exergy destruction rate of various components under design conditions for ambient temperature of 8 °C and heat demand of 8 MW

6.2.1.3 Variation in pinch point temperature difference in domestic heat exchanger

Figure 6.9 depicts the pinch point temperature difference in the domestic heat exchanger ($\Delta T_{pp,DHE}$). This difference is measured by the temperature variation between the outgoing hot stream of geothermal hot water and the incoming cold stream of district water within the exchanger, specifically ($T_{18} - T_{14}$). The range of these temperature differences can span from 5 K to 20 K.

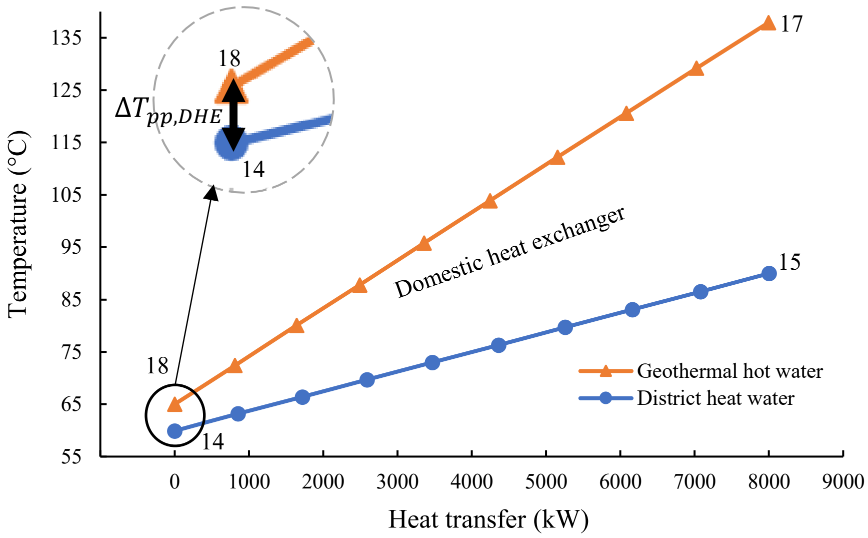

Figure 6.9: Heat transfer process in the domestic heat exchanger versus temperature

Figure 6.10 illustrates how the pinch point temperature difference in domestic heat exchanger affects the mass flow rate of geothermal water and the effectiveness of the domestic heat exchanger under design conditions with an ambient temperature of 8 °C and a heat demand of 8 MW. The mass flow rate of geothermal hot water increases with an increase in the $\Delta T_{pp,DHE}$, moving from 25.9 kg/s at a pinch point temperature difference of 5 K to 32.6 kg/s at a pinch point difference of 20 K. As the $\Delta T_{pp,DHE}$, the outlet temperature and consequently the enthalpy of the geothermal hot water decreases. To meet the 8 MW heat demand, the mass flow rate of geothermal water needs to be increased. The effectiveness of the domestic heat exchanger decreases with an increase in the pinch point temperature difference in domestic heat exchanger. The effectiveness of the domestic heat exchanger reaches 0.74 at a pinch point temperature difference of 20 K, down from 0.94 at a pinch point temperature difference of 5 K. According to Ref. [153], the effectiveness in a domestic heat exchanger is defined as the ratio of the temperature difference between the inlet and outlet of the geothermal hot water to the temperature difference between the inlet streams of the geothermal hot water and district water. Given the boundary conditions listed in Table 5.8, the temperature difference between the inlet hot and cold side streams remains constant. However, the temperature difference between the inlet and outlet on the geothermal hot water decreases with an increase in $\Delta T_{pp,DHE}$. Therefore, the effectiveness of the domestic heat exchanger decreases.

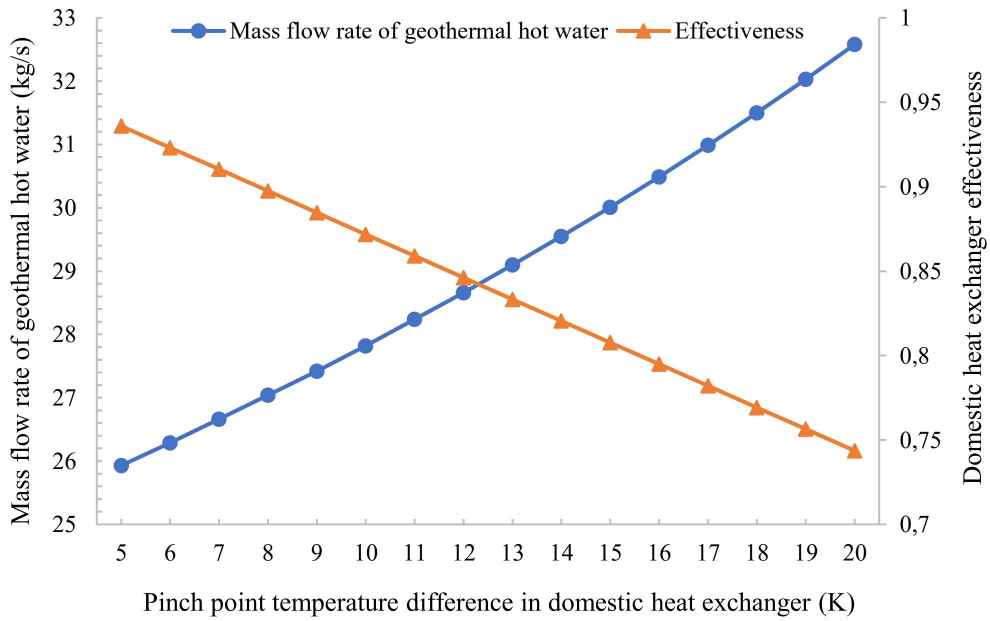

Figure 6.10: The impact of pinch point temperature difference in the domestic heat exchanger on mass flow rate of geothermal water and its effectiveness under design condition for ambient temperature of 8 °C and heat demand of 8 MW

Figure 6.11 demonstrates how changes in the pinch point temperature difference in the domestic heat exchanger impact the net produced power and turbine mass flow rate, under winter design conditions with an ambient temperature of 8 °C and a heat demand of 8 MW. It shows that an increase in the $\Delta T_{pp,DHE}$ corresponds with a reduction in net produced power, which falls from 3363 kW at a 5 K difference to 3125 kW at a 20 K difference. While the specific turbine work remains constant across variations in the pinch point temperature difference, this consistency results from stable boundary conditions concerning the turbine. Nevertheless, the figure indicates that the turbine mass flow rates decrease, subsequently lowering the net produced power since the net power is the product of specific turbine work and turbine mass flow rate. As illustrated in Figure 6.10, an increase in the $\Delta T_{pp,DHE}$, necessary to meet the 8 MW heat demand, causes the mass flow rate of geothermal hot water in the domestic heat exchanger to increase. Consequently, this leads to a decrease in the mass flow rate supplied to the Kalina cycle, which in turn results in a reduction of the turbine mass flow rate.

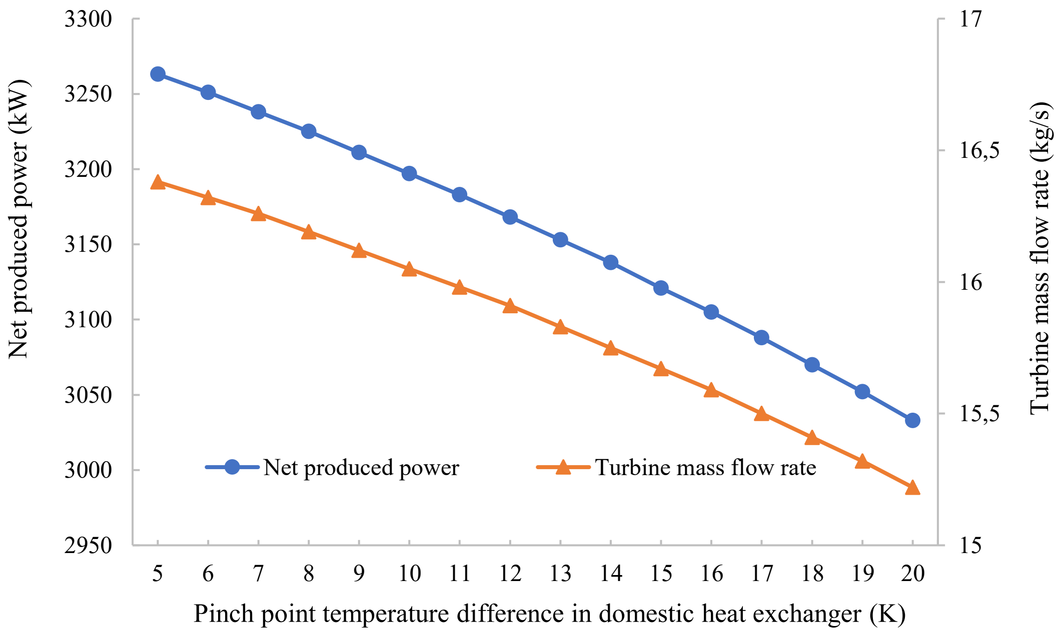

Figure 6.11: The influence of pinch point temperature difference in the domestic heat exchanger on net produced power and turbine mass flow rate, given design conditions with an ambient temperature of 8 °C and a heating demand of 8 MW during winter days

Figure 6.12 illustrates how the exergy destruction rate of various components fluctuates with changes in the pinch point temperature difference in the domestic heat exchanger, set under design conditions that include an ambient temperature of 8 °C and a heat demand of 8 MW during winter days. The figure shows that the majority of the exergy destruction rate is linked to the Kalina cycle condenser. This rate decreases as the $\Delta T_{pp,DHE}$ increases, falling from 1095 kW at a 5 K difference to 1018 kW at a 20 K difference. This decrease is due to a reduction in the mass flow rate through the condenser. Furthermore, as shown in Figure 6.11, the turbine mass flow rate, and therefore the mass flow rate through the condenser, also declines as the

$\Delta T_{pp,DHE}$ increases. Additionally, the rising temperature difference between the cold and hot streams at the inlet of the domestic heat exchanger, resulting from an increase in the $\Delta T_{pp,DHE}$ leads to increased irreversibilities within the domestic heat exchanger. Consequently, this increase in irreversibilities contributes to a higher exergy destruction rate. As depicted in Figure 6.12, the exergy destruction rate in the domestic heat exchanger increases from 457 kW at a pinch point temperature difference of 5 K to 588 kW at a pinch point temperature difference of 20 K. Furthermore, the exergy destruction rate in the boiler, pre-boiler, internal heat exchanger, pump, and turbine decreases due to the decreasing mass flow rate of the ammonia-water solution in each component. Overall, the total exergy destruction rate in the domestic heat exchanger decreases with an increase in the $\Delta T_{pp,DHE}$.

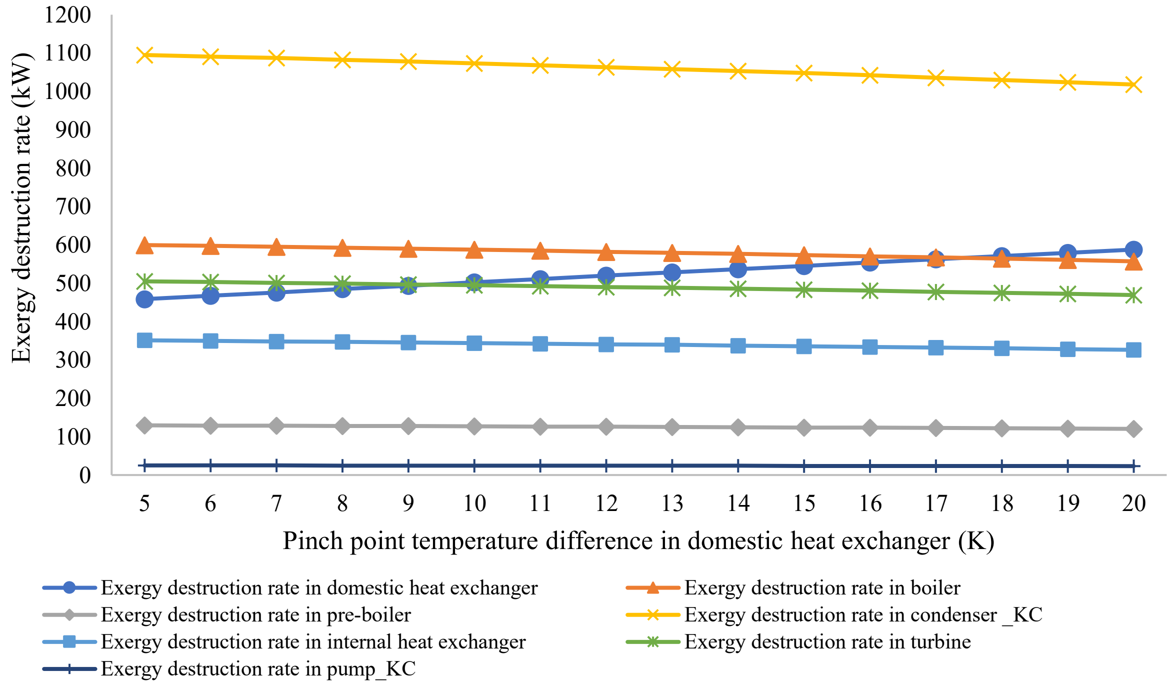

Figure 6.12: The impact of pinch point temperature difference in the domestic heat exchanger on exergy destruction rate of various components under design condition for ambient temperature of 8 °C and heat demand of 8 MW

6.2.1.4 Variation in pinch point temperature difference in Kalina cycle condenser

Figure 6.13 illustrates the pinch point temperature difference in the Kalina cycle condenser ($\Delta T_{pp,CON\_KC}$). This difference is determined by the temperature disparity between the outgoing hot ammonia-water solution stream and the incoming cold air stream used to cool the ammonia-water solution within the exchanger, specifically (T_1-T_{12}). These temperature differences can vary from 5 K to 20 K.

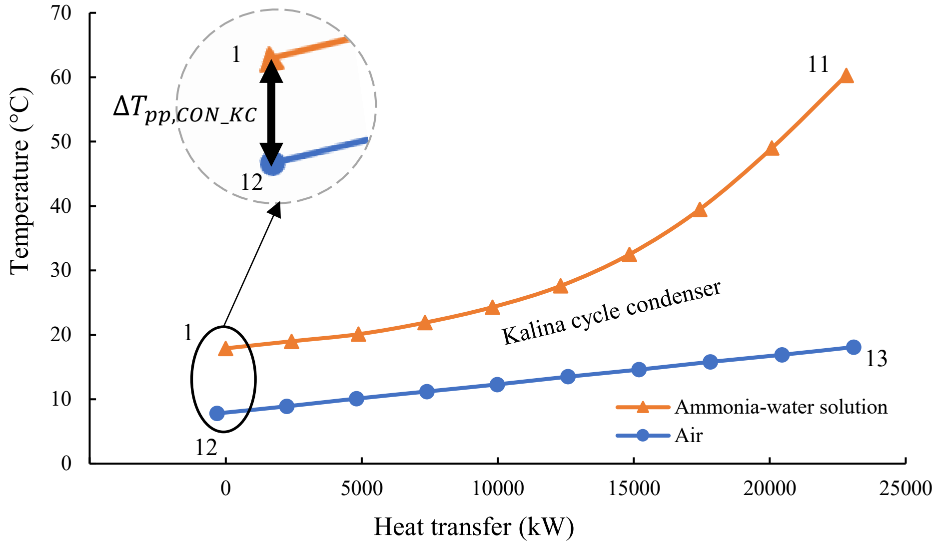

Figure 6.13: Heat transfer process in the Kalina cycle condenser versus temperature

Figure 6.14 demonstrates the impact of changes in the pinch point temperature difference in the condenser of the Kalina cycle on the net produced power and the turbine back pressure during winter days. This analysis is conducted under design conditions with an ambient temperature of 8 °C and a heating demand of 8 MW. As shown, an increase in the $\Delta T_{pp,CON\_KC}$ leads to a decrease in the net produced power, which drops from 3588 kW at a 5 K pinch point temperature difference to 2632 kW at a 20 K pinch point temperature difference. Although the turbine mass flow rate remains constant despite variations in the pinch point temperature difference, this constancy is because all boundary conditions related to the mass flow rate of the Kalina cycle remain unchanged. However, as illustrated in the figure, the turbine back pressure increases. When the $\Delta T_{pp,CON\_KC}$ increases, the condenser temperature and consequently the condenser pressure, or turbine back pressure, also increase. The condenser pressure corresponds to the saturated pressure at the condenser temperature. This increase in the turbine back pressure leads to a reduction in turbine specific work and net produced power since net power is the product of specific turbine work and turbine mass flow rate. The inlet enthalpy of the ammonia-water solution in the turbine (h_8) remains constant; however, the outlet enthalpy (h_9) increases, and the turbine specific work decreases with an increase in the $\Delta T_{pp,CON\_KC}$. The work of the Kalina cycle pump decreases with an increase in the $\Delta T_{pp,CON\_KC}$ due to the reduction in the pressure difference across the pump, although this decrease does not significantly impact the overall performance of the system.

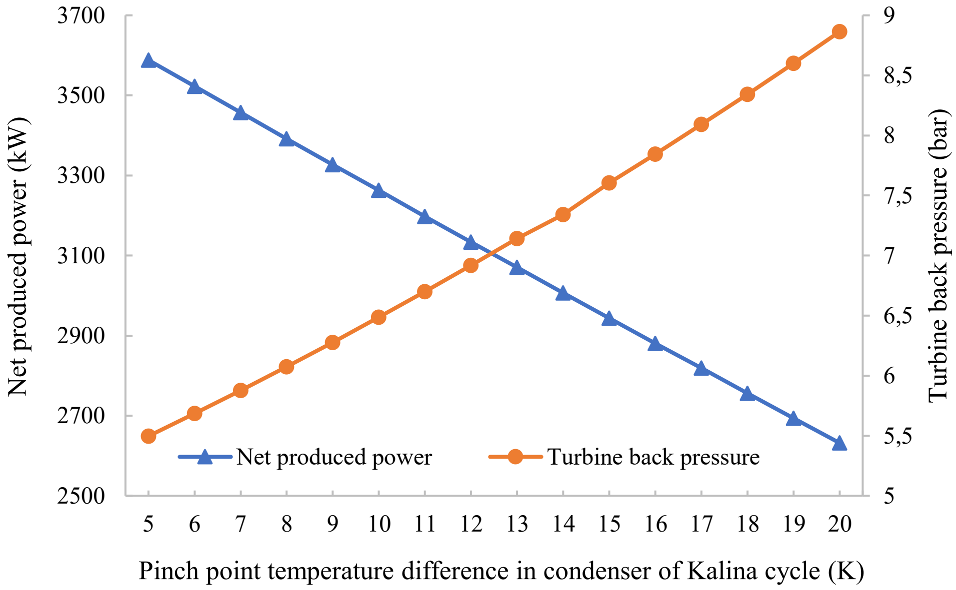

Figure 6.14: The impact of pinch point temperature difference in the condenser of Kalina cycle on net produced power and turbine back pressure under design conditions, with an ambient temperature of 8 °C and a heat demand of 8 MW during winter days

In Figure 6.15, the impact of the pinch point temperature difference in the condenser of Kalina cycle on the total exergy destruction rate and input exergy is depicted during winter, under design conditions with an ambient temperature of 8 ℃ and a heating demand of 8 MW. The total exergy destruction rate increases as the $\Delta T_{pp,CON\_KC}$ increases, moving from 2974 kW at a 5 K pinch point temperature difference to 3741 kW at a 20 K pinch point temperature difference. The variation in $\Delta T_{pp,CON\_KC}$ does not affect the mass flow rate and temperature of the geothermal hot water in the domestic heat exchanger due to the constant boundary condition. However, the temperature of the geothermal hot water from the pre-boiler increases due to the constant mass flow rate, leading to a rise in the reinjection temperature of the geothermal hot water. Consequently, the input exergy decreases. The exergy heat of the system remains constant due to stable boundary conditions in the domestic heat exchangers. As a result, as illustrated in Figure 6.14, the net produced power decreases Furthermore, although the exergy losses in the Kalina cycle condenser decrease, this reduction has a minimal effect on the overall exergy destruction rate. The slope of the reduction in net produced power is greater than the reduction in input exergy. Ultimately, based on Equation (5.28), the total exergy destruction rate increases.

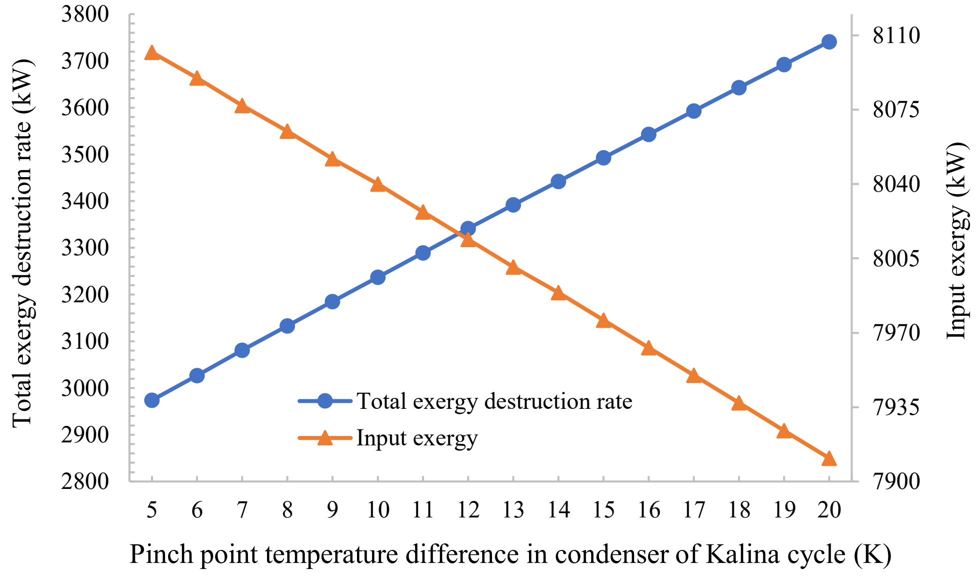

Figure 6.15: The influence of pinch point temperature difference in the condenser of Kalina cycle on total exergy destruction rate and input exergy during winter days, under design conditions with an ambient temperature of 8 °C and a heating demand of 8 MW

Figure 6.16 demonstrates the fluctuation in the exergy destruction rate of various components in response to changes in the pinch point temperature difference in the condenser of Kalina cycle. This is based on design conditions, which include an ambient temperature of 8 °C and a heat demand of 8 MW during winter days. The figure shows that the majority of the exergy destruction rate is linked to the Kalina cycle condenser. This rate increases as the $\Delta T_{pp,CON\_KC}$ increases, falling from 706 kW at a 5 K difference to 182 kW at a 20 K difference. This increase is attributed to a rising temperature difference between the cold and hot streams at the inlet of the Kalina cycle condenser. As a result, an increase in $\Delta T_{pp,CON\_KC}$ leads to greater irreversibilities within the Kalina cycle condenser. Consequently, this rise in irreversibilities contributes to a higher exergy destruction rate. As depicted in Figure 6.16, the exergy destruction rate in other components remains nearly constant. Overall, the total exergy destruction rate in the domestic heat exchanger decreases with an increase in the $\Delta T_{pp,CON\_KC}$.

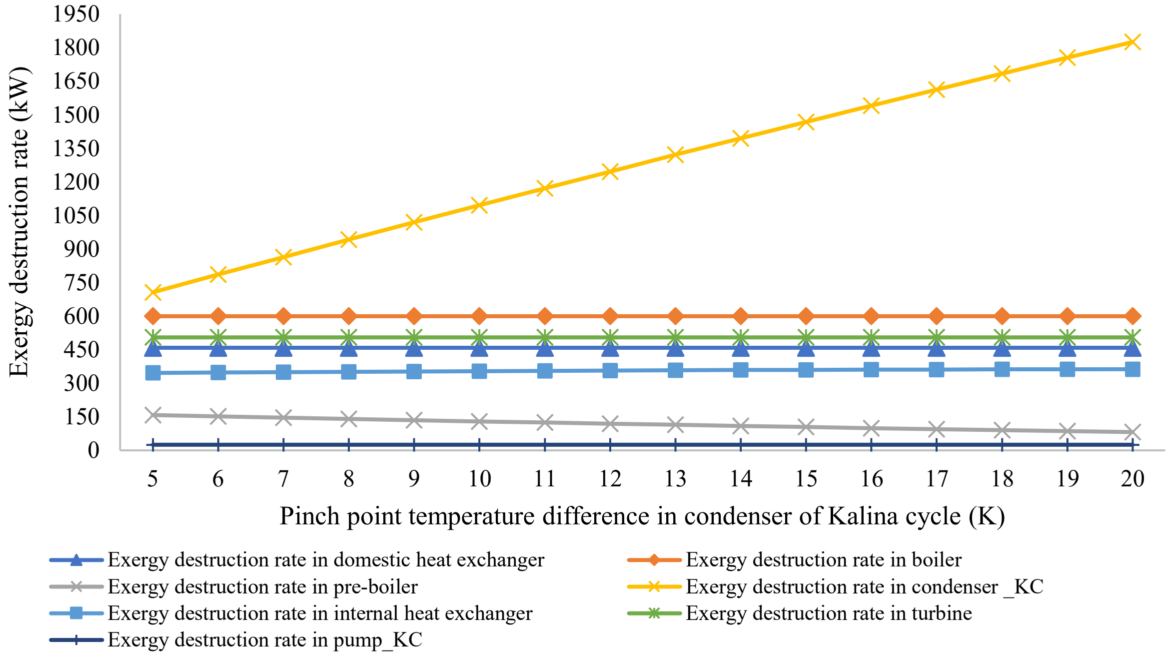

Figure 6.16: The impact of pinch point temperature difference in the condenser of Kalina cycle on exergy destruction rate of various components under design condition for ambient temperature of 8 °C and heat demand of 8 MW

6.2.1.5 Impact of Pressure drops in heat exchangers

As mentioned before, the pressure drops in heat exchangers are neglected in the design analysis to simplify the calculations, focus on key decision parameters, and maintain a manageable model. This approach facilitates a clearer understanding of how each individual parameter influences the performance of the system under ideal conditions. However, to fully understand the behaviour of the system, it is important to examine the impact of pressure drops in heat exchangers. Therefore, in this section, the effect of pressure drops on system performance is evaluated. In the design conditions, a pressure drop of 1 bar is considered for each heat exchanger [151]. The analysis is performed under winter conditions with an ambient temperature of 8 °C and a heating demand of 8 MW.

Figure 6.17 illustrates the impact of varying the turbine inlet pressure on net produced power and total exergy destruction rate in two scenarios under design conditions: one without pressure drops in heat exchangers and one with pressure drops. As Shown in Figure 6.17(a) the net produced power at all values of turbine inlet pressure is almost 7 % lower in the scenario with pressure drop in heat exchangers compared to the scenario without pressure drop. This occurs because the pressure drops in heat exchangers result in a change in the pressure and temperature of the stream entering and exiting the turbine, which in turn reduces the power output of the turbine. Additionally, the increased resistance and frictional losses within the heat exchangers contribute to a higher energy consumption for fluid circulation, further diminishing the net produced power.

The total exergy destruction rate in the system with pressure drop calculation increases by 3 % compared to the analyses with no pressure drop in heat exchangers across all variations of turbine inlet pressures as shown in Figure 6.17(b). This happens due to the increase in irreversibilities caused by higher frictional losses and additional pressure drops within the heat exchangers, leading to greater entropy generation and reduced overall system efficiency.

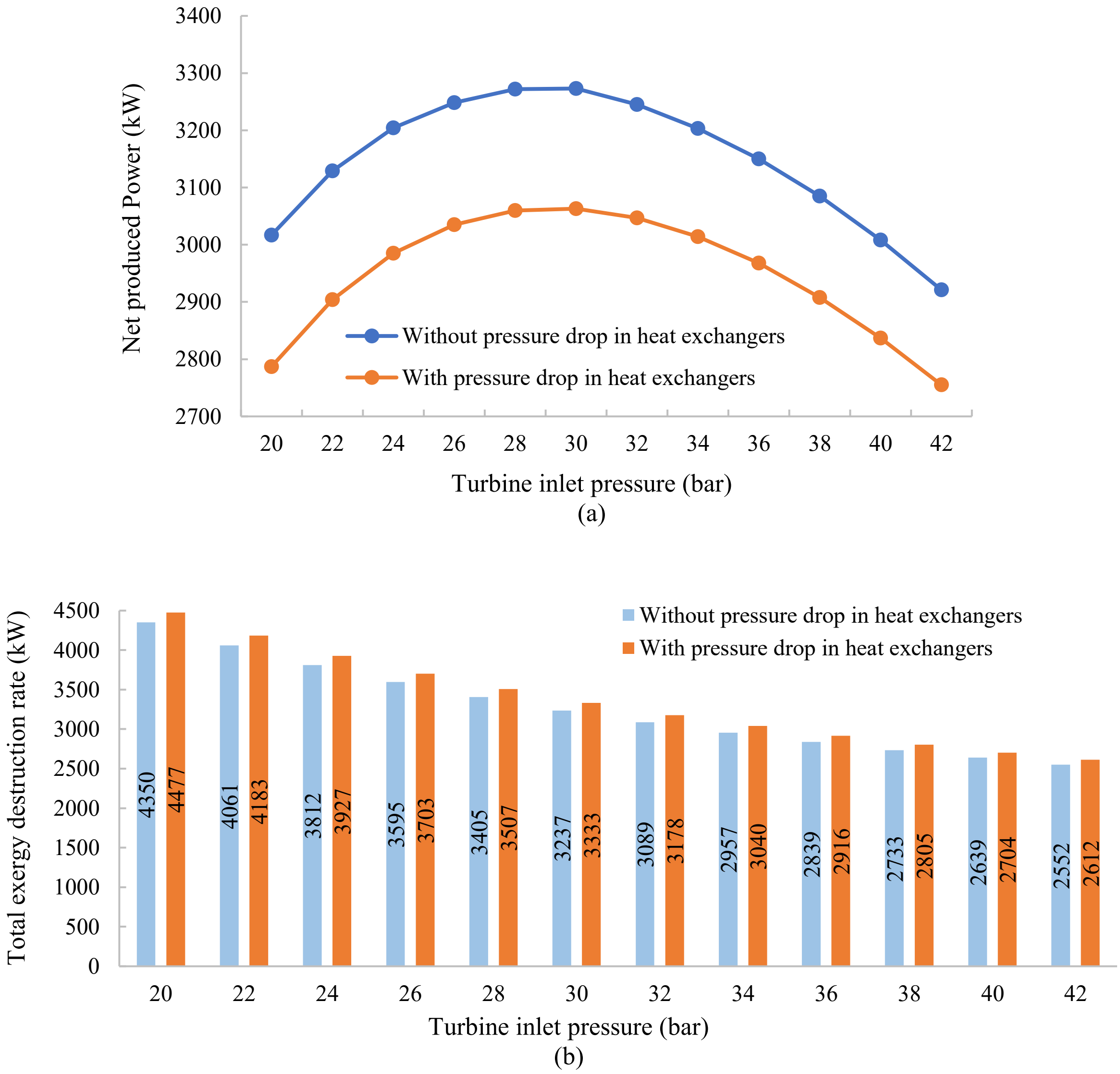

Figure 6.17: (a) Net produced power (b) Total exergy destruction rate versus turbine inlet pressure under design conditions for two scenarios: without pressure drop in heat exchangers and with pressure drop in heat exchangers (winter days)

Figure 6.18 shows the effect of varying the pinch point temperature difference in the boiler on net produced power and total exergy destruction rate under design conditions, comparing scenarios with and without pressure drops in heat exchangers. In Figure 6.18(a), the net produced power is approximately 6.5 % lower in the scenario with pressure drops than without. Figure 6.18(b) indicates that the total exergy destruction rate is 3 % higher in the scenario with pressure drops compared to without. The reasons for this reduction in system performance are further illustrated in Figure 6.17.

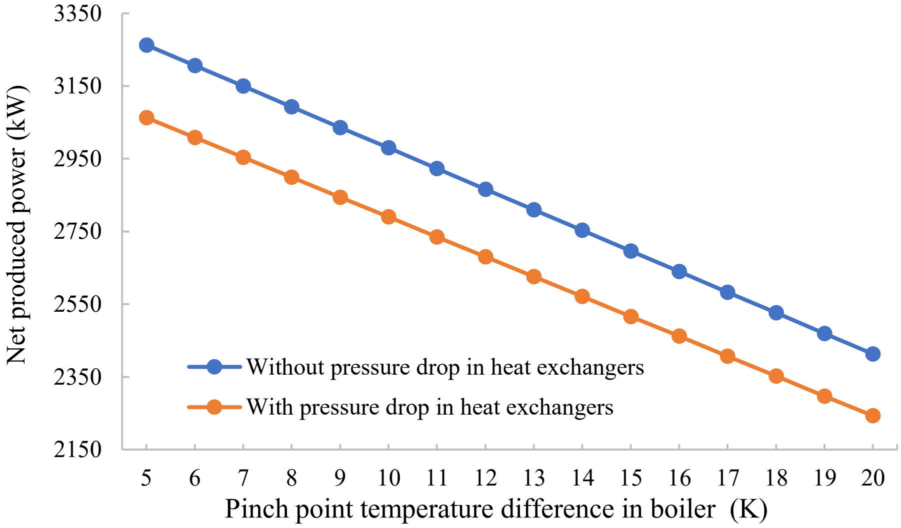

(a)

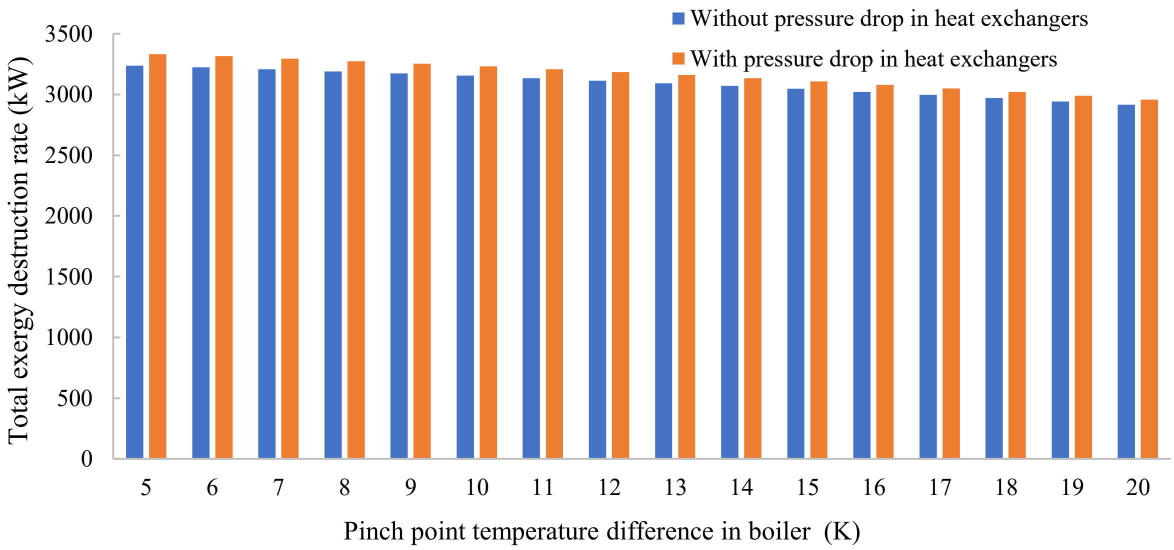

(b)

Figure 6.18: (a) Net produced power (b) Total exergy destruction rate versus the pinch point temperature difference in the boiler under design conditions for two scenarios: without pressure drop in heat exchangers and with pressure drop in heat exchangers (winter days)

6.2.2 Parametric analysis during summer days: on-design mode

The thermodynamic properties and mass flow rates of the different streams of the separated system shown in Figure 4.1, under design conditions for summer days, are listed in Table A.2 for the power section (Kalina cycle) and in Table A.3 for the cooling section in Appendix A. According to Table 5.8, the system meets a heat demand of 2 MW and a cooling demand of 4 MW at an ambient temperature of 20 °C, which is used to analyze the system during summer days.

To satisfy a 2 MW heat demand, 6.5 kg/s of geothermal hot water at 138 °C enters the domestic heat exchanger and exits at 65 °C. On the cold side of the domestic heat exchanger, 15.9 kg/s of water at 60 °C absorbs heat from the geothermal hot water, raising its temperature to 90 °C. After fulfilling the heat demand, the remaining 113.2 kg/s of geothermal hot water is directed to the boiler and pre-boiler of the Kalina cycle, generating 2764 kW of electricity. The geothermal hot water exits the Kalina cycle at 75.8 °C and, after mixing with the stream leaving the domestic heat exchanger at 65 °C, is directed to the generator of the absorption refrigeration cycle at 75.2 °C.

The thermodynamic properties and mass flow rates of the different streams of the combined system shown in Figure 4.5, under design conditions for summer days, are listed in Table A.4 for the power section (Kalina cycle) and in Table A.5 for the cooling section in Appendix A. According to Table 5.8, the system satisfies a heat demand of 2 MW and a cooling demand of 4 MW at an ambient temperature of 20 °C, which is used to evaluate the system during summer days. The electricity produced in the turbine of this tri-generation system is 2662 kW, which is 4 % lower than the power produced in the turbine of a separated system. The geothermal hot water exits the Kalina cycle at 83 °C and, after mixing with the stream from the domestic heat exchanger, is directed to the generator of the absorption refrigeration cycle at 82 °C. A comparative analysis of the separated and combined systems shows that the heat transfer rate in the condenser of the Kalina cycle in the separated system is 20 % higher than in the combined system. However, the heat transfer rate in the condenser of the absorption refrigeration cycle in both the separated and combined systems is almost the same. This is due to the system concept in both systems. The heat transfer rate in the absorber in the combined system is 29 % higher than the heat transfer rate in the absorber of the separated system. As seen in Figure 4.1 and Figure 4.5, the inlet stream (state 40) to the absorber is a combination of three different streams: states 35, 38, and 39. Due to the absence of a solution heat exchanger in the combined system, the liquid phase of the exiting stream from the generator is directed to the absorber. As a result, the temperature of state 39 increases, consequently raising the temperature of the stream entering the absorber. This causes the heat transfer rate in the condenser of the ARC to be higher.

6.3 Design of heat exchanger

To design the heat exchangers, as illustrated in Figure 5.5, one essential step is to determine their maximum heat transfer rate under design conditions. This allows for the calculation of the UA (overall heat transfer coefficient times the heat exchanger area) and initiates the design process. The capacities of the heat exchangers, along with their respective *UA* values, are detailed in Table 6.9.

Referring Table 6.9, in the heating section, the domestic heat exchanger features a heat transfer capacity of 12,000 kW and a *UA* value of 632 kW/K. In the power section, the boiler and Kalina cycle condenser exhibit the highest heat transfer rates. The boiler, with a significant heat transfer rate of 19,831 kW, has a *UA* value of 3076 kW/K, indicating its high efficiency in heat exchange. The Kalina cycle condenser also plays a crucial role with substantial heat transfer capabilities. In the cooling section, the evaporator handles the maximum cooling heat transfer of 5000 kW, with a *UA* value of 1375 kW/K. in addition, in the cooling section, the highest heat transfer rate belongs to the generator, with a heat capacity of 9366 kW and a *UA* value of 2745 kW/K.

Table 6.9: Heat exchanger capacity and UA under on-design condition

	Heat transfer capacity (kW)	UA (kW/K)
Heating section		
Domestic heat exchanger	12,000	632
Power section		
Boiler	19,831	3076
Pre-boiler	2852	222
Internal heat exchanger	2514	78
Kalina cycle condenser	19,670	877
Cooling section		
Generator	9366	2745
Dephlegmator	500	16
Solution heat exchanger	4428	495
ARC condenser	6930	575
Absorber	6980	1124
Evaporator	5000	1375

Table 6.10 provides a comprehensive set of design parameters for various shell and tube heat exchangers used in both combined and separate systems. In all the shell and tube heat exchangers used within the systems, each features a single shell. The tube layouts are primarily arranged at a 90-degree angle, except for the internal and solution heat exchangers, which have a 30-degree tube pattern. The domestic and internal heat exchangers, and the generator, are designed with six tube passes. The pre-boiler is constructed with one tube pass, the solution heat exchanger with five passes, while the boiler has four tube passes, and the evaporator features eight tube passes. Both the boiler and generator are configured as kettle reboilers and do not contain baffles. Apart from these two heat exchangers, the others are equipped with baffles cut at 25 degrees. The evaporator and internal heat exchanger each have 12 baffles, the

domestic heat exchanger has five baffles, the pre-boiler has 11 baffles, and the solution heat exchanger is fitted with 16 baffles. The outside diameter of the tubes in all heat exchangers, except for the generator and evaporator, is 19 mm. In the generator and evaporator, the outside diameter of the tubes is 25.4 mm. Additionally, the tube wall thickness in all the heat exchangers is 2.1 mm.

A detailed set of design parameters for the air-cooled heat exchangers utilized in both combined and separate systems outline in Table 6.11. All air-cooled heat exchangers in the systems are designed with two bundles per bay. The condenser of the Kalina cycle includes 9 bays per unit, while the dephlegmator has 2 bays per unit. According to Table 6.11, the condenser in the absorption refrigeration cycle is equipped with 5 bays per unit and the absorber with 4 bays per unit. The tube pattern in all these air-cooled heat exchangers is set at a 30-degree angle, and the tube pitch uniformly measures 0.6 m across all units. While the absorber is designed with 8 tube passes, the remaining exchangers have 4 tube passes. The outside diameter of the tubes in all the exchangers, except for the condenser in the Kalina cycle, is 25.4 mm; the tubes of the Kalina cycle condenser have an outside diameter of 19 mm. The tube wall thickness for all the heat exchangers is consistent at 1.7 mm. Additionally, the fin tip diameter in all the exchangers is maintained at 57.2 mm.

Based on the various key parameters outlined above for designing the heat exchangers, Table 6.12 lists the area of different heat exchangers as depicted in Figure 4.1 and Figure 4.5. Additionally, the different steps involved in calculating the overall heat transfer coefficient for a domestic heat exchanger are detailed as an example in Appendix D.

Table 6.10: Design data of shell and tube heat exchangers utilized in both separated and combined systems

Parameters	Domestic heat exchanger	Pre-boiler	Boiler	Internal heat exchanger	Generator	Solution heat exchanger	Evaporator
Shell side							
Inside diameter (m)	1.35	0.65	1.905	0.4826	2.19	0.5397	1.85
Shells in series	1	1	1	1	1	1	1
Shells in parallel	1	1	1	1	1	1	1
Tube side							
Tube pattern	90	90	90	30	90	30	30
Number of tubes (-)	740	208	1800	251	3410	328	1325
Tube pitch (mm)	23.8	23.8	25.4	23.8	31.8	23.8	31.8
Tube passes	6	1	4	6	6	2	8
Outside diameter (mm)	19	19	19	19	25.4	19	25.4
Tube wall thickness (mm)	2.1	2.1	2.1	2.1	2.1	2.1	2.1
Tube length (m)	3.5		4	3.2	2.3	4.96	6
Baffle							
Baffle cut (%)	25	25	-	25	-	25	25
Baffle spacing center-center (mm)	627.5	292.6	-	291.4	-	267	370
Baffle spacing at inlet/outlet (mm)	627.5	353.2	-	291.4	-	486	884.5
Number of baffles	5	11	-	12	-	16	12

Table 6.11: Design data of air-cooled heat exchangers utilized in both separated and combined systems

Parameters	Kalina cycle condenser	Dephlegmator	ARC condenser	Absorber
Unit Geometry				
Bays per unit	10	2	5	4
Bundles per bay	2	2	2	2
Tube				
Tube layout angle pattern	30	30	30	30
Number of tubes (-)	100	112	156	148
Tube pitch (m)	0.6	0.6	0.6	0.6
Tube passes	8	4	4	8
Outside diameter (mm)	19	25.4	25.4	25.4
Tube wall thickness (mm)	1.7	1.7	1.7	1.7
Tube length (m)	6.9	9.82	6	9.83
Fin				
Fin tip diameter (mm)	57.2	57.2	57.2	57.2
Fin frequency (#/m)	275	433	254	254
Fin thickness (mm)	0.3	0.3	0.3	0.3
Fan diameter (m)	3.66	3.66	3.66	3.66

Table 6.12: The area of different heat exchangers

	Area (m^2)
Heating section	
Domestic heat exchanger	156
Power section	
Boiler	430
Pre-boiler	47
Internal heat exchanger	48
Kalina cycle condenser	14,162
Cooling section	
Generator	625
Dephlegmator	3264
Solution heat exchanger	98
ARC condenser	9487
Absorber	10,043
Evaporator	1236

6.4 Results under off-design conditions

In our comprehensive exergetic analysis, particular attention was devoted to evaluating the performance of the system under off-design conditions. This involved a detailed examination of the effects of various boundary conditions, as outlined in Table 5.8, on the exergy efficiency and losses of the system. These conditions are calculated by incorporating models for both heat exchanger and turbine operations under off-design scenarios.

Each component, treated as a distinct control volume, underwent thorough mass, energy, and exergy balance analyses. The design and operational state of heat exchangers, a pivotal aspect of our study, are assessed using an off-design model specific to heat exchangers. Similarly, the performance of the turbine under off-design conditions was evaluated using a specialized off-design model for turbines. This approach was instrumental in revealing how changes in operational parameters affect the overall efficiency and exergy destruction within the turbine, and consequently, the entire system. Certain boundary conditions are calculated in accordance with the Heat Exchanger off-design model and the Turbine off-design model. These models provided a framework for accurately determining how specific boundary conditions affect system performance, particularly under varying operational scenarios.

In addition, aligning the heating and cooling demands with the data in Table 5.8, based on ambient temperature scenarios, was crucial to ensure realistic and applicable system performance assessments. The heating demand of district network is met by adjusting the geothermal mass flow rate, with the excess being directed to the Kalina cycle for power generation. This comprehensive approach, combining off-design models for both heat exchangers and turbines, provided invaluable insights into the adaptability of the system and efficiency under a range of the operational conditions. Pressure and heat losses in the heat exchangers and pipelines are disregarded to streamline the analysis and concentrate on the critical decision parameters. The analysis not only deepened our understanding of theoretical exergetic efficiency but also offered practical guidance for optimizing system design and operation, thereby enhancing the system's sustainability and economic feasibility.

6.4.1 Parametric analysis during winter days: off-design mode

Table B.1 in appendix B displays the thermodynamic properties and mass flow rates of different streams, as shown in Figure 4.1, under off-design conditions during the winter. Table 5.8 indicates that a heat demand of 8 MW is satisfied at an ambient temperature of 8 °C, providing a basis for system analysis during winter days. According Table B.1, to satisfy an 8 MW heating requirement, 32.1 kg/s of geothermal hot water at 138 °C is fed into the domestic heat exchanger and exits at 79.1 °C. On the cold side of this exchanger, 63.6 kg/s of water at 60 °C absorbs the heat from the geothermal hot water, which increases its temperature to 90 °C, suitable for district heating needs. Once the heat demand is fulfilled, the residual 87.9 kg/s of geothermal hot water is channeled to the boiler and pre-boiler to heat the ammonia-water solution. Exiting the pre-boiler at 82.4 °C, the geothermal hot water mixes with the outflow from the domestic heat exchanger and is returned to the reinjection sources at 81.5 °C. The solution containing 80 % ammonia exits the boiler at 95.8 °C in a two-phase state with a quality of 0.5033. This two-phase mixture is then split into saturated liquid and vapor streams, both at the same temperature. The less concentrated, poor saturated liquid, with 60.79 % ammonia, is channelled to the internal heat exchanger to preheat the fluid entering the pre-boiler. Conversely, the rich saturated vapor, containing 98.96 % ammonia, is fed into the turbine at 95.77 °C and 30 bar, where it expands to a pressure of 6.49 bar. Subsequently, the low-pressure solution, cooled to 32.6 °C, enters the condenser and is further cooled to 18 °C upon exiting. This stream is then pressurized to the high pressure of the system of 30 bar by a pump.

The performance of the system during winter days under design and off-design conditions is listed in Table 6.13. As shown, under off-design conditions, the heat transfer rates in the boiler and Kalina cycle condenser are lower than those observed in design conditions. Conversely, in the pre-boiler and internal heat exchanger, heat transfer rates under off-design conditions exceed those in design mode. These changes occur due to variations in operational parameters such as pinch point temperatures differences and mass flow rates across different components. Additionally, according Table 6.13 under off-design conditions, the heat transfer rate from geothermal hot water to the ammonia-water solution in the boiler and pre-boiler is 16,555 kW and 4155 kW, respectively. These rates are 27 % lower in the boiler and 25 % higher in the pre-boiler compared to the rates observed under design conditions. Additionally, the heat transfer rate in the internal heat exchanger under off-design mode is 3545 kW, which is 21 % higher than the on-design calculation. Moreover, the heat transfer rate from the ammonia-water solution in the Kalina cycle condenser to air for cooling the ammonia-water solution is calculated to be 18,408 kW under off-design conditions, which is 19 % lower than the on-design conditions. Besides, the turbine work in off-design conditions is calculated at 2425 kW, which is 28 % less than during design conditions. As well, the net produced power in off-design conditions is determined to be 2277 kW, marking a 30 % decrease from the design conditions. The input exergy to the system in off-design mode is 11 % lower than in the design condition due to the higher reinjection temperature of the geothermal water. These comparisons between on-design and off-design calculations indicate that the performance of the system significantly deteriorates under off-design conditions, reflecting reduced efficiency and output when operating parameters deviate from optimal settings. The exergy efficiency of the system is 51.5 % in off-design mode and 57.7 % in design mode, making the exergy efficiency in off-design mode 10 % lower than in design conditions. Furthermore, the exergy destruction rate is 3427 kW in off-design mode and 3237 kW in design mode. This means the exergy destruction rate is 6 % higher in off-design mode because of increased irreversibilities under these conditions. These irreversibilities arise from inefficiencies in the heat exchange processes and increased entropy generation.

Table 6.13. Performance of the system during winter days under design and off-design conditions

	Off-design calculation	Design calculation
Heat transfer rate in domestic heat exchanger (kW)	8000	8000
Heat transfer rate in boiler (kW)	16,555	22,770
Heat transfer rate in pre-boiler (kW)	4155	3309
Heat transfer rate in internal heat exchanger (kW)	3545	2916
Heat transfer rate in Kalina cycle condenser (kW)	18,408	22,816
Work of the turbine (kW)	2425	3363
Work of the Kalina cycle pump (kW)	123	100
Work of the fan in the Kalina cycle (kW)	25	-
Net produced power (kW)	2277	3263
Heating Exergy (kW)	1378	1378
Input exergy (kW)	7098	8040
Exergy efficiency (%)	51.5	57.7
Exergy destruction rate (kW)	3427	3237

Figure 6.19 illustrates the exergy flow and destruction rates of the proposed system designed to meet a heating demand of 8 MW at an ambient temperature of 8 ℃. The arrows in the diagram, whose thickness is proportional to the exergy values, depict the flow of exergy through various system components. The gray arrows specifically represent the exergy destruction rates in these components. Out of the 10,457 kW of input exergy from the geothermal heat source, 2795 kW enters the domestic heat exchanger while 7662 kW is directed to the boiler. In the domestic heat exchanger, 2226 kW of exergy is utilized to heat the district networks, although this process incurs a loss of 580 kW due to exergy destruction. A significant exergy loss occurs in the boiler, where out of the initial 7662 kW of exergy input from geothermal heated water, only 3368 kW is transferred to the pre-boiler due to an exergy destruction of 1087 kW in the boiler. Within the pre-boiler, 274 kW of exergy is destroyed, but it still manages to output 2526 kW, which merges with the output of the domestic heat exchanger of 837 kW. The merged exergy flow of 3362 kW is then fed into the heat source. Further in the system, the saturated vapor generated in the boiler is conveyed to the turbine, where it enters with an exergy content of 280,486 kW and subsequently expands to a lower pressure of the system with an exergy of 277,633 kW to generate power. In the turbine, during the process of producing power, 2423 kW of exergy is destroyed. The liquid phase ammonia-water solution with an exergy of 167,521 kW transfers 358 kW in the internal heat exchanger as fuel exergy to heat the outgoing stream from the pump. The outgoing low-pressure stream of the turbine, after mixing with the streams from the internal heat exchanger with an exergy of 166,924 kW, cools in the Kalina cycle condenser, where 15 kW of exergy is lost. Overall, from 10,457 kW of input exergy from geothermal hot water, 2423 kW is converted to net produced power and 1378 kW to heating capacity. Additionally, 15 kW of the input exergy is lost. Furthermore, 3362 kW of input exergy is returned to the geothermal heat source. Consequently, the exergy destruction rate in the system under off-design conditions is calculated to be 3424 kW.

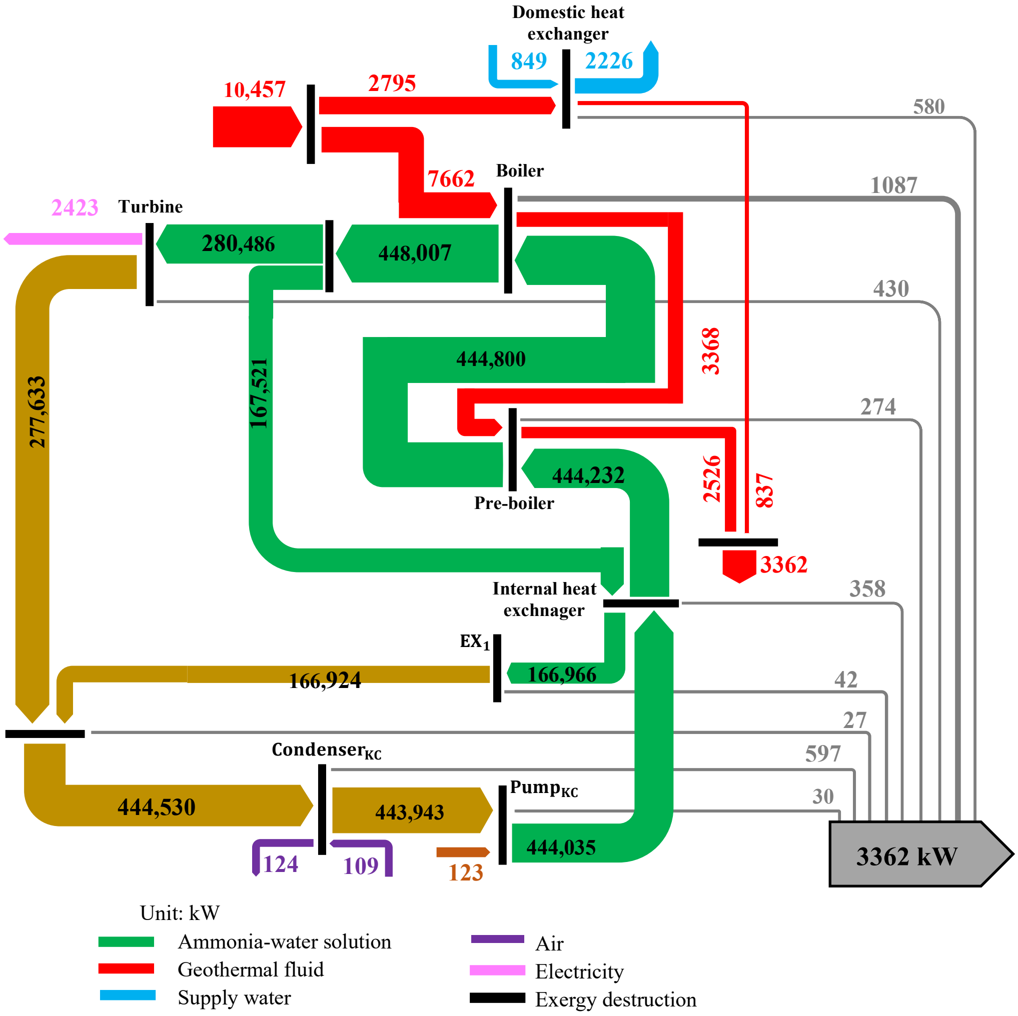

Figure 6.19: The exergy flow diagram of the proposed system during winter days

The variations in exergy destruction rates across the components indicate key opportunities for enhancement, particularly within the boiler and condenser. Improving performance could involve optimizing the phase change processes in the boiler. By carefully adjusting operational parameters such as pressure and temperature to better match the thermodynamic properties of the ammonia-water mixture, it is possible to reduce irreversibilities in heat transfer and phase.

Figure 6.20 presents the exergy analysis of the system under off-design conditions, with an ambient temperature of 8 °C and heating demand of 8 MW during winter days. The analysis highlights the boiler, which has a fuel exergy of 4294 kW, product exergy of 3207 kW, and an exergy destruction of 1087 kW, indicating a high rate of exergy destruction. This is primarily due to the relatively high temperature difference between the geothermal water and the ammonia-water solution in the boiler, which raises thermal gradients, leading to increased entropy production and consequently higher exergy destruction. Moreover, the phase change dynamics of the ammonia-water mixture in the boiler further enhance entropy generation, thus intensifying the exergy destruction compared to other system components.

The condenser with a loss exergy rate of 16kW, a fuel exergy rate of 613 kW, and an exergy destruction rate of 597 kW has the second highest exergy destruction rate among the components. Meanwhile, the domestic heat exchanger, which has a fuel exergy of 1958 kW, product exergy of 1378 kW, and an exergy destruction of 580 kW, also exhibits a high destruction rate.

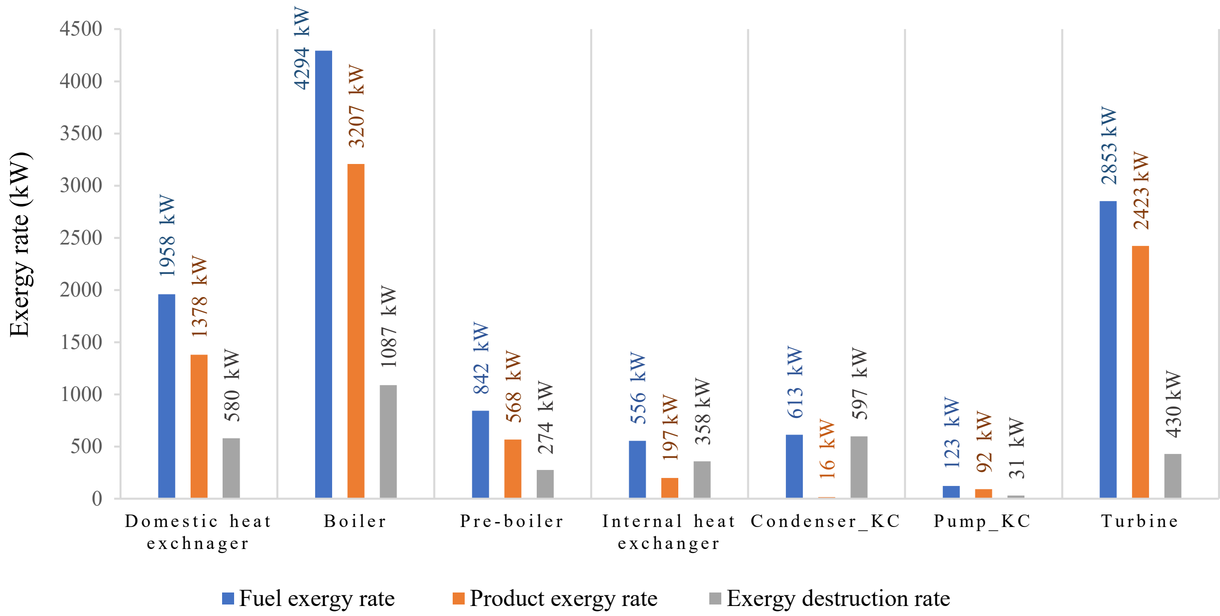

Figure 6.20: Fuel, product, and destruction exergy rates for various components in the proposed systems during winter days ($T_0 = 8$ °C , $\dot{Q}_H = 8$ MW)

The pump exhibits the lowest exergy destruction rate among the components, at 31 kW. This reduced rate of exergy destruction is primarily due to the minimal temperature gradients it encounters during operation. Pumps are primarily involved in the mechanical transfer of energy and do not engage in extensive thermal energy exchanges typical of components like boilers or condensers. The absence of significant thermal gradients greatly diminishes the potential for entropy generation from heat transfer, thereby leading to lower exergy destruction.

6.4.1.1 Variation in Heating demand: Winter Days

The variation of the exergy efficiency, as well as the net produced power, heating exergy, and input exergy with heating demand, are illustrated in Figure 6.21 for a system operating under off-design conditions at an ambient temperature of 8 ℃ during winter days. According Figure 6.21, at the lowest reported heating demand of 5 MW, the exergy efficiency is measured at approximately 48 %. As the heating demand increases to 10 MW, the exergy efficiency rises to around 53 %. Further increasing the heating demand to 15 MW, the efficiency continues to ascend, reaching about 56 %. The graph culminates with the highest heating demand of 20 MW, where the exergy efficiency peaks just above 58 %.

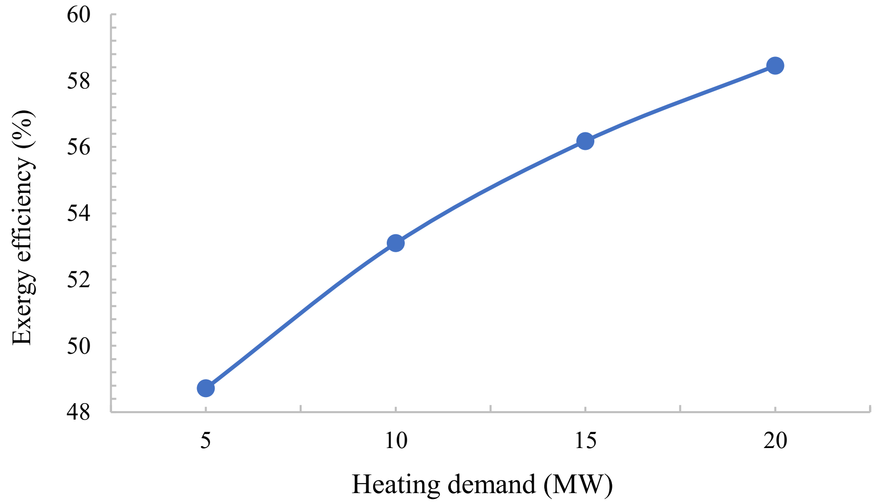

(a)

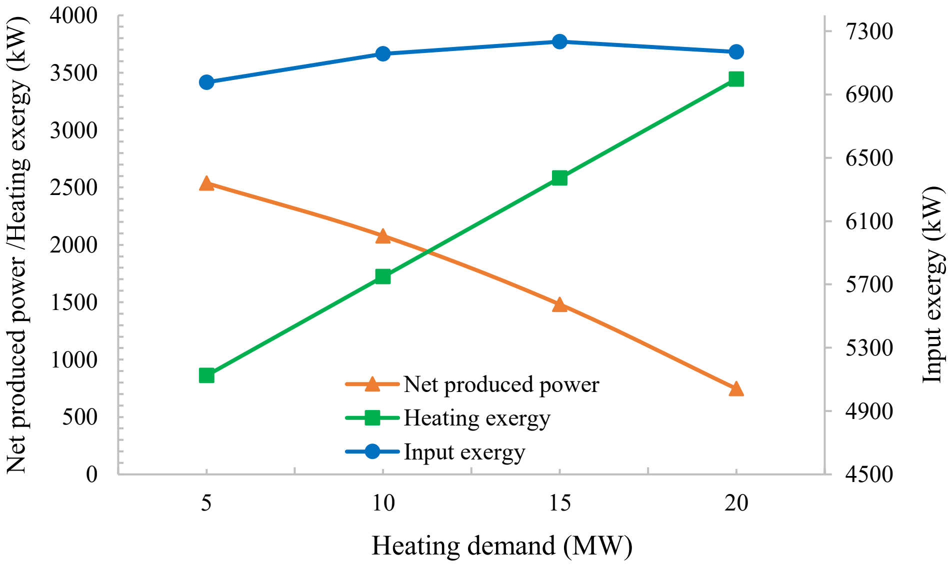

(b)

Figure 6.21: The impact of varying heating demands on a) exergy efficiency, and b) net produced power, as well as on the heating exergy and input exergy during winter days ($T_0 = 8$ °C)

According to Figure 6.21, the data indicates that exergy efficiency increases concurrently with an increase in heating demand. This efficiency growth is associated with the heating exergy generated within the domestic heat exchanger, which experiences growth as the heating demand rises. The underlying cause for this growth is attributed to the enhanced mass flow rate of geothermal hot water circulating through the domestic heat exchanger. Moreover, Figure 6.21(b) delineates a decrease in net produced power as the heating demand ascends. This occurrence happens due to a reduction in the proportion of geothermal heat source water that is directed to the Kalina cycle. Consequently, both the mass flow rate and the inlet temperature of the turbine decrease, leading to a consequent reduction in the net produced power. Essentially, the system arranges the fulfilment of the heating demand, and in doing so, the energy that would typically be converted into electricity within the Kalina cycle is instead utilized to meet the thermal load, causing a decrease in electrical output. However, that variations in heating demand exert a negligible influence on the overall input exergy rate of the system, which remains relatively stable. The rate at which the heating exergy increases surpasses the rate of reduction in net produced power. This inverse relationship between the two parameters culminates in an increase in their cumulative sum.

A comparative analysis of part load percentages under winter condition across a range of heating demands from 5 MW to 20 MW, is presented in Figure 6.22. In the winter condition with an ambient temperature of 8 °C, there is a decline in part load percentage as the heating demand increases. The system operates near peak efficiency (close to 80 %) at a low heating demand of 5 MW, but part load drops quickly as demand escalates, reaching its lowest point at 20 MW. The heating demand in question is met by a domestic heat exchanger utilizing water streams at temperatures of 60 °C and 90 °C. At a heating demand of 5 MW, the required mass flow rate of geothermal water at 138 °C is 19.9 kg/s to fulfill this heating requirement. Conversely, for a heating demand of 20 MW, the mass flow rate of geothermal water needed increases significantly to 85.2 kg/s. Consequently, only 34.8 kg/s of geothermal water is available for the Kalina cycle, which is utilized for electricity generation, compared to the 100.1 kg/s directed to the Kalina cycle when the heating demand is at 5 MW. This reallocation of geothermal water from electricity generation to direct heating needs at higher heating demands is the primary reason for the observed decrease in part load performance at the 20 MW heating demand level. This trend suggests that the system under winter conditions is optimized for lower heating demands, with its efficiency being compromised at higher demands due to potentially increased losses or operational limitations.

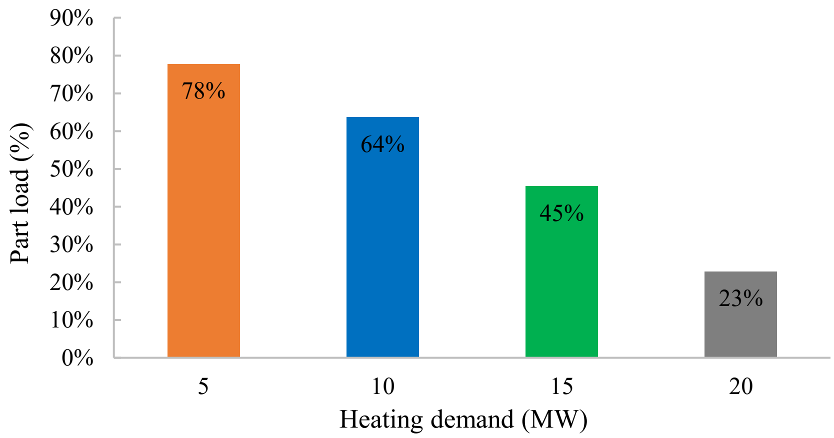

Figure 6.22. Part load performance comparison across heating demands for winter condition (T_0 = 8 °C)

In the analysis depicted in Figure 6.23, the exergy destruction rates of various system components are compared across different heating demands, ranging from 5 MW to 20 MW, under winter conditions with an ambient temperature of 8 °C. The exergy destruction rate of the system at a heating demand of 5 MW is 3558 kW, which decreases to 2984 kW at a heating demand of 20 MW. At heating demands of 5 MW and 10 MW, the boiler accounts for the largest portion of the exergy destruction rate, contributing 34.5 % and 29.6 %, respectively. However, at heating demands of 15 MW and 20 MW, the domestic heat exchanger constitutes the largest portion of the exergy destruction rate, contributing 35.2 % and 48.1 %, respectively. In addition, the exergy destruction rate of the condenser in the Kalina cycle decreases with an increase in heating demand. Its share of the total exergy destruction rate decreases from 17.8 % at a heating demand of 5 MW to 8.2 % at a heating demand of 20 MW. With an increase in heating demand, the contribution of the internal heat exchanger and pre-boiler to the total exergy destruction rate decreases. The contribution of the exergy destruction rate in the turbine does not fluctuate significantly with an increase in heating demand. The lowest share in the total exergy destruction rate belongs to the pumps, with 1 %.

As showed in Figure 6.23, as the heating demand increases, the exergy destruction rates across most components decrease, and consequently, the total exergy destruction rate also decreases, demonstrating improved efficiency at higher heating demand. One exception to this trend is observed in the domestic heat exchanger, where exergy destruction rates increase with rising heating demands. With an increase in heat demand, the mass flow rate of geothermal water through the domestic heat exchanger increases. This increase in mass flow rate leads to higher exergy destruction due to several factors. Increased flow rates result in higher fluid velocity, which reduces the effectiveness of heat transfer by decreasing the residence time of the fluid. Additionally, higher flow rates cause greater pressure drops, indicating energy losses from fluid friction and resistance. In addition, the increase in heat demand leads to a reduction in the mass flow rate. This reduction results in a decrease in the contribution to the total exergy destruction rate in other components, as mentioned previously.

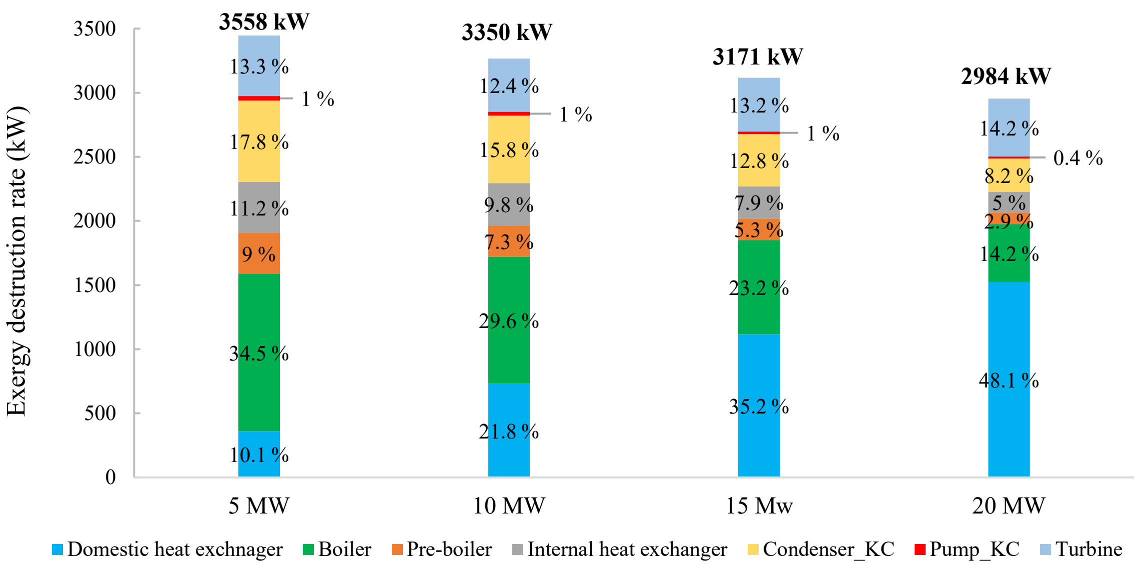

Figure 6.23: Exergy destruction rate comparison across different heating demands for different components during winter condition ($T_0 = 8$ °C)

6.4.1.2 Variation in ambient temperature: winter days

Figure 6.24 illustrates the variation in exergy efficiency with different ambient temperatures for a system operating under off-design conditions with a heating demand of 8 MW during winter days. At the lowest reported ambient temperature of -10 ℃, the exergy efficiency is 52.4 %. As the ambient temperature increases to -1 ℃, the exergy efficiency rises to a local optimum value of 54 %. Further increasing the ambient temperature to 16 ℃ results in a decrease in efficiency, reaching about 46.7 %. The causes of this local maximum in exergy efficiency with varying ambient temperatures are explained in Figure 6.25.

Figure 6.25 shows a decline in net produced power as the ambient temperature increases. This occurs due to an increase in turbine back pressure, which leads to a reduction in turbine specific work and net produced power, since net power is the product of specific turbine work and turbine mass flow rate. While the inlet enthalpy of the ammonia-water solution in the turbine (h_8) remains constant, the outlet enthalpy (h_9) increases, causing the turbine specific work to decrease with rising ambient temperature. Additionally, the heating exergy of the system decreases with an increase in ambient temperature due to varying dead state temperature (T_{dead}). According to equation (5.9), as the heat state increases, the specific exergy of that state ($(h - h_0) - T_0(s - s_0)$) decreases, consequently reducing the exergy rate of heating with an increase in ambient temperature. Furthermore, variations in ambient temperature also decrease the input exergy rate of the system. This occurs because of the varying dead state temperature, although the inlet temperature and reinjection temperature of the geothermal hot water remain almost constant. The reduction slopes of net produced power, heating exergy, and input exergy occur in such a way that an optimum value in the exergy efficiency of the system is observed.

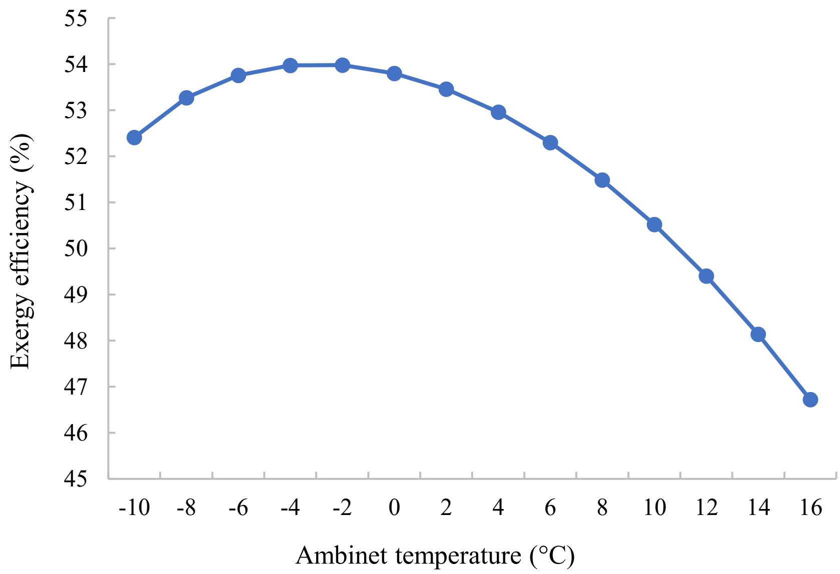

Figure 6.24: The impact of varying ambient temperature on exergy efficiency under off-design condition during winter days ($\dot{Q}_H = 8$ MW)

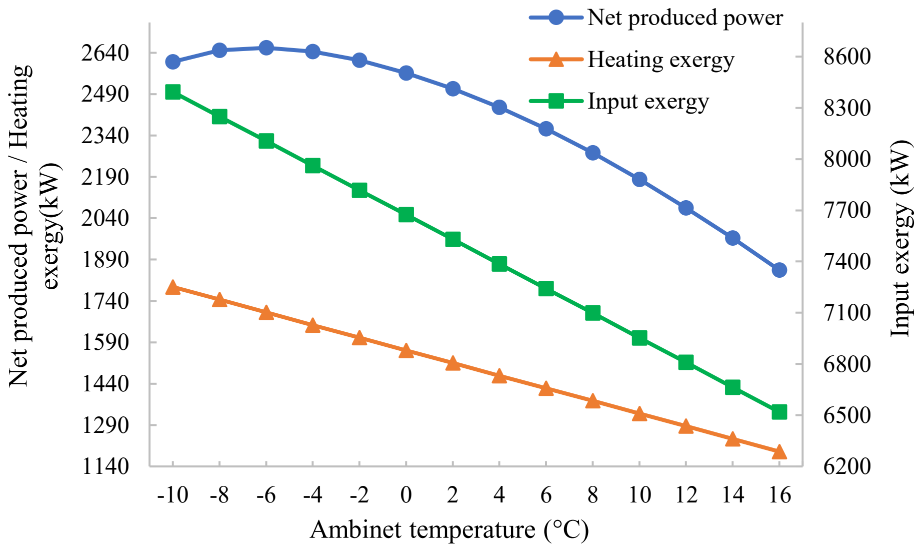

Figure 6.25: The impact of varying ambient temperature on net produced power, heating exergy and input exergy under off-design condition during winter days ($\dot{Q}_H$ = 8 MW)

In Figure 6.26, the impact of ambient temperature on the total exergy destruction rate is depicted during winter, under off-design conditions with a heating demand of 8 MW. As the ambient temperature increases from -10 °C to 8 °C, the total exergy destruction rate decreases from 3907 kW to a local minimum of 3427 kW. However, further increasing the ambient temperature to 16 °C results in a rise in the exergy destruction rate, reaching 3468 kW. As shown in Figure 6.25, the heating exergy, net produced power, and input exergy to the system decrease with rising ambient temperatures. Additionally, exergy losses in the Kalina cycle condenser decrease due to the reduced temperature gradients. Lower temperature gradients reduce irreversibilities, thereby decreasing the exergy destruction rate. The slope of the reduction in input exergy is greater than the reductions in heating exergy and net produced power. Consequently, according to Equation (5.28), the total exergy destruction rate reaches a local minimum at an ambient temperature of 8 °C.

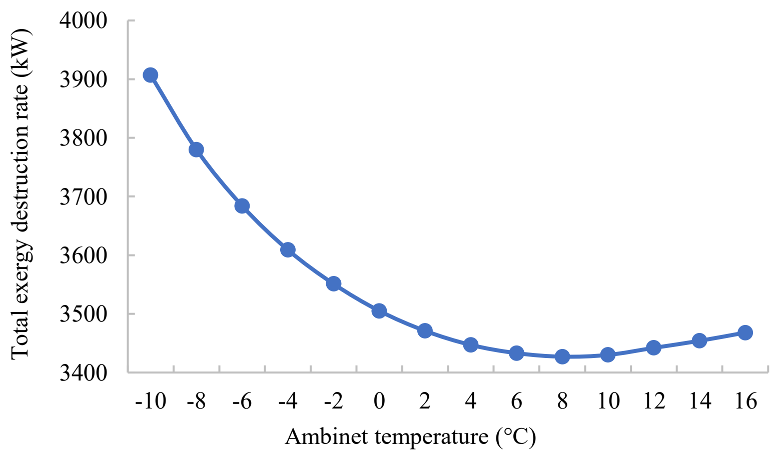

Figure 6.26: The impact of varying ambient temperature on total exergy destruction rate under off-design condition during winter days ($\dot{Q}_H$ = 8 MW)

6.4.1.3 Consequences of pressure drops in heat exchangers: winter days

As mentioned before, the pressure drops in heat exchangers are neglected in the off-design analysis to simplify the calculations, focus on key decision parameters, and maintain a manageable model. This simplification allows for a clearer understanding of how each individual parameter affects the system performance without the added complexity of accounting for pressure and heat losses. However, to gain a comprehensive understanding of the behavior of the system, it is essential to examine the consequences of pressure drops in heat exchangers. Under off-design conditions, the pressure drops are determined based on the type and concept of each heat exchanger. Therefore, in this section, the effect of pressure drops on system performance is assessed. The correlation in Refs. [132, 153-155] was used to determine the pressure drop for various system components.

The performance of the system in scenarios with and without considering pressure drops in heat exchangers is summarized in Table 6.14. The analysis is performed under winter conditions with an ambient temperature of 8 ℃ and a heating demand of 8 MW. Table C.1 in Appendix C shows the thermodynamic properties of different states of the system as determined in Figure 4.1, considering pressure drops. In addition, Table C.2 in Appendix C presents the pressure drops in the heat exchangers using pressure drop correlations. According to Table 6.14, in scenarios accounting for pressure drops, all heat transfer rates in the heat exchangers are lower than those observed without considering pressure drops. These changes result from variations in operational parameters, such as pinch point temperature differences and mass flow rates, due to altered inlet and outlet pressures and temperatures in the components. In scenarios accounting for pressure drops, the heat transfer rate from geothermal hot water to the ammonia-water solution in the boiler and pre-boiler is 2 % and 3 % lower, respectively, in scenarios without considering pressure drops. Additionally, the heat transfer rate from the ammonia-water solution in the Kalina cycle condenser to air is 17,580 kW, which is 4.5 % lower than the rate in scenarios without pressure drop considerations. Turbine work, when accounting for pressure drops, is calculated at 2243 kW, 7.5 % less than in scenarios without pressure drops. The net produced power with pressure drops is 2090 kW, marking an 8 % decrease compared to scenarios without pressure drops. Furthermore, the input exergy to the system remains almost the same in both scenarios. However, these comparisons indicate that system performance deteriorates under pressure drop conditions, reflecting reduced efficiency and output. The exergy efficiency of the system with pressure drops is 49 %, which is 5 % lower than without pressure drops. The exergy destruction rate is 3505 kW with pressure drops, 2 % higher than without pressure drops due to increased irreversibilities arising from inefficiencies in the heat exchange processes and increased entropy generation.

Table 6.14: Performance of system during winter, with and without pressure drop in heat exchangers

	Without pressure drop	With pressure drop
Heat transfer rate in domestic heat exchanger (kW)	8000	8000
Heat transfer rate in boiler (kW)	16,555	16,223
Heat transfer rate in pre-boiler (kW)	4155	4026
Heat transfer rate in internal heat exchanger (kW)	3545	3468
Heat transfer rate in Kalina cycle condenser (kW)	18,408	17,580
Work of the turbine (kW)	2425	2243
Work of the Kalina cycle pump (kW)	123	127.9
Work of the fan in the Kalina cycle (kW)	25	26
Net produced power (kW)	2277	2090
Heating Exergy (kW)	1378	1378
Input exergy (kW)	7098	7084
Exergy efficiency (%)	51.5	49
Exergy destruction rate (kW)	3427	3505

Figure 6.27 demonstrates the effects of varying heating demand on net produced power and total exergy destruction rate under two off-design scenarios: one without pressure drops in heat exchangers and one with pressure drops. As depicted in Figure 6.27 (a), the net produced power is approximately 6.5 % lower across all heating demand values in the scenario with pressure drops compared to the scenario without. This reduction is due to changes in pressure and temperature of the stream entering and exiting the turbine caused by the pressure drops, which diminish the turbine's power output. Furthermore, the increased resistance and frictional losses within the heat exchangers lead to higher energy consumption for fluid circulation, further reducing the net produced power. In the scenario considering pressure drops, the net produced power decreases from 2382 kW at a 55 MW heating demand to 638 kW at a 20 MW heating demand.

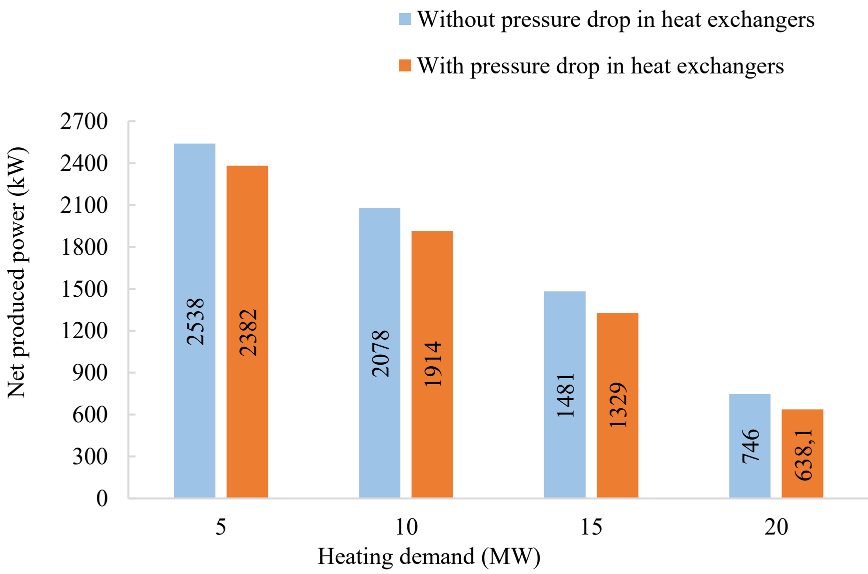

(a)

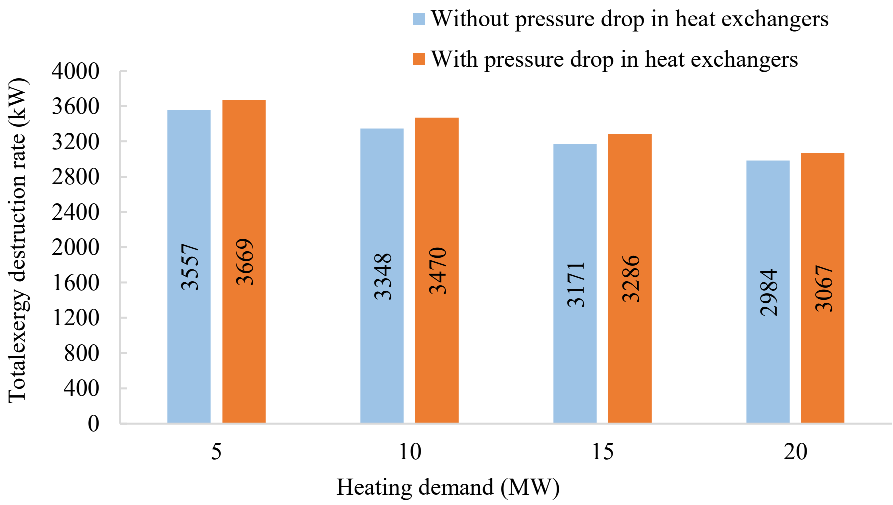

(b)

Figure 6.27: (a) Net produced power (b) Total exergy destruction rate versus different heating demand difference in the boiler under off-design conditions for two scenarios: without pressure drop in heat exchangers and with pressure drop in heat exchangers (under winter condition)

In addition, as shown in Figure 6.27 (b), the total exergy destruction rate in the system with pressure drop calculations increases by 3 % compared to the analyses without pressure drops in heat exchangers, across all variations of heating demand. This increase is due to greater irreversibilities from higher frictional losses and additional pressure drops within the heat exchangers, leading to increased entropy generation and reduced overall system efficiency. In the scenario considering pressure drops, the total exergy destruction rate decreases from 3669 kW at a 5 MW heating demand to 307 kW at a 20 MW heating demand.

6.4.2 Parametric Analysis During Summer Days: Off-design mode

The performance of the system during summer days under design and off-design conditions for separated and combined systems is listed in Table 6.15 and Table 6.16, respectively. As shown, the heating demand of 2 MW and cooling demand of 4 MW in both design and off-design conditions are the same. Under off-design conditions in both separated and combined systems, the heat transfer rates in the boiler, Kalina cycle condenser, and dephlegmator are lower than those observed in design conditions. Conversely, in the other heat exchangers, heat transfer rates under off-design conditions exceed those in design mode. These changes occur due to variations in operational parameters such as pinch point temperature differences and mass flow rates across different components.

As shown in Table 6.15, the turbine work in off-design conditions in the separated system is calculated at 2278 kW, which is 18 % less than during design conditions. Also, the net produced power in off-design conditions in the separated system is determined to be 1977 kW, marking a 25 % decrease from the design conditions. The input exergy to the separated system in off-design mode is 2 % lower than in the design condition due to the higher reinjection temperature of the geothermal water. Additionally, the exergy efficiency of the separated system is 34.1 %

in off-design mode and 42.8 % in design mode, making the exergy efficiency in off-design mode 20 % lower than in design conditions. Furthermore, the exergy destruction rate in the separated system is 4720 kW in off-design mode and 3962 kW in design mode. This means the exergy destruction rate is 19 % higher in off-design mode because of increased irreversibilities under these conditions. These irreversibilities arise from inefficiencies in the heat exchange processes and increased entropy generation.

Table 6.15: Performance of the system during summer days under design and off-design conditions in separated system

	Off-design calculation	Design calculation
Heating section		
Heat transfer rate in domestic heat exchanger (kW)	2000	2000
Power section		
Heat transfer rate in boiler (kW)	21,156	27,479
Heat transfer rate in pre-boiler (kW)	4532	2388
Heat transfer rate in internal heat exchanger (kW)	4039	2966
Heat transfer rate in Kalina cycle condenser (kW)	23,565	27,203
Work of the turbine (kW)	2278	2764
Work of the Kalina cycle pump (kW)	154.1	101
Work of the fan in the Kalina cycle (kW)	76	-
Cooling section		
Heat transfer rate in generator (kW)	9321	5970
Heat transfer rate in dephlegmator (kW)	351.4	351.7
Heat transfer rate in solution heat exchanger (kW)	3835	3071
Heat transfer rate in ARC condenser (kW)	4415	4299
Heat transfer rate in absorber (kW)	8610	5342
Heat transfer rate in evaporator (kW)	4000	4000
Work of the ARC pump (kW)	55.7	22.3
Work of the fan in Absorber (kW)	20.1	-
Work of the fan in dephlegmator (kW)	1.5	-
Work of the fan in ARC condenser (kW)	13.4	-
System performances		
Net produced power (kW)	1977	2641
Heating Exergy (kW)	275.4	275.4
Cooling exergy (kW)	241	246.2
Input exergy (kW)	7302	7399
Exergy efficiency (%)	34.1	42.8
Exergy destruction rate (kW)	4720	3962

As shown in Table 6.16, the turbine work in off-design conditions in the combined system is calculated to be 2480 kW, which is 7 % lower than during design conditions. Additionally, the net produced power in off-design conditions in the combined system is determined to be 2056 kW, representing an 18 % decrease from the design conditions. The input exergy to the combined system is 7176 kW in off-design mode and 7073 kW in design mode. The exergy efficiency of the combined system is 34.1 % in off-design mode and 42.5 % in design mode, resulting in a 16 % reduction in exergy efficiency under off-design conditions. Furthermore, the exergy destruction rate in the combined system is 4478 kW in off-design mode and 3813 kW in design mode. This indicates a 17 % increase in the exergy destruction rate in off-design mode due to increased irreversibilities under these conditions. These irreversibilities are caused by inefficiencies in the heat exchange processes and increased entropy generation.

Table 6.16: Performance of the system during summer days under design and off-design conditions in combined system

	Off-design calculation	Design calculation
Heating section		
Heat transfer rate in domestic heat exchanger (kW)	2000	2000
Power section		
Heat transfer rate in boiler (kW)	20,913	22,229
Heat transfer rate in pre-boiler (kW)	4682	4208
Heat transfer rate in internal heat exchanger (kW)	4088	3159
Heat transfer rate in Kalina cycle condenser (kW)	21,122	21,949
Work of the turbine (kW)	2480	2662
Work of the Kalina cycle pump (kW)	153.2	129.9
Work of the fan in the Kalina cycle (kW)	182.7	-
Cooling section		
Heat transfer rate in generator (kW)	8273	6584
Heat transfer rate in dephlegmator (kW)	496	748.1
Heat transfer rate in ARC condenser (kW)	6209	4300
Heat transfer rate in absorber (kW)	7731	7505
Heat transfer rate in evaporator (kW)	4000	4000
Work of the ARC pump (kW)	16.86	13.65
Work of the fan in Absorber (kW)	32.3	-
Work of the fan in dephlegmator (kW)	1.6	-
Work of the fan in ARC condenser (kW)	38.84	-
System performances		
Net produced power (kW)	2056	2518
Heating Exergy (kW)	257.4	257.4
Cooling exergy (kW)	212.2	211.7
Input exergy (kW)	7176	7073
Exergy efficiency (%)	35.5	42.5
Exergy destruction rate (kW)	4478	3813

These comparisons between on-design and off-design calculations indicate that the system's performance significantly deteriorates under off-design conditions, reflecting reduced efficiency and output. This deterioration occurs due to less favorable pinch point temperature differences in heat exchangers, mismatched heat transfer capacities due to varying mass flow rates, and decreased thermodynamic efficiency as components operate away from optimal conditions. Consequently, increased exergy destruction and entropy generation lead to higher thermal losses and lower overall system efficiency.

Figure 6.28 presents the exergy analysis of the both separated and combined systems under off-design conditions, with an ambient temperature of 20 °C, heating demand of 8 MW and cooling demand of 4 MW during summer days. destruction, respectively.

The analysis indicates that the boiler contributes the largest portion of the exergy destruction rate in both systems, accounting for 31.8 % in the separated system and 33 % in the combined system. The main reason is the substantial temperature difference between the geothermal hot water and the ammonia-water solution in the boiler, which elevates thermal gradients, leading to increased entropy production and, consequently, higher exergy destruction. The second largest portion of exergy destruction occurs in the Kalina cycle condenser, accounting for

15.6 % in the separated system and 10.2 % in the combined system. This higher exergy destruction rate in the condenser is due to less efficient heat transfer and larger temperature gradients, which increase irreversibilities and consequently lead to greater exergy destruction. In both systems, the turbine, internal heat exchanger, and pre-boiler account for approximately 7.5 %, 11.6 %, and 6 % of the total exergy As shown in Figure 6.28, the exergy destruction rate in the power section (Kalina cycle) is nearly the same in both systems. However, in the cooling section, differing boundary conditions and the absence of a solution heat exchanger in the combined system result in varying exergy destruction portions across different components. The generator accounts for 8 % of the exergy destruction rate in the combined system and 4.9 % in the separated system. Additionally, In the absorber, the exergy destruction portion is 4.6 % in the combined system and 5 % in the separated system. Furthermore, in the separated system, the solution heat exchanger accounts for 4.6 % of the total exergy destruction. Overall, the exergy destruction rate in the combined system, at 4478 kW, is lower than that in the separated system, which is 4720 kW.

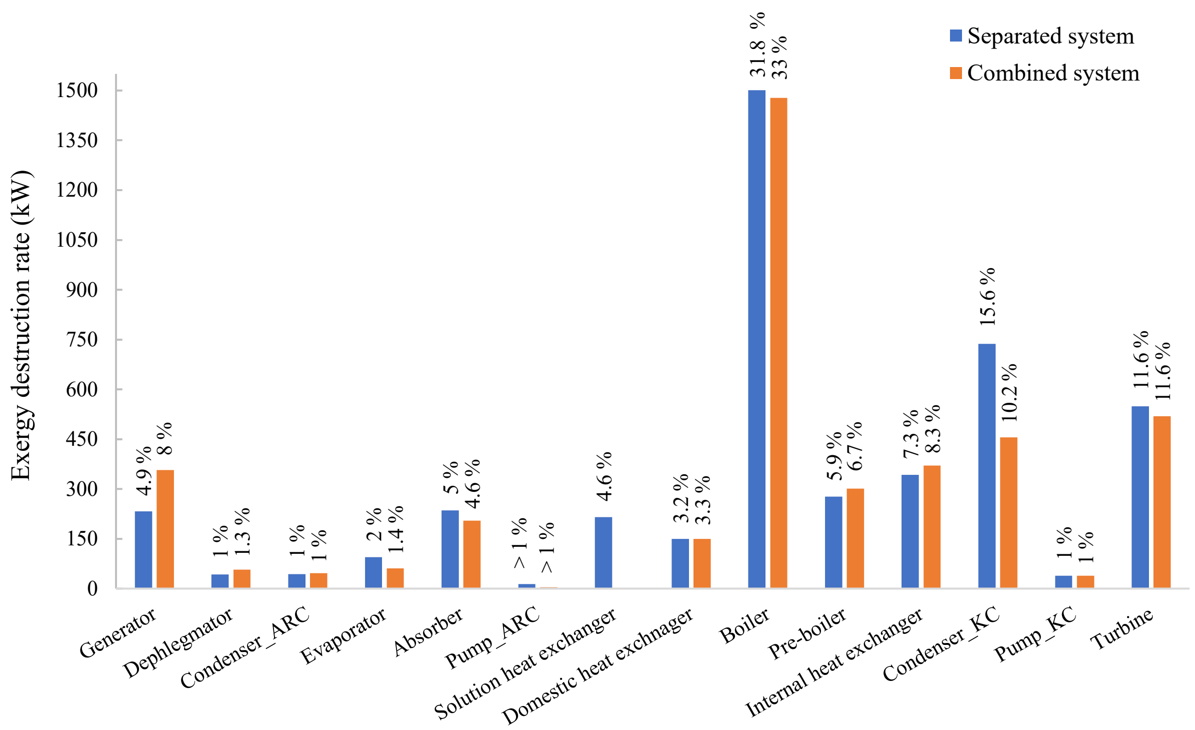

Figure 6.28: Comparative analysis of exergy destruction rates across various components in the separated and combined systems during summer days ($T_0 = 20$ °C , $\dot{Q}_H = 2$ MW , $\dot{Q}_C = 4$ MW)

6.4.2.1 Variation in heating demand: summer days

In Figure 6.29, the variations in exergy efficiency and net produced power are depicted for separated and combined systems operating under off-design conditions during summer days. The operations of the systems conducted at a cooling demand of 4 MW and an ambient temperature of 20 °C, typical for summer days. It is shown that with the increase in heating demand, an increase in exergy efficiency is observed for both systems. For the separated system, starting from just over 34.1 % at 2 MW, it increases steadily, reaching close to 36 % at 4 MW, approximately 37.5 % at 6 MW, and nearly 38.8 % at 8 MW. For the combined system, it begins at around 35.5 % at 2 MW, then progresses to about 37.7 % at 4 MW, approximately 39.7 % at 6 MW, and goes just above 41.5 % at 8 MW. This increase in exergy efficiency is linked to the heating exergy produced by the domestic heat exchanger, which rises with the growing heating demand. The primary reason for this growth is the improved mass flow rate of geothermal hot water circulating through the domestic heat exchanger. Furthermore, Figure 6.29 (b) illustrates a decline in net produced power as the heating demand increases. As discussed in Figure 6.21, this happens because a smaller portion of the geothermal heat source water is allocated to the Kalina cycle. As a result, the mass flow rate of the turbine decreases, leading to a drop in net produced power. The mass flow rate of geothermal hot water to the Kalina cycle decreases in both the separated and combined systems, dropping from 112 kg/s at 2 MW to 87.9 kg/s at 8 MW. Although the specific turbine work remains nearly constant due to the consistent boundary conditions at the inlet and outlet of the turbine, the specific turbine work is higher in the combined system compared to the separated system. These higher values are attributed to variations in operational parameters, such as pinch point temperature differences and mass flow rates across different components. The turbine specific work is measured at 136 kJ/kg in the combined system and 122 kJ/kg in the separated system. Additionally, the work required for fans in the separated system is higher than in the combined system. As a result, the net produced power in the combined system is greater than in the separated system for all considered heating demands, as shown in Figure 6.29 (b). Moreover, the input exergy of the system increases with rising heating demand in both the separated and combined systems. However, due to the lower reinjection temperature associated with higher heating demand, the input exergy in the combined system is lower than in the separated system. Additionally, the reinjection temperature in the combined system is higher than in the separated system for all considered heating demands. As a result, due to the higher net produced power and lower input exergy in the combined system, the exergy efficiency in the combined system is higher than in the separated system for all considered heating demands, as shown in Figure 6.29 (a).

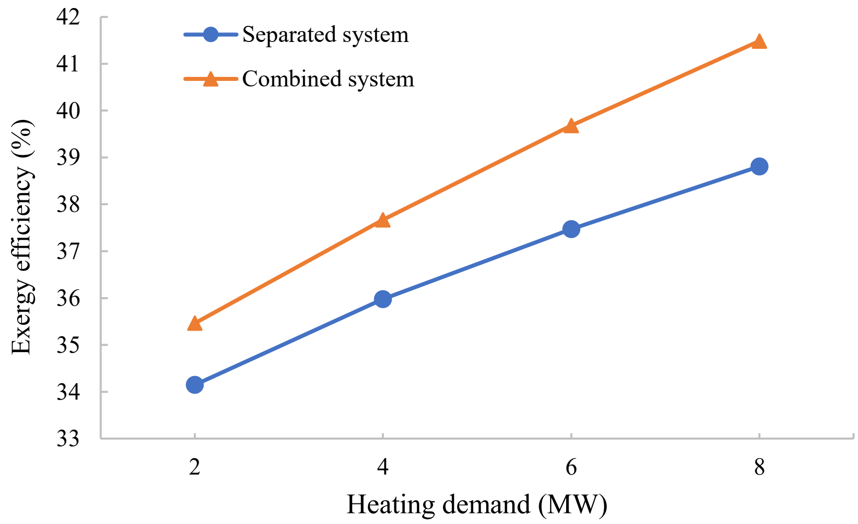

(a)

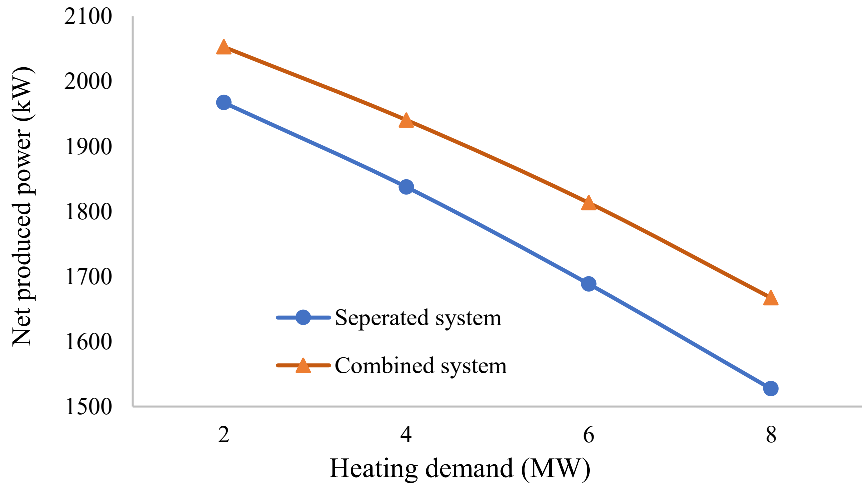

(b)

Figure 6.29. The impact of varying heating demands on a) exergy efficiency, and b) net produced power during summer days ($T_0 = 20$ °C, $\dot{Q}_C = 4$ MW).

Figure 6.30 presents a comparative analysis of part load percentages for separated and combined systems under off-design analysis. The analysis is conducted under summer conditions with an ambient temperature of 20 ℃, across a range of 4 MW cooling demand and heating demands from 2 MW to 8 MW. As depicted in Figure 6.30, the part load percentage of the combined system is consistently higher than that of the separated system across various heating demand levels. At a heating demand of 2 MW, the part load for the combined system stands at 63 %, whereas the separated system exhibits a slightly lower part load of 60 %. This higher part load performance in the combined system can be attributed to its greater net produced power, which in turn is due to the reduced power required for operating pumps and fans within the system. In addition, when the heating demand increases, there is a decline in the

part load for both systems, indicative of a common trend where increased demand typically leads to a decrease in part load performance due to lower mass flow rates of geothermal hot water in the Kalina cycle. Despite this overall decrease, the combined system maintains a higher part load percentage compared to the separated system at these elevated demands.
Specifically, at the highest heating demand of 8 MW presented in the Figure 6.30, the part load of the combined system is at 51 %, in comparison to the separated system which is slightly lower at 50 %. This analysis underscores the enhanced efficiency of the combined system over the separated system, particularly in its ability to sustain higher part load percentages as the heating demand escalates, resulting from its more efficient design and lower auxiliary power consumption.

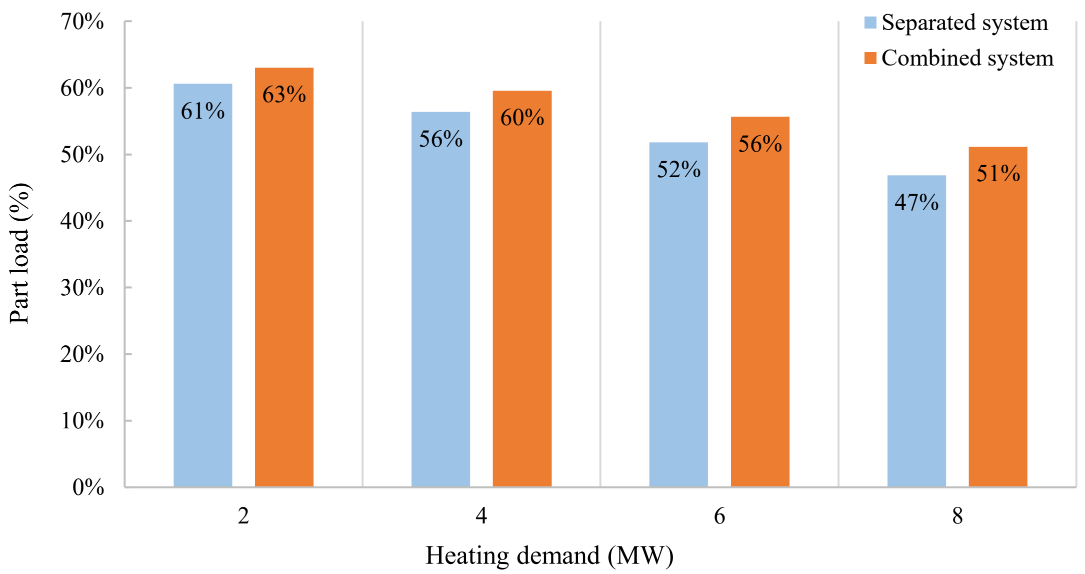

Figure 6.30. Part load performance comparison across heating demands in summer days for Separated and combined system (T_0 = 20 °C, $\dot{Q}_C$ = 4 MW)

In the analysis depicted in Figure 6.31, the exergy destruction rates of the separated and combined systems under off-design mode are compared across different heating demands, ranging from 2 MW to 8 MW. This comparison is conducted under summer conditions with an ambient temperature of 20 °C. The exergy destruction rate of the combined system at a heating demand of 2 MW is 4525 kW, which decreases to 4157 kW at a heating demand of 8 MW. Conversely, the exergy destruction rate of the separated system is 4650 kW at 2 MW and decreases to 4369 kW at 8 MW. As shown in the figure, the exergy destruction rate decreases in both the separated and combined systems with an increase in heating demand. This occurs due to the lower mass flow rate of the ammonia-water solution in both systems. This reduction is a result of the increasing mass flow rate of geothermal hot water in the domestic heat exchanger to meet the heating demand. As explained in Figure 6.23, the exergy destruction rates across most components decrease as heating demand increases, leading to a reduction in the total exergy destruction rate and indicating improved efficiency at higher heating demands.

However, an exception to this trend is found in the domestic heat exchanger, where exergy destruction rates rise with increasing heating demands. As depicted in the Figure 6.31, the exergy destruction rate in the combined system is lower than in the separated system for all considered heating demands. This occurs due to the lower work required for fans and pumps and the higher net produced power in the combined system compared to the separated system.

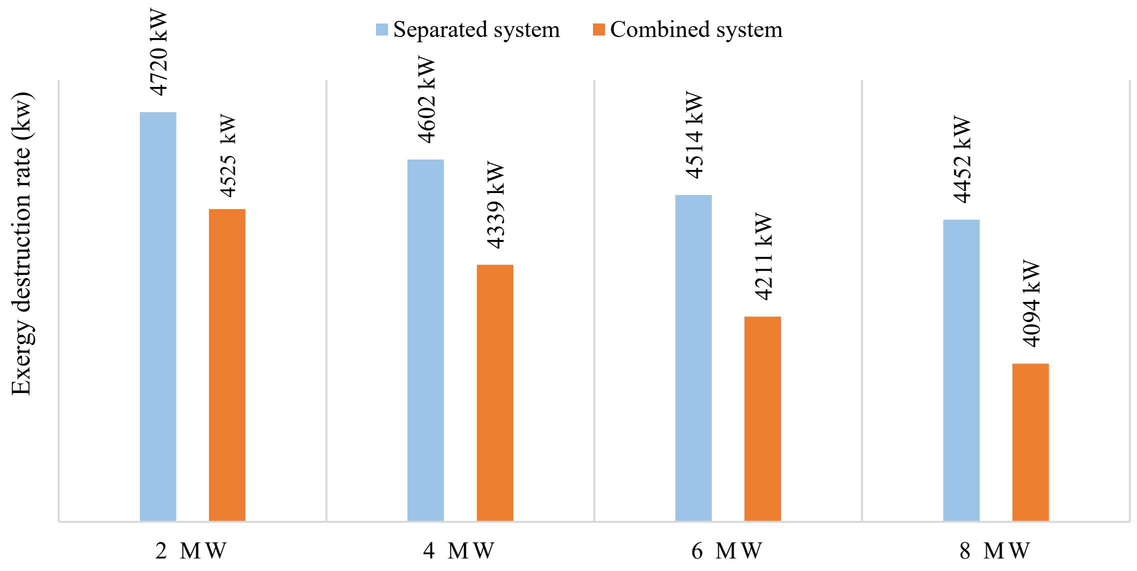

Figure 6.31: Comparison of exergy destruction rates across various heating demands during summer days ($T_0 = 20\,°C, \dot{Q}_C = 4$ MW)

6.4.2.2 Variation in ambient temperature: summer days

Figure 6.32 illustrates the variation in exergy efficiency with different ambient temperatures for separated and combined systems operating under off-design conditions. The systems are operating with a heating demand of 2 MW and a cooling demand of 4 MW during summer days. At the lowest reported ambient temperature of 18 °C, the exergy efficiency in the separated and combined systems is approximately 34.5 % and 36.5 %, respectively. As the ambient temperature increases, the exergy efficiency decreases in both systems. However, in the ambient temperature reaches 23.5 °C, the exergy efficiency of the combined system remains higher than that of the separated system. Further increasing the ambient temperature from 23.5 °C to 30 °C results in higher exergy efficiency values for the separated system compared to the combined system.The causes of this reduction in exergy efficiency in both systems with varying ambient temperatures are explained in Figure 6.33.

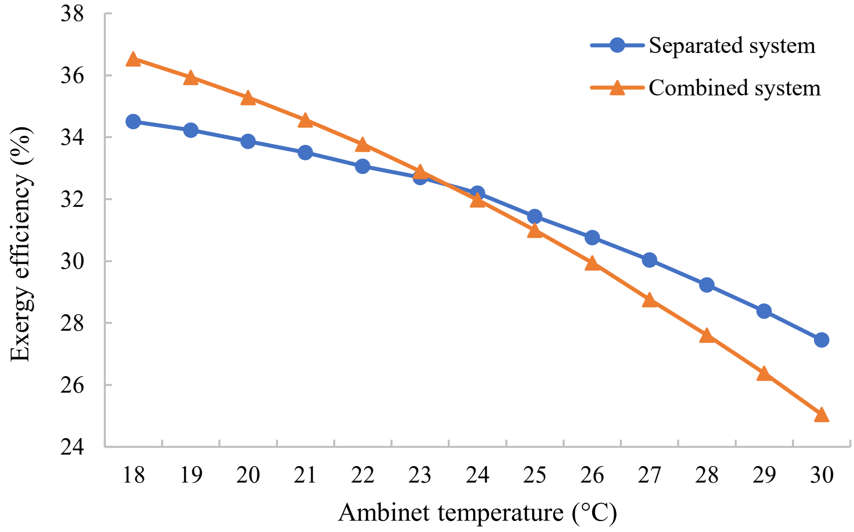

Figure 6.32: The impact of varying ambient temperature on exergy efficiency under off-design conditions during summer days ($\dot{Q}_H = 2$ MW, $\dot{Q}_C = 2$ MW)

Figure 6.33 (a) shows a decline in net produced power as the ambient temperature increases in both the separated and combined systems. However, the net produced power in the combined system is higher at all ambient temperatures compared to the separated system. This decline is attributed to an increase in turbine back pressure, leading to a reduction in turbine specific work and net produced power. Additionally, the heating exergy of the system decreases with increasing ambient temperature due to varying dead state temperature (T_{dead}), and the heating exergy is the same in both systems. Furthermore, the cooling exergy in the separated system remains almost constant at 235 kW, while the cooling exergy in the combined system decreases from 216.5 kW at 18 °C to 142 kW at 30 °C. Variations in ambient temperature also decrease the input exergy rate of both systems, as shown in Figure 6.30(b). This occurs due to the varying dead state temperature. As illustrated in Figure 6.33(b), the input exergy of the combined system is lower than that of the separated system as the ambient temperature increases until 22 °C. Beyond this temperature, the input exergy of the separated system becomes higher than that of the combined system. This is due to the higher exergy rate of the reinjection geothermal hot water stream in the combined system up to 22 °C compared to the separated system. As a result, while net produced power, input exergy, heating exergy, and cooling exergy decrease with increasing ambient temperature, the exergy efficiency initially increases. Additionally, because of the lower input exergy rate in the combined system compared to the separated system until 22 °C, the exergy efficiency in the combined system is higher at ambient temperatures lower than 23.5 °C.

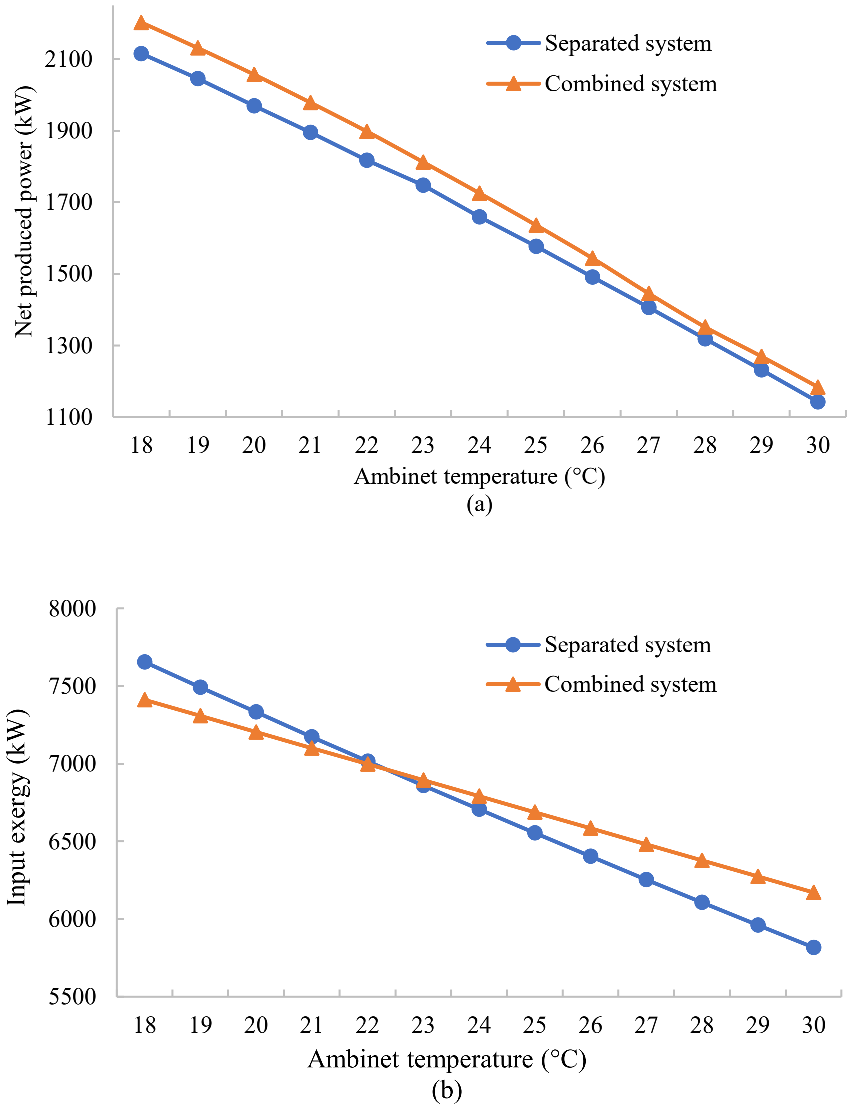

Figure 6.33: The impact of varying ambient temperature on (a) net produced power and (b) input exergy under off-design condition during summer days ($\dot{Q}_H = 8$ MW, $\dot{Q}_C = 2\ MW$)

In Figure 6.34, the impact of ambient temperature on the total exergy destruction rate of both separated and combined systems is depicted during summer, under off-design conditions with a heating demand of 2 MW and a cooling demand of 4 MW. As the ambient temperature increases from 18 °C to 30 °C, the total exergy destruction rate in the separated system decreases from 4952 kW to 4068 kW. In the combined system, it decreases from 4582 kW at 18 °C to 4429 kW at 30 °C. As described in Figure 6.33, the heating exergy, net produced power, and input exergy to the system decrease with rising ambient temperatures. Consequently, according to Equation (5.28), the total exergy destruction rate decreases with an increase in ambient temperature. Additionally, due to the lower input exergy until 22 °C in the combined system compared to the separated system, the exergy destruction rate in the combined system is higher than in the separated system at ambient temperatures lower than 23.5 °C.

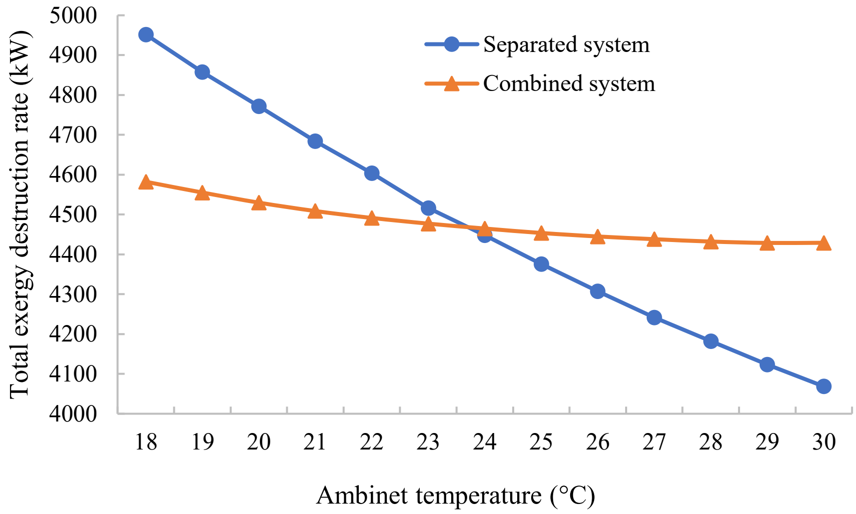

Figure 6.34: The impact of varying ambient temperature on total exergy destruction rate under off-design condition during summer days ($\dot{Q}_H = 8$ MW, $\dot{Q}_C = 2$ MW)

6.5 Annual Simulation

To analyze the system performance annually under various weather conditions, simulations for both design and off-design scenarios, reflecting different demands as specified in Table 5.7, were conducted. These simulations encompass a wide range of climatic variations to understand the system's robustness and efficiency across different scenarios. By incorporating both typical and extreme weather conditions, the study aims to identify potential weaknesses and areas for improvement. Additionally, this thorough examination helps in forecasting the behavior of the system under future climatic trends, ensuring long-term sustainability and reliability.

6.5.1 Design conditions

Figure 6.35 demonstrates the net power generation, heating, and cooling exergies for both separate and combined systems across various ambient temperatures under design conditions, along with the corresponding heating and cooling demands listed in Table 5.7.
The data in Figure 6.35 shows that heating exergy values increase with higher heating demands, peaking at 12 MW. For a heating demand of 12 MW, the heating exergy reaches 2549 kW at an ambient temperature of -6 °C and 2342 kW at 0 °C. The lowest heating exergy is observed in summer due to decreased heating demand, with a minimum of 275.4 kW at 20 °C. The maximum net produced power of 3719 kW is achieved at a heating demand of 5.8 MW and an ambient temperature of 5 °C, whereas in summer, it falls to a minimum of 2518 kW at 20 °C. Increased heating demand leads to a reduction in system part load because more geothermal mass flow rate is diverted to the domestic heat exchanger, reducing the flow to the Kalina cycle,

thereby decreasing turbine mass flow rate and net produced power. Additionally, cooling exergy rises with increased heating demand.

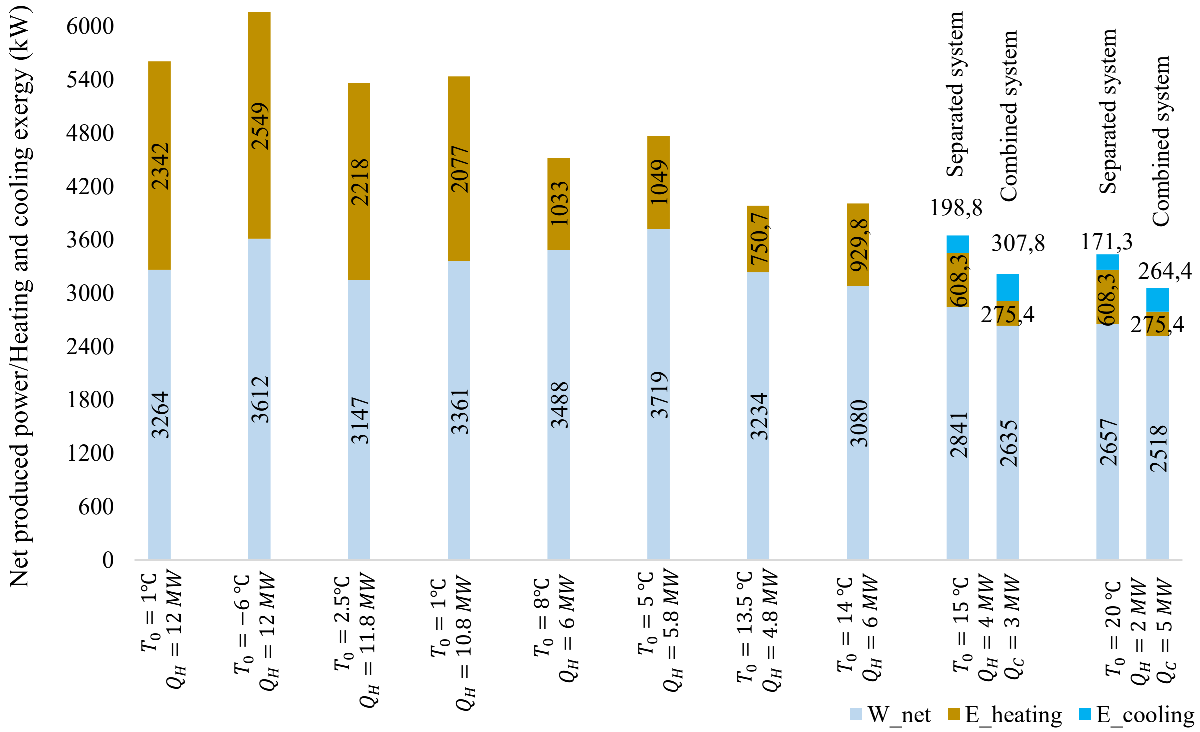

Figure 6.35: Net produced power, heating, and cooling exergies of the separated and combined systems according to different annual ambient temperature, heating, and cooling demand in Table 5.7 (under design conditions)

6.5.2 Off-design conditions

Figure 6.36 illustrates the net produced power, heating, and cooling exergies for both separated and combined systems under off-design condition at various ambient temperatures, as well as the corresponding heating and cooling demands outlined in Table 5.7.

As shown in Figure 6.36, heating exergy values are higher when heating demand is greater, reaching its peak of 12 MW. Specifically, at a heating demand of 12 MW, the heating exergy is higher at an ambient temperature of -6 °C (2549 kW) compared to 0 °C (2342 kW). The lowest heating exergy occurs during summer due to reduced heating demand, with a minimum of 275.4 kW at 20 °C. The net produced power reaches its maximum value of 2375 kW at a heating demand of 5.8 MW and an ambient temperature of 5 °C, operating at a part load of 80 %. This part load represents the ratio of net produced power in off-design mode to that in on-design mode. During summer, net produced power decreases, hitting a minimum of 1578 kW at 20 °C, with the system operating at part loads of 63 % to 69 %. Increased heating demand reduces the part load of the system due to more geothermal mass flow rate being directed to the domestic heat exchanger, thereby decreasing the flow to the Kalina cycle and subsequently reducing turbine mass flow rate and net produced power. Additionally, cooling exergy increases with higher ambient temperatures, with a maximum cooling exergy of 300 kW at 20 °C.

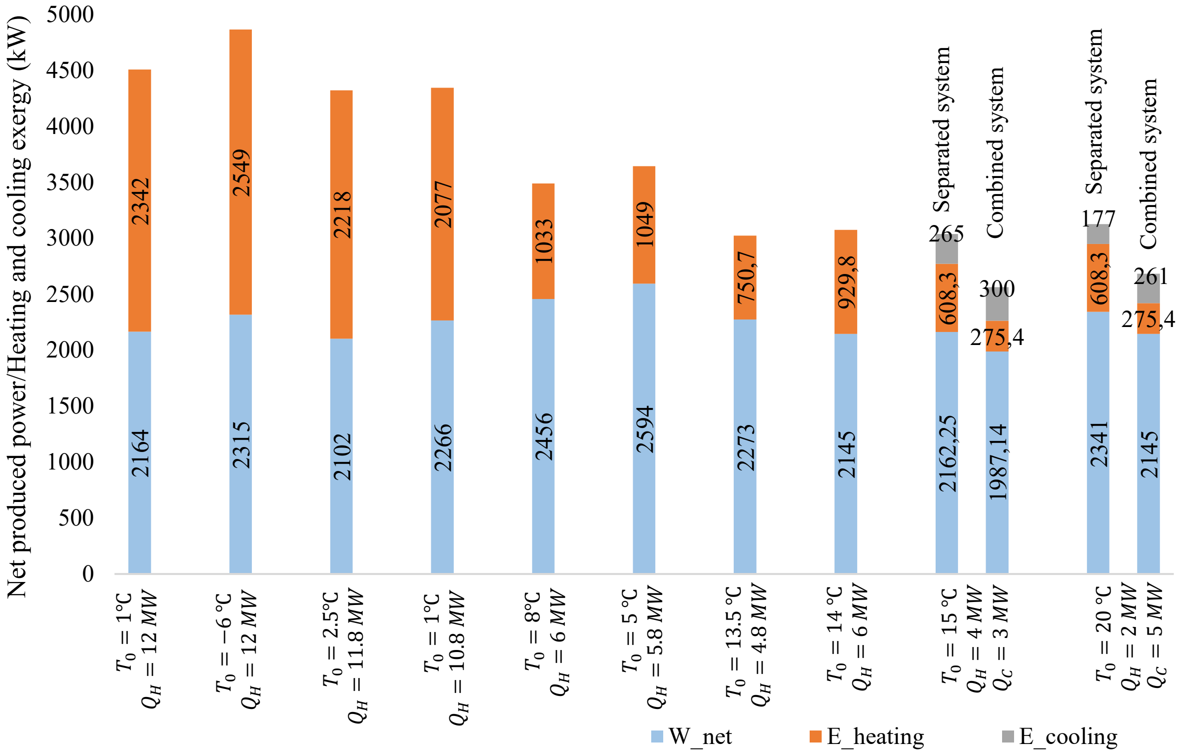

Figure 6.36: Net produced power, heating, and cooling exergies of the separated and combined systems according to different annual ambient temperature, heating, and cooling demand in Table 5.7 (under off-design conditions)

6.6 Economic results

As mentioned, the successful performance of a thermal design project hinges on the accurate estimation of significant financial factors such as the total capital investment, operating and maintenance expenses, and the cost of final products. These estimations are made within the context of economic, technological, and legal parameters and are informed by principles of engineering economics. This chapter delves into the economic aspects critical for (a) assessing capital investment costs, (b) determining the costs of main products under practical assumptions like discount, escalation, and inflation rate for the tri-generation system, and (c) appraising the financial attractiveness of various investment options.

6.6.1 Economic considerations

Table 6.17 provides the purchase costs of various components used in both separated and combined systems, with these costs being aligned with the areas of different heat exchangers as detailed in Table 6.12. Within the Kalina cycle, the condenser occurs as the most expensive component, reflecting its substantial role in the efficiency and operation of the system. On the other hand, the pump represents the least expensive investment, indicating a smaller proportion of the overall costs. Similarly, in the absorption refrigeration cycle, across both separated and combined systems, the condenser holds the greatest price, underscoring its significance in the cooling process. As with the Kalina cycle, the pump within the absorption cycle accounts for the smallest share of the total investment cost.

It is notable that the heat exchangers, essential for transferring heat within the system, vary in cost, potentially reflecting differences in their sizes, the complexity of their design, or the materials required for their construction. These costs give an indication of the capital required to establish such a system, and they serve as a baseline for evaluating the economic feasibility pf the system. The investment in these components is a critical factor in the overall financial model and will directly influence the levelized cost of electricity and the return on investment for the tri-generation system.

Table 6.17: The purchased costs of all components in both separated and combined systems

	Purchase cost ($)
Heating section	
Domestic heat exchanger	31,419
Power section	
Boiler	63,073
Pre-boiler	19,860
Internal heat exchanger	19,986
Kalina cycle condenser	727,445
Turbine	313,439
Kalina cycle pump	12,921
Fan of the Kalina cycle condenser	9563
Cooling section	
Generator	87,773
Dephlegmator	29,497
Solution heat exchanger	12,679
ARC condenser	653,350
Absorber	349,570
Evaporator	176,903
ARC pump	7409
Fans in cooling section	33,919

The necessary assumptions for simplifying the mathematical model of economic evaluation are outlined in Table 6.18. Additionally, the costs of separators, mixers, and expansion valves are disregarded. As mentioned in Table 5.7, the number of winter days, defined as days when the ambient temperature is below 15 °C, is 279 days, totaling 6696 hours. In contrast, the number of summer days, when the ambient temperature exceeds 15 °C, is 86 days, totalling 2064 hours. According to Table 6.18, the discount rate, escalation rate, and inflation rate are assumed to be 7 %, 2 %, and 1.2 %, respectively. The lifetime of the investment is 30 years; however, the first 2 years are allocated for construction.

Table 6.18: Economic modeling assumption

Parameters		Value
Drilling cost	$C_{drilling}$	20 M$
Heating price	$c_{heating}$	0.08 $/kWh
Cooling price	$c_{cooling}$	0.12 $/kWh
Annual hours of operation (winter days)	$t_{op,winter}$	6696 h
Annual hours of operation (summer days)	$t_{op,summer}$	2064 h
Discount rate [30]	i_d	7 %
Escalation rate [30]	i_c	2 %
Inflation rate [30]	i_i	1.2 %
Lifetime of investment	n	30 years

6.6.2 Analysing variation in design operational parameters

The effect of pinch point temperature difference in the boiler on the levelized cost of electricity (LCOE) is illustrated in Figure 6.37 for both separated and combined systems. As shown in the figure, the LCOE increases with an increase in the pinch point temperature difference in boiler ($\Delta T_{pp,BOI}$). In the separated system, the LCOE increases from 13.4 ¢/kWh at a $\Delta T_{pp,BOI}$ of 5 K to 18 ¢/kWh at a $\Delta T_{pp,BOI}$ of 20 K. However, in the combined system, the LCOE values are approximately 7 % lower than in the separated system.

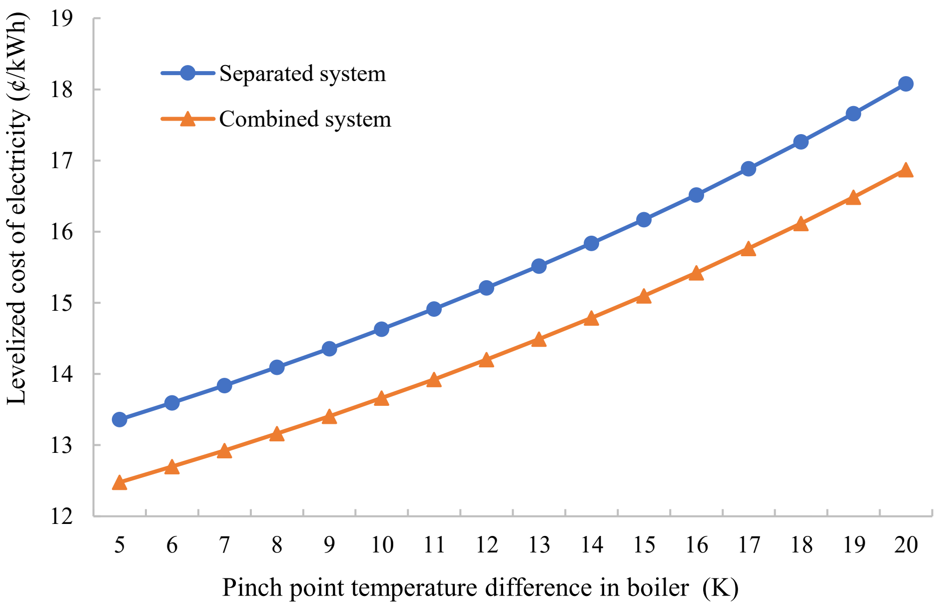

Figure 6.37: The influence of pinch point temperature difference in boiler on the levelized cost of electricity in combined versus separated systems

At a $\Delta T_{pp,BOI}$ of 5 K, the LCOE is 12.5 ¢/kWh in the combined system, and it increases to 17 ¢/kWh at a $\Delta T_{pp,BOI}$ of 20 K. The higher values of LCOE in the combined system are due to the higher values of net produced power in the combined system during summer days compared to the separated system. In winter days, both systems have the same net produced power. Additionally, as mentioned in Figure 6.6, the net produced power decreases with an increase in $\Delta T_{pp,BOI}$. On the other hand, the total cost of the combined system is lower than the separated system due to the absence of a solution heat exchanger, resulting in an increase in LCOE with an increase in $\Delta T_{pp,BOI}$, according to equation (5.43).

The impact of pinch point temperature difference in the domestic heat exchanger ($\Delta T_{pp,DHE}$) on the levelized cost of electricity (LCOE) is depicted in Figure 6.38 for both separated and combined systems. As illustrated, the LCOE rises as the $\Delta T_{pp,DHE}$ increases. In the separated system, the LCOE climbs from 13.4 ¢/kWh at a $\Delta T_{pp,DHE}$ of 5 K to 14.4 ¢/kWh at a $\Delta T_{pp,DHE}$ of 20 K. In contrast, the LCOE values in the combined system are approximately 7 % lower than those in the separated system. At a $\Delta T_{pp,DHE}$ of 5 K, the LCOE is 13 ¢/kWh in the combined system, increasing to 14 ¢/kWh at a $\Delta T_{pp,DHE}$ of 20 K. Although the net produced power in summer days is 2 % higher in the separated system compared to the combined system, the higher total cost of the separated system results in the LCOE being about 3 % lower in the combined system across all $\Delta T_{pp,DHE}$ values. In winter days, when the cooling section is not operational, both systems produce the same net power. Additionally, as noted in Figure 6.11, the net produced power decreases as $\Delta T_{pp,DHE}$ increases, leading to a corresponding increase in LCOE as indicated by equation (5.43).

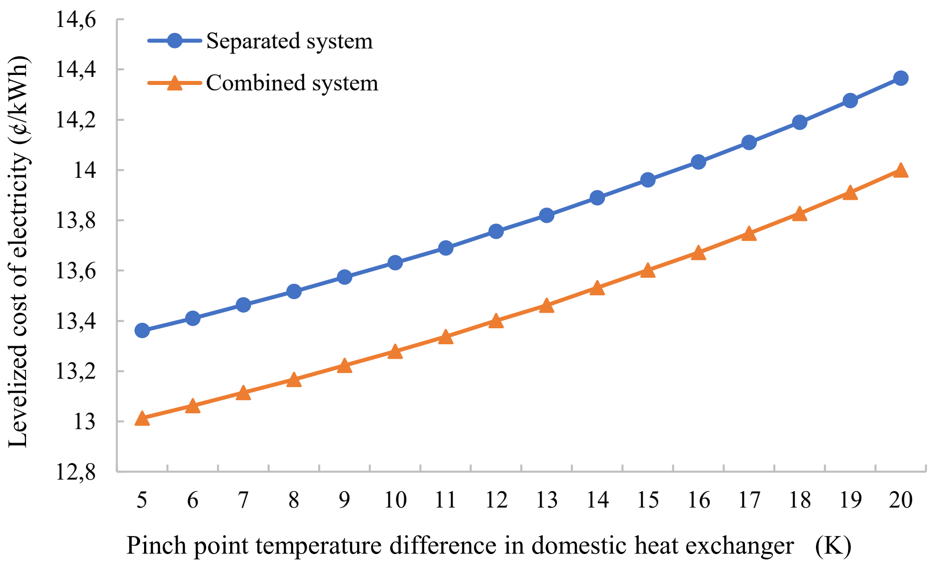

Figure 6.38: The influence of pinch point temperature difference in domestic heat exchanger on the levelized cost of electricity in combined versus separated systems

The impact of pinch point temperature difference in the condenser of the Kalina cycle ($\Delta T_{pp,CON\_KC}$) on the levelized cost of electricity (LCOE) is depicted in Figure 6.39 for both separated and combined systems. As illustrated, the LCOE rises as the $\Delta T_{pp,CON\_KC}$ increases. Additionally, as noted in Figure 6.14, the net produced power decreases as $\Delta T_{pp,CON\_KC}$ increases, leading to a corresponding increase in LCOE as indicated by equation (5.43). As indicated in the figure, the LCOE in both separated and combined systems is almost the same. In both systems, the LCOE climbs approximately from 12 ¢/kWh at a $\Delta T_{pp,CON\_KC}$ of 5 K to 16 ¢/kWh at a $\Delta T_{pp,CON\_KC}$ of 20 K. However, the net produced power in summer days is almost 18 % higher in the separated system compared to the combined system. The higher total cost of the separated system results in almost the same LCOE for both systems.

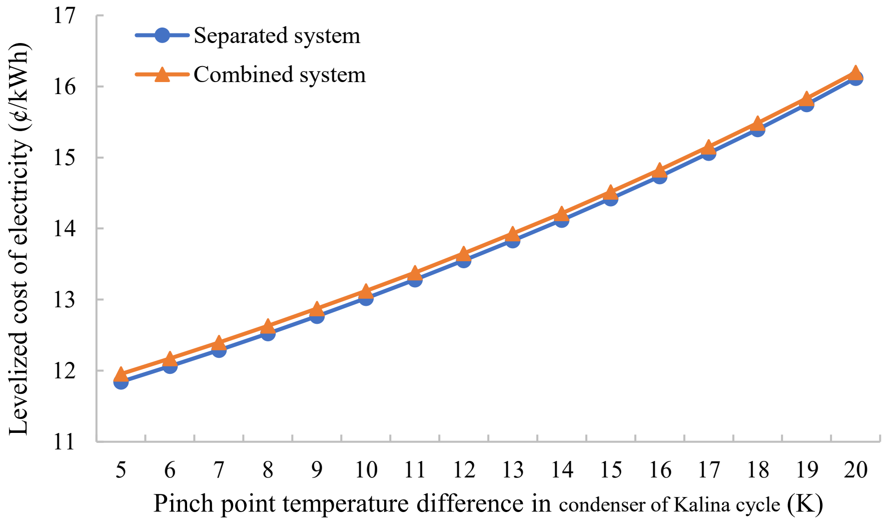

Figure 6.39: The influence of pinch point temperature difference in condenser of Kalina cycle on the levelized cost of electricity in combined versus separated systems

The net produced power, which is used to evaluate the levelized cost of electricity in the variation of the $\Delta T_{pp,BOI}$, $\Delta T_{pp,DHE}$, and $\Delta T_{pp,CON\_KC}$, is considered under design conditions. This means that the power output calculations are based on the intended operational parameters of the system which are shown in Table 5.8.

6.6.3 Analysing variation in supply heating and geothermal temperatures

The influence of supply heating temperature (T_{15}) on the levelized cost of electricity is illustrated in Figure 6.40 for both separated and combined systems. As indicated in the figure, the LCOE increases in both systems as the heating supply temperature rises. This happens because the net produced power decreases with an increase in T_{15}. When T_{15} increases, a larger portion of the geothermal hot water mass flow rate is directed to the domestic heat exchanger to meet the heating demand at the required temperature of T_{15}. Consequently, the portion of geothermal hot water mass flow rate directed to the Kalina cycle decreases. This reduction in mass flow rate results in a decrease in turbine mass flow rate, leading to a reduction in net produced power. According to equation (5.43), with a reduction in net produced power, the LCOE increases. In addition, Figure 6.40 shows that the LCOE in the combined system is lower at all values of supply heating temperature compared to the separated system. This is due to the higher net produced power in the combined system and the lower total investment cost, as the combined system lacks a solution heat exchanger compared to the separated system.

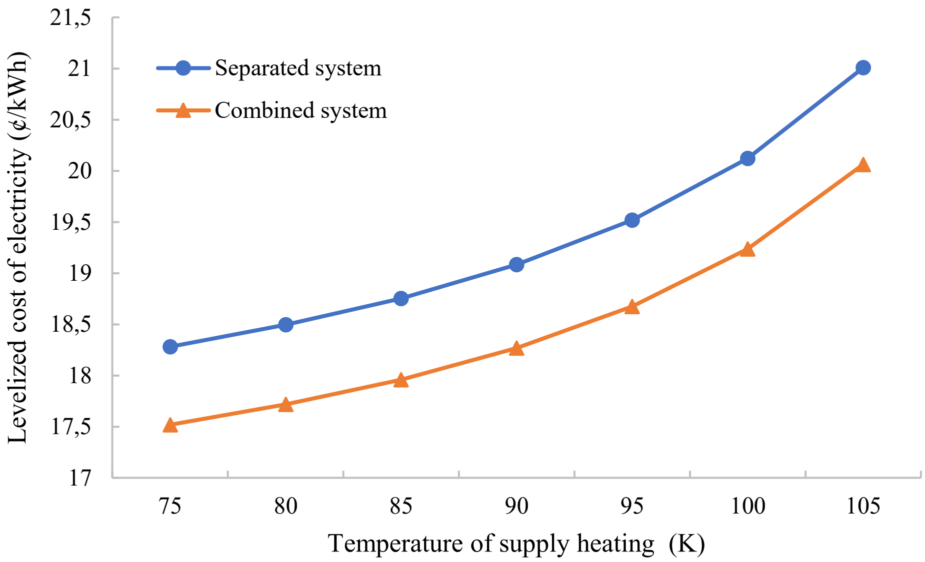

Figure 6.40: The effect of heating supply temperature (T_{15}) on the levelized cost of electricity in combined and separated systems

The influence of geothermal hot water temperature (T_{16}) on the levelized cost of electricity is shown in Figure 6.41 for both separated and combined systems. As shown in the figure, the LCOE decreases in both systems as the geothermal hot water temperature increases. In both systems, the LCOE drops from approximately 37 ¢/kWh at a T_{16} of 120 °C to 14 ¢/kWh at a T_{16} of 20 °C. This occurs because the net produced power increases as T_{16} rises. When T_{16} increases, a smaller portion of the geothermal hot water mass flow rate is directed to the domestic heat exchanger to meet the heating demand at the required supply heating temperature of 90 °C. Consequently, the portion of geothermal hot water mass flow rate directed to the Kalina cycle increases. This increase in mass flow rate leads to a higher turbine mass flow rate, resulting in a rise in net produced power. According to equation (5.43), with an increase in net produced power, the LCOE decreases. In addition, Figure 6.41 demonstrates that the LCOE in the combined system is approximately 4 % lower across all geothermal hot water temperature values compared to the separated system. This advantage is attributed to the higher net produced power in the combined system and the lower total investment costs, as it does not require a solution heat exchanger, unlike the separated system.

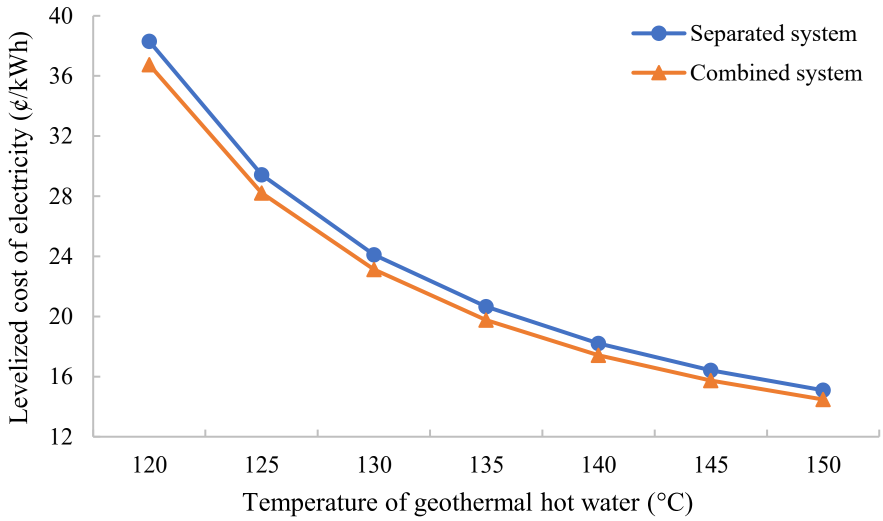

Figure 6.41: The effect of geothermal hot water temperature (T_{16}) on the levelized cost of electricity in combined and separated systems

6.6.4 Analysing variation in drilling cost

Figure 6.42 illustrates the variations in the levelized cost of electricity with the drilling cost for both separated and combined systems. The LCOE increases with rising drilling costs in both separated and combined systems. As drilling costs rise, the total investment cost increases according to equation (5.29). Consequently, maintenance and operation costs also escalate, resulting in a higher LCOE. In addition, the LCOE in the combined system is lower than in the separated system across all drilling cost values. This difference is due to the higher net produced power in the combined system. The greater electricity output in the combined system results in lower overall costs, making it a more economical option compared to the separated system.

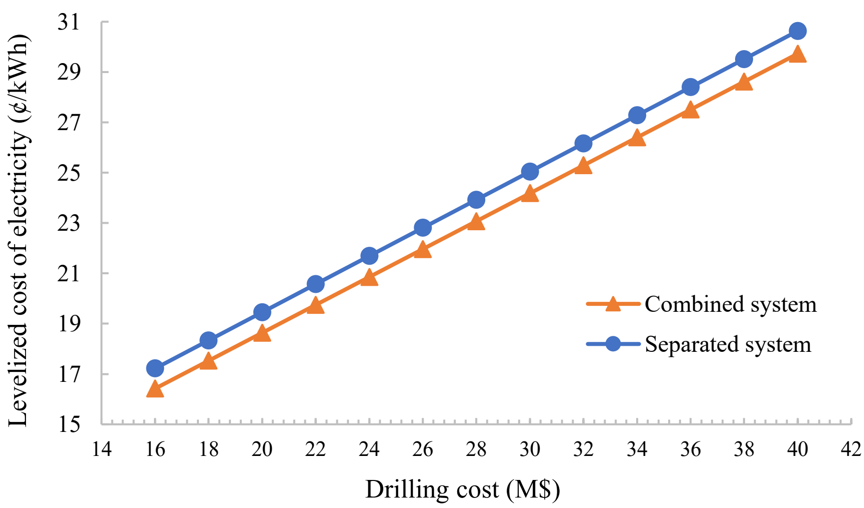

Figure 6.42: The influence of drilling cost on the levelized cost of electricity in combined versus separated systems

6.6.5 Analysing variation in discount and escalation rates

The comparative analysis of net present value (NPV) against discount rates for both separated and the combined systems, is illustrated in Figure 6.43. NPV is a critical financial metric utilized to evaluate the profitability of investments, with a positive NPV indicating a favourable return and a negative NPV suggesting a deficit when comparing projected earnings against costs. As observed, when the discount rate increases, the NPV decreases for both the combined and the separated systems, reflecting the time value of money principle, where future cash flows become less valuable when discounted at higher rates. This decrease in NPV is due to the fact that a higher discount rate implies a greater opportunity cost of capital and a higher perceived risk, leading to a more substantial reduction in the present value of future cash flows. Additionally, the point at which the NPV becomes zero is important, as it signifies the break-even discount rate beyond which the return of the investment does not justify the risk. For both separated and combined system, this occurs at approximately a 12 % discount rate, beyond which the NPV becomes negative, indicating that the cost of the investment outweighs the present value of its future cash flows and rendering it financially unworkable. Furthermore, the sensitivity of the NPV to discount rates plays a pivotal role in assessing the financial resilience of the tri-generation systems. The slower rate of NPV decline, as the discount rate increases, suggests a lower sensitivity to interest rate fluctuations, indicating a more robust and less risky investment compared to the separated system. This characteristic is particularly valuable in environments of economic volatility, where discount rates can fluctuate significantly.

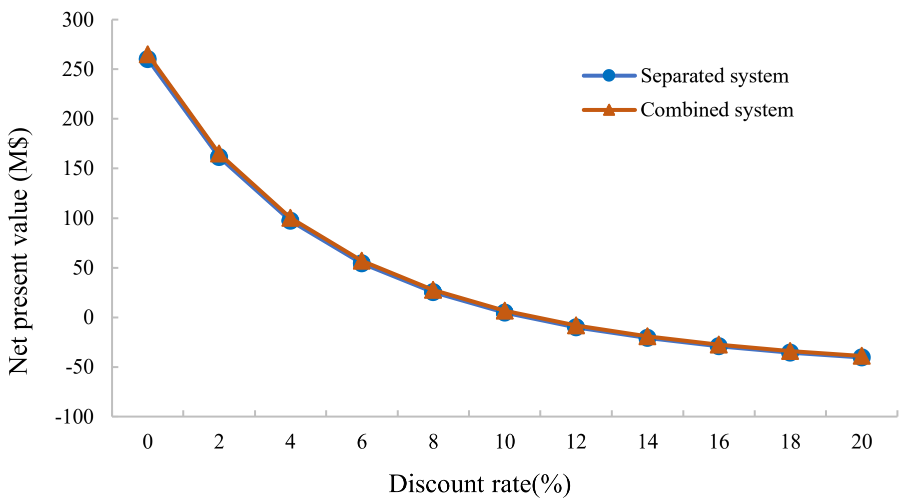

Figure 6.43. Comparison of net present value for combined versus separated systems at varying discount rates.

Figure 6.44 displays a comparative assessment of the net present values for both combined and separated systems over various escalation rates ranging from -5 % to +5 %. At the beginning of the scale with an escalation rate of -5 %, the separated system is shown to have a negative

NPV. This outcome suggests that, under the conditions where costs are forecasted to decrease over the investment period, the future cash flow generated by the separated system would not be sufficient to recover the initial capital outlay, leading to a potential financial loss. As the escalation rate rises, there is an observable improvement in the NPV for both separated and combined systems, which crosses from negative to positive around the -2 % mark. This transition to positive NPV indicates a turning point where both systems begin to yield a financial return, suggesting that it becomes a viable investment when the rate at which costs increase, or decrease is minimal. The improvement in NPV as the escalation rate moves towards zero implies that the financial performance of systems is sensitive to cost escalation rates, and it benefits from conditions where the costs are either stable or exhibit a slight upward trend. The trend of NPV turning positive before reaching a 0 % escalation rate also reflect the capacity of the system to adapt to modest increases in operational costs without significantly undermining profitability.

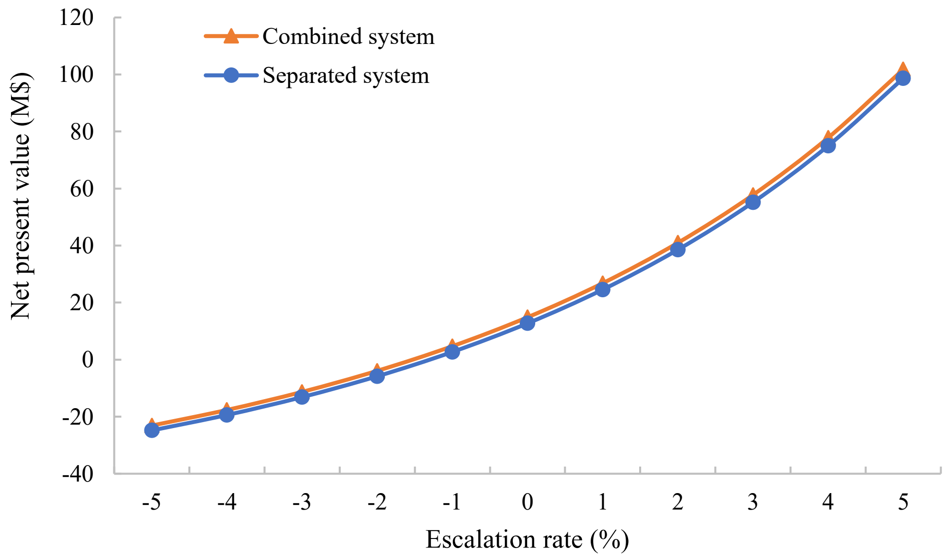

Figure 6.44. Comparison of net present value of the combined versus separated systems at varying escalation rates.

7 Summary

In an effort to stop climate change, the energy sector is increasingly turning to renewable resources. In Germany, where a substantial amount of energy consumption is attributed to heating and cooling, there is a growing need for renewable and sustainable heat generation methods alongside electricity. Geothermal reservoirs present a promising solution, capable of providing heating, cooling, and power. Particularly, systems that can flexibly harness geothermal resources are crucial for efficient energy utilization.

This research explores various concepts of geothermal heat and power plants, examining their thermodynamic and economic performance. Annual simulations, based on typical days as per the VDI 4655 guideline, have been conducted. These days are categorized by time of year, user behavior, and cloud cover. Heat demand profiles for the district heating network are formulated using data from an existing geothermal heat plant in southern Germany, incorporating the real daily fluctuating heat demands of the plant.

For electricity generation, the study focuses on a Kalina Cycle modeled after an operational power plant in the southern German Molasse Basin, with a particular focus on plant operation under variable loads, assuming quasi-stationary. Additionally, an absorption refrigeration system is considered for meeting cooling demands, with calculations made to determine these requirements.

The model established in this study facilitates a comprehensive analysis of geothermal heating and power generation. The following summarizes the findings in response to the research questions posed by this study.

i. How does the net produced power of tri-generation systems respond to changes in the pinch point temperature differences in the heat exchangers during winter days under design condition?

Under winter conditions with an ambient temperature of 8 °C and a heating demand of 8 MW, the net produced power decreases as the pinch point temperature difference in the boiler increases, due to the reduced turbine mass flow rates.

Additionally, increasing the pinch point temperature difference in the domestic heat exchanger ($\Delta T_{pp,DHE}$) also reduces net produced power, dropping from 3363 kW at a $\Delta T_{pp,DHE}$ of 5 K to 3125 kW at 20 K.

Furthermore, the net produced power declines with an increase in the pinch point temperature difference in the condenser of the Kalina cycle ($\Delta T_{pp,CON\_KC}$), falling from 3588 kW at the $\Delta T_{pp,CON\_KC}$ of 5 K to 2632 kW at 20 K.

ii. How do the exergy efficiency, net produced power, and part load performances of tri-generation systems respond to changes in heating demand during winter days under off-design condition, and what is the underlying reason for this variation?

In the context of winter conditions with an ambient temperature of 8 °C, the exergy efficiency of the system is observed to increase with rising heating demand. As the heating demand increases from 5 MW to 20 MW, there is an increase in exergy efficiency, which is calculated based on the useful energy that can be harnessed from the system compared to the energy put into it. Within a 5 MW heating demand, the exergy efficiency is recorded at around 48 %. As the demand escalates to 10 MW, the efficiency improves, reaching approximately 53 %. The trend continues upward, with the efficiency climbing to around 56 % at a 15 MW heating demand. The highest point is observed at a 20 MW heating demand, where the exergy efficiency peaks just above 58 %. This efficiency growth is directly linked to the performance of the domestic heat exchanger within the system. As the heating demand rises, the heat exchanger operates more effectively due to an increased mass flow rate of geothermal hot water. The larger the demand, the greater the mass flow rate through the domestic heat exchanger, leading to more optimized heat transfer processes. Consequently, a higher proportion of the geothermal resource is converted into usable heat, thereby improving the exergy efficiency of the system.

Regarding net produced power, when the heating demand is at 5 MW, the net power output is about 2538 kW. As the heating demand rises to 10 MW, the net produced power falls to roughly 2078 kW. This decreasing pattern persists, with net produced power reducing to around 1481 kW at a 15 MW heating demand. The lowest net power output occurs at a 20 MW heating demand, where it is slightly above 750 kW. This reduction in net produced power occurs due to a decrease in the proportion of geothermal heat source water directed to the Kalina cycle.

Considering part load, the part load of the system decreases as heating demand rises. Initially operating near peak efficiency (around 80 %) at 5 MW, the part load drops significantly at higher demands, reaching its lowest at 20 MW. This decline is due to the reallocation of geothermal water from the Kalina cycle to the domestic heat exchanger.

iii. How do the exergy efficiency, net produced power and part load performances of tri-generation systems respond to changes in heating demand during summer days under off-design condition, and what could be the underlying reason for this variation?

In response to changes in heating demand during summer days with an ambient temperature of 20 °C, the exergy efficiency of both separated and combined heating systems increases as the heating demand rises. When the heating demand grows from 2 MW to 8 MW, there is a corresponding increase in exergy efficiency for both systems. This improvement in exergy efficiency is linked to the increase in heating exergy produced by the domestic heat exchanger as the heating demand grows. Additionally, the combined system not only shows an increase in exergy efficiency with higher heating demands but also consistently maintains higher efficiency compared to the separated system at each level of demand. These higher exergy efficiencies are attributed to variations in operational parameters, such as pinch point temperature differences and mass flow rates across different components.

Regarding net produced power, as heating demand increases, the net produced power decreases due to a smaller portion of the geothermal heat source water being allocated to the Kalina cycle. In both the separated and combined systems, the mass flow rate of geothermal hot water to the Kalina cycle decreases from 112 kg/s at 2 MW to 88 kg/s at 8 MW.

Considering part load, as the heating demand rises, the part load percentage in both systems decreases. Across various heating demand levels, the part load percentage of the combined system remains consistently higher than that of the separated system.

iv. How does the total exergy destruction rate of tri-generation systems respond to changes in heating demand during winter and summer days under off-design condition?

As heating demand increases during winter days with an ambient temperature of 8 °C from 5 MW to 20 MW, the exergy destruction rate decreases from 3558 kW at a 5 MW heating demand to 2984 kW at a 20 MW heating demand. In winter, the boiler exhibits a higher exergy destruction rate at part loads of 5 MW and 10 MW. However, at heating demands of 15 MW and 20 MW, the domestic heat exchanger accounts for the largest portion of the exergy destruction rate. In the domestic heat exchanger, the exergy destruction rate increases with rising heating demands due to the increased mass flow rate of geothermal water through the exchanger. Except for the domestic heat exchanger, the exergy destruction rate in other components decreases with an increase in heating demand.

In summer days with an ambient temperature of 20 °C, the exergy destruction rate decreases in both separated and combined systems as heating demand increases from 2 MW to 8 MW. This decrease is attributed to the lower mass flow rate of the ammonia-water solution in both systems. The reduction in mass flow rate is a result of the increasing mass flow rate of geothermal hot water in the domestic heat exchanger to meet the rising heating demand. Additionally, the exergy destruction rate in the combined system is lower than in the separated system for all considered heating demands. This is because the combined system requires less work for fans and pumps and has higher net produced power compared to the separated system.

v. How do ambient temperature variations affect the exergy efficiency of tri-generation systems during different seasonal conditions under off-design condition, and what are the observed net produced power trends for tri-generation systems in both winter and summer days?

For winter conditions with an ambient temperature of 8 °C, the exergy efficiency is 52.5 % at the lowest reported ambient temperature of -10 °C. The exergy efficiency rises to a local optimum value of 54 %, as the ambient temperature increases to -1 °C. Further increasing the ambient temperature to 16 °C results in a decrease in efficiency, reaching about 47 %. In addition, during winter days, there is a decline in net produced power as the ambient temperature increases. This occurs due to an increase in turbine back pressure, which reduces turbine specific work and net produced power.

In summer days with an ambient temperature of 20 °C, as the ambient temperature increases, the exergy efficiency decreases in both systems. However, until the ambient temperature reaches 23.5 °C, the exergy efficiency of the combined system remains higher than that of the separated system. Further increasing the ambient temperature from 23.5 °C to 30 °C results in higher exergy efficiency values for the separated system compared to the combined system. Additionally, the net produced power decreases with an increase in ambient temperature during summer days. However, the net produced power in the combined system is higher at all ambient temperatures compared to the separated system.

vi. How does the total exergy destruction rate of tri-generation systems respond to changes in ambient temperature during winter and summer days under off-design condition?

Under winter conditions with heating demand of 8 MW, the total exergy destruction rate decreases from 3907 kW at an ambient temperature of -10 °C to a local minimum of 3427 kW at an ambient temperature of 8 °C. However, when the ambient temperature is further increased to 16 °C, the exergy destruction rate rises again, reaching 3468 kW. In the Kalina cycle condenser, exergy losses are reduced due to lower temperature gradients and irreversibilities.

Under summer conditions with heating demand of 2 MW, as the ambient temperature rises from 18 °C to 30 °C, the total exergy destruction rate in the separated system decreases from 4952 kW to 4068 kW. In the combined system, it decreases from 4582 kW at 18 °C to 4429 kW at 30 °C.

vii. How does the levelized cost of electricity for tri-generation systems relate to the pinch point temperature differences in the heat exchangers?

The LCOE increases with the rise in the pinch point temperature difference in the domestic heat exchanger ($\Delta T_{pp,DHE}$). In addition, the LCOE is consistently lower in the combined system compared to the separated system for all $\Delta T_{pp,DHE}$ values.

The LCOE increases as the pinch point temperature difference in the condenser of the Kalina cycle ($\Delta T_{pp,CON\_KC}$) rises. The LCOE in both separated and combined systems is almost the same. In both systems, the LCOE climbs approximately from 12 ¢/kWh at a $\Delta T_{pp,CON\_KC}$ of 5 K to 16 ¢/kWh at a $\Delta T_{pp,CON\_KC}$ of 20 K.

viii. How does the levelized cost of electricity for tri-generation systems relate to the supply heating and geothermal hot water temperatures?

The LCOE increases in both systems as the heating supply temperature (T_{15}) rises due to a decrease in net produced power. As T_{15} increases, more geothermal hot water is directed to the domestic heat exchanger, reducing the flow to the Kalina cycle and decreasing the turbine mass flow rate. This reduction in power leads to a higher LCOE. Additionally, the combined system consistently has a lower LCOE than the separated system at all supply heating temperatures. The LCOE decreases in both systems as the geothermal hot water temperature (T_{16}) increases. It drops from around 37 ¢/kWh at a T_{16} of 120 °C to 14 ¢/kWh at a T_{16} of 20 °C. This reduction occurs because the net produced power increases with higher T_{16}. As T_{16} rises, less geothermal hot water mass flow rate is needed for the domestic heat exchanger to maintain the required supply heating temperature of 90 °C. Consequently, more geothermal hot water mass flow rate is directed to the Kalina cycle, increasing the turbine mass flow rate and net produced power. In addition, the LCOE in the combined system is approximately 4 % lower across all geothermal hot water temperature values compared to the separated system.

8 Zusammenfassung

Im Zuge der Bemühungen zur Eindämmung des Klimawandels setzt der Energiesektor zunehmend auf erneuerbare Ressourcen. In Deutschland, wo ein erheblicher Anteil des Energieverbrauchs auf Heizung und Kühlung entfällt, besteht ein wachsender Bedarf an nachhaltigen und erneuerbaren Wärmebereitstellungstechnologien neben der Stromerzeugung. Geothermische Reservoire bieten in diesem Zusammenhang eine vielversprechende Lösung, da sie in der Lage sind, Wärme, Kälte und Strom bereitzustellen. Insbesondere Systeme, die eine flexible Nutzung geothermischer Ressourcen ermöglichen, sind für eine effiziente Energienutzung von entscheidender Bedeutung.

Im Rahmen dieser Arbeit werden verschiedene Konzepte geothermischer Heizkraftwerke untersucht und hinsichtlich ihrer thermodynamischen sowie ökonomischen Leistungsfähigkeit bewertet. Auf Grundlage typischer Tage gemäß der VDI-Richtlinie 4655 wurden jahreszeitlich differenzierte Jahressimulationen durchgeführt. Diese typischen Tage berücksichtigen sowohl die Jahreszeit als auch das Nutzerverhalten und die Bewölkung. Die Wärmebedarfsprofile für das angeschlossene Fernwärmenetz basieren auf Daten einer bestehenden geothermischen Heizzentrale in Süddeutschland und spiegeln die realen, tageszeitlich schwankenden Wärmeanforderungen wider.

Für die Stromerzeugung konzentriert sich diese Arbeit auf einen Kalina-Kreislauf, der einem real betriebenen Kraftwerk im süddeutschen Molassebecken nachempfunden ist. Ein besonderer Fokus liegt auf dem Anlagenbetrieb unter variablen Lastbedingungen bei der Annahme quasistationärer Zustände. Darüber hinaus wird eine Absorptionskältemaschine zur Deckung des Kältebedarfs betrachtet; die entsprechenden Anforderungen werden rechnerisch ermittelt.

Das im Rahmen dieser Arbeit entwickelte Modell ermöglicht eine umfassende Analyse der geothermischen Wärme- und Stromerzeugung. Die folgenden Abschnitte fassen die Ergebnisse im Hinblick auf die in dieser Arbeit formulierten Forschungsfragen zusammen.

i. Wie reagiert die Netto-Stromerzeugung von Trigenerationssystemen auf Änderungen der Pinch-Point-Temperaturdifferenzen in den Wärmetauschern während Wintertagen unter Auslegungsbedingungen?

Unter Winterbedingungen mit einer Umgebungstemperatur von 8 °C und einem Wärmebedarf von 8 MW nimmt die Netto-Stromerzeugung mit zunehmender Pinch-Point-Temperaturdifferenz im Verdampfer ab. Dies ist auf die reduzierten Massenströme durch die Turbine zurückzuführen.

Darüber hinaus führt eine Erhöhung der Pinch-Point-Temperaturdifferenz im Haushaltswärmetauscher zu einer Reduktion der Netto-Stromerzeugung von 3363 kW bei 5 K auf 3125 kW bei 20 K.
Ferner sinkt die Netto-Stromerzeugung mit zunehmender Pinch-Point-Temperaturdifferenz im Kondensator des Kalina-Kreislaufs von 3588 kW bei 5 K auf 2632 kW bei 20 K.

ii. Wie reagieren die Exergieeffizienz, die Netto-Stromerzeugung und die Teillastleistung von Trigenerationssystemen auf Änderungen des Wärmebedarfs an Wintertagen unter Nicht-Auslegungsbedingungen, und was ist der zugrunde liegende Grund für diese Variation?

Unter Winterbedingungen mit einer Umgebungstemperatur von 8 °C zeigt sich, dass die Exergieeffizienz des Systems mit steigendem Heizwärmebedarf zunimmt. Bei einem Heizbedarf von 5 MW beträgt die Exergieeffizienz etwa 48 %. Mit einem Anstieg des Bedarfs auf 10 MW verbessert sich die Effizienz auf rund 53 %. Dieser Trend setzt sich fort. Bei 15 MW steigt die Effizienz auf etwa 56 % und erreicht bei einem Heizbedarf von 20 MW mit etwas über 58 % ihren Höchstwert. Diese Effizienzsteigerung ist direkt auf die verbesserte Leistungsfähigkeit des Haushaltswärmetauschers im System zurückzuführen. Mit zunehmendem Heizwärmebedarf erhöht sich der Massenstrom des geothermischen Heißwassers, wodurch der Wärmetauscher effektiver arbeitet. Ein höherer Massenstrom führt zu optimierten Wärmeübertragungsprozessen, sodass ein größerer Anteil der geothermischen Ressource in nutzbare Wärme umgewandelt werden kann. Dies wirkt sich positiv auf die Exergieeffizienz des Gesamtsystems aus. Bezüglich der Netto-Stromerzeugung zeigt sich ein gegenläufiger Trend. Bei einem Heizwärmebedarf von 5 MW liegt die Nettoleistung bei etwa 2538 kW. Bei 10 MW fällt sie auf etwa 2078 kW. Mit weiter steigendem Heizbedarf sinkt sie weiter, zunächst auf rund 1481 kW bei 15 MW und schließlich auf knapp über 750 kW bei 20 MW. Dieser Rückgang ist darauf zurückzuführen, dass mit wachsendem Heizbedarf ein größerer Anteil des geothermischen Heißwassers vom Kalina-Kreislauf abgezweigt und dem Haushaltswärmetauscher zugeführt wird. Dadurch steht dem Kreisprozess weniger Energie zur Verfügung. Der Teillastwirkungsgrad des Systems sinkt mit zunehmendem Heizwärmebedarf. Während das System bei einem Bedarf von 5 MW noch nahe an seiner maximalen Effizienz (etwa 80 %) arbeitet, sinkt die Teillastleistung bei höheren Wärmeanforderungen deutlich ab. Bei einem Heizbedarf von 20 MW erreicht sie ihren niedrigsten Wert. Auch diese Entwicklung ist auf die Umverteilung des geothermischen Heißwassers vom Kalina-Kreislauf zum Haushaltswärmetauscher zurückzuführen.

iii. Wie reagieren die Exergieeffizienz, die Netto-Stromerzeugung und das Teillastverhalten von Tri-Generationssystemen auf Veränderungen des Heizwärmebedarfs an Sommertagen unter Nicht-Auslegungsbedingungen, und was könnten die zugrunde liegenden Ursachen für diese Veränderungen sein?

Unter sommerlichen Bedingungen mit einer Umgebungstemperatur von 20 °C steigt die Exergieeffizienz sowohl bei getrennten als auch bei kombinierten Heizsystemen mit zunehmendem Heizwärmebedarf. Wenn der Heizbedarf von 2 MW auf 8 MW anwächst, ist bei beiden Systemen ein entsprechender Anstieg der Exergieeffizienz zu beobachten. Diese Verbesserung lässt sich auf den zunehmenden Exergieertrag des Haushaltswärmetauschers zurückführen, da mit wachsender Heizlast mehr exergiereiche Wärme bereitgestellt werden kann. Darüber hinaus zeigt das kombinierte System nicht nur eine Effizienzsteigerung bei höheren Heizwärmebedarfen, sondern weist auch durchgängig höhere Exergieeffizienzen auf als das getrennte System – und zwar auf allen untersuchten Lastniveaus. Diese Effizienzunterschiede sind auf unterschiedliche Betriebsparameter zurückzuführen, insbesondere auf abweichende Pinch-Point-Temperaturdifferenzen sowie Massenströme in den verschiedenen Systemkomponenten. Mit Blick auf die netto erzeugte elektrische Leistung zeigt sich ein entgegengesetzter Trend. Wenn der Heizbedarf steigt, nimmt die Netto-Stromerzeugung ab. Dies liegt daran, dass ein geringerer Anteil des geothermischen Heißwassers dem Kalina-Kreislauf zugeführt wird. In beiden Systemen sinkt der entsprechende Massenstrom von 112 kg/s bei einem Heizbedarf von 2 MW auf 88 kg/s bei 8 MW. Auch das Teillastverhalten verändert sich im Zuge des steigenden Heizwärmebedarfs. In beiden Systemen nimmt der Teillastanteil mit wachsender Last ab. Das kombinierte System weist jedoch auf allen Heizniveaus höhere Teillastanteile auf als das getrennte System, was auf eine insgesamt bessere Ausnutzung des thermischen Potenzials hinweist.

iv. Wie reagiert die gesamte Exergiedestruktionsrate von Trigenerationssystemen auf Veränderungen des Heizwärmebedarfs während Winter- und Sommertagen unter Nicht-Auslegungsbedingungen?

Während Wintertagen mit einer Umgebungstemperatur von 8 °C sinkt die Exergiedestruktionsrate mit steigendem Heizbedarf. Bei einem Heizbedarf von 5 MW beträgt die Rate etwa 3558 kW, während sie bei 20 MW auf etwa 2984 kW abnimmt. Im Winter zeigt der Verdampfer bei Teillastbedingungen von 5 MW und 10 MW die höchsten Exergieverluste. Bei Heizwärmebedarfen von 15 MW und 20 MW hingegen wird der größte Anteil der Exergiedestruktion im Haushaltswärmetauscher verzeichnet. Im Haushaltswärmetauscher steigt die Exergiedestruktionsrate mit wachsendem Heizbedarf an. Grund dafür ist der zunehmende Massenstrom des geothermischen Wassers, der durch den Tauscher fließt. In den übrigen Komponenten des Systems sinkt die Exergiedestruktionsrate mit zunehmendem Heizbedarf, ausgenommen der Haushaltswärmetauscher. An Sommertagen mit einer Umgebungstemperatur von 20 °C nimmt die Exergiedestruktionsrate sowohl im getrennten als auch im kombinierten System ab, wenn der Heizwärmebedarf von 2 MW auf 8 MW steigt. Diese Abnahme ist auf den verringerten Massenstrom der Ammoniak-Wasser-Lösung in beiden Systemen zurückzuführen. Die Reduktion des Lösungsmassenstroms steht im Zusammenhang mit dem steigenden Massenstrom des geothermischen Heißwassers im Haushaltswärmetauscher, welcher erforderlich ist, um die zunehmende Heizlast zu decken. Darüber hinaus liegt die Exergiedestruktionsrate im kombinierten System bei allen betrachteten Heizlasten unterhalb der Werte des getrennten Systems. Dies lässt sich durch den geringeren Energiebedarf für Lüfter und Pumpen sowie die höhere netto erzeugte Leistung im kombinierten System erklären.

v. Wie wirken sich Schwankungen der Umgebungstemperatur auf die Exergieeffizienz von Trigenerationssystemen unter Auslegungsabweichungen in verschiedenen Jahreszeiten aus, und welche Tendenzen lassen sich hinsichtlich der Netto-Stromerzeugung an Winter- und Sommertagen beobachten?

Unter Winterbedingungen mit einer Umgebungstemperatur von 8 °C beträgt die Exergieeffizienz 52,5 % bei der niedrigsten untersuchten Außentemperatur von −10 °C. Mit steigender Umgebungstemperatur auf −1 °C erhöht sich die Exergieeffizienz auf ein lokales Maximum von 54 %. Wird die Außentemperatur weiter bis auf 16 °C erhöht, sinkt die Effizienz auf etwa 47 %. Zusätzlich ist an Wintertagen eine Abnahme der Stromerzeugung mit steigender Umgebungstemperatur zu beobachten. Diese Entwicklung ist auf den Anstieg des Turbinenrückdrucks zurückzuführen, der die spezifische Arbeit der Turbine sowie die Nettoleistung reduziert. An Sommertagen mit einer Umgebungstemperatur von 20 °C nimmt die Exergieeffizienz beider Systeme mit steigender Außentemperatur ab. Bis zu einer Umgebungstemperatur von 23,5 °C bleibt die Exergieeffizienz des kombinierten Systems jedoch höher als jene des getrennten Systems. Wird die Außentemperatur weiter auf 30 °C erhöht, weist das getrennte System höhere Exergieeffizienzen auf als das kombinierte. Auch im Sommer sinkt die netto erzeugte Leistung mit zunehmender Umgebungstemperatur. Das kombinierte System erzielt jedoch über den gesamten Temperaturbereich hinweg eine höhere Nettoleistung als das getrennte System.

vi. Wie reagiert die gesamte Exergiedestruktionsrate von Trigenerationssystemen auf Veränderungen der Umgebungstemperatur während Winter- und Sommertagen unter Nicht-Auslegungsbedingungen?

Unter Winterbedingungen bei einem Heizwärmebedarf von 8 MW nimmt die gesamte Exergiedestruktionsrate mit steigender Umgebungstemperatur zunächst ab. Sie sinkt von 3907 kW bei −10 °C auf ein lokales Minimum von 3427 kW bei 8 °C. Wird die Umgebungstemperatur weiter auf 16 °C erhöht, steigt die Exergiedestruktionsrate erneut leicht an und erreicht 3468 kW. Im Kondensator des Kalina-Kreislaufs gehen die Exergieverluste aufgrund geringerer Temperaturgradienten und reduzierter Irreversibilitäten zurück. Unter Sommerbedingungen bei einem Heizwärmebedarf von 2 MW verringert sich die Exergiedestruktionsrate im getrennten System mit zunehmender Umgebungstemperatur von 4952 kW bei 18 °C auf 4068 kW bei 30 °C. Im kombinierten System zeigt sich ein ähnlicher

Trend, wobei die Exergiedestruktionsrate von 4582 kW bei 18 °C auf 4429 kW bei 30 °C abnimmt.

vii. Wie hängen die Stromgestehungskosten (LCOE) von Trigenerationssystemen mit den Pinch-Point-Temperaturdifferenzen in den Wärmetauschern zusammen?

Die Stromgestehungskosten steigen mit zunehmender Pinch-Point-Temperaturdifferenz im Haushaltswärmetauscher. Zudem liegen die Stromgestehungskosten im kombinierten System bei allen untersuchten Werten der Pinch-Point-Temperaturdifferenz im Haushaltswärmetauscher durchgängig unter denen des getrennten Systems. Auch mit zunehmender Pinch-Point-Temperaturdifferenz im Kondensator des Kalina-Kreislaufs steigen die Stromgestehungs-kosten. In diesem Fall sind die Stromgestehungskosten im getrennten und im kombinierten System nahezu identisch. In beiden Systemen erhöhen sich die Stromgestehungskosten von etwa 12 ct/kWh bei einer Pinch-Point-Temperaturdifferenz von 5 K auf rund 16 ct/kWh bei einer Temperaturdifferenz von 20 K.

viii. Wie hängen die Stromgestehungskosten (LCOE) von Trigenerationssystemen mit den Vorlauftemperaturen der Heizung und den Temperaturen des geothermischen Heißwassers zusammen?

Die Stromgestehungskosten steigen in beiden Systemen mit zunehmender Vorlauftemperatur der Heizungsversorgung. Ursache dafür ist die sinkende Netto-Stromerzeugung. Mit steigender Vorlauftemperatur wird mehr geothermisches Heißwasser dem Haushaltswärmetauscher zugeführt, wodurch der Massenstrom zum Kalina-Kreislauf verringert wird. Dies führt zu einer Reduktion der Turbinenleistung und somit zu einem Anstieg der Stromgestehungskosten. Das kombinierte System weist bei allen untersuchten Vorlauftemperaturen durchgängig niedrigere LCOE-Werte auf als das getrennte System. Umgekehrt sinken die Stromgestehungskosten in beiden Systemen mit steigender Temperatur des geothermischen Heißwassers. Bei einer Temperatur des Heißwassers von 120 °C liegen die Stromgestehungskosten bei etwa 37 ct/kWh. Bei einer Temperatur von 200 °C sinken sie auf rund 14 ct/kWh. Diese Reduktion ist auf die steigende netto erzeugte Leistung zurückzuführen. Bei höherer Heißwassertemperatur wird für die Bereitstellung der konstanten Vorlauftemperatur von 90 °C ein geringerer Massenstrom im Haushaltswärmetauscher benötigt. Dadurch kann ein größerer Anteil des geothermischen Wassers dem Kalina-Kreislauf zugeführt werden, was zu einem höheren Turbinenmassenstrom und somit zu einer gesteigerten Stromproduktion führt. Zusätzlich zeigt das kombinierte System bei allen untersuchten Temperaturen des geothermischen Heißwassers eine um etwa 4 % geringere LCOE als das getrennte System.

References

[1] J. Nairn, A. Moise, B. Ostendorf, The impact of humidity on Australia's operational heatwave services, Climate Services, 27 (2022), 100315.
https://doi.org/10.1016/j.cliser.2022.100315
[2] Climate Council (Australia), Hitting Home Report, online:
https://www.climatecouncil.org.au/wp-content/uploads/2021/01/hitting-home-report-V7-210122.pdf
[3] R. Serrano-Notivoli, E. Tejedor, P. Sarricolea, O. Meseguer-Ruiz, M. de Luis, M. Á. Saz, L. A. Longares, J. Olcina, Unprecedented warmth: A look at Spain's exceptional summer of 2022, Atmospheric Research, 293 (2023), 106931.
https://doi.org/10.1016/j.atmosres.2023.106931
[4] R. M. Trigo, A. M. Ramos, P. J. Nogueira, F. D. Santos, R. Garcia-Herrera, C. Gouveia, F. E. Santo, Evaluating the impact of extreme temperature based indices in the 2003 heatwave excessive mortality in Portugal, Environmental Science & Policy, 12 (2009), 844-854.
https://doi.org/10.1016/j.envsci.2009.07.007
[5] O. Beyraghdar Kashkooli, S. Karimian, R. Modarres, Spatiotemporal variability of the Persian Gulf and Oman Sea marine heatwaves during 1982–2020, Marine Pollution Bulletin, 184 (2022), 114174.
https://doi.org/10.1016/j.marpolbul.2022.114174
[6] M. Yu, S. Zhang, H. Ning, Z. Li, K. Zhang, Assessing the 2023 Canadian wildfire smoke impact in Northeastern US: Air quality, exposure and environmental justice, Science of The Total Environment, 926 (2024), 171853.
https://doi.org/10.1016/j.scitotenv.2024.171853
[7] Government of Canada, Surviving heat: Impacts of the 2021 Western heat dome in Canada, online:
https://science.gc.ca/site/science/en/blogs/science-health/surviving-heat-impacts-2021-western-heat-dome-canada
[8] F. Roubille, E. Matzner-Lober, S. Aguilhon, M. Rene, L. Lecourt, M. Galinier, J.-E. Ricci, N. Molinari, Impact of global warming on weight in patients with heart failure during the 2019 heatwave in France, Archives of Cardiovascular Diseases Supplements, 15 (2023), 38-39.
https://doi.org/10.1016/j.acvdsp.2022.10.068
[9] Deutscher Wetterdienst (DWD), Temperature records (tmax, tmin), online:
https://rcccm.dwd.de/DWD-RCCCM/EN/products/significant/records/records_tmax_tmin.pdf?__blob=publicationFile&v=11
[10] P. Bissolli, T. Deutschländer, F. Imbery, S. Haeseler, C. Lefebvre, J. Blahak, R. Fleckenstein, J. Brever, M. Rocek, F. Kreienkamp, S. Rösner, K.-J. Schreiber, Hitzewelle Juli 2019 in Westeuropa – neuer nationaler Rekord in Deutschland, online:
https://www.dwd.de/DE/leistungen/besondereereignisse/temperatur/20190801_hitzerekord_juli2019.pdf
[11] Zahlen und Fakten zum Klimawandel in Deutschland, in: Deutscher Wetterdienst (DWD) (Hrsg.), Klima-Pressekonferenz des Deutschen Wetterdienstes, Berlin, 26.03.2019, 2019.
[12] B. Alahmad, A. F. Shakarchi, H. Khraishah, M. Alseaidan, J. Gasana, A. Al-Hemoud, P. Koutrakis, M. A. Fox, Extreme temperatures and mortality in Kuwait: Who is vulnerable?, Science of The Total Environment, 732 (2020), 139289.
https://doi.org/10.1016/j.scitotenv.2020.139289
[13] A. Merlone, H. Al-Dashti, N. Faisal, R. S. Cerveny, S. AlSarmi, P. Bessemoulin, M. Brunet, F. Driouech, Y. Khalatyan, T. C. Peterson, F. Rahimzadeh, B. Trewin, M. M. Abdel Wahab, S. Yagan, G. Coppa, D. Smorgon, C. Musacchio, D. Krahenbuhl, Temperature extreme records: World Meteorological Organization metrological and meteorological evaluation of the 54.0 °C observations in Mitribah, Kuwait and Turbat, Pakistan in 2016/2017, International Journal of Climatology, 39 (2019), 5154-5169.
https://doi.org/10.1002/joc.6132
[14] Umweltbundesamt, Emissionsquellen, Online:
https://www.umweltbundesamt.de/themen/klima-energie/treibhausgas-emissionen/emissionsquellen
[15] AGEB AG Energiebilanzen e.V., Anwendungsbilanzen zur Energiebilanz Deutschland: Endenergieverbrauch nach Energieträgern und Anwendungszwecken, online:
https://ag-energiebilanzen.de/8-0-Anwendungsbilanzen.html
[16] International Energy Agency (IEA), Renewables 2020, online:
https://www.iea.org/reports/renewables-2020

[17] Energy Information Administration (EIA), Annual Energy Review (Renewables), online:
https://www.eia.gov/renewable/annual/
[18] Ministry of New and Renewable Energy, Annual Report 2020–21, online:
https://mnre.gov.in/img/documents/uploads/file_f-1616137811140.pdf
[19] Danish Energy Agency, Denmark's Energy and Climate Outlook 2021, online:
https://ens.dk/en/our-responsibilities/energy-climate-outlook
[20] Red Eléctrica de España, The Spanish Electricity System 2020, online:
https://www.ree.es/en/datos/publications/spanish-electricity-system/annual-report/spanish-electricity-system-2020
[21] U.S. Department of Energy, Renewable Energy Data Book, online:
https://www.energy.gov/eere/analysis/articles/renewable-energy-data-book
[22] National Bureau of Statistics of China, China Statistical Yearbook 2024, online:
https://www.stats.gov.cn/english/Statisticaldata/yearbook/
[23] Fraunhofer Institute for Solar Energy Systems ISE, Energy Charts: Share of Renewable Energy in Germany, online:
https://www.energy-charts.de/energy_pie.htm?year=2023
[24] Umweltbundesamt, Erneuerbare Energien in Deutschland: Daten zur Entwicklung im Jahr 2019, Dessau-Roßlau, März 2020, online:
https://www.umweltbundesamt.de/publikationen/erneuerbare-energien-in-deutschland-2019
[25] Clean Energy Wire, Total electricity consumption in Germany largely stable in 2018, online:
https://www.cleanenergywire.org/news/total-electricity-consumption-germany-largely-stable-2018
[26] German Federal Ministry for Economic Affairs and Climate Action (BMWK), Renewable Energy, online:
https://www.bmwk.de/Redaktion/EN/Dossier/renewable-energy.html
[27] International Energy Agency (IEA), Germany’s Renewable Energy Act, online:
https://www.iea.org/policies/12392-germanys-renewables-energy-act
[28] International Renewable Energy Agency (IRENA), Geothermal Power, online:
https://www.irena.org/geothermal
[29] European Geothermal Energy Council, online:
https://www.egec.org.
[30] T. Eller, Thermoökonomische Untersuchung verschiedener Anlagenkonzepte zur geothermischen Strom- und Wärmeerzeugung, PhD thesis, Berlin: Logos, 2021, XII, 152 S., (Reihe: D. Brüggemann (Hrsg.): Thermodynamik – Energie, Umwelt, Technik; 36), ISBN 978-3-8325-5367-8
[31] H. Ghaebi, B. Farhang, T. Parikhani, H. Rostamzadeh, Energy, exergy and exergoeconomic analysis of a cogeneration system for power and hydrogen production purpose based on TRR method and using low grade geothermal source, Geothermics, 71 (2018), 132-145.
https://doi.org/10.1016/j.geothermics.2017.08.011
[32] S. M. S. Mahmoudi, M. Akbari Kordlar, A new flexible geothermal based cogeneration system producing power and refrigeration, Renewable Energy, 123 (2018), 499-512.
https://doi.org/10.1016/j.renene.2018.02.060
[33] M. Coroiu, Geothermal energy for residential co-generation, Procedia - Social and Behavioral Sciences, 195 (2015), 2501-2510.
https://doi.org/10.1016/j.sbspro.2015.06.340
[34] M. Kolahi, A. Nemati, M. Yari, Performance optimization and improvement of a flash-binary geothermal power plant using zeotropic mixtures with PSO algorithm, Geothermics, 74 (2018), 45-56.
https://doi.org/10.1016/j.geothermics.2018.02.004
[35] T. Gholizadeh, M. Vajdi, H. Rostamzadeh, A new trigeneration system for power, cooling, and freshwater production driven by a flash-binary geothermal heat source, Renewable Energy, 148 (2019), 31-43.
https://doi.org/10.1016/j.renene.2019.11.154
[36] F. S. T. Haklıdır, R. Şengün, H. Aydın, Characterization and comparison of geothermal fluids geochemistry within the Kızıldere geothermal field in Turkey: New findings with power capacity expanding studies, Geothermics, 94 (2021), 102110.
https://doi.org/10.1016/j.geothermics.2021.102110
[37] M. H. Nabat, S. Sharifi, A. R. Razmi, Thermodynamic and economic analyses of a novel liquid air energy storage (LAES) coupled with thermoelectric generator and Kalina cycle, Journal of Energy Storage, 45 (2022), 103711.
https://doi.org/10.1016/j.est.2021.103711
[38] F. Musharavati, S. Khanmohammadi, A. H. Pakseresht, S. Khanmohammadi, Enhancing the performance of an integrated CCHP system including ORC, Kalina, and refrigeration cycles through employing TEG: 3E analysis and multi-criteria optimization, Geothermics, 89 (2021), 101973.
https://doi.org/10.1016/j.geothermics.2020.101973

[39] M. Ebadollahi, H. Rostamzadeh, M. Z. Pedram, H. Ghaebi, M. Amidpour, Proposal and assessment of a new geothermal-based multigeneration system for cooling, heating, power, and hydrogen production, using LNG cold energy recovery, Renewable Energy, 135 (2019), 66-87.
https://doi.org/10.1016/j.renene.2018.11.108
[40] E. Assareh, S. M. Alirahmi, P. Ahmadi, A sustainable model for the integration of solar and geothermal energy boosted with thermoelectric generators (TEGs) for electricity, cooling and desalination purpose, Geothermics, 92 (2021), 102042.
https://doi.org/10.1016/j.geothermics.2021.102042
[41] Y. Cao, M. A. Ehyaei, Energy, exergy, exergoenvironmental, and economic assessments of the multigeneration system powered by geothermal energy, Journal of Cleaner Production, 313 (2021), 127823.
https://doi.org/10.1016/j.jclepro.2021.127823
[42] L. Ozgener, A. Hepbasli, I. Dincer, Energy and exergy analysis of the Gonen geothermal district heating system, Turkey, Geothermics, 34 (2005), 632-645.
https://doi.org/10.1016/j.geothermics.2005.06.001
[43] U.S. Environmental Protection Agency (EPA), CHP Benefits, online:
https://www.epa.gov/chp/chp-benefits
[44] International Energy Agency (IEA), Official website, online:
https://www.iea.org/
[45] A. Bloess, Modeling of combined heat and power generation in the context of increasing renewable energy penetration, Applied Energy, 267 (2020), 114727.
https://doi.org/10.1016/j.apenergy.2020.114727
[46] H. Yuan, P. Zhou, N. Mei, Performance analysis of a solar-assisted OTEC cycle for power generation and fishery cold storage refrigeration, Applied Thermal Engineering, 90 (2015), 809-819.
http://dx.doi.org/10.1016/j.applthermaleng.2015.07.072
[47] X. Li, Z. Wang, M. Yang, G. Yuan, Modeling and simulation of a novel combined heat and power system with absorption heat pump based on solar thermal power tower plant, Energy, 186 (2019), 115845.
https://doi.org/10.1016/j.energy.2019.07.172
[48] J. Wang, J. Wang, P. Zhao, Y. Dai, Proposal and thermodynamic assessment of a new ammonia-water based combined heating and power (CHP) system, Energy Conversion and Management, 184 (2019), 277-289.
https://doi.org/10.1016/j.enconman.2019.01.062
[49] S. Khanmohammadi, F. Musharavati, O. Kizilkan, D. D. Nguyen, Proposal of a new parabolic solar collector assisted power-refrigeration system integrated with thermoelectric generator using 3E analyses: Energy, exergy, and exergo-economic, Energy Conversion and Management, 220 (2020), 113055.
https://doi.org/10.1016/j.enconman.2020.113055
[50] H. Chen, K. Xue, Y. Wu, G. Xu, X. Jin, W. Liu, Thermodynamic and economic analyses of a solar-aided biomass-fired combined heat and power system, Energy, 214 (2021), 119023.
https://doi.org/10.1016/j.energy.2020.119023
[51] EcoMENA, Trigeneration systems, online:
https://www.ecomena.org/trigeneration-systems/
[52] N. Ghasemzadeh, S. S. Laleh, S. Soltani, M. Yari, M. A. Rosen, Using green energy sources in trigeneration systems to reduce environmental pollutants: Thermodynamic and environmental evaluation, Sustainability, 17 (2023), 13222.
https://doi.org/10.3390/su151713222
[53] E. Assareh, S. M. Alirahmi, P. Ahmadi, A Sustainable model for the integration of solar and geothermal energy boosted with thermoelectric generators (TEGs) for electricity, cooling and desalination purpose, Geothermics, 92 (2021), 102042.
https://doi.org/10.1016/j.geothermics.2021.102042
[54] S. M. Babaei, M. H. Nabat, F. Lashgari, M. Z. Pedram, A. Arabkoohsar, Thermodynamic analysis and optimization of an innovative hybrid multi-generating liquid air energy storage system, Journal of Energy Storage, 43 (2021), 103262.
https://doi.org/10.1016/j.est.2021.103262
[55] E. Akrami, A. Chitsaz, H. Nami, S. M. S. Mahmoudi, Energetic and exergoeconomic assessment of a multi-generation energy system based on indirect use of geothermal energy, Energy, 124 (2017), 625–639.
https://doi.org/10.1016/j.energy.2017.02.006
[56] U. Sahoo, R. Kumar, P. C. Pant, R. Chaudhary, Development of an innovative polygeneration process in hybrid solar-biomass system for combined power, cooling and desalination, Applied Thermal Engineering, 120 (2017), 560-567.
https://doi.org/10.1016/j.applthermaleng.2017.04.034
[57] B. Eisavi, S. Khalilarya, A. Chitsaz, M. A. Rosen, Thermodynamic analysis of a novel combined cooling, heating and power system driven by solar energy, Applied Thermal Engineering, 129 (2018), 1219-1229.

https://doi.org/10.1016/j.applthermaleng.2017.10.132
[58] J. Wang, C. Ma, J. Wu, Thermodynamic analysis of a combined cooling, heating and power system based on solar thermal biomass gasification, Applied Energy, 247 (2019), 102-115.
https://doi.org/10.1016/j.apenergy.2019.04.039
[59] S. M. Alirahmi, S. R. Dabbagh, P. Ahmadi, S. Wongwises, Multi-objective design optimization of a multi-generation energy system based on geothermal and solar energy, Energy Conversion and Management, 205 (2020), 112426.
https://doi.org/10.1016/j.enconman.2019.112426
[60] Y. Chen, J. Xu, D. Zhao, J. Wang, P. D. Lund, Exergo-economic assessment and sensitivity analysis of a solar-driven combined cooling, heating and power system with organic Rankine cycle and absorption heat pump, Energy, 230 (2021), 120717.
https://doi.org/10.1016/j.energy.2021.120717
[61] U. Serpen, R. DiPippo, Turkey - A geothermal success story: A retrospective and prospective assessment, Geothermics, 101 (2022), 102370.
https://doi.org/10.1016/j.geothermics.2022.102370
[62] M. De Rosa, K. Gainsford, F. Pallonetto, D. P. Finn, Diversification, concentration and renewability of the energy supply in the European Union, Energy, 253 (2022), 124097.
https://doi.org/10.1016/j.energy.2022.124097.
[63] T. Eller, F. Heberle, D. Brüggemann, Transient simulation of geothermal combined heat and power generation for a resilient energetic and economic evaluation, Energies, 12 (2019), 894.
https://doi.org/10.3390/en12050894
[64] O. Barkhordarian, A. Behbahaninia, R. Bahrampoury, A novel ammonia-water combined power and refrigeration cycle with two different cooling temperature levels, Energy, 120 (2017), 816-826.
http://dx.doi.org/10.1016/j.energy.2016.11.127
[65] T. H. Çetin, J. Zhu, E. Ekici, M. T. Kanoglu, Thermodynamic assessment of a geothermal power and cooling cogeneration system with cryogenic energy storage, Energy Conversion and Management, 260 (2022), 115616.
https://doi.org/10.1016/j.enconman.2022.115616
[66] Y. Wang, L. Yu, B. Nazir, L. Zhang, H. Rahmani, Innovative geothermal-based power and cooling cogeneration system; Thermodynamic analysis and optimization, Sustainable Energy Technologies and Assessments, 44 (2021), 101070.
https://doi.org/10.1016/j.seta.2021.101070
[67] M. Leveni, R. Cozzolino, Energy, exergy, and cost comparison of Goswami cycle and cascade organic Rankine cycle/absorption chiller system for geothermal application, Energy Conversion and Management, 227 (2021), 113598.
https://doi.org/10.1016/j.enconman.2020.113598
[68] A. H. Mosaffa, L. Garousi Farshi, S. Khalili, A novel enhanced ammonia-water power/cooling cogeneration system with dual level cooling temperature: Thermodynamic and economic assessments, Energy Conversion and Management, 244 (2021), 114530.
https://doi.org/10.1016/j.enconman.2021.114530
[69] J. W. Lund, G. W. Huttrer, A. N. Toth, Characteristics and trends in geothermal development and use, 1995 to 2020, Geothermics, 147 (2022), 102522.
https://doi.org/10.1016/j.geothermics.2022.102522
[70] M. Kauw, R. M. J. Benders, C. Visser, Green methanol from hydrogen and carbon dioxide using geothermal energy and/or hydropower in Iceland or excess renewable electricity in Germany, Energy, 90 (2015), 208-217.
https://doi.org/10.1016/j.energy.2015.06.002
[71] K. Menberg, F. Heberle, C. Bott, D. Brüggemann, P. Bayer, Environmental performance of a geothermal power plant using a hydrothermal resource in the Southern German Molasse Basin, Renewable Energy, 167 (2020), 20-31. https://doi.org/10.1016/j.renene.2020.11.028
[72] H. Ghaebi, A. Shekari Namin, H. Rostamzadeh, Performance assessment and optimization of a novel multi-generation system from thermodynamic and thermoeconomic viewpoints, Energy Conversion and Management, 165 (2018), 419-439.
https://doi.org/10.1016/j.enconman.2018.03.055
[73] F. Musharavati, S. Khanmohammadi, A. Pakseresht, A novel multi-generation energy system based on geothermal energy source: Thermo-economic evaluation and optimization, Energy Conversion and Management, 230 (2021), 113829.
https://doi.org/10.1016/j.enconman.2021.113829
[74] F. Yilmaz, Performance and environmental impact assessment of a geothermal-assisted combined plant for multi-generation products, Sustainable Energy Technologies and Assessments, 46 (2021), 101291.
https://doi.org/10.1016/j.seta.2021.101291

[75] H. Gnaifaid, H. Ozcan, Development and multiobjective optimization of an integrated flash-binary geothermal power plant with reverse osmosis desalination and absorption refrigeration for multi-generation, Geothermics, 89 (2021), 101949.
https://doi.org/10.1016/j.geothermics.2020.101949
[76] P. Behnam, A. Arefi, M. B. Shafii, Exergetic and thermoeconomic analysis of a trigeneration system producing electricity, hot water, and fresh water driven by low-temperature geothermal sources, Energy Conversion and Management, 157 (2018), 266–276.
https://doi.org/10.1016/j.enconman.2017.12.014
[77] M. Akbari Kordlar, F. Heberle, D. Brüggemann, Evaluation and optimization of the annual performance of a novel tri-generation system driven by geothermal brine in off-design conditions, Applied Sciences, 10 (2020), 10186532.
https://doi.org/10.3390/app10186532
[78] A. I. Kalina, Combined-cycle system with novel bottoming cycle, Journal of Engineering for Gas Turbines and Power, 106 (1984), 737-742.
https://doi.org/10.1115/1.3239632
[79] F. P. E. Carré, Improvement in apparatus for freezing liquids, U.S. Patent 30,201, 1860.
[80] A. I. Kalina, H. M. Liebovitz, Kalina cycle promises improved efficiency, Modern Power Systems Review, 7 (1987), 19-23.
[81] A. Kalina, M. Tribus, Y. El-Sayed, A theoretical approach to the thermophysical properties of two-miscible-component mixtures for the purpose of power-cycle analysis, ASME Paper 86-WA/HT-54, 1986.
[82] P. Srikhirin, S. Aphornratana, S. Chungpaibulpatana, A review of absorption refrigeration technologies, Renewable and Sustainable Energy Reviews, 5 (2001), 343-372.
https://doi.org/10.1016/S1364-0321(01)00003-X
[83] T. Eller, F. Heberle, D. Brüggemann, Techno-economic analysis of novel working fluid pairs for the Kalina cycle, Energy Procedia, 129 (2017), 113–120.
https://doi.org/10.1016/j.egypro.2017.09.175
[84] F. Heberle, T. Eller, D. Brüggemann, Thermoeconomic evaluation of one- and double-stage ORC for geothermal combined heat and power production, in: Proceedings of the European Geothermal Congress, Strasbourg, France, 2016, 19-23.
[85] S. B. Mousavi, M. H. Nabat, A. R. Razmi, A comprehensive study and multi-criteria optimization of a novel sub-critical liquid air energy storage (SC-LAES), Energy Conversion and Management, 258 (2022), 115549.
https://doi.org/10.1016/j.enconman.2022.115549
[86] K. A. Klein, F. L. Alvarado, *EES: Engineering Equation Solver*, Version 6.648 ND, F-Chart Software, Middleton, WI, USA, 2004.
[87] O. M. Ibrahim, S. A. Klein, Thermodynamic properties of ammonia-water mixtures, ASHRAE Transactions, 1993, 1495–1502.
[88] W. Wagner, A. Pruß, The IAPWS formulation 1995 for the thermodynamic properties of ordinary water substance for general and scientific use, Journal of Physical and Chemical, 31 (2002).
https://aip.scitation.org/doi/10.1063/1.1461829
[89] T. Fujita, S. Kikuchi, Vapor pressure of Aqueous Solutions of Ethylene Glycol, Transactions of the Japan Society of Refrigerating and Air Conditioning Engineers, 6 (2011), 183-186.
[90] D. J. Lee, W. H. Huang, Enthalpy-entropy compensation in micellization of sodium dodecyl sulphate in water/methanol, water/ethylene glycol and water/glycerol binary mixtures, Colloid and Polymer Science, 274 (1996), 160–165. https://doi.org/10.1007/BF00663448
[91] Aspen Technology Inc., ASPEN PLUS, Version 10, 2017.
[92] M. H. Nabat, A. R. Razmi, S. Sharifi, A. Arabkoohsar, M. Shahbakhti, Liquid air energy storage, in: Future Grid-Scale Energy Storage Solutions, 2023, 345-408.
https://doi.org/10.1016/B978-0-323-90786-6.00016-9
[93] F. Heberle, M. Hofer, N. Ürlings, H. Schröder, T. Anderlohr, D. Brüggemann, Techno-economic analysis of a solar thermal retrofit for an air-cooled geothermal Organic Rankine Cycle power plant, Renewable Energy, 113 (2017), 494-502.
https://doi.org/10.1016/j.renene.2017.06.031
[94] O. Aljolani, F. Heberle, D. Brüggemann, Thermo-economic and environmental analysis of a CO_2 residential air conditioning system in comparison to HFC-410A and HFC-32 in temperate and subtropical climates, Applied Energy, 353 (2023), 122073.
https://doi.org/10.1016/j.apenergy.2023.122073
[95] O. Aljolani, F. Heberle, D. Brüggemann, Thermodynamic analysis of a CO_2 air-conditioning concept for multi-family houses in temperate and subtropical climates based on experimental data, Applied Thermal Engineering, 234 (2023), 121273.
https://doi.org/10.1016/j.applthermaleng.2023.121273

[96] H. Caliskan, S. Ekici, Y. Sohret, Advanced exergy analysis of the turbojet engine main components considering mexogenous, endogenous, exegenous, avoidable and unavoidable exergy destructions, Propulsion and Power Research, 11 (2022), 391-400.
https://doi.org/10.1016/j.jppr.2022.07.002
[97] M. Akbari Kordlar, S. M. S. Mahmoudi, Exergeoconomic analysis and optimization of a novel cogeneration system producing power and refrigeration, Energy Conversion and Management, 134 (2017), 208-220.
https://doi.org/10.1016/j.enconman.2016.12.007
[98] S. Khatoon, S. Ishaque, M. Kim, Modeling and analysis of air-cooled heat exchanger integrated with supercritical carbon dioxide recompression Brayton cycle, Energy Conversion and Management, 232 (2021), 113895.
https://doi.org/10.1016/j.enconman.2021.113895
[99] E. Khodaei, M. Yari, S. M. S. Mahmoudi, Thermoeconomic optimization for a solar power generating system capable of storing energy by using calcium looping process, Energy Conversion and Management, 293 (2023), 117403.
https://doi.org/10.1016/j.enconman.2023.117403
[100] J. G. Andreasen, E. Baldasso, M. Ryhl Kærn, T. Weith, F. Heberle, D. Brüggemann, F. Haglind, Techno-economic feasibility analysis of zeotropic mixtures and pure fluids for organic Rankine cycle systems, Applied Thermal Engineering, 192 (2021), 116791.
https://doi.org/10.1016/j.applthermaleng.2021.116791
[101] R. Turton, R. C. Bailie, W. B. Whiting, J. A. Shaeiwitz, Analysis, synthesis, and design of chemical processes, Prentice Hall, 2009.
[102] G. Ulrich, P. Vasudevan, Chemical engineering process design and economics, 2nd ed., Process Publishing, Durham, NH, USA, 2004.
[103] A. Bejan, Thermal design and optimization, John Wiley & Sons, 1996.
[104] Marshall and Swift Equipment Cost Index (Q1 2015), online:
https://scholars.unh.edu/cost/6/
[105] D. Toselli, F. Heberle, D. Brüggemann, Techno-economic analysis of hybrid binary cycles with geothermal energy and biogas waste heat recovery, Energies, 12 (2019) 1969.
https://doi.org/10.3390/en12101969
[106] D. H. Cooke, On Prediction of Off-Design Multistage Turbine Pressures by Stodola's Ellipse, Journal of Engineering for Gas Turbines and Power, 107 (1985), 596-606.
https://doi.org/10.1115/1.3239778
[107] A. Stodola, L. C. Lowenstein, Steam and Gas Turbines, McGraw-Hill, New York, 1927, Vol. 1, p. 316.
[108] H. Li, D. Hu, M. Wang, Y. Dai, Off-design performance analysis of Kalina cycle for low temperature geothermal source, Applied Thermal Engineering, 107 (2016), 728-737.
https://doi.org/10.1016/j.applthermaleng.2016.07.014
[109] J. Wang, J. Wang, Y. Dai, P. Zhao, Assessment of off-design performance of a Kalina cycle driven by low-grade heat source, Energy, 138 (2019), 459-472.
https://doi.org/10.1016/j.energy.2017.07.081
[110] R. Gabbrielli, A novel design approach for small scale low enthalpy binary geothermal power plants, Energy Conversion and Management, 64 (2012), 263-272.
https://doi.org/10.1016/j.enconman.2012.04.017.
[111] F. Heberle, D. Brüggemann, Thermo-Economic Analysis of Zeotropic Mixtures and Pure Working Fluids in Organic Rankine Cycles for Waste Heat Recovery, Energies, 9 (2016).
https://doi.org/10.3390/en9040226
[112] K. Thulukkanam, Heat exchanger design handbook, CRC Press, Taylor & Francis Group, 2013.
[113] A. S. Lavine, F. P. Incropera, D. P. DeWitt, T. L. Bergman, Fundamentals of Heat and Mass Transfer, 8th Edition (2018).
[114] B. Liang, M. Chen, Y. Orooji, Effective parameters on the performance of ground heat exchangers: A review of latest advances, Geothermics, 98 (2022), 102283.
https://doi.org/10.1016/j.geothermics.2021.102283
[115] K. J. Bell, Delaware Method for Shell-Side Design, in Heat Transfer Equipment Design, edited by R. K. Shah, E. C. Subbarao, and R. A. Mashelkar, Hemisphere Publishing, Washington, DC (1988), pp. 227–254.
[116] J. Taborek, Shell-and-Tube Heat Exchangers: Single-Phase Flow, in Handbook of Heat Exchanger Design, edited by G. F. Hewitt, Begell House, New York (1998), pp. 3.3.3-1–3.3.11-5.
[117] R. K. Shah, D. P. Sekulić, Fundamentals of heat exchanger design, John Wiley & Sons, 2003.
[118] K. J. Bell, Final report of the cooperative research program on shell-and-tube heat exchangers, Univ. of Delaware Engineering Experiment Station Bulletin, Vol. 5, 1963.
[119] R. W. Serth, Process Heat Transfer: Principles, Applications and Rules of Thumb, Heat Transfer Research, Inc., 2014.

[120] C. Cai, H. Feng, L. Chen, Z. Wu, Z. Xie, Constructal design of a shell-and-tube evaporator with ammonia-water working fluid, International Journal of Heat and Mass Transfer, 135 (2019), 541-547. https://doi.org/10.1016/j.ijheatmasstransfer.2019.01.142
[121] G. F. Hewitt, G. L. Shires, T. R. Bott, Process Heat Transfer, CRC Press, Boca Raton, FL, 1994.
[122] H. K. Forster, N. Zuber, Dynamics of vapor bubbles and boiling heat transfer, AIChE Journal, 1(1955), 531-535.
[123] E. U. Schlünder, Heat transfer in nucleate boiling of mixtures, International Chemical Engineering., 23 (1983), 589–599.
[124] M. P. H. Mishra, K. Varma, C. P. Sharma, Heat transfer coefficients in forced convection evaporation of refrigerant mixtures, Letters in Heat and Mass Transfer 8 (1981) 127-136. https://doi.org/10.1016/0094-4548(81)90034-5
[125] M. R. Kærn, A. Modi, J. K. Jensen, J. G. Andreasen, F. Haglind, An assessment of in-tube flow boiling correlations for ammonia-water mixtures and their influence on heat exchanger size, Applied Thermal Engineering, 93 (2016), 623-638. https://doi.org/10.1016/j.applthermaleng.2015.09.106
[126] W. Rivera, R. Best, Boiling heat transfer coefficients inside a vertical smooth tube for water/ammonia and ammonia lithium nitrate mixtures, International Journal of Heat and Mass Transfer 42 (5) (1999) 905–921. https://doi.org/10.1016/S0017-9310(98)00211-7
[127] T. Khir, R. K. Rahim, N. Ghaffour, A. B. Brahim, Experimental study on forced convective boiling of ammonia – water mixtures in a vertical smooth tube, The Arabian Journal for Science and Engineering, 30 (2005), 47-63, ISSN 1319-8025.
[128] V. L. Lea, A. Kheiri, M. Feidt, S. Pelloux-Prayer, Thermodynamic and economic optimizations of a waste heat to power plant driven by a subcritical ORC (Organic Rankine Cycle) using pure or zeotropic working fluid, Energy, 78 (2014), 622-638. https://doi.org/10.1016/j.energy.2014.10.051
[129] J. W. Palen, Shell-and-tube reboilers, in Heat Exchanger Design Handbook, Vol. 3, Hemisphere Publishing Corp., New York, 1988.
[130] S. W. Churchill, H. H. S. Chu, Correlating equations for laminar and turbulent free convection from a horizontal cylinder, International Journal of Heat and Mass Transfer, 18 (1975), 1049–1053.
[131] D. M. Smith, Mean temperature difference in cross flow, Engineering, 1934, 479–481, 606–608.
[132] K. G. Schmidt, Heat transfer to finned tubes, in: VDI Heat Atlas, Springer, Berlin, 2016. https://doi.org/10.1007/978-3-540-77877-6_94
[133] W. M. Kays, A. L. London, Compact heat exchangers, McGraw-Hill, New York, 1964.
[134] A. L. London, R. A. Seban, A generalization of the methods of heat exchanger analysis, Stanford University, 1942; also in International Journal of Heat and Mass Transfer, 23 (1980), 5–16.
[135] S. M. Jeter, Effectiveness and LMTD Correction Factor of the Cross Flow Exchanger: a Simplified and Unified Treatment, ASEE Southeast Section Conference, 2006.
[136] M. M. Shah, A general correlation for heat transfer during film condensation inside pipes, International Journal of Heat and Mass Transfer, 22 (1979), 547–556.
[137] K. J. Bell, A. J. Mueller, Wolverine engineering data book II, Wolverine Tube Inc., 2001.
[138] K. J. Bell, M. A. Ghaly, An approximate generalized method for multicomponent partial condenser, AIChE Symposium Series, 69 (1973), 72–79.
[139] A. Ganguli, S. S. Tung, J. Taborek, Parametric study of air-cooled heat exchanger finned tube geometry, AIChE Symposium Series, 81 (1985), 122–128.
[140] K. K. Robinson, D. E. Briggs, Pressure drop of air flowing across triangular pitch banks of finned tubes, Chemical Engineering Progress Symposium Series, 62 (1965), 177-184.
[141] T. Eller, F. Heberle, D. Brüggemann, Transient Simulation of Geothermal Combined Heat and Power Generation for a Resilient Energetic and Economic Evaluation, Energies, 12 (2019), 894. https://doi.org/10.3390/en12050894
[142] Verein Deutscher Ingenieure (VDI), VDI 4655: Reference load profiles of single-family and multi-family houses for the use of CHP systems, Beuth Verlag, Düsseldorf, 2008.
[143] Carrier, Hourly analysis program (HAP), Version 5.11, 2018.
[144] G. F. Hundy, Refrigeration, air conditioning and heat pumps, 5th ed., 2016.
[145] M. Akbari Kordlar, S. M. S. Mahmoudi, F. Talati, M. Yari, A. H. Mosaffa, A new flexible geothermal based cogeneration system producing power and refrigeration, part two: The influence of ambient temperature, Renewable Energy, 134 (2019), 875-887. https://doi.org/10.1016/j.renene.2018.11.082

[146] H. Li, Y. Yang, Z. Cheng, Y. Sang, Y. Dai, Study on off-design performance of transcritical CO_2 power cycle for the utilization of geothermal energy, Geothermics, 71 (2018), 369-379.
https://doi.org/10.1016/j.geothermics.2017.09.002
[147] S. Kim, T. S. Kim, J. J. Lee, Off-design performance analysis of organic Rankine cycle using real operation data from a heat source plant, Energy Conversion and Management, 133 (2017), 284-291.
https://doi.org/10.1016/j.enconman.2016.12.016
[148] G. Manente, A. Toffolo, A. Lazzaretto, M. Paci, An Organic Rankine Cycle off-design model for the search of the optimal control strategy. Energy, 58 (2013), 97-106.
https://doi.org/10.1016/j.energy.2012.12.035
[149] F. Heberle, M. Hofer, D. Brüggemann, A retrofit for Geothermal Organic Rankine Cycles based on Concentrated Solar Thermal Systems. Energy Procedia, 129 (2017), 692-699.
https://doi.org/10.1016/j.egypro.2017.09.148
[150] C. Liu, T. Gao, Off-design performance analysis of basic ORC, ORC using zeotropic mixtures and composition-adjustable ORC under optimal control strategy, Energy, 171 (2019), 95-108.
https://doi.org/10.1016/j.energy.2018.12.195
[151] S. Ogriseck, Integration of Kalina cycle in a combined heat and power plant: A case study, Applied Thermal Engineering, 29 (2009), 2843-2848.
https://doi.org/10.1016/j.applthermaleng.2009.02.006

[152] S. A. Adewusi, S. M. Zubair, Second law based thermodynamic analysis of ammonia–water absorption systems, Energy Conversion and Management, 45 (2004), 2355-2369.
https://doi.org/10.1016/j.enconman.2003.11.020

[153] R. K. Shah, D. P. Sekulić, Fundamentals of Heat Exchanger Design, John Wiley & Sons, Inc. (2003), pp. 593-597 and 652-658.
[154] R. K. Shah, D. P. Sekulić, Fundamentals of Heat Exchanger Design, John Wiley & Sons, Inc. (2003), pp. 593-597 and 391-424.
[155] R. W. Serth, Process Heat Transfer: Principles, Applications and Rules of Thumb, Heat Transfer Research, Inc. (2014) Page: 453-466.

Publications

M. Akbari Kordlar, F. Heberle, D. Brüggemann, Thermo-economic evaluation of a tri-generation system driven by geothermal brine to cover flexible heating and cooling demand, Geothermics, 110 (2023), 102678.
https://doi.org/10.1016/j.geothermics.2023.102678

M. Akbari Kordlar, F. Heberle, D. Brüggemann, Evaluation and Optimization of the Annual Performance of a Novel Tri-Generation System Driven by Geothermal Brine in Off-Design Conditions, Applied Sciences, 10 (2020), 10186532.
https://doi.org/10.3390/app10186532

Appendix A

Table A.1: Thermodynamic properties of different streams under design conditions during winter days ($T_0 = 8$ °C , $\dot{Q}_H = 8$ MW)

		Temperature (°C)	Pressure (bar)	Ammonia concentration (%)	Quality (-)	Mass flow rate (kg/s)
1	NH3-H2O	18	6.49	80	0	22.5
2	NH3-H2O	18.6	30	80	Subcooled	22.5
3	NH3-H2O	46.1	30	80	Subcooled	22.5
4	NH3-H2O	75.8	30	80	0	22.5
5	NH3-H2O	130	30	80	0.7278	22.5
6	NH3-H2O	130	30	42.14	0	6.1
7	NH3-H2O	26.6	30	42.14	Subcooled	6.1
8	NH3-H2O	130	30	94.16	1	16.4
9	NH3-H2O	67	6.49	94.16	0.9371	16.4
10	NH3-H2O	27.1	6.49	42.14	Subcooled	6.1
11	NH3-H2O	60.4	6.49	80	0.66	22.5
12	Air	8	-	-	-	2272
13	Air	18	-	-	-	2272

Table A.2: Thermodynamic properties of different streams in power section (Kalina cycle) of the separated system under design conditions during summer days ($T_0 = 20$ °C , $\dot{Q}_H = 2$ MW, $\dot{Q}_c = 2$ MW)

		Temperature (°C)	Pressure (bar)	Ammonia concentration (%)	Quality (-)	Mass flow rate (kg/s)
1	NH3-H2O	35	10.88	80	0	27.1
2	NH3-H2O	35.6	30	80	Subcooled	27.1
3	NH3-H2O	58.3	30	80	Subcooled	27.1
4	NH3-H2O	75.8	30	80	0	27.1
5	NH3-H2O	130	30	80	0.73	27.1
6	NH3-H2O	130	30	42.14	0	7.4
7	NH3-H2O	43.6	30	42.14	Subcooled	7.4
8	NH3-H2O	130	30	94.16	1	19.8
9	NH3-H2O	86.6	10.88	94.16	0.96	19.8
10	NH3-H2O	43.92	10.88	42.14	Subcooled	7.4
11	NH3-H2O	80	10.88	80	0.68	27.2
12	Air	20	-	-	-	2708
13	Air	30	-	-	-	2708

Table A.3: Thermodynamic properties of different streams in cooling section (absorption refrigeration cycle) of the separated system under design conditions during summer days ($T_0 = 20\ °\mathrm{C}$, $\dot{Q}_H = 2\ \mathrm{MW}$, $\dot{Q}_c = 2\ \mathrm{MW}$)

		Temperature (°C)	Pressure (bar)	Ammonia concentration (%)	Quality (-)	Mass flow rate (kg/s)
24	WEG	10				224
25	WEG	5				224
26	NH3-H2O	25.1	10	56	Subcooled	22.7
27	NH3-H2O	54.8	10	56	0	22.7
28	NH3-H2O	67.4	10	56	0.1572	22.7
29	NH3-H2O	67.4	10	99.9	1	3.6
30	NH3-H2O	67.4	10	48	0	19.1
31	NH3-H2O	31.8	10	48	Subcooled	19.1
32	NH3-H2O	46.4	10	99.99	0.975	3.6
33	NH3-H2O	46.6	10	99.8	1	3.6
34	NH3-H2O	46.6	10	62.53	0	0.08
35	NH3-H2O	46.4	4.1	62.53	0.7278	0.08
36	NH3-H2O	25	10	99.8	0	3.5
37	NH3-H2O	-1.3	4.1	99.8	0.01	3.5
38	NH3-H2O	4	4.1	99	0.98	3.5
39	NH3-H2O	31.9	4.1	48	Subcooled	19.1
40	NH3-H2O	34.8	4.1	56	0.136	22.7
41	NH3-H2O	25	4.1	56	0	22.7
42	Air	20	-	-	-	35
43	Air	30	-	-	-	35
44	Air	20	-	-	-	428
45	Air	30	-	-	-	428
46	Air	20	-	-	-	531.7
47	Air	30	-	-	-	531.7

Table A.4: Thermodynamic properties of different streams in power section (Kalina cycle) of the combined system under design conditions during summer days ($T_0 = 20\ °\mathrm{C}$, $\dot{Q}_H = 2\ \mathrm{MW}$, $\dot{Q}_c = 4\ \mathrm{MW}$)

		Temperature (°C)	Pressure (bar)	Ammonia concentration (%)	Quality (-)	Mass flow rate (kg/s)
1	NH3-H2O	28	8.87	80	0	32
2	NH3-H2O	28.6	30	80	Subcooled	32
3	NH3-H2O	49.4	30	80	Subcooled	32
4	NH3-H2O	75.8	30	80	0	32
5	NH3-H2O	103	30	80	0.57	32
6	NH3-H2O	103	30	56.12	0	13.9
7	NH3-H2O	55.6	30	56.12	Subcooled	13.9
8	NH3-H2O	103	30	98.39	1	18.1
9	NH3-H2O	41.3	8.87	98.93	0.96	18.1
10	NH3-H2O	54.8	8.87	56.12	0.003	13.9
11	NH3-H2O	45.4	8.87	80	0.5	32
12	Air	20	-	-	-	2185
13	Air	30	-	-	-	2185

Table A.5: Thermodynamic properties of different streams in cooling section of the combined system under design conditions during summer days ($T_0 = 20$ °C , $\dot{Q}_H = 2$ MW, $\dot{Q}_c = 4$ MW)

		Temperature (°C)	Pressure (bar)	Ammonia concentration (%)	Quality (-)	Mass flow rate (kg/s)
24	WEG	10				224
25	WEG	5				224
26	NH3-H2O	25.1	10	56	Subcooled	13.9
27	NH3-H2O	54.8	10	56	0	13.9
28	NH3-H2O	80.67	10	56	0.27	13.9
29	NH3-H2O	80.7	10	97	1	3.7
30	NH3-H2O	80.7	10	41	0	10.2
31	NH3-H2O	80.6	10	41	0.004	10.2
32	NH3-H2O	40.4	10	97	0.93	3.7
33	NH3-H2O	46.4	10	99.8	1	3.5
34	NH3-H2O	46.4	10	62.53	0	0.2
35	NH3-H2O	46.4	4.1	62.53	0.7278	0.2
36	NH3-H2O	25	10	99.8	0	3.5
37	NH3-H2O	-1.1	4.1	99.8	0.096	3.5
38	NH3-H2O	4	4.1	99	0.98	3.5
39	NH3-H2O	56.9	4.1	41	0.07	10.2
40	NH3-H2O	52.5	4.1	56	0.3	13.9
41	NH3-H2O	25	4.1	56	0	13.9
42	Air	20	-	-	-	74.5
43	Air	30	-	-	-	74.5
44	Air	20	-	-	-	428
45	Air	30	-	-	-	428
46	Air	20	-	-	-	747
47	Air	30	-	-	-	747
48	NH3-H2O					

Appendix B

Table B.1: Thermodynamic properties of different streams of the system in off-design conditions under winter condition ($T_0 = 8$ °C , $\dot{Q}_H = 8$ MW)

		Temperature (°C)	Pressure (bar)	Ammonia concentration (%)	Quality (-)	Mass flow rate (kg/s)
1	NH3-H2O	18	6.49	80	0	27.9
2	NH3-H2O	18.6	30	80	Subcooled	27.9
3	NH3-H2O	45.6	30	80	Subcooled	27.9
4	NH3-H2O	75.8	30	80	0	27.9
5	NH3-H2O	95.8	30	80	0.5033	27.9
6	NH3-H2O	95.8	30	60.79	0	13.8
7	NH3-H2O	42	30	60.79	Subcooled	13.8
8	NH3-H2O	95.8	30	98.96	1	14.1
9	NH3-H2O	18.7	6.49	98.96	0.9522	14.1
10	NH3-H2O	37.7	6.49	60.79	0.026	13.8
11	NH3-H2O	32.6	6.49	80	0.4818	27.9
12	Air	8	-	-	-	1254
13	Air	22.6	-	-	-	1254
14	Supply water	60	-	-	-	63.6
15	Supply water	90	-	-	-	63.6
16	Geothermal water	138	-	-	-	120
17	Geothermal water	138	-	-	-	32.1
18	Geothermal water	79.1	-	-	-	32.1
19	Geothermal water	138	-	-	-	87.9
20	Geothermal water	75.8	-	-	-	87.9
21	Geothermal water	82.4	-	-	-	87.9
22	Geothermal water	81.5	-	-	-	120

Appendix C

Table C.1: Thermodynamic properties of different streams of the system in off-design conditions with consider the pressure drop in heat exchangers under winter condition ($T_0 = 8$ °C, $\dot{Q}_H = 8$ MW)

		Temperature (°C)	Pressure (bar)	Ammonia concentration (%)	Quality (-)	Mass flow rate (kg/s)
1	NH3-H2O	21	7.141	80	0	28.3
2	NH3-H2O	21.6	30.98	80	Subcooled	28.3
3	NH3-H2O	47.6	30.39	80	Subcooled	28.3
4	NH3-H2O	76.2	30.26	80	0	28.3
5	NH3-H2O	95.4	30	80	0.5	28.3
6	NH3-H2O	95.4	30	61	0	14.2
7	NH3-H2O	44.2	28.77	61	Subcooled	14.2
8	NH3-H2O	95.4	30	98.98	1	14.2
9	NH3-H2O	25.7	7.941	98.96	0.956	14.2
10	NH3-H2O	40.6	7.941	61	0.014	14.2
11	NH3-H2O	38.7	7.941	80	0.48	28.3
12	Air	20	-	-	-	1045
13	Air	30	-	-	-	1045
14	Supply water	60	-	-	-	63.6
15	Supply water	90	-	-	-	63.6
16	Geothermal water	138	-	-	-	120
17	Geothermal water	138	-	-	-	32.1
18	Geothermal water	79.1	-	-	-	32.1
19	Geothermal water	138	-	-	-	87.9
20	Geothermal water	93.5	-	-	-	87.9
21	Geothermal water	82.6	-	-	-	87.9
22	Geothermal water	81.7	-	-	-	120

Table C.2: Pressure drop in different heat exchangers under winter condition ($T_0 = 8$ °C, $\dot{Q}_H = 8$ MW)

Component	**Pressure drop (bar)**
Boiler (shell side)	0.27
Pre-boiler (shell side)	0.13
Internal heat exchanger (shell side)	0.6
Internal heat exchanger (tube side)	1.23
Kalina cycle condenser (tube side)	0.8

Appendix D

Appendix D shows the different steps involved in determining the overall heat transfer coefficient for TEMA E shell and tube heat exchanger, using the domestic heat exchanger as an example. The thermodynamic properties of inlet and outlet streams are shown in Table D.1. These properties are calculated in off-design mode at the ambient temperature of 8 ℃ and heating demand of 8 MW.

Table D.1: Thermodynamic properties of inlet and outlet streams in domestic heat exchanger

	Temperature (°C)	Mass flow rate (kg/s)	Density (kg/m^3)	Specific heat (J/kg.K)	Dynamic viscosity (Pa.s)	Thermal conductivity ($W/m^2.K$)	Prandtl Number
17	138	23.94	927.9	4.278	0.0001996	0.6908	1.236
18	78.81	23.94	972.5	4.196	0.0003597	0.6705	2.251
14	60	47.67	983.2	4.165	0.0004664	0.6542	2.983
15	90	47.67	965.3	4.205	0.0003144	0.6778	1.951

According to the geometrical characteristics outlined in Table A.1, the crossflow area for the 90° tube layout bundle with plain tubes at or near the shell centreline for one crossflow section is calculated as 0.1587 m^2 [153]. Consequently, the shell-side Reynolds number is obtained as 15,107. According to Equation (5.90), the h_{id} is calculated as 11,455 W/m^2 K. The different coefficients represented in Equation (5.89) are as follows to find the shell side heat transfer coefficient based on the Bell-Delaware method:

$J_c = 0.998$

$J_l = 0.822$

$J_b = 0.9446$

$J_s = 0.98$

$J_r = 1$

In this regard, the shell side heat transfer coefficient is found to be around 8700 W/m^2 K.

The tube-side Reynolds number is obtained as 64,561. Using Equation (5.78), heat transfer in the single-phase process in the tube side is achieved as 9157 W/m^2 K. Based on Equation (5.74) the overall heat transfer coefficient in domestic heat exchanger is 3309 W/m^2 K.